# Kent Academic Repository

**Albanese, Valentina (2023) *Developing an innovative approach to identify novel talin-binding ligands in the brain.* Master of Research (MRes) thesis, University of Kent.**

## Downloaded from

https://kar.kent.ac.uk/101809/ The University of Kent's Academic Repository KAR

## The version of record is available from

https://doi.org/10.22024/UniKent/01.02.101809

## This document version

UNSPECIFIED

## DOI for this version

## Licence for this version

CC BY-NC-ND (Attribution-NonCommercial-NoDerivatives)

## Additional information

## Versions of research works

### Versions of Record

If this version is the version of record, it is the same as the published version available on the publisher's web site. Cite as the published version.

### Author Accepted Manuscripts

If this document is identified as the Author Accepted Manuscript it is the version after peer review but before type setting, copy editing or publisher branding. Cite as Surname, Initial. (Year) 'Title of article'. To be published in ***Title of Journal*** , Volume and issue numbers [peer-reviewed accepted version]. Available at: DOI or URL (Accessed: date).

## Enquiries

If you have questions about this document contact ResearchSupport@kent.ac.uk. Please include the URL of the record in KAR. If you believe that your, or a third party's rights have been compromised through this document please see our Take Down policy (available from https://www.kent.ac.uk/guides/kar-the-kent-academic-repository#policies).

University of Kent

# Developing an innovative approach to identify novel talin-binding ligands in the brain

School of Biosciences

Valentina Lucia Albanese
2022

# Acknowledgements

I would like to give a huge thank you to everyone who has supported me throughout this project, most specifically my amazing supervisor Professor Ben Goult who truly raises the bar for supervisors in the academic field with his endless assistance, patience, and guidance. The incredible drive and passion he has for his work is something that motivates me beyond words, and I will undoubtedly work to obtain a similar level of success for the rest of my career. The encouragement, skills, and knowledge gained from Dr Lorena Varela-Alvarez's kind and meticulous guidance will stay with me forever. I hope one day that I am able to repay the favour and inspire another generation as she inspired me. Thank you to Jack Doolan for always helping me no matter the question or task! I would also like to thank the members of Mulvihill lab, Dr Karen Baker and Dr Tara Eastwood for their friendship, assistance, and advice, with special thanks to Dr Jonathan Rebera-Walklate who graciously allowed me to work alongside him all year! I am incredibly grateful for the kindness, assistance, and support provided by Kevin Howland and the Fenton lab, specifically Dr Tim Fenton, Dr Maxmilan Jeyakumar, Dr Nicola Smith, and Paige Policelli, who taught me so much. I wish to likewise express my gratitude to Dr Jose Ortega-Roldan's lab, Technical Services, Bioscience Stores, NATS PGR, and the additional members of Goult lab: Tom Paige, Matthew Rice, William Edwards, and Yasumi Otani. A further thank you to our collaborators: Xuyao Priscilla Liu (National University of Singapore), Dr Guillaume Jacquemet (Turku Bioscience BioCity, Finland), and Dr Devrim Kilinc (Institut Pasteur de Lille, France). Finally, a huge thank you to all my family and friends for their ongoing support and patience!

# Abstract

Cell adhesion, a process underlying the maintenance and development of multicellularity, is fundamentally dependent on the activity of talin as a mechanosensitive signalling nexus. Talin couples integrin-mediated cell-to-matrix adhesions to the actin cytoskeleton, facilitating the formation of integrin adhesion complexes, which act as sophisticated information processing centres. Variation of talin rod domain conformation, following adhesion, promotes different talin-mediated recruitment and signalling outputs, enabling the modification of a cell's internal programming. The recently published MeshCODE theory describes how information in the brain may be stored binarily via the mechanicalistic alteration of talin rod binary switches, highly enriched at every synapse.

To validate this theory and discover a connection between neuronal activity and talin-mediated mechanical signalling, an innovative method, termed the talin 'fishing' rod experiment, was developed to identify novel talin-binding ligands in murine neuronal extract. Many proteins were identified as promising neuronal talin-binding ligands, including dynamin-1, synaptojanin-1, and myosin-Va, all of which exhibit particular significance to many aspects of synaptic transmission, particularly in the regulation of synaptic vesicle endo- and exocytosis. A bioinformatics pipeline and subsequent scoring system was also developed to accompany this experimental approach, enabling the identification of probable talin-binding sites in known synaptic vesicle proteins through I/LD motif evaluation. Whilst only weak binding was demonstrated between several talin rod domains and the proteins selected through bioinformatics analysis, it implies that both the bioinformatics pipeline and scoring system is effective in identifying promising talin-binding I/LD motifs. The identification of adhesome proteins, prior to this project, was restricted to cell lines and fibroblasts, limiting our knowledge of talin-binding ligands outside of these cell types. However, the talin 'fishing' rod experiment, developed in this project, can be utilised to help fill this current knowledge gap. Validation of the promising interactors, identified in this study, will support the concepts presented in the MeshCODE theory, potentially enabling the scientific community to achieve understanding regarding the enigma of memory storage at long last.

# Contents

# List of Figures

# List of Tables

# Abbreviations

| | |
|---|---|
| ABS | Actin Binding Site |
| AMPAR | A-Amino-3-Hydroxy-5-Methyl-4-Isoxazolepropionic Acid Receptor |
| AP2 | Adaptor Protein 2 |
| ARHGDIA | Rho GDP Dissociation Inhibitor Alpha |
| BAR | Bin-Amphiphysin-Rvs |
| BE | Bulk Endocytosis |
| BCA | Bicinchoninic Acid |
| BSE | Bundle Signalling Element |
| CAM | Cell-Adhesion Molecules |
| CaMKII | $Ca^{2+}$/Calmodulin-Dependent Protein Kinase II |
| CD | Circular Dichroism |
| CHC1 | Clathrin heavy chain 1 |
| CME | Clathrin-mediated Endocytosis |
| CSK | Cytoskeletal |
| ECL | Enhanced Chemiluminescence |
| ECM | Extracellular Matrix |
| ELVS | Endosome-like Vacuole Structure |
| FEME | Fast Endophilin-Mediated Endocytosis |
| FERM | Four-Point-One, Ezrin, Radixin, Moesin |
| FP | Fluorescence Polarisation |
| GED | GTPase Effector Domain |
| GPCR | G-Protein Coupled Receptors |
| GSH | Glutathione |
| GST | Glutathione S-Transferase |
| GTD | Globular Tail Domain |
| HSC 70 | Heat Shock Cognate 70 |
| HRP | Horseradish Peroxidase |
| ICAMs | Intercellular Adhesion Molecules |
| IACs | Integrin Adhesion Complexes |
| ICAP1 | Integrin Cytoplasmic Domain–Associated Protein-1 |
| IgCAMs | Immunoglobulin Superfamily CAMs |
| ILK | Integrin Linked Kinase |
| LB | Lysogeny Broth |

| | |
|---|---|
| LC-MS/MS | Liquid Chromatography-Mass Spectrometry/Mass Spectrometry |
| LDCV | Large Dense-Core Vesicle |
| LTD | Long-Term Depression |
| LTP | Long-Term Potentiation |
| mGluR1 | Metabotropic Glutamate Receptor 1 |
| MS | Mass Spectrometry |
| NMDA | N-Methyl-D-Aspartate |
| N-WASP | Neural Wiskott-Aldrich Syndrome Protein |
| PICAL | Phosphatidylinositol-Binding Clathrin Assembly Protein |
| PBS | Phosphate Buffered Saline |
| PI | Phosphatidylinositol |
| PH | Pleckstrin Homology |
| PI4P | Phosphatidylinositol-4-Phosphate |
| PIP2 | Phosphatidylinositol 4,5-Bisphosphate |
| PIPKIγ | Phosphatidylinositol Phosphate Kinase Type 1γ |
| PRPs | Plasticity-Related Proteins |
| PRD | Proline-Rich Domain |
| PSD | Postsynaptic Density |
| PSMs | Peptide-Spectrum Matches |
| RIAM | Rap1-Interacting Adapter Molecule |
| RIPA | Radioimmunoprecipitation Assay |
| SH3 | Src Homology 3 |
| SNAP 25 | Synaptosomal-Associated Protein 25 |
| SV | Synaptic Vesicle |
| SVE | Synaptic Vesicle Endocytosis |
| SVR | Synaptic Vesicle Recycling |
| T-SNARE | Nerve Terminal- Associated SNARE |
| TBS | Talin-Binding Site |
| TBST | Tris-Buffered Saline with Tween 20 |
| UFE | Ultrafast Endocytosis |
| V-SNARE | Vesicle-Associated SNARE |
| VASP | Vasodilator-Stimulated Phosphoprotein |
| VBS | Vinculin Binding Site |
| VD1 | Vinculin Domain 1 |

# 1 Introduction

## 1.1 Cell Adhesion

The highly regulated and exquisitely choreographed process of cell adhesion is vital to the development and maintenance of multicellular life. Cell-adhesion molecules (CAMs) are a subgroup of transmembrane proteins, which enable either cell-to-cell adhesion, through the formation of cell-to-cell junctions, or cell-matrix adhesion. Depending on the types of cell junctions formed, CAMs are typically categorised into four classes: cadherins, the immunoglobulin superfamily, integrins, and selectins; however, occasionally a fifth 'other' category is mentioned to include mucins, which allow selectins to mediate cell-to-cell adhesion (Figure 1.1) (Harjunpää et al., 2019; Janiszewska et al., 2020). CAMs mediate adhesion either through homophilic interactions, whereby the same CAM receptors bind to one another, or heterophilic interactions, whereby a CAM binds to the receptor of another adhesive molecule (Figure 1.1) (Lodish, 2007).

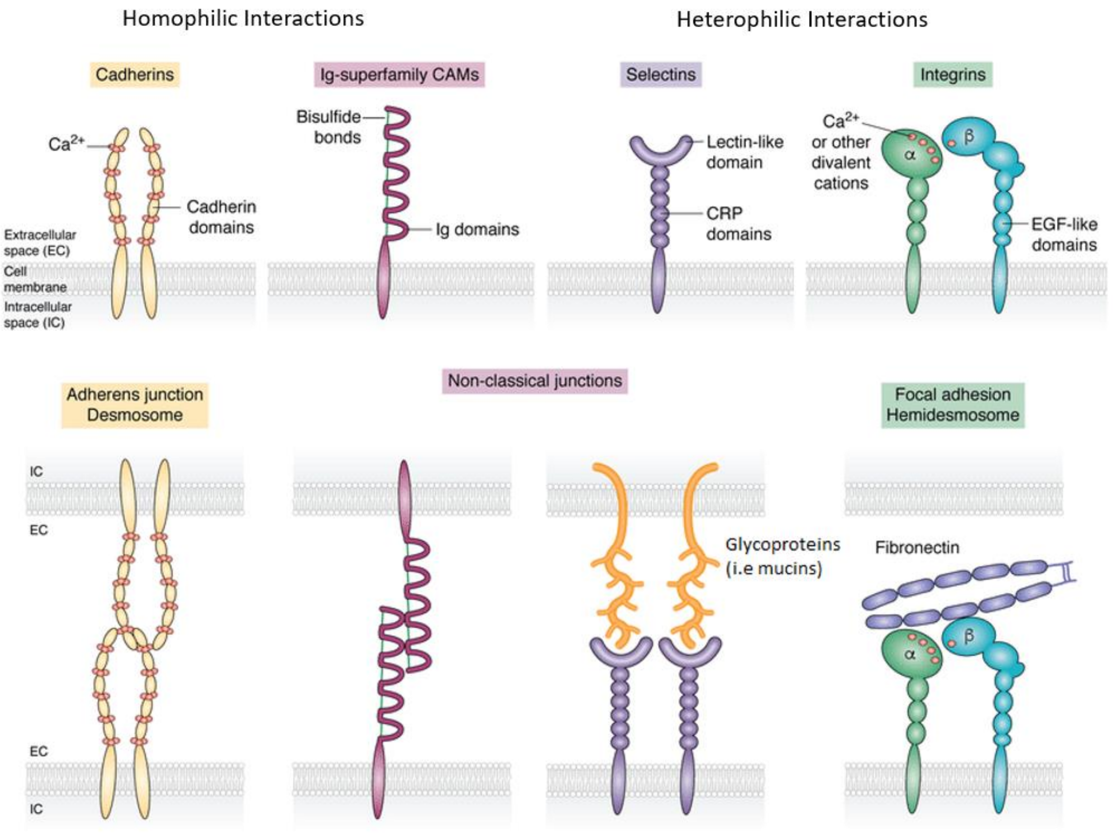

***Figure 1.1: The four main classes of cell-adhesion molecules.***
*Cadherins, the immunoglobulin superfamily, integrins, and selectins are the four main classes of cell-adhesion molecules, which can mediate adhesion through homophilic or heterophilic interactions to form various adhesion complexes, such as adherens junctions or focal adhesions. Figure adapted from (Janiszewska et al., 2020).*

## 1.2 Integrins

Integrins are a large family of heterodimeric transmembrane glycoproteins, which act as both adhesion receptors and CAMs to facilitate both cell-to-cell and cell-to-matrix adhesions (Yancey, 2017). Integrin subunits, α and β, each consist of a large extracellular domain utilised for ligand binding, a single transmembrane region, and a short cytoplasmic tail, with the exception of β4, which mediates signalling through indirect interaction with the actin cytoskeleton (Sun et al., 2019). A different combination of the 18 α and 8 β integrin subunits, non-covalently linked through their extracellular domains, can form 24 integrin heterodimers, with the different combination of subunits dictating the signalling and ligand binding properties of each heterodimer (Janiszewska et al., 2020). When classified by ligand binding specificity, integrins can be broadly categorised into RGD motif-recognising, leukocyte-specific, collagen-binding, and laminin-binding integrins (Mishra & Manavathi, 2021; Takada et al., 2007). However, they can also be classified as either αI-containing or αI-less integrins depending on the presence or absence of the inserted domain, an additional autonomous folding domain present in the α subunits (Zhang & Chen, 2012). As integrin-mediated signalling and adhesion are invaluable for many biological processes, such as haemostasis, mechanotransduction, and leukocyte trafficking, dysregulation of integrins can lead to numerous disease states (Mishra & Manavathi, 2021; Zhang & Chen, 2012).

### Integrin Activation

Integrins can exist in three different states based on ligand affinity: a bent-closed, inactive conformation, an extended-closed conformation, which permits low-affinity ligand interactions, or a fully active, high-affinity, extended-open conformation (Sun et al., 2019). Integrins are bivalent-cation dependent; therefore, the absence or presence of these ions can determine the integrin conformation, binding specificity, and affinity. Two modes of integrin activation exist; however, they are frequently linked: ‘outside-in’, whereby extracellular ligand binding activates integrin-initiated signalling pathways, or ‘inside-out’, whereby internal signalling triggers integrin activation (Figure 1.2). Upon integrin activation, various adaptor proteins and enzymes assemble to form integrin adhesion complexes (IACs), allowing the transmission of signals between the extracellular matrix (ECM) and the cell interior through the actin cytoskeleton (Mishra & Manavathi, 2021). Adhesion between cells and the ECM, predominantly facilitated by integrins, has been shown to regulate gene expression and subsequent differential tissue formation. As substrate stiffness has been shown to dictate stem cell differentiation, this demonstrates that integrin-mediated adhesion sites are highly sophisticated information processing hubs, with the ability to completely rewrite the programming of a cell depending on its attachments (Cigognini et al., 2013).

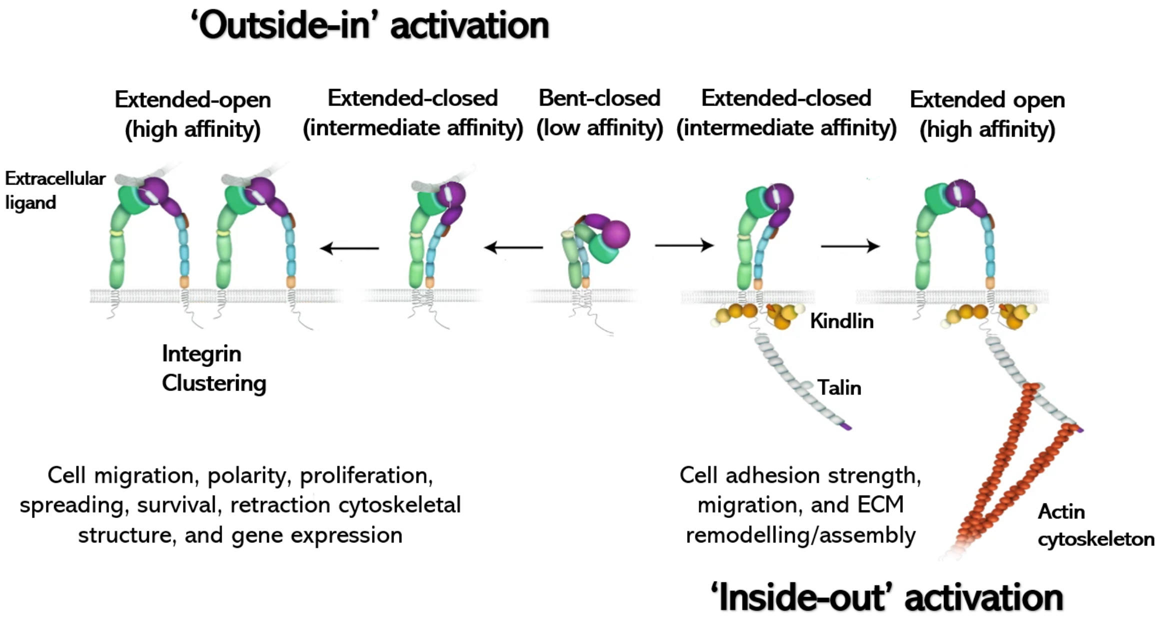

***Figure 1.2: 'Outside-in' and 'inside-out' integrin activation.***
*'Outside-in' integrin activation occurs following extracellular ligand binding, whilst 'inside-out' activation occurs through the actions of two adaptor proteins: talin and kindlin. Figure adapted from (Shattil et al., 2010; Sun et al., 2019).*

### 1.2.1 'Outside-in' Activation

'Outside-in' integrin activation typically occurs to sense changes in the cell's extracellular environment and transmits this information internally, allowing the cell to react accordingly. Extracellular ligands typically bind to the αI domain in αI-containing integrins and βI domains in αI-less integrins, with divalent cations binding to the metal ion-dependent adhesion site(s) present in these I domains (Zhang & Chen, 2012). The multivalency of these ligands can trigger integrin clustering, the precursor to focal adhesions, which is essential for achieving a full adhesion response (Karimi et al., 2018). After ligand binding, to enable the interaction of integrin cytoplasmic tails with intracellular signalling enzymes or adaptors, conformational changes must occur within the integrin heterodimer, such as the 'swing-out' of hybrid domains in the β subunit and separation of the α/β 'legs' and transmembrane domains (Campbell & Humphries, 2011; Sun et al., 2019; Takada et al., 2007). Dynamic adhesion structures, i.e. focal adhesions and podosomes, include many 'outside-in' signalling proteins, such as Src tyrosine kinases, which undergo autophosphorylation and activation through interaction with the β3 cytoplasmic tail after integrin clustering (Arias-Salgado et al., 2003; Ginsberg et al., 2005). The intracellular signalling pathways induced through 'outside-in' signalling, via ligand binding and subsequent integrin clustering, are vital for the regulation of processes such as cell migration, proliferation, survival, and gene expression (Shattil et al., 2010; Shen et al., 2012).

### 1.2.2 ‘Inside-out’ Activation

‘Inside-out’ activation regulates integrin activity and occurs through internal signalling, which is often initiated by the action of other cell surface receptors. Integrins are kept in their inactive state through the close association of α and β cytoplasmic tails; therefore, dissociation of this interaction, typically through the activation of cytokine-induced GPCR signalling, triggers integrin activation (Sun et al., 2019). During the association of the integrin β-cytoplasmic tail with intracellular activator proteins, such as kindlin and talin, the ligand binding affinity of integrin is increased. As a result of ‘inside-out’ integrin activation, stable adhesion between ECM proteins and integrin can be achieved, enabling sufficient force transmission for processes such as cell migration, ECM remodelling, and ECM assembly (Shattil et al., 2010).

Whilst ‘outside-in’ and ‘inside-out’ activation are discussed as separate concepts, they are often mutually cooperative. Integrins typically exist on the cell surface in a low-affinity state; therefore, ‘inside-out’ signalling can activate integrin, dramatically increasing the affinity for ligand binding, enabling ‘outside-in’ signalling (J. H. Wang, 2012). The opposite can also occur, as integrin-ligand binding can result in internal signalling, promoting ‘inside-out’ integrin activation (Shattil et al., 2010).

#### Talin

The large cytoskeletal protein, talin, is the predominant adaptor protein indispensable for integrin activation and causes dissociation of the α and β tails by interacting with the integrin beta cytoplasmic tail (Takada et al., 2007). Two isoforms of talin exist in mammals, talin 1 and talin 2, with ~74-76% amino acid homology between the two proteins (Debrand et al., 2009; Goult et al., 2018). As talin 1 is almost ubiquitously expressed in tissues and is fundamental in an extensive array of integrin-mediated processes, studies have primarily focused on the first talin isoform (Gough & Goult, 2018). However, although the role of talin 2 is less apparent, it is the more predominant isoform present in the brain, and underlying defects, such as mild dystrophy and variable survival, have been observed in talin 2 knock-out mice populations (Debrand et al., 2009, 2012). Whilst the introns of talin 1 appear to be much smaller in comparison to talin 2, ~30kb and ~190kb respectively, the domain structure of both isoforms is indistinguishable (Debrand et al., 2009; Goult et al., 2018). Talin comprises of a globular N-terminal head and a large flexible C-terminal rod, connected through a short, disordered linker of 80 amino acids (Figure 1.3). A FERM (Four-point-one, Ezrin, Radixin, Moesin) domain is present in the talin head, subdivided into four domains (F0, F1, F2, and F3), whilst the rod contains 13 four- or five-helix bundles, termed R1-13, and a single terminal α-helix required for talin dimerization, known as the dimerization domain (Goult et al., 2013, 2018; Sun et al., 2019). As a large multidomain protein, talin contains many binding sites for numerous proteins of the integrin adhesome (Figure 1.3 B) and has been described as the principal determinant of organisation within IACs (Liu et al., 2015).

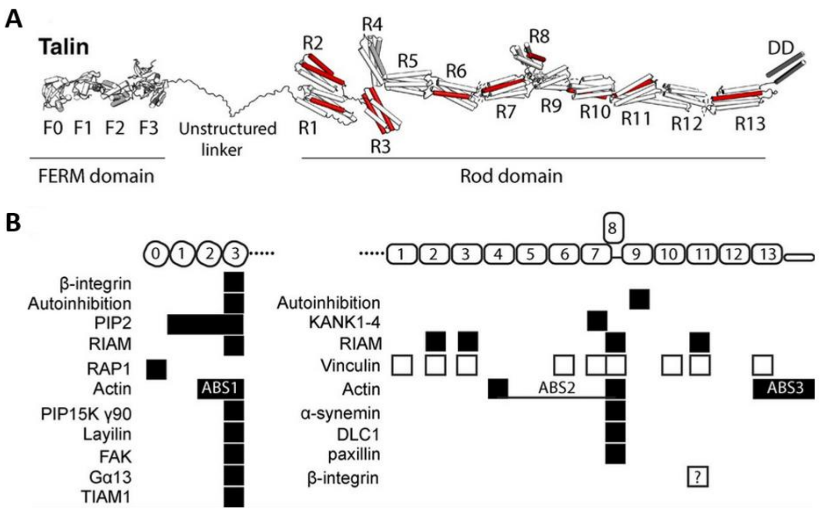

***Figure 1.3: Structure and binding domains of talin (Goult et al., 2018).***
***(A)** Structure of talin, with the vinculin binding sites highlighted in red. R2, 3, 4, and 8 domains are composed of four-helix bundles, whilst R1, 5, 6, 7, 9, 10, 11, and 12 domains are composed of five-helix bundles (Goult et al., 2013). **(B)** Several protein binding domains are present in talin.*

### Kindlin

Kindlins are a family of three ~75 kDa FERM domain-containing proteins (kindlin 1-3), consisting of ~680 amino acids (Rognoni et al., 2016). Similar to talin, kindlin isoform expression is tissue-specific: kindlin- 2 is expressed almost ubiquitously, with the exception of blood cells, kindlin-1 is primarily expressed in epithelial cells, and kindlin 3 is mainly present in haematopoietic cells, with low expression in endothelial cells (Rognoni et al., 2016; Ussar et al., 2006). Whilst kindlin is an indispensable integrin co-activator, varying effects occur depending on the cell type and interaction of the three kindlin isoforms with the different subunits present in an integrin heterodimer (Shattil et al., 2010; Ussar et al., 2006). Kindlin and talin share similar domain structure, as a FERM domain consisting of F0-F3 is also present in kindlin, with both domains binding to NxxY motifs in β-integrin tails (Goult, Bouaouina, et al., 2009). However, unlike talin, the F2 domain of kindlin contains an inserted pleckstrin homology (PH) domain, and kindlin binds to a membrane distal NxxY motif, as opposed to the membrane-proximal talin-binding NPxY/F motif (Baade et al., 2019; Calderwood et al., 2013; Shattil et al., 2010).

Whilst studies have shown that integrin activation is kindlin dependent, the exact mechanism for kindlin-mediated integrin activation is presently unknown. Nevertheless, many models have been suggested. As kindlin has previously demonstrated an inability to promote talin-integrin binding or bind directly to talin, kindlin is thought to act after talin is recruited to the membrane (Calderwood et al., 2013; Kahner et al., 2012). The F0, PH, and F1 kindlin domains contain phosphoinositide membrane-binding sites (Bouaouina et al., 2012). Therefore, through the kindlin F3-β-integrin interaction and binding to anionic membrane phospholipids, maximum exposure of the NPxY/F talin-binding site is considered to occur, potentiating the talin-facilitated separation of integrin cytoplasmic tails and subsequent integrin activation (Calderwood et al., 2013). Kindlins have also been thought to promote integrin activation through the displacement of integrin inhibitors either directly, as binding sites for two inhibitors (filamin and ICAP1) in integrin intersect the kindlin-binding site, or indirectly via the recruitment of activator proteins (Calderwood et al., 2013; Kahner et al., 2012). Kindlin is known to act as a protein-protein interaction hub, initiating signalling pathways and recruiting or interacting with many additional proteins to benefit the formation of an integrin adhesion complex (Sun et al., 2019). Recruitment of adaptor proteins, such as paxillin, and the subsequent formation of complexes, initiates many signalling pathways to promote cell proliferation, survival, spreading, and actin polymerisation (Sun et al., 2019; Theodosiou et al., 2016). Another model of kindlin-mediated integrin activation occurs through the promotion of integrin clustering to increase integrin avidity as opposed to improving the binding affinity of a single ligand. This can occur directly or indirectly, through adaptor protein recruitment, specifically ILK and migfilin, which link integrin to the actin cytoskeleton (Calderwood et al., 2013). Furthermore, even though kindlin does not interact directly with talin to mediate integrin activation, it has been suggested that kindlin-recruited adaptor proteins may promote integrin activation through cooperation with talin (Calderwood et al., 2013).

### Talin-mediated integrin activation

Talin synergizes with kindlin, facilitating integrin activation by binding to the membrane-proximal NPxY/F motif present in the integrin β-tail through the phosphotyrosine binding-like domain present in F3, thereby disrupting the interaction between integrin cytoplasmic tails. Upon this disruption, conformational changes occur, resulting in integrin activation. Whilst the exact mechanism for talin-mediated integrin activation is under debate, different models have been proposed. Talin-integrin binding involving the platelet integrin αIIbβ3, demonstrated that talin binding disrupts the salt bridge between αIIb-Arg$^{995}$ and β3-Asp$^{723}$, enabling a salt bridge to re-form between F3-Lys$^{324}$ and β3-Asp$^{723}$, thereby stabilising the integrin-talin interaction (Calderwood et al., 2013; Campbell & Humphries, 2011; Ginsberg et al., 2005; Vinogradova et al., 2002). Other N-terminal talin domains are also thought to aid in the interaction with integrin, possibly by modifying talin orientation to achieve optimal integrin binding (Bouaouina et al., 2008). The F2 talin domain is thought to form electrostatic interactions with the membrane between numerous positively charged lysine or arginine residues in F2 and negatively charged residues in the membrane (Calderwood et al., 2013; Campbell & Humphries, 2011). The talin-membrane interactions cause the talin-integrin complex to rotate, increasing the already present tilt of the β transmembrane region, prompting the separation of α and β transmembrane and cytoplasmic domains (Calderwood et al., 2013; Campbell & Humphries, 2011). Upon the subsequent separation of integrin α and β lower legs, the interaction between the lower leg domains and integrin heads is disrupted, resulting in integrin elongation and activation (Luo et al., 2007).

To ensure that integrin is not constitutively active throughout 'inside-out' signalling, strict regulation of talin is required. Talin can exist in several different conformations, including an elongated active state, as seen in Figure 1.3, and a globular inactive autoinhibited form. The predominant bonds facilitating this autoinhibited conformation are between F3 and R9 (through hydrophobic interactions involving F3-Tyr-$^{377}$) and electrostatic attraction between a loop of basic residues in F3 (at positions 316-326) and acidic residues in the fourth helix of R9 (Goult, Bate, et al., 2009). The Glu-$^{1770}$ residue located in R9 (1655-1822) is fundamental to talin autoinhibition, as a mutation of this residue (E1770A) dramatically hindered F3-R9 binding, disrupting autoinhibition (Goult, Bate, et al., 2009). To strengthen the talin globular structure, an anti-parallel talin homodimer is formed through the binding of talin dimerization domains and weak interactions between F2/3 and R1/2 (Khan & Goult, 2019). In this state, the F3 domain of talin, required for integrin activation, is sterically hidden and bound to the R9 domain in the talin rod; therefore, it cannot be used to activate integrin.

Fortunately, not all binding sites in autoinhibited talin are hidden, and the N-terminal of Rap1-interacting adapter molecule (RIAM) contains a short amphipathic helix (residues 6-30), termed talin-binding site 1 (TBS1), with the ability to bind to the accessible folded R2R3 domains in the autoinhibited conformation of talin (Calderwood et al., 2013; Khan & Goult, 2019). Upon activation of GTPase Rap1, following GPCR stimulation, RIAM and its binding partner talin are recruited to the membrane. Whilst RIAM-talin rod interactions promote talin recruitment, RIAM also aids in antagonising talin autoinhibition; it binds to F3, competing with the F3-R9 autoinhibitory interaction, and in doing so facilitates exposure of the integrin-binding site (J. Yang et al., 2014). RIAM and phosphatidylinositol 4,5-bisphosphate (PIP2), a component of the plasma membrane, have been shown to act cooperatively in disrupting talin autoinhibition. An electrostatic 'pull and push' mechanism has been proposed to explain the PIP2-mediated disruption of autoinhibition, with PIP2 'pulling' the positively charged talin F2/F3 domains to the membrane through strong electrostatic attraction, whilst simultaneously and forcefully repelling or 'pushing' the negatively charged (R9/10) domains, perturbing the F3-R9 autoinhibitory interaction (Song et al., 2012; J. H. Wang, 2012). Autoinhibition is not fully disrupted upon interference of the F3-R9 interaction; however, talin F3 is now able to bind to integrin, and the C-terminal actin-binding site (ABS) 3 is accessible for actin binding. ABS3 comprises of two five-helix bundle R13 domains linked through the helical dimerization domains in a talin homodimer (Gingras et al., 2008). Upon ABS3 binding to the retrograde flow of actin present in the cell, force is exerted on talin, which can further disrupt talin autoinhibition and destabilise the folded conformation of talin rod domains (Goult et al., 2013; Khan & Goult, 2019).

Depending on whether the rod domains are in their folded or unfolded conformation, various ligands can bind. Due to a stretch of four threonine residues buried in the hydrophobic core of R3, it is the weakest rod domain and has consistently been shown to unfold at forces of ~5 pN (Goult et al., 2018; Yao et al., 2014). Prior to the relief of autoinhibition, RIAM binds to the folded R3 domain; however, upon the exertion of force by the retrograde flow of actin, R3 unfolds, displacing RIAM and exposing two previously buried high-affinity vinculin binding sites (VBSs).

### Vinculin

Vinculin is a ~116 kDa actin-binding protein highly enriched in integrin adhesion complexes, such as focal adhesions, due to its fundamental role in cell adhesion regulation (Ziegler et al., 2006). Structurally, vinculin consists of anti-parallel helices subdivided into five separate domains; however, the structure of vinculin can also be separated into the vinculin head, linker, and tail (Figure 1.4) (Bays & DeMali, 2017). The vinculin head, consisting of the first four domains: three four-helix bundles (VD1, VD2, VD4) and a two-helix bundle (VD3), is essential for binding to proteins such as talin, α-actinin, α-catenin, and a recently discovered amphipathic helix in vinexin α, whilst the tail, a five-helix bundle known as VD5, is implicated in actin-, PIP2-, and paxillin-binding (Bays & DeMali, 2017; Carisey & Ballestrem, 2011; Hino et al., 2019). The vinculin head and tail are connected by a proline-rich linker, responsible for binding to VASP, the Src homology 3 (SH3) domains of vinexin, ponsin, and Arp2/3 (Bays & DeMali, 2017; Kioka et al., 1999). Like talin, vinculin can exist in both an open, active conformation and a closed, autoinhibited state, which is achieved through extremely strong interactions that have an estimated Kd of <1 nM between the vinculin head and tail, specifically VD5 with VD1 and VD4 (Figure 1.4) (Bays & DeMali, 2017; Cohen et al., 2005).

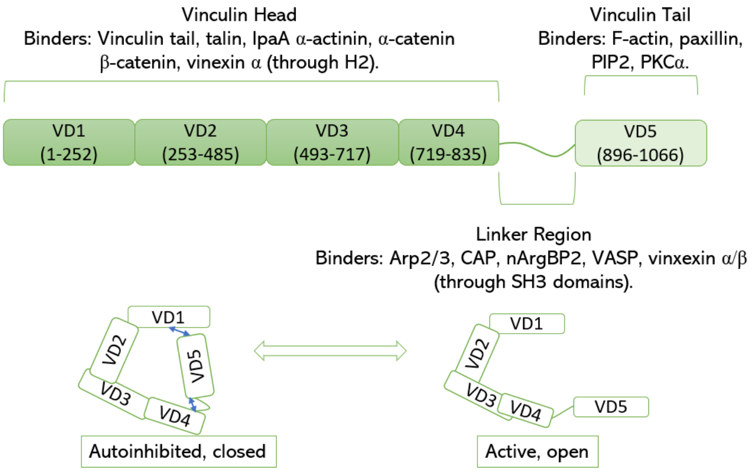

***Figure 1.4: Vinculin structure and binding proteins.***
*Vinculin consists of a vinculin head (VD1-4), linker region, and vinculin tail (VD5) that can bind to a variety of proteins. It can exist in an autoinhibited, closed conformation or an active, open conformation. Autoinhibitory interactions are illustrated in blue between VD5 and VD1/VD4. Figure inspired by (Bays & DeMali, 2017; Carisey & Ballestrem, 2011).*

Exposure of the high-affinity VBSs in talin promotes vinculin recruitment to the membrane. Whilst several models have been suggested that depict vinculin activation, the precise mechanism is under debate, although the combinatorial activation model, which describes how vinculin autoinhibition is disrupted through a combination of ligands and forces, is currently the most favoured (Carisey & Ballestrem, 2011). Talin is considered the predominant protein involved in vinculin activation and studies previously theorised that talin could disrupt vinculin autoinhibition autonomously, in a model termed helical bundle conversion (Bays & DeMali, 2017; Izard et al., 2003). The amphipathic helix present in talin VBS3 (1945-1970) was found to disrupt the VD1-VD5 autoinhibitory interaction in purified VD1 and tail domains (Izard et al., 2003). However, these studies were conducted prior to the discovery of the second autoinhibitory interaction in vinculin between VD4 and 5; therefore, it is unlikely that talin alone is able to activate vinculin, as the autoinhibitory interaction present in full-length vinculin has an affinity 1000 times greater than the purified VD1 subunit (Bays & DeMali, 2017; Cohen et al., 2005). Recently, single-molecule experiments demonstrated that mechanical exposure of a VBS by itself was sufficient to activate vinculin, so although the precise mechanism for vinculin activation is currently unknown, it appears to be a force-dependent process, with loss of tension shown to promote vinculin inactivation (Grashoff et al., 2010; Y. Wang et al., 2021). In the autoinhibited conformation of vinculin, the high-affinity VD1-VD5 autoinhibitory interaction restricts VD1-talin interactions, whilst steric hindrance limits actin-VD5 interactions (Golji & Mofrad, 2010). Simultaneous anchorage of VD1 to talin and electrostatic attraction of VD5 to actin is considered to generate tension, causing the separation of both domains, thus activating vinculin (Golji & Mofrad, 2010). Phosphorylation is also thought to promote vinculin activation through vinculin priming, as the phosphorylation of certain residues, such as Tyr-$^{100}$, Ser-$^{1033}$, Ser-$^{1045}$ and Tyr-$^{1065}$, hinders the stability of autoinhibition by altering the probability of force-induced vinculin activation (Bays & DeMali, 2017; Golji et al., 2012).

### The integrin-talin-actin backbone

The talin R3 unfolding event is a mechanical checkpoint to encourage the maturation from less stable nascent adhesions to larger focal adhesions (Goult et al., 2013). Upon the relief of talin autoinhibition and RIAM displacement, vinculin binds to the two high-affinity binding sites now accessible in talin R3 (Figure 1.5) (Goult et al., 2013). The second ABS in talin, ABS2, is present in R4-8, yet it is autoinhibited if R3 or R9 are closely situated (Khan & Goult, 2019) However, upon vinculin binding to R3, the inhibitory effect of R3 on ABS2 is disrupted, allowing the binding of F-actin to ABS2, with a series of hydrophobic and positively charged amino acids thought to promote actin binding, as mutation of these residues impacted talin-actin binding by ~60% (Atherton et al., 2015). Whilst actin binding to ABS3 is thought to promote initial focal adhesion assembly, ABS2 binding is fundamental to allow the production of maximal traction force, stabilisation, and maturation of focal adhesion complexes (Atherton et al., 2015). Actin binding to ABS2, which occurs following R3-vinculin binding, inhibits R3 refolding, stabilising the active state of ABS2. Vinculin-talin binding allows the adhesion complex to associate with the actin cytoskeleton through both vinculin- and talin-actin interactions, via ABS2 and 3, locking the talin and subsequently integrin, in an active conformation (Atherton et al., 2015; Goult et al., 2013). Vinculin has been shown to promote the formation and modification of actin structures, through crosslinking and bundling (Bays & DeMali, 2017; Wen et al., 2009). This may promote the application of further force on talin, exposing new VBSs upon talin rod domain unfolding, which in turn recruits additional vinculin molecules, leading to a stronger interaction with the actin cytoskeleton (Figure 1.5) (Yao et al., 2014). The ternary integrin-talin-actin complex also facilitates focal adhesion growth through potentiating integrin clustering (Humphries et al., 2007). Therefore, stabilisation of the adhesion is achieved, promoting the conversion from a previously RIAM-positive, small nascent adhesion which quickly disassembles, to a stronger, larger focal adhesion (Goult et al., 2013).

The integrin-talin-actin complex forms the backbone of focal adhesions, which are large stable dynamic structures comprising of over 200 proteins (Collins et al., 2017). Upon vinculin activation, many cryptic binding sites are uncovered, allowing the recruitment of many additional adhesion proteins, i.e. paxillin, vinexin, Arp2/3, and vasodilator-stimulated phosphoprotein (VASP), linking vinculin to many signalling pathways (Carisey & Ballestrem, 2011). Paxillin, also recruited by kindlin-2 upon phosphorylation of specific serine and tyrosine residues, aids in recruiting scaffolding and signalling proteins required for cell migration (López-Colomé et al., 2017; Zhu et al., 2019). Vinexin, VASP, and Arp2/3 are actin regulators involved in cell migration, with VASP required for actin remodelling and profilin binding, Arp2/3 controlling actin polymerisation, and both Arp2/3 and vinexin upregulating actin organisation (Goley & Welch, 2006; Kioka et al., 1999; Kwiatkowski et al., 2003). Vinexin has also recently been shown to act as a mechanosensor, and in response to high intracellular tension, which occurs when cells are grown on rigid ECM, vinexin increases the amount of actin-associated vinculin by stimulating vinculin activation (Yamashita et al., 2014). Although previously, vinexin was thought to only bind to the vinculin linker, through its SH3 domains, an amphipathic helix termed H2 (residues 329-355) was identified, which can bind to the vinculin head, specifically VD1 (Hino et al., 2019). Through simultaneous binding of H2 and the SH3 domains to VD1 and the vinculin linker respectively, vinexin mediates vinculin activation, whilst talin VBS3 is shown to promote this interaction and bind to vinexin-bound vinculin, forming a ternary complex (Hino et al., 2019). Due to the variety and number of adaptor proteins that can be found in focal adhesions, focal adhesion composition is incredibly dynamic, and the distinct proteins present, depending on the cell microenvironment, control the subsequent signalling processes activated through adhesion (Goult et al., 2018; Mishra & Manavathi, 2021). Therefore, once formed, focal adhesions act as signalling hubs to regulate a variety of cellular processes, such as migration, proliferation, and polarity (Atherton et al., 2015).

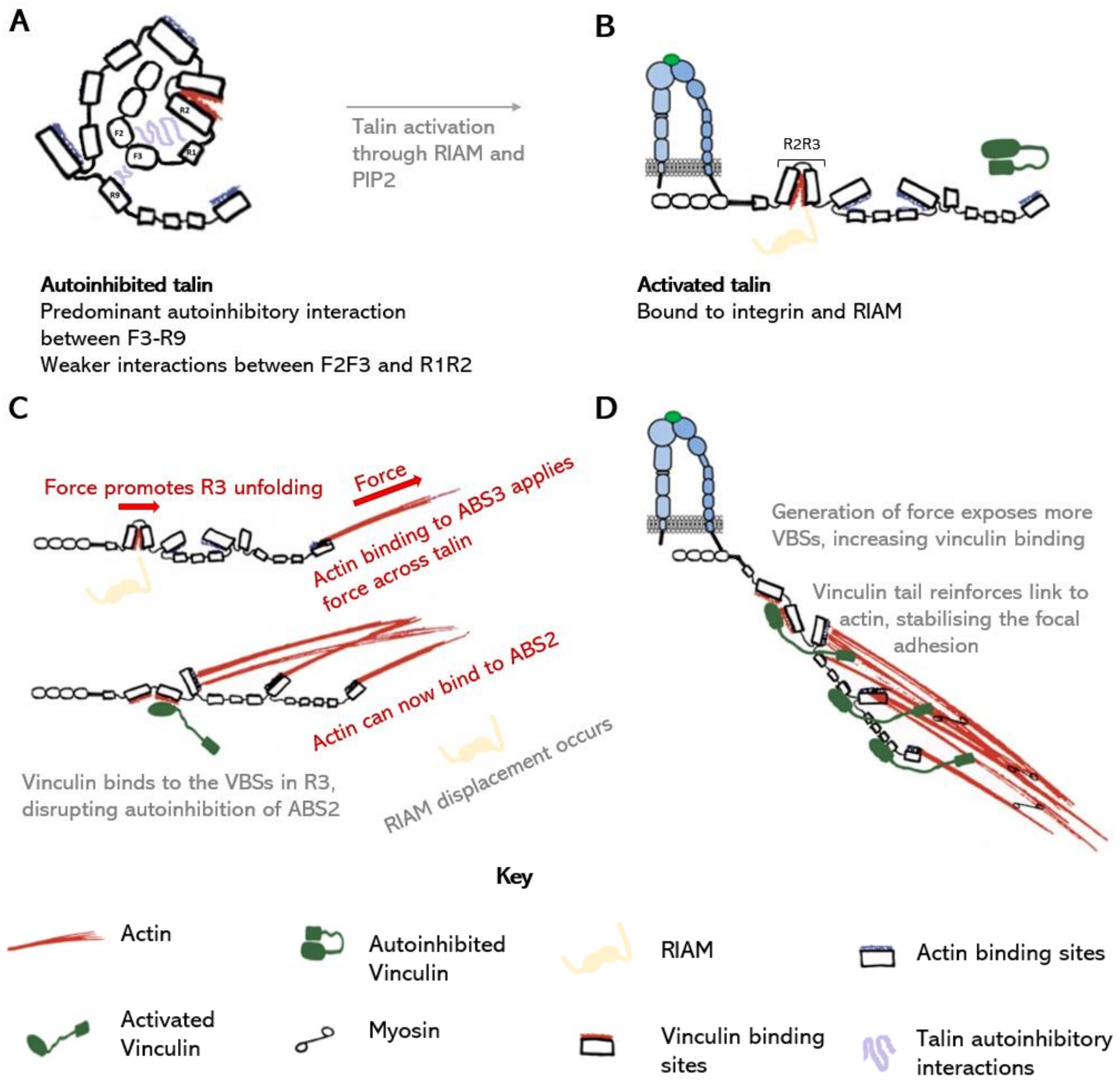

***Figure 1.5: Simplified generation of the integrin-talin-actin backbone, present in focal adhesions.***
***(A)*** *Talin is autoinhibited primarily through the interaction of F3 and R9, although weaker interactions between F2F3 and R1R2 also occur.* ***(B)*** *Through the action of PIP2 and RIAM, talin autoinhibition is disrupted, allowing talin F3 to bind to the integrin* $\beta$*-cytoplasmic tail.* ***(C)*** *After the relief of talin autoinhibition, actin can bind to the now accessible ABS3, applying force to the talin molecule and triggering the unfolding of R3. This displaces RIAM, as RIAM can only bind to the folded R2R3 domains; however, two high affinity VBSs in talin are now exposed, enabling vinculin binding. Autoinhibition of ABS2, which occurs due to the close proximity of R3, is disrupted through vinculin binding, therefore enabling further actin binding.* ***(D)*** *The increased force exerted on talin, exposes additional VBSs in the talin rod, recruiting additional vinculin molecules, reinforcing the link to actin. The combination of both talin-actin interactions and vinculin-actin interactions locks talin and subsequently integrin in an active formation, stabilising the adhesion. Not all vinculin binding sites are highlighted, and talin is depicted as a monomer for simplicity. Figure adapted from (Atherton et al., 2015; Soe et al., 2021).*

## 1.3 The Mechanosensitive Nature of Talin

### 1.3.1 Mechanical Switches

The rod domains of talin act as a sequence of 13 mechanical switches, which can exist in two thermodynamically stable states (Goult et al., 2018). This property of talin is best characterised during the talin-vinculin interaction in focal adhesions, as actin-mediated force exertion on talin promotes the unfolding of talin rod domains, triggering the exposure of previously hidden VBSs to potentiate talin-vinculin binding (Yao et al., 2014). A series of studies have used magnetic tweezers to identify the mechanical stability of each domain and the characteristic unfolding/refolding events which occur under force (Yan et al., 2015; Yao et al., 2016). The 13 rod domains consist of either four-or five-helix bundles, 5 nm in length, whose characteristic topology results in two distinct unfolding mechanisms. Four-helix bundles are arranged vertically and undergo an unzipping mechanism during unfolding, whilst five-helix bundles are arranged horizontally and undergo a shearing mechanism (Figure 1.6 A) (Yan et al., 2015). Upon full extension following domain unfolding, four-and five-helix bundles experience a ~10-fold increase in length from 5 nm to 46 and 55 nm, respectively (Figure 1.6 B) (Barnett & Goult, 2022). Although four-helix bundles have been found to typically unfold at forces between ~5-10 pN, whilst five-helix domains are able to withstand more force, exceptions to this occur for R2 and R8 (Yan et al., 2015). Due to stabilising hydrophobic interactions between the four-helix bundle R2 and R1, R1R2 is considered a double domain and undergoes an unfolding mechanism more similar to shearing than unzipping (Figure 1.6 C) (Goult et al., 2013; Yan et al., 2015). The four-helix bundle R8 is shielded from force as it is inserted into a loop between α3 and α4, two of the five helices present in R7, and is subsequently removed from the linear force pathway present across the talin rod; therefore R7R8 is usually considered a nine-helix bundle (Gingras et al., 2010; Yan et al., 2015). Whilst isolated R8 has been shown to unfold at ~5 pN and isolated R7 unfolds at ~15 pN, force exertion on the entire talin rod demonstrates that R7R8 unfolds in a large, single, cooperative event at ~15 pN, via a shearing mechanism, extending talin by ~80-110 nm (Barnett & Goult, 2022; Yan et al., 2015; Yao et al., 2016).

Over the course of 6 unfolding cycles, the talin rod domains rapidly and accurately re-fold after each cycle, with the unfolding of each domain occurring at a consistent level of force which remains relatively unchanged by the vast amounts of force applied to the protein in the previous unfolding cycle (Figure 1.6 D) (Yao et al., 2016). To avoid protein misfolding, which can result in aggregation and amyloid fibrils, proteins like titin require low sequence conservation; however, talin demonstrates an extensive ability to refold correctly, despite the presence of repetitive helical domain structure (Wright et al., 2005; Yao et al., 2016). The ease of talin domain unfolding and refolding emphasises the importance of this ability and how often it occurs in vivo (Yao et al., 2016). Talin rod domains can be classified into four groups based upon unfolding stability: group I (unfolding occurs at forces less than 8 pN), group II (unfolding occurs at forces between 8-15 pN), group III (unfolding occurs at forces 15-21 pN), and group IV (unfolding occurs at forces greater than 21pN) (Yao et al., 2016). However, although rod domains may unfold at far greater forces, rod domain refolding only occurs when force exertion is reduced to less than ~3 pN, indicating that rod domains display hysteresis (Goult et al., 2018; Yao et al., 2016).

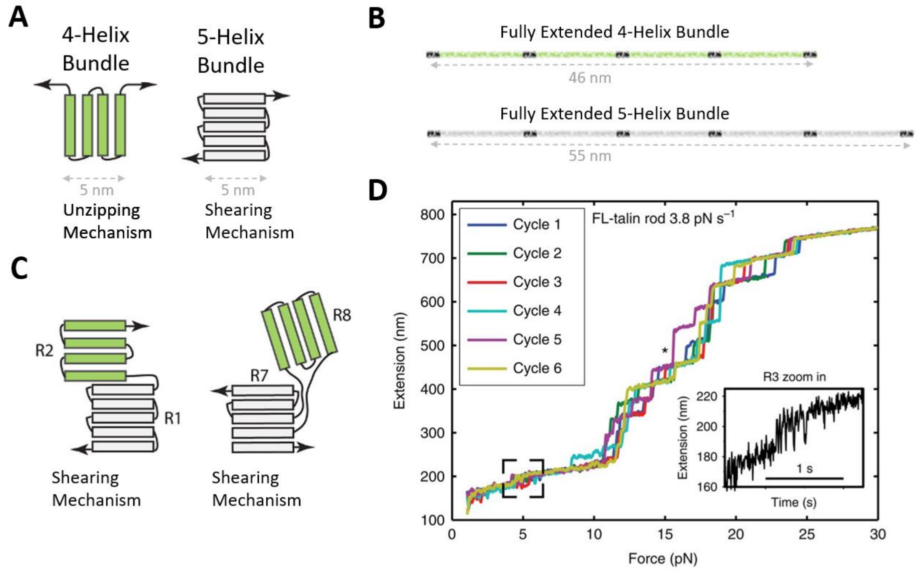

***Figure 1.6: Talin domain unfolding.***
***(A)*** *Talin four-helix bundle domains undergo an unzipping mechanism upon unfolding, whilst five-helix bundle domains undergo a shearing mechanism.* ***(B)*** *The full extension length of four-and five-helix bundles.* ***(C)*** *Unusual topology of R1R2 and R7R8 results in both R2 and R8 four-helix domains unfolding in a shearing mechanism.* ***(D)*** *A talin unfolding force-extension curve, generated using a single molecule of talin at a loading rate of 3.8 pN s$^{-1}$ (Yao et al., 2016). Figure adapted from (Yan et al., 2015; Yao et al., 2016).*

### 1.3.2 Talin-binding ligands

As the talin rod domains can exist in both folded and unfolded states depending on the conformation, varying ligands can bind. This has been effectively demonstrated in section 1.2 as RIAM is able to bind to the folded R2R3 domain, yet upon unfolding of R3, due to force exertion, the RIAM binding site is disrupted and RIAM is displaced. However, two previously concealed high-affinity VBSs are now accessible once R3 is in an unfolded conformation, promoting vinculin binding, which consequently locks R3 in an unfolded configuration. Therefore, for all 13 rod domains, there is likely a group of proteins which can bind to the folded or unfolded state, and upon ligand binding, the domain conformation is stabilised, facilitating further ligand interactions (Goult et al., 2018). Furthermore, the sheer increase in length upon full domain extension demonstrates that ligand binding is dictated by accessibility to talin, through a combination of spatial organisation and altered domain conformation (Barnett & Goult, 2022). The spatial positioning modification of talin upon domain unfolding occurs in a linear formation from the integrin-talin interaction at the plasma membrane to the site of force exertion (Barnett & Goult, 2022). Therefore, whilst the spatial organisation of talin can dictate ligand binding through locational accessibility, it can also regulate all downstream signal transduction pathways by altering the positioning of bound ligands within a cell, consequently modifying their zone of activity and protein interactions (Barnett & Goult, 2022).

The hysteresis property of talin, demonstrates that rod domains retain the memory of their current unfolded formation, even after force exertion on talin is reduced beyond the point required for unfolding (Yao et al., 2016). This further establishes that upon domain unfolding, the unfolded state may be retained to possibly enable additional occupation of the ligand-binding sites inaccessible in the folded conformation (Goult et al., 2018). Helix addition mechanisms, which have been known to occur in adhesion signalling, i.e. between paxillin and FAK, describe the process where a protein is able to bind to multiple ligands without any structural changes (Tran Van Nhieu & Izard, 2007). Rod domains contain four or five regions that can accommodate ligand binding between each helix, depending on whether they are four-or five-helix bundles. If ligands bind through a helix addition mechanism, as opposed to competing for the same binding site, this raises the ligand binding potential of talin substantially (Goult et al., 2018).

In a typical cell, 1-9 rod domains are thought to be in their unfolded state (Yao et al., 2016). Talin is considered to act as a mechanosensitive signalling hub, as the proteins currently known to interact with talin rod domains in either conformation, and the subsequent signalling molecules they regulate, are fundamental to most aspects of cell life (Goult et al., 2018). From transcription, microtubule, and cell cycle regulators to sodium/proton exchangers and multiple kinases, depending on the different pattern of folded and unfolded domains, many different biological processes are induced (Beaty et al., 2014; Gough et al., 2021; M. Yu et al., 2019). The mechanosensitive stability of each domain is predictable and well established; therefore, the application of a certain amount of force on talin can stimulate reproducible outcomes. This is known as the talin code: the huge array of talin molecules present on the cytoplasmic face of integrin forms a meshwork, and based upon differential force exertion, a varying combination of ligands may bind with diverse zones of activity, giving rise to predictable signalling events (Barnett & Goult, 2022; Goult et al., 2018). As each cell contains a specific proteome, a different combination of talin-binding ligands may or may not be present, allowing the talin-induced signalling capacity to be incredibly diverse in nature (Goult et al., 2018).

## 1.4 Synaptic Transmission

Communication in the brain occurs through synaptic transmission and is fundamental for brain function. Individual neurons are not typically in contact with each other; therefore, neuronal interaction occurs at specialised biological junctions called synapses (Lovinger, 2008). There are two primary modes of synaptic transmission: chemical and electrical (Figure 1.7 A/B). The information at chemical synapses is transmitted through the release of neurotransmitters from one neuron to another, via synaptic vesicle exocytosis, whilst information at electrical synapses is transferred bidirectionally, as ions and signalling molecules diffuse through two neurons linked via a gap junction (Lovinger, 2008; Pereda, 2014). Chemical synapses were considered more abundant in the mammalian brain, whereas electrical synapses were considered more abundant in the central nervous systems of invertebrates and cold-blooded vertebrates (Pereda, 2014). Therefore, the study of electrical synapses was often overlooked in favour of their chemical counterpart; however, more recent evidence indicates that electrical synapses are also widely utilised in the mammalian central nervous system (Connors & Long, 2004).

The generation of an action potential, which describes the change of electric resting potential across a cell membrane, promotes the diffusion of ions and small molecules less than 700 Da, i.e. cAMP, through the gap junctions connecting two neurons (Purves et al., 2004). The diffusion of ions or small molecules across gap junctions to generate coupling potentials, is almost instantaneous, enabling rapid information transmission across electrical synapses with no synaptic delay (Figure 1.7 B) (Faber & Pereda, 2018). This allows the coordination of electrical transmission across multiple neuron populations, which is fundamental in the coordinative and pulsative release of many hormones, such as gonadotropin-releasing hormone 1 (Faber & Pereda, 2018; Ma et al., 2015; Purves et al., 2004).

In chemical synapses, pre and postsynaptic neurons are not connected and contain a 20-50 nm synaptic cleft between each other (Lovinger, 2008). Upon receiving an action potential, the change in voltage triggers the opening of voltage-gated calcium channels and an influx of $Ca^{2+}$ at the presynaptic active zone, which binds to synaptotagmin, promoting synaptic vesicle exocytosis (Purves et al., 2004; Südhof & Rizo, 2011). Following the fusion of synaptic vesicles into the presynaptic membrane, and subsequent neurotransmitter release, the neurotransmitters diffuse across the synaptic cleft and bind to ionotropic or metabotropic receptors on the postsynaptic membrane (Figure 1.7 A) (Lovinger, 2008). This promotes the alteration of membrane potential, through the opening of additional ion channels, or the activation of signalling cascades to stimulate an inhibitory or excitatory amplification effect on neurotransmission (Lovinger, 2008; Pereda, 2014; Purves et al., 2004). Therefore, whilst chemical synaptic transmission is slower than electrical transmission, chemical synapses are able to amplify the signal, which cannot occur at electrical synapses, and the coupling potential in electrical synapses is often smaller than the original action potential (Figure 1.7 B).

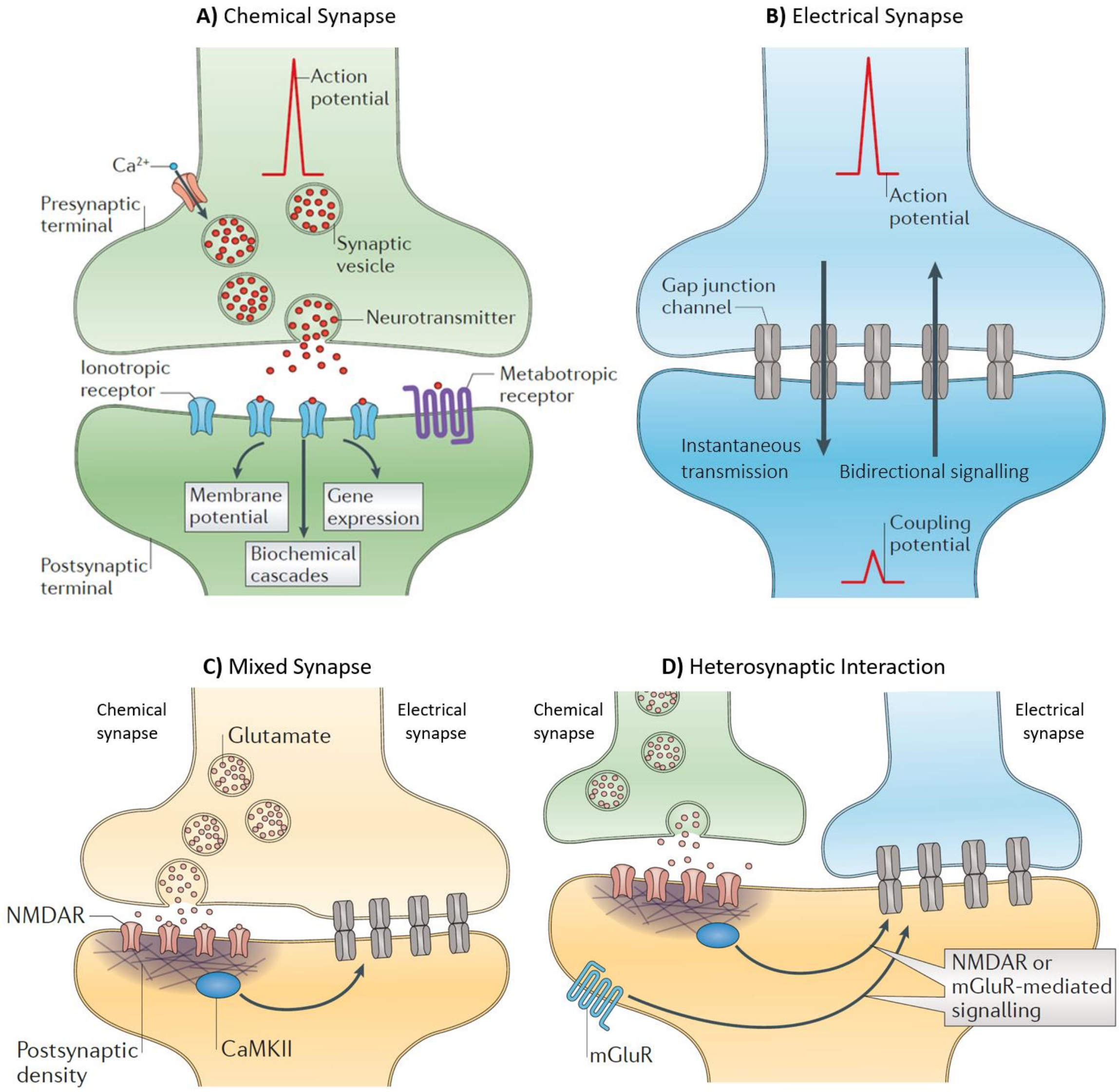

***Figure 1.7: Modes of synaptic transmission and interaction.***
***(A)*** *Chemical synapses require an influx of Ca*$^{2+}$*, triggered by an action potential, to promote neurotransmitter release across the synaptic cleft through synaptic vesicle exocytosis. Upon binding to an ionotropic or metabotropic receptor, neurotransmitter release can trigger a range of processes.* ***(B)*** *Electrical synapses are coupled by gap junctions, allowing the instantaneous, bidirectional transmission of ions and small molecules to a second neuron.* ***(C)*** *Interaction of chemical and electrical transmission at a mixed synapse, whereby NMDA receptor (NMDAR) and CaMKII activation mediates potentiation of electrical signalling.* ***(D)*** *Heterosynaptic interaction of chemical and electrical transmission, whereby NMDAR, CaMKII, and metabotropic glutamate receptor (mGluR) activation mediates regulation of electrical signalling. Figure adapted from (Pereda, 2014).*

Whilst chemical and electrical synapses were considered to work independently, evidence has shown that their interaction/cooperation may be fundamental to brain development and function in adulthood (Pereda, 2014). During development, gap junctions are initially formed between neurons, providing the foundation of neuronal signalling (Pereda, 2014). This promotes the formation of chemical synapses, which then stimulate the termination of neuronal coupling through gap junctions in numerous neuronal networks (Arumugam et al., 2005; Pereda, 2014). In adulthood, the regulation of electrical synapses is known to occur through the action of glutamatergic chemical synapses (Pereda, 2014). This is theorised to occur via a mixed synapse interaction, whereby one synapse, which can undergo both chemical and synaptic signalling, interacts with another neuron; however, it may also occur through a heterosynaptic interaction, whereby two synaptic neurons, each one utilising electrical or chemical signalling, interacts with one postsynaptic neuron (Figure 1.7 C/D) (Pereda, 2014). Potentiation of electrical synapses has been shown to occur from the activation of N-methyl-D-aspartate (NMDA) receptors, in response to glutamate neurotransmission, and $Ca^{2+}$/calmodulin-dependent protein kinase II (CaMKII), a highly abundant PSD protein associated with synaptic plasticity at chemical synapses (Pereda, 2014; Pereda et al., 1998; X. da Yang et al., 1990). The activation of metabotropic glutamate receptor 1 (mGluR1), with assistance from endocannabinoids, can also enhance the activity of both chemical and electrical synapses through the mediation of dopamine release and a cAMP-PKA-facilitated mechanism; however, mGluR activation has also been shown to promote long-term depression (LTD) across electrical synapses (Cachope et al., 2007; Landismari & Connors, 2005; Pereda, 2014). Therefore, although chemical synapses are thought to be the primary mode of transmission in the brain, synaptic transmission is an incredibly complex process, with many undiscovered elements, and requires highly dynamic interactions of both chemical and electrical signalling for effective brain function.

## 1.5 The MeshCODE Theory

Recently a unifying theory of memory storage, termed the MeshCODE theory, has been proposed, which details the possibility that data in the brain is stored in the force-dependent switches of mechanosensitive proteins, such as talin (Goult, 2021). If the talin rod conformations are considered in a binary format with ‘0’ and ‘1’ representing the folded and unfolded conformations respectively, in the presence of force, the conformation of talin can be read as a binary sequence of information (Figure 1.8). The mechanical aspect of synapses has been investigated as CAMs, major elements of mechanotransduction, are highly abundant in synapses and aid in processes such as the regulation of synaptic and dendritic spine plasticity (Kilinc, 2018; Lilja & Ivaska, 2018). However, the MeshCODE theory could revolutionise the extent of what is known regarding the role of mechanotransduction in neuronal signalling.

Synapses are surrounded by adhesion scaffolding, particularly integrin-mediated adhesion to the ECM, which is considered to regulate many mechanisms fundamental to synaptic transmission, i.e. synaptic plasticity, often in a subunit-dependent fashion (Figure 1.8 A) (Kilinc, 2018). Long-term potentiation (LTP), a major mechanism of synaptic plasticity, refers to the strengthening of synaptic connection through repeated neuronal activation, leading to a long-lasting increase in synaptic transmission efficacy (Bliss & Cooke, 2011; Kumar, 2011; Leal et al., 2017). α3β1-integrins are thought to regulate LTP, as α3 or β1-integrin loss in mice was found to impair LTP and working memory, whilst β3 integrins are considered fundamental to rapid adjustment of synaptic strength, through regulation of α-amino-3-hydroxy-5-methyl-4-isoxazolepropionic acid receptor (AMPAR) endocytosis (Chan et al., 2006, 2007; Cingolani et al., 2008; Kilinc, 2018). However, whilst integrin is considered a crucial component in many regulatory synaptic processes, talin was previously thought to predominantly function in synapses as a structural element, and the potential of talin for data storage has not yet been investigated.

Talin mechanotransduction occurs as a response to the combined forces exerted on talin from both the cell interior and exterior. However, in an environment where force exertion from the cell exterior is constant or predictable, the interior forces alone dictate the talin code present in the cell (Goult, 2021). ECM in the brain is extensively controlled and forms a cross-linked meshwork gel of proteins and proteoglycans surrounding every cell, isolating neurons from extracellular forces (Goult, 2021; Levy et al., 2014). Therefore, the ECM in the brain is considered a perfect environment to ensure that the folding or unfolding of talin domains occurs solely as a response to internal stimuli, such as a synaptic signalling event (Goult, 2021).

Due to the extent of adhesion scaffolding at each synapse, the huge array of talin molecules present form a meshwork of binary switches underneath the synaptic ionic or chemical signalling layers, which can be read as a code (the MeshCODE) (Goult, 2021). The MeshCODE theory illustrates that in response to synaptic transmission, contraction of the actin cytoskeleton exerts force on talin, changing the current binary switch pattern present in that neuron (Goult, 2021). The modified switch pattern would consequently alter the ligands bound to talin, their spatial location, and the subsequent signalling events which occur, changing the talin code for that neuron (Figure 1.8 E). Therefore, as a response to synaptic signalling, talin acts to store information by altering the binary switch code, which can be read and processed by the cell, through the reorganisation of ligand binding (Goult, 2021).

As talin is a major promoter of adhesion, the formation of adhesive complexes is also thought to contribute to synaptic signalling. Following synaptic transmission, the interaction of talin with actin will differ depending on the switches flicked, modifying the dynamics of the adhesive structures present in the neuron (Goult, 2021). Therefore, adhesive structures might be more likely to form in stimulated synapses, yet in unstimulated synapses, a lack of adhesive structures may contribute to atrophy (Goult, 2021). Through post-translational modification, certain switch domains may be locked or regulated to complement signalling function; therefore, depending on the expression or distribution of proteins and the post-translational modifications of talin present in each synapse, the resulting signalling cascade will differ between neurons (Goult, 2021). The MeshCODE theory illustrates how information can be stored quickly and easily, as the switch states are stabilised rapidly through ligand binding, enabling the formation of adhesion signalling structures to facilitate a range of biological functions (Goult, 2021). However, the switch pattern may also be short-lived if ligands are not recruited, indicating that two different responses can occur to complement the signalling requirement (Goult, 2021).

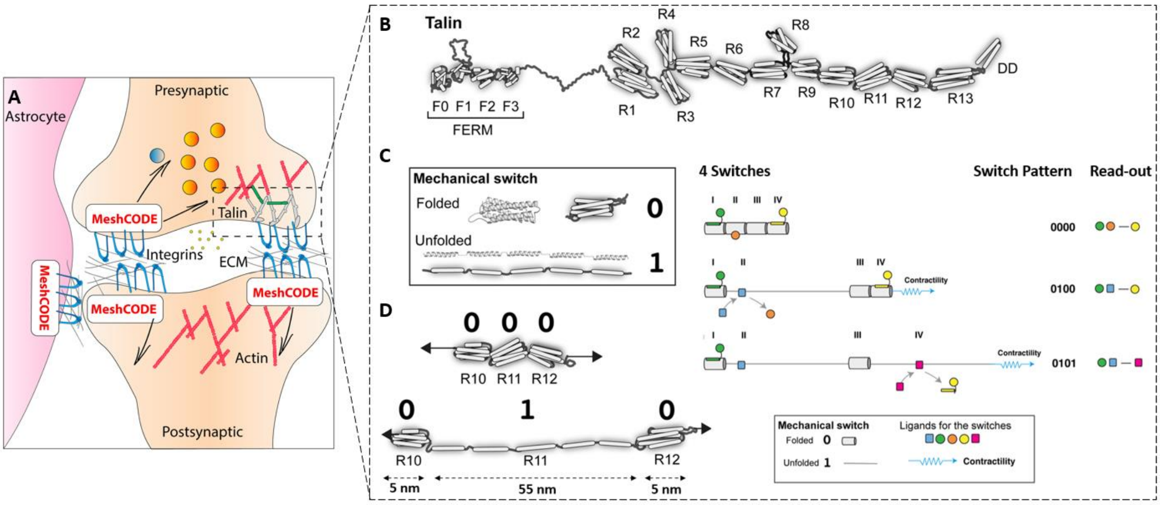

***Figure 1.8: Visualisation of talin acting as a data storage protein in the MeshCODE theory.***
***(A)*** *Adhesion structures, including many talin molecules, scaffold every synapse.* ***(B)*** *The structure of talin.* ***(C)*** *The folded or unfolded conformations of talin can be represented in a binary format as 0 or 1, respectively.* ***(D)*** *The application of force can change the binary switch pattern i.e. from 000 to 010.* ***(E)*** *The change of switch pattern, resulting from synaptic signalling, can be read by the cell through the different ligands bound to talin, following domain unfolding or refolding. Figure adapted from (Goult, 2021)****.***

The availability of proteins has been shown to contribute to synaptic plasticity, which is first illustrated in the synaptic tagging and capture hypothesis, proposed in 1997 (Frey & Morris, 1997; Ramiro-Cortés et al., 2014). LTP, a major mechanism of synaptic plasticity, is considered the predominant model for studying memory formation, with the transition of early to late-phase LTP thought to occur through ‘synaptic tagging’ (Frey & Morris, 1997). The creation of a ‘synaptic tag’ marks a synapse, promoting the synthesis/recruitment or ‘capture’ of proteins, called plasticity-related proteins (PRPs), to enable late-phase LTP, thereby potentiating synaptic transmission (Cassini & Lee, 2018; Frey & Morris, 1997). Inverse synaptic signalling may also occur, which describes the tagging of a synapse in a way that prevents the strengthening of synaptic transmission (Okuno et al., 2018). Synaptic cooperation occurs when available proteins are shared between synapses, enabling LTP across multiple synapses and dendritic spine growth (Ramiro-Cortés et al., 2014). However, synaptic competition occurs when available proteins are used at one synapse, yet depleted from another, which can cause spine shrinkage and long-term depression (Ramiro-Cortés et al., 2014). The MeshCODE theory may provide a mechanism for synaptic plasticity, as an increase in synaptic signalling may facilitate the formation of a different switch pattern. This acts as the 'synaptic tag' to drive the synthesis or recruitment of PRPs, through the exposure of previously hidden binding sites and subsequent activation of signalling pathways, enabling late-phase LTP to occur, potentiating synaptic transmission (Goult, 2021). The opposite process may also occur for inverse synaptic tagging, enabling LTD to prevent the strengthening of synaptic transmission (Goult, 2021). Synaptic signalling may cause multiple talin molecules to have the same switch pattern, which could result in synaptic competition, or depending on the prior switch pattern of talin, the same level of force will result in a different switch pattern, thereby recruiting different ligands, enabling synaptic cooperation (Goult, 2021). Due to the synaptic capacity of each neuron, the negative or positive regulation of synapses (through synaptic tagging, competition, or cooperation) enables the stimulation of specific synapses to be achieved, subsequently allowing information to be directed to the correct synapses for accurate memory storage (Goult, 2021). Therefore, as the MeshCODE theory describes how data is stored physically in the conformations of talin, this information is also easily addressable and can be modified through targeted signalling (Goult, 2021).

### 1.5.1 Implications of the MeshCODE theory

Talin has previously been shown to play a role in the regulation of neurotransmitter release, through synaptic vesicle recycling via clathrin-mediated endocytosis (Morgan et al., 2004). To ensure that neurotransmitter release is correctly maintained, synaptic vesicle endocytosis is firmly coupled to synaptic vesicle exocytosis, to produce the required vesicles and conserve the vesicle pool (Morgan et al., 2013). Phosphatidylinositol phosphate kinase type 1γ (PIPKIγ) is highly abundant in synapses and is known to generate PIP2, through the phosphorylation of phosphatidylinositol-4-phosphate (PI4P) (di Paolo et al., 2002). The generation and maintenance of PIP2 pools in the synapse is essential, as PIP2 acts as a fundamental promotor of clathrin-mediated endocytosis through interactions with proteins to potentiate the stabilisation and nucleation of actin and clathrin coats (Morgan et al., 2004; Wenk et al., 2001). PIPKIγ is recruited and regulated through binding to the FERM domain of talin, which results in a 15-fold increase in PIPKIγ activity (di Paolo et al., 2002). As previously mentioned, PIP2 promotes talin activation in adhesion complex formation and has also been known to interact with or regulate other adhesion proteins, such as vinculin (Sechi & Wehland, 2000). Therefore, the synthesis of PIP2 through talin-mediated PIPKIγ activation and the role of PIP2 on talin activation indicates that these interactions occur through a positive feedback mechanism, to mediate the formation of actin complexes in adhesion and synaptic vesicle endocytosis (di Paolo et al., 2002).

At the site of endocytosis, vesicles are typically surrounded by actin structures, as self-organisation and actin bending encourages the storage of elastic energy, driving the internalisation of endocytic pits (Akamatsu et al., 2020). However, upon disruption of the talin-PIPKIγ interaction, a substantial decrease in actin-mediated fluorescence, visualised by fluorescently labelled phalloidin, was observed (Morgan et al., 2004). The decrease in PIP2 may have caused the loss of actin structures through reduced interaction with actin regulatory proteins, i.e. dynamin, which promote actin structure formation, or through perturbation of talin activation and subsequent integrin-talin-actin interactions. Following perturbation of talin-PIPKIγ binding, a ten-fold increase of clathrin-coated pits visualised with abnormally wide necks, an average 33% decrease in synaptic vesicles, and a two-fold increase in plasma membrane length were all observed, indicating a defect or arrest in the early stages of clathrin-mediated endocytosis (Morgan et al., 2004). The wide-necked, unconstricted clathrin coat phenotype, exhibited from the disruption of talin-PIPKIγ interactions, mimics the phenotype observed upon the use of actin-disrupting toxins (Shupliakov et al., 2002). Therefore, talin is considered to promote actin formation and clathrin-mediated synaptic vesicle endocytosis, through the generation of PIP2 (Morgan et al., 2004). The strength of a synapse, in low $Ca^{2+}$ levels, is predominantly determined by the probability of vesicular release; however, in high $Ca^{2+}$ levels, the number of available vesicles has been shown to limit synaptic strength (Dürst et al., 2020). Therefore, as talin has previously been shown to promote vesicle formation through the generation of PIP2 pools, following the theory that talin is the predominant data storage protein in the brain, it is possible that talin may play a greater, yet currently unexplored, role in other aspects of synaptic vesicle regulation and subsequently be responsible for facilitating synaptic strength (Goult, 2021). Upon synaptic signalling, alteration of the talin binary switch pattern may regulate the number of available vesicles or the probability of vesicular release through undiscovered binding to synaptic vesicle proteins, enabling talin to control homeostatic synaptic scaling in the brain, via the regulation of synaptic strength (Goult, 2021; Turrigiano, 2008).

## 1.6 Project Aims

The fundamental aim of this project is to validate the concepts presented in the MeshCODE theory by uncovering a link between talin-mediated mechanical signalling and neuronal activity. The talin-binding ligands identified thus far, have solely been from fibroblasts and/or cancer cell lines; therefore, a knowledge gap exists regarding the potential neuronal ligands that may interact with talin. The goal of this project was to address this knowledge gap, which will be conducted through multiple methodologies:

a) **Identification of neuronal talin-binding ligands through bioinformatics**
   From the assumption that talin plays a greater role than previously anticipated in synaptic vesicle activity, a bioinformatics pipeline will be developed and applied to the synaptic vesicle proteins listed in Takamori et al., 2006, to identify any potential talin binders.

b) **Development of a novel method to identify talin-binding ligands**
   As the role of talin has predominantly been determined in cell lines and fibroblasts, there is a lack of information regarding adhesome proteins outside of these limited cell types. Therefore, a novel method will be developed to identify talin binders in a variety of cell extracts.

c) **Utilisation of the novel method to identify undiscovered talin-binding ligands**
   Once validated, this novel method will then be used to identify new talin binders in murine neuronal extract, which will aid in validating the MeshCODE theory.

d) **Combined experimental and bioinformatics approach**
   To narrow down the list of potential talin-binding ligands obtained in c), the bioinformatics pipeline, developed in a), will be used to identify the most promising talin-binding ligands.

A side project will also be conducted to characterise vinculin interactions.

a) **Vinculin A50I**
   The binding between the vinculin A50I mutant, which is considered a 'talin non-binding' mutant, and various VBSs in talin will be investigated to validate the conclusions of Mandal et al., 2021, which determined that talin-vinculin interactions are not required for vinculin-dependant axon growth.

b) **Vinexin α**
   The theorised binding of VD1 and a recently discovered amphipathic helix in vinexin α will be determined to develop the recent findings of Hino et al., 2019, which discovered that vinexin α is able to bind to VD1 through an amphipathic helix termed H2.

# 2 Materials and Methods

## 2.1 Materials

***Table 2.1: A list of the predominant buffers or growth media used in this project and their prospective components, unless otherwise stated.***

| Buffer or Growth Media | Components | pH |
|---|---|---|
| **CSK Buffer** | 10 mM PIPES, 300 mM Sucrose, 100 mM NaCl, 3mM $MgCl_2$, 1 mM EDTA, 0.5% Triton X-100, 100 µL 1x PhosSTOP Phosphatase Inhibitor Stock Solution (Roche), 400 µL 1x cOmplete™Mini EDTA-free Protease Inhibitor Stock Solution (Roche), 1.6 µL Benzonase Nuclease (Sigma Aldrich) | - |
| **Gel Filtration Buffer** | 20 mM Tris, 150 mM NaCl, 2 mM DTT | 8 |
| **GFP-Trap Acidic Glycine Buffer** | 200 mM Glycine | 2.5 |
| **GFP-Trap Dilution Buffer** | 10 mM Tris, 150 mM NaCl, 0.5 mM EDTA | 7.5 |
| **GFP-Trap Neutralisation Buffer** | 1 M Tris | 10.4 |
| **GFP-Trap Stringent Wash Buffer** | 500 mM NaCl, 10 mM Tris, 0.5 mM EDTA and 0.1% Triton X-100 | 7.5 |
| **GFP-Trap Regular Wash Buffer** | 150 mM NaCl, 10 mM Tris, 0.5 mM EDTA and 0.1% Triton X-100 | 7.5 |
| **5x Laemmli Buffer** | 10% SDS, 50% Glycerol, 300 mM Tris-HCl, 0.05% Bromophenol Blue, 100 mM DTT | 6.8 |
| **LB** | Per 1L: 10 g Tryptone, 10 g NaCl, 5 g Yeast Extract | 7.2 |
| **LB Agar** | Per 200 mL: 2 g Tryptone, 2 g NaCl, 1 g Yeast Extract, 3 g Agar | 7.2 |
| **Nickel (Ni) Buffer A** | 20 mM Tris, 500 mM NaCl, 20 mM Imidazole | 8 |
| **Nickel (Ni) Buffer B** | 20 mM Tris, 500 mM NaCl, 500 mM Imidazole | 8 |
| **PBS** | 138 mM NaCl, 10 mM $Na_2HPO_4$, 1.8 mM $KH_2PO_4$ | 7.4 |
| **Q Buffer A** | 20 mM Tris, 50 mM NaCl | 8 |
| **Q Buffer B** | 20 mM Tris, 1 M NaCl | 8 |
| **S Buffer A** | 20 mM $NaH_2PO_4.2H_2O$, 50 mM NaCl | 6.5 |
| **S Buffer A** | 20 mM $NaH_2PO_4.2H_2O$, 1 M NaCl | 6.5 |
| **SDS Running Buffer (Regular)** | 50 mM Tris, 50 mM MOPS, 0.1% SDS, 1 mM EDTA | 7.7 |

| | | |
|---|---|---|
| **SDS Running Buffer (Bio-Rad)** | 10 mM Tris-HCl, 15 mM Tris Base, 191 mM Glycine, 3.5 mM SDS | 8.3 |
| **TBS** | 137 mM NaCl, 20 mM Tris | 7.6 |
| **TBST** | 137 mM NaCl, 20 mM Tris, 0.1% Tween 20 | 7.6 |

## 2.2 *E. coli* Cell Culture

### 2.2.1 Production of Competent *E. coli* Cells

BL21 (DE3) Star competent cells were streaked on Lysogeny Broth (LB) agar plates in the absence of antibiotic and incubated overnight at 37°C. One colony was inoculated with 40 mL of LB in a 500 mL conical flask and incubated at 37°C until an $OD_{600}$ of 0.3-0.4 was reached. Cells were left on ice for 10 minutes, harvested via centrifugation for 10 minutes at 3000 rpm, 4°C, and resuspended in 20 mL ice-cold filter sterilised 0.1 M $CaCl_2$. Cells were left on ice for a further 20 minutes, harvested via centrifugation for 10 minutes at 3000 rpm, 4°C, and resuspended in 2 mL of ice-cold filter sterilised 0.1 M $CaCl_2$, 15% glycerol. Cells were aliquoted on ice in ice-cold Eppendorf tubes at 30 µL, flash-frozen in liquid nitrogen, and stored at -80°C.

### 2.2.2 *E. coli* Transformation

1 µL of plasmid DNA was added to a 30 µL aliquot of BL21 (DE3) Star competent cells and left on ice for 25 minutes. Cells were heat-shocked at 42°C for 45 seconds and placed back on ice for a further 2 minutes. The cells were incubated at 37°C at 150 rpm for 40 minutes in 200 µL LB, streaked on LB agar plates with 100 µg/µl ampicillin, and incubated overnight at 37°C.

### 2.2.3 *E. coli* Starter Culture Preparation

To prepare a starter culture, an individual colony from the *E. coli* transformation was placed in 5-10 mL LB with 100 µg/µl ampicillin and left to incubate overnight at 37°C, 150 rpm. For glycerol stock production, which can be used as a substitute for individual colonies in starter culture preparation, 220 µL of overnight starter culture was combined with 220 µL of filter sterilised 50% glycerol and stored at -80°C.

### 2.2.4 Plasmid DNA Purification

A plasmid of interest was transformed, as described in section 2.2.2; however, DH10β competent cells were used in place of BL21 (DE3) Star. Starter cultures were set up, as described in section 2.2.3, and following overnight incubation at 37°C, were spun down in a Rotana 460 R centrifuge (Hettich) for 10 minutes at 4000 rpm, 4°C. The supernatant was discarded and a miniprep was conducted to purify plasmid DNA using a QIAprep Miniprep kit (QIAGEN), according to manufacturer protocol.

### 2.2.5 *E. coli* Growth

In a 2 L baffled flask, 750 mL of autoclaved LB and 100 µg/µl ampicillin was inoculated with an appropriate volume of overnight starter culture (section 2.2.3) to produce an initial $OD_{600}$ of 0.05. The cells were left to grow in a shaking incubator at 180 rpm, 37°C until an $OD_{600}$ of 0.7 was reached. Protein induction varied depending on protein stability, with flasks either left to incubate for 3 hours at 37°C, 180 rpm with 1 mM IPTG or overnight at 20°C, 180 rpm with 0.2 mM IPTG. 500 µL samples of inoculated LB, before and after induction, were taken and harvested via centrifugation for 2 minutes at 13,000 rpm. The pellets were resuspended in 100 µL of 5x reducing Laemmli sample buffer, boiled for 60 seconds at 95°C, and analysed by SDS-PAGE, to confirm whether the protein of interest had been expressed.

Cells were harvested by centrifugation at 6000 rpm in a JA-10 rotor (Beckman) at 4°C for 10 minutes and resuspended in 25 mL of suitable buffer, i.e. Ni buffer A, PBS with 5 mM DTT, or GFP-Trap dilution buffer. If the protein was susceptible to degradation, 1 cOmplete™Mini EDTA-free protease inhibitor cocktail tablet (Roche) was added per litre of cells. The pellets were lysed immediately or frozen and stored at -20°C.

### 2.2.6 *E. coli* Cell Lysis

Once fully defrosted, cell pellets, from section 2.2.5, were lysed on ice using 5 cycles of sonication, 30 seconds on, 30 seconds off at 55% amplitude. The cell debris was centrifuged using a JA25.5 rotor (Beckman) for 40 minutes at 21,000 rpm, 4°C. The supernatant was retained and passed through a 0.45 µm filter, whilst the pellet was resuspended in 30 mL of suitable buffer i.e. Ni buffer A, PBS with 5 mM DTT, or GFP-Trap dilution buffer. 10 µL samples of the filtered cell lysate and the resuspended pellet were collected for analysis via SDS-PAGE, to ascertain whether the protein of interest was soluble and present in the supernatant.

### 2.2.7 CaSki Cell Lysate Preparation

Trypsinized cell pellets of the epidermoid cervical carcinoma CaSki cell line were generously gifted by the Tim Fenton lab, University of Kent and resuspended in fresh ice-cold cytoskeletal (CSK) buffer to isolate cytoskeletal-binding proteins (Choo et al., 1994; Yamashita et al., 2014). Cells were vortexed, left on ice for 15 minutes, and centrifuged at maximum speed on a table-top centrifuge (14,800 rpm) at 4°C for 10 minutes. The supernatant was transferred to a fresh Eppendorf tube and stored at -20°C.

## 2.3 Protein Purification

### 2.3.1 Immobilised Metal Ion Chromatography

As the protein constructs used in this project contained either an N- or C-terminal 6x His-Tag, protein purification via immobilised metal ion chromatography, which enables the purification of recombinant proteins attached to a peptide affinity tag, could be performed. For His-tagged purification, bacterial cell pellets (from section 2.2.5) required resuspension in Ni buffer A. Immobilised nickel ion chromatography was performed at room temperature using an ÄKTA start (GE Healthcare) and a 5 mL HisTrap HP column (GE Healthcare), pre-packed with $Ni^{2+}$ charged immobilised agarose beads. The column was equilibrated with Ni buffer A and B at a flow rate of 5 mL/min. The filtered cell lysate (section 2.2.6) was loaded into the column at 2 mL/min, followed by 25-30 mL Ni buffer A, to remove additional unbound proteins. As cell lysate flows through the column, the His-Tagged protein interacts with the $Ni^{2+}$ charged agarose and is retained in the column, separating itself from the additional proteins, which do not interact and are immediately eluted. During loading, the flow-through was collected and a sample was taken for analysis by SDS-PAGE, to ensure that the protein of interest had indeed bound to the column. The protein was eluted in 3.5 mL fractions at 5 mL/min using Ni buffer A and a linear gradient of Ni buffer B from 0-100%. The high imidazole content of Ni buffer B competes with the His-Tag, enabling protein displacement from the column. An increase in UV, which occurs during protein elution, was observed to ascertain which eluted fractions contained the protein of interest, and samples of these fractions were analysed via SDS-PAGE for confirmation. For proteins susceptible to precipitation, Ni buffer A was added to the eluted protein fractions to dilute the imidazole content. Following elution, the column was washed with 20% ethanol at 1 mL/min and stored at 4°C.

### 2.3.2 Batch Purification: Ni-NTA Resin

Protein purification was also conducted via batch method, whereby 1 mL of HisPur Ni-NTA resin (Thermo Fisher Scientific) was used per litre of inoculated LB. The resin was washed via resuspension in ~30 mL Ni buffer A and spun down at 4000 rpm in a Rotana 460 R centrifuge (Hettich) at 4°C. The supernatant was discarded, and the process was repeated once more with an additional 30 mL Ni buffer A. The filtered cell lysate was added to the washed beads and left to agitate. Agitation conditions were optimised depending on the protein of interest. Typically, 30 minutes of agitation on a see-saw rocker (Stuart) at room temperature was sufficient; however, if the protein was susceptible to degradation, agitation was carried out at a lower temperature, 4°C, for 30-60 minutes. After agitation, the beads and cell lysate were spun down in a Rotana 460 R centrifuge (Hettich) at 4000 rpm, 4°C, and the supernatant was transferred to a separate falcon tube. A sample of the supernatant was taken for SDS-PAGE analysis to ascertain whether the protein had bound to the Ni resin. The resin was resuspended in 40 mL Ni buffer A, centrifuged at 4000 rpm in a Rotana 460 R centrifuge (Hettich) at 4°C, and the supernatant was discarded. The washing step was repeated 6 times in total and a sample of the washed beads was taken for SDS-PAGE analysis to confirm whether the protein had effectively bound to the resin. The beads were resuspended in 5-10 mL Ni buffer A and poured into a gravity flow column (Bio-Rad), previously equilibrated with ~5 mL Ni buffer A. Using ~5 mL Ni buffer B per 1 mL resin, the protein was eluted in 1 mL fractions and diluted with 500 µL Ni buffer A to prevent protein precipitation. A sample of each eluted fraction was analysed via SDS-PAGE to confirm whether the protein had successfully been eluted.

### 2.3.3 Buffer Exchange: Dialysis

Prior to further purification, either by GSH resin or ion exchange chromatography, 10K MWCO SnakeSkin dialysis tubing (Thermo Fisher Scientific) was used to buffer exchange the combined eluted protein samples, from section 2.3.1 or 2.3.2, into 5 L of suitable buffer at 4°C, on a magnetic stirrer (Stuart) overnight. For subsequent purification by GSH resin, the combined elution protein fractions were dialysed into 5 L of PBS. However, for subsequent purification by ion exchange chromatography, depending on the isoelectric point of the protein, calculated using ExPASy ProtParam, the combined elution protein fractions were dialysed into either 5 L of Q buffer A or S buffer A (Gasteiger et al., 2005). The isoelectric point of the protein determined whether anionic or cationic exchange was required. Typically for isoelectric points below 7.25, Q buffer (pH 8) was used as anion exchange was needed; however, for isoelectric points above 7.25, S buffer (pH 6.5) was utilised, as cationic exchange was required.

During buffer exchange, TEV cleavage was also performed via the addition of 0.6 mg/mL TEV protease to the combined elution protein fractions, in a 5:1 mL ratio of protein: TEV protease.

### 2.3.4 Ion Exchange Chromatography

Ion exchange chromatography was performed at room temperature using an ÄKTA start (GE Healthcare) and a 5 mL HiTrap SP/Q HP column (GE Healthcare), pre-packed with charged resin. If the protein was in Q buffer, it had an isoelectric point lower than the pH and a negative charge; therefore, anion exchange was carried out using a Q column comprised of positively charged resin. If the protein was in S buffer, it had an isoelectric point higher than the pH and a positive charge; therefore, cation exchange was carried out using an S column comprised of negatively charged resin.

The column was equilibrated with Q buffer A/B or S buffer A/B. After dialysis, the protein was filtered through a 0.45 µm syringe and loaded into the column at 2 mL/min, followed by an extra 5-10 mL S/Q buffer A. During loading, the flow-through was collected and a sample was taken for analysis by SDS-

PAGE to confirm protein-column binding. The protein was eluted in 3.5 mL fractions at 5 mL/min using buffer A and a linear gradient of buffer B from 0-100%. Buffer B contained a higher salt content, disrupting the protein-column interactions and enabling protein elution. Ion exchange chromatography allows the separation of molecules depending on their charge. Therefore, the protein can be purified as it has a different charge to potential impurities (i.e. the affinity tags, TEV protease, etc.), which will either not bind to the column or will elute in different fractions. The eluted fractions containing the protein of interest were ascertained by observing the UV peak, which increased significantly upon protein elution. Samples of these fractions were analysed via SDS-PAGE to confirm that the protein was present. The column was washed in 20% ethanol at 1 mL/min and stored at 4°C.

### 2.3.5 Protein Concentration Determination and Storage

Once the eluted samples were confirmed to contain the protein of interest through SDS-PAGE, protein concentration was determined using a NanoPhotometer N50 (IMPLEN) with the protein molecular weight and extinction coefficient, as calculated using the ExPASy ProtParam tool (Gasteiger et al., 2005). The protein was either used as is, or flash-frozen in liquid nitrogen and stored at -20°C.

For TEV protease production, ion exchange chromatography was not required. After overnight dialysis into PBS and concentration determination, TEV protease was aliquoted in a 1:1 ratio with glycerol, mixed thoroughly, flash-frozen in liquid nitrogen, and stored at -20°C.

### 2.3.6 GST-Tagged Protein Purification

Protein constructs with a Glutathione S-transferase (GST) affinity tag can be purified using glutathione resin. The GST tag on the protein of interest will bind to the glutathione (GSH) molecules covalently coupled to the agarose beads, allowing the protein to be separated from any additional proteins or impurities upon bead washing. 1 mL of Pierce™ glutathione agarose beads were washed via resuspension in 30 mL PBS, 5 mM DTT with 0.1% Triton X, and the beads were spun down in a Rotana 460 R centrifuge (Hettich) for 4 minutes at 4000 rpm, 4°C. The supernatant was discarded, and the beads were incubated for 1 hour on a see-saw rocker (Stuart) at room temperature with either filtered cell lysate (section 2.2.6) or Ni-purified protein, from section 2.3.3 following PBS buffer exchange via dialysis in the absence of TEV. After incubation, a sample was taken for SDS-PAGE analysis and the incubated protein was centrifuged in a Rotana 460 R centrifuge (Hettich) for 4 minutes at 4000 rpm, 4°C. The supernatant was removed, and a sample was taken for analysis by SDS-PAGE. The beads were washed through resuspension in 30 mL of PBS, centrifuged at 4000 rpm, 4°C for 4 minutes, and the supernatant was removed. After the washing cycle was repeated 5 times, a sample of the washed beads was taken for SDS-PAGE analysis.

## 2.4 Biochemical Assays

### 2.4.1 GST Pulldowns

To validate protein interactions with the GST-tagged protein of interest, GST pulldown assays were conducted. 30-40 µL of glutathione agarose beads (Pierce) bound to the protein of interest (as detailed in section 2.3.6), were added to 170 µL of 150 µM protein and incubated for one hour on a see-saw rocker (Stuart) at room temperature. After incubation, a sample was taken for SDS-PAGE analysis and the incubated beads were spun down in a tabletop centrifuge for 3 minutes at 4000 rpm, 4°C. A sample of the supernatant was taken for analysis by SDS-PAGE, and the remaining supernatant was discarded. The beads were washed through resuspension in 1 mL of PBS, centrifuged at 4000 rpm for 3 minutes at 4°C, and the supernatant was removed. This was repeated three times and a sample of the washed beads was taken for SDS-PAGE analysis. By comparing the bead samples, the supernatant fraction and the sample taken after incubation, binding to the GST-bait protein could be determined.

### 2.4.2 Bicinchoninic Acid Assay

The Pierce™ Bicinchoninic Acid (BCA) protein assay kit (Thermo Fisher Scientific) was used to quantify protein samples in lysed CaSki cells, as per the manufacturer's instructions.

### 2.4.3 GFP-Trap Immunoprecipitation: *E. coli* Protein Binding

GFP-Trap® agarose (ChromoTek) consists of agarose beads coupled to a GFP nanobody. GFP-tagged protein constructs bind to the GFP nanobody on the agarose beads, enabling purification from other proteins in *E. coli* cell lysate. 50 µL of GFP-Trap® agarose beads (ChromoTek) were washed through resuspension in 1.5 mL of GFP-Trap dilution buffer, centrifuged at 2,500 x g for 5 minutes at 4°C, and the supernatant was removed. Filtered cell lysate, from section 2.3.6, was incubated with the beads to produce a suitable band on SDS-PAGE gels. Table 2.2 demonstrates the volume of cell lysate required for the negative control, GFP, and the protein of interest, GFP-talin 1 rod (R1-13). The cell lysate was incubated with the washed GFP-Trap beads on a see-saw rocker (Stuart) at 4°C for 1 hour. After incubation, the beads were spun down at 2,500 x g for 5 minutes at 4°C, and a sample of the supernatant was taken for analysis by SDS-PAGE. The beads were washed 5 times through resuspension in 1.5 mL of GFP-Trap stringent wash buffer, centrifugation at 2,500 x g, 4°C for 5 minutes, and the supernatant was removed. The washing step was repeated once more using GFP-Trap dilution buffer. A 5 µL sample of the fully washed beads was taken for analysis by SDS-PAGE to verify that the protein had effectively bound.

***Table 2.2: The volume of cell lysate required for effective binding to GFP-Trap beads.***

| **Construct** | **Volume required for incubation with GFP-Trap beads** |
|---|---|
| **GFP-talin 1 rod (R1-13)** | 5 mL of cell lysate from a 750 mL LB pellet. |
| **GFP** | 0.5 mL of cell lysate from a 750 mL LB pellet in a twofold dilution. |

### 2.4.4 GFP-Trap Immunoprecipitation: Incubation with CaSki cell lysate or murine neuronal extract

The talin-bound GFP-Trap beads were used as bait to isolate potential ligands from mammalian cells. Murine neuronal extract was obtained from Devrim Kilinc, PhD, Institut Pasteur de Lille, France. The lysed CaSki cells from section 2.2.7 or murine neuronal extract were diluted to 1100 µL with GFP-Trap dilution buffer, and a sample was taken for SDS-PAGE analysis. 490 µL of diluted CaSki lysate or murine neuronal extract was incubated with the GFP and GFP-talin rod-bound beads for one hour on a see-saw rocker (Stuart) at 4°C. The incubated beads in lysate or extract were spun down at 2,500 x g, 4°C for 5 minutes, a sample of the supernatant was taken for SDS-PAGE analysis, and the remaining supernatant was discarded. The beads were washed through resuspension in GFP-Trap regular wash buffer, centrifuged at 2,500 x g for 5 minutes, and the supernatant was removed. The washing cycle was repeated twice more, and the bead samples were mixed with equal amounts of 5x Laemmli buffer for analysis on SDS-PAGE.

#### Adapted Method

Following the first mass spectrometry (MS) proteomics results, to reduce the overwhelming presence of talin found in the samples and enable easy, confident identification of potential talin binders, the proteins bound to the talin were eluted from the GFP-talin rod on the GFP-Trap beads. Once all three washing cycles were completed, 10 µL GFP-Trap acidic glycine elution buffer was added to the beads, which were vortexed and left on ice for 5 minutes, before immediate neutralisation with 1 µL GFP-Trap neutralisation buffer. The elution process was repeated twice more, the beads were centrifuged at 2,500 x g 4°C for 5 minutes, and the elution supernatant was transferred to a separate 1.5 mL Eppendorf tube. The bead and elution samples were mixed with equal amounts of 5x Laemmli buffer for analysis on SDS-PAGE.

### 2.4.5 Circular Dichroism

Circular Dichroism (CD) spectroscopy is a useful technique to determine protein thermal stability and secondary structure. Optically active molecules, i.e. the chiral peptides in a protein backbone, exhibit differences in absorbance of right- and left-handed circular polarised light, which can be measured using CD (Berndt & Birkbeck College, 1996). Depending on the secondary structures present in a protein, the psi and pi angles in the peptide backbone will differ and preferentially absorb right or left-handed circular polarised light, giving rise to the characteristic far UV CD spectra demonstrated in Figure 2.1 (Berndt & Birkbeck College, 1996). Therefore, the different secondary structures present in a protein (i.e. alpha-helices, beta-sheets, coils, etc.) can be determined by measuring the CD from 200-260 nm and observing the characteristic CD spectra.

CD spectroscopy was conducted using a J715 spectropolarimeter (JASCO) and a PTC 423S/15 Peltier temperature controller (JASCO). Using a 0.1 cm quartz cuvette (Starna Scientific), far UV CD was performed on VD1 at 21.2 µM and VD1$^{A50I}$ at 22.4 µM in PBS from 204-260 nm, first at 20°C then 90°C, with a response of 0.5 seconds and a 1 nm bandwidth at 50 nm/min.

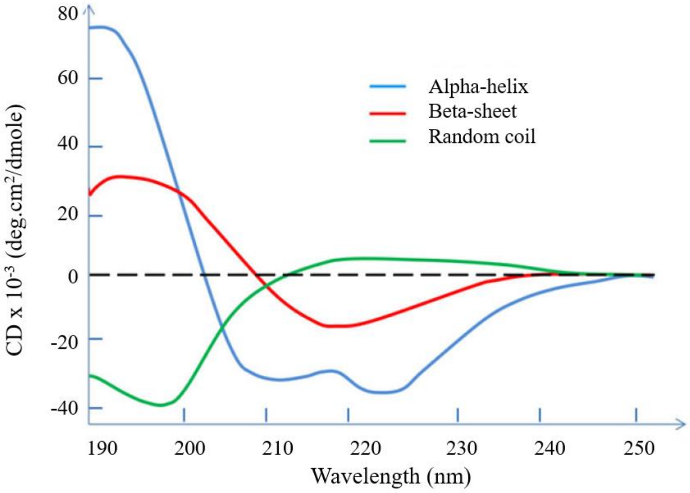

***Figure 2.1: Different secondary structures give rise to characteristic CD spectra (Wei et al., 2014).***
*The three predominant secondary structures present in a protein (alpha helices, beta sheets, and random coils) produce distinctive CD spectra.*

The thermal stability of the protein is shown by measuring the CD at 222 nm and varying the temperature from 20 to 90°C. As the temperature rises, the protein unfolds, resulting in a CD increase. A melting curve was generated for both VD1 at 21.2 µM and VD1$^{A50I}$ at 22.4 µM in PBS, by measuring the CD at 222 nm (the wavelength of maximal alpha-helical signal) across a temperature gradient from 20°C-90°C at 0.5°C intervals, with a response of 0.5 seconds and a 1 nm bandwidth. The melting curves were used to calculate the melting temperature ($T_m$) of both proteins, by identifying the temperature halfway between the fully folded and unfolded configurations.

### 2.4.6 Fluorescence Polarisation

Fluorescence Polarisation (FP) is a technique used to identify and quantify potential binding between a protein and a fluorescently labelled peptide. When a fluorophore on an unbound fluorescently labelled peptide is excited by polarised light, molecular tumbling promotes fluorophore reorientation, resulting in depolarised light emission (Moerke, 2009). However, if the fluorescently labelled peptide is bound to a protein larger than 10 kDa, the majority of light emitted will remain polarised, as the reorientation and subsequent molecular tumbling occurs at a slower rate (Moerke, 2009). Therefore, the degree of polarisation observed is proportional to the binding of the fluorescently labelled peptide and protein.

FP was carried out using protein concentrations between 200-300 µM in PBS. The protein was serially diluted in a black Nunc F96 plate (Thermo Fisher Scientific) across 12 wells, with well 1 containing no protein and well 12 containing the highest concentration of protein. Identical volumes of the fluorescently labelled peptide were added to each well, producing a final peptide concentration of 1 µM. FP was measured using a plate reader with polarising filters (CLARIOstar) at room temperature. The data was visualised in Prism software (GraphPad) and underwent a non-linear regression one site total analysis, to obtain the Kd and subsequent NS values. The one site total binding equation is as follows:

$$y = \frac{Bmax \cdot x}{(Kd + x)} + NS \cdot x + Background$$

where y = the fluorescence polarisation measured by the plate reader, x = protein concentration [µM], Bmax = the maximum specific binding, Kd = the protein concentration required for 50% binding at equilibrium (the equilibrium dissociation constant), NS = the slope of non-specific binding, and Background = the nonspecific binding amount with no additional fluorescently labelled peptide (GraphPad, 2020).

### 2.4.7 Gel Filtration Chromatography

Gel filtration, also known as size-exclusion chromatography, separates molecules based on their size and hydrodynamic volume (ConductScience, 2019). The solution of interest is passed through a column consisting of porous beads. Whilst larger molecules exit the column quickly by passing around the beads, smaller molecules diffuse through the pores, moving through the column at a slower rate. Gel filtration was performed at room temperature using an ÄKTA pure (GE Healthcare) and a Superdex G200 Increase 10/300 GL column (Cytiva). The column was first equilibrated with water, then gel filtration buffer at 0.75 mL/min. VD1 and VD1$^{A50I}$ in 20 mM Tris, 335 mM NaCl at 100 µM were loaded individually onto the column at a flow rate of 2 mL/min. The column was washed at 0.75 mL/min with water, then 20% ethanol, and stored at 4°C.

## 2.5 Bioinformatics

To identify potential talin binders from the synaptic vesicle proteins listed in Takamori et al., 2006, a bioinformatics pipeline was developed. Proteins were analysed for potential talin-binding sites, through evaluation of the most characterised talin-binding motif, (I/L D X□ □ X X□ X X X X X X□), where '□' represents a hydrophobic residue, in predicted alpha-helical intracellular regions identified by PSIPRED. A scoring system was developed to compare the similarity between the identified I/LD motifs and those present in known talin binders. T-coffee was used to align the promising I/LD motifs in mice with corresponding motifs in other organisms and evaluate whether they are conserved. The predicted protein structures, obtained through AlphaFold, were aligned to the structure of DLC1 bound to talin R7/8 (PDB: 5FZT) in PyMOL, to evaluate talin binding accessibility.

## 2.6 Molecular Biology Techniques

### 2.6.1 SDS-PAGE

10% SDS-PAGE gels were cast in Novex cassettes (Thermo Fisher Scientific), according to the manufacturer's instructions.

Most samples, excluding the before and after induction samples mentioned in section 2.2.5, were prepared using a 1:1 ratio of sample: 5X reducing Laemmli sample buffer, and boiled at 95°C for 60 seconds. The boiled samples were run on a gel for 30-40 minutes at 200 V. The gels were stained in 0.075% Coomassie Brilliant Blue R-250, 40% Methanol, 10% Glacial Acetic Acid for 10 minutes and destained twice with 25% methanol, 7% glacial acetic acid for 20 minutes.

### 2.6.2 Chemiluminescent Western Blotting (Immunoblotting)

Samples were run at 200V in 4–15% Criterion™ TGX™ precast midi protein gels (Bio-Rad), in a Criterion™ vertical electrophoresis cell (Bio-Rad) on a PowerPac HC high-current power supply (Bio-Rad) for 40 minutes. The samples on the gel were transferred to a PVDF membrane using Trans-Blot Turbo midi 0.2 µm PVDF transfer packs (Bio-Rad) and a Trans-Blot Turbo transfer system (Bio-Rad). The membrane was blocked for one hour at room temperature in TBST, 5% milk and washed with TBST three times for 6 minutes. The blot was incubated overnight at 4°C in a falcon tube with filter sterilised TBST, 5% BSA, and a primary antibody in a suitable dilution, specified by the manufacturer. The membrane was washed with TBST three times for 6 minutes and incubated for one hour at room temperature in TBST, 5% milk, and a 1 in 10,000 dilution of secondary antibody. The membrane was washed once more with TBST three times for 6 minutes, and detection of the proteins was achieved through chemiluminescence. The primary and corresponding secondary antibodies used are shown in

Table 2.3. The secondary antibodies were conjugated to Horseradish Peroxidase (HRP) and raised against the animals used for primary antibody production. The anti-His primary antibody, however, was already coupled to HRP; therefore, incubation with a secondary antibody was not necessary. To visualise the bands, ECL (enhanced chemiluminescence) (Bio-Rad), composed of luminol and peroxidase, was added to the membrane after incubation with the secondary antibody. The HRP catalyses the oxidation of the luminol in ECL to the unstable, excited 3-aminophthalate, which emits light at 425 nm upon decay. The light was captured using Amersham TM Hyperfilm (Cytiva) or a G:BOX Chemi XRQ gel doc system (Syngene), which utilises a CCD camera to detect chemiluminescence, enabling band visualisation.

***Table 2.3: Primary and corresponding secondary antibodies used.***
** The anti-GFP antibody was generously gifted by the Garrett laboratory at the University of Kent and produced by Bill Gullick at the Institute of Cancer Research; therefore, it is not commercially available.*

| Primary Antibody | Company | Product Code | Secondary Antibody Required | Company | Product Code |
|---|---|---|---|---|---|
| **Anti-1433G** | Thermo Fisher Scientific Invitrogen | MA1-16588 | Anti-Mouse HRP Affinity | Invitrogen | A16011 |
| **Anti-ARHGDIA** | Sigma-Aldrich | HPA021407 | Anti-Rabbit HRP Affinity | Invitrogen | A16023 |
| **Anti-CDK1** | Cell Signalling Technology | 9116 | Anti-Mouse HRP Affinity | Invitrogen | A16011 |
| **Anti-GFP*** | N/A | N/A | Anti-Mouse HRP Affinity | Invitrogen | A16011 |
| **Anti-His** | Sigma-Aldrich | A7058-1VL | N/A | - | - |
| **Anti-KANK1** | ATLAS Antibodies | HPA005539 | Anti-Rabbit HRP Affinity | Invitrogen | A16023 |
| **Anti-KANK2** | ATLAS Antibodies | HPA015643 | Anti-Rabbit HRP Affinity | Invitrogen | A16023 |
| **Anti-Septin-2** | Thermo Fisher Scientific Invitrogen | PA5-53814 | Anti-Rabbit HRP Affinity | Invitrogen | A16023 |

### 2.6.3 Synthetic Peptide Design of Potential Talin Binders

Following the identification of promising talin binders through I/LD motif analysis, synthetic peptides of these motifs were ordered from GL Biochem. At least two residues before and one following the motif were included, to ensure that the potential binding motif was fully incorporated in the synthetic peptide and binding of the full protein could be simulated. The majority of synthetic peptide sequences were ordered with a C-terminal cysteine residue, to enable fluorescein coupling. However, if the peptide contained a cysteine residue within its sequence, the peptide was instead ordered with an N-terminal fluorescein. The requested peptides are shown in Table 2.4; however, two peptides were not able to be synthesised effectively; therefore, peptides were only purchased if they were able to be made with a 95% purity.

***Table 2.4: Peptide constructs requested from GL Biochem.***

| Peptide | Protein | Uniprot ID | Sequence | Purity | Obtained |
|---|---|---|---|---|---|
| **mPICAL_FAM_38-60** | Phosphatidylinositol-binding clathrin assembly protein | Q7M6Y3 | 5-FAM-KKKHLDYLIQCTNEMNVNIPQLA | 85% | No |
| **mSNAPIN_FAM_55-78** | SNARE-associated protein Snapin | Q9Z266 | 5-FAM-REQIDNLATELCRINEDQKVALD | 95% | Yes |
| **mSNAPIN_71-97C** | SNARE-associated protein Snapin | Q9Z266 | DQKVALDLDPYVKKLLNARRRVVLVNNC | 95% | Yes |
| **mSNP25_176-198C** | Synaptosomal-associated protein 25 | P60879 | RQIDRIMEKADSNKTRIDEANQRC | 95% | Yes |
| **mSTX6_213-235C** | Syntaxin 6 | Q9JKK1 | RQIDRIMEKADSNKTRIDEANQRC | 85% | No |

### 2.6.4 Coupling Peptides to Fluorescein

The anhydrous peptides ordered with a C-terminal cysteine residue were dissolved in PBS and 100 µM was added to 951.5 µL PBS, 0.1% Triton X-100, 2.5 mM TCEP and 25 µL fluorescein dye, for a total volume of 1 mL. The coupling solution was wrapped in foil and incubated at room temperature for 2 hours on a carousel rotating shaker. The 1 mL coupling reaction was added to a PD-10 desalting column (GE Healthcare), previously equilibrated with 25 mL PBS. A further 1.5 mL PBS was added, and the peptide was eluted with 2.5 mL PBS. The peptide was typically eluted after 1 mL and collected in 3 x 0.5 mL fractions. The successfully eluted peptide fractions were combined, aliquoted at 50 µL, flash-frozen with liquid nitrogen, and stored at -20°C.

## 2.7 Tandem Mass Spectrometry Proteomics

### 2.7.1 Sample Preparation

#### 2.7.1.1 Band Excision

Samples (10 µL) were separated by SDS-PAGE at 100 V until the dye had travelled for ~1 cm. The gel was stained in Coomassie, destained, and allowed to reswell in 1% acetic acid. The sample well, band, and the entire lane above where the sample had travelled through the gel were excised and cut into ~2 x 1 mm pieces.

#### 2.7.1.2 Reduction and Alkylation

The gel pieces were washed in 150 µL 50 mM $NH_4HCO_3$: acetonitrile (1:1) for 15 minutes, shrunk in 150 µL acetonitrile for 15 minutes, and swelled in 100 µL 10 mM DTT, 50 mM $NH_4HCO_3$ for 30 minutes at 56°C. The samples were shrunk briefly in 100 µL acetonitrile for 1 minute, incubated in the dark for 20 minutes with 100 µL 55 mM chloroacetamide, 50 mM $NH_4HCO_3$, and washed once more in 150 µL 50 mM $NH_4HCO_3$: acetonitrile (1:1) for 15 minutes. The gel pieces were washed in 150 µL 50 mM $NH_4HCO_3$ for 15 minutes and 100 µL acetonitrile was added directly to the samples suspended in 50mM $NH_4HCO_3$. The gel pieces were left to incubate for 5 minutes and shrunk in 200 µL acetonitrile for 15 minutes. After each step, the samples were centrifuged for 1 minute at 5,000 rpm, and the supernatant was removed.

#### 2.7.1.3 In-gel Trypsin Digest

The samples were rehydrated in 50 µL 12.5 mM $NH_4HCO_3$, 10% acetonitrile, 5 ng/µL trypsin for 30 minutes. An additional 10 µL 12.5 mM $NH_4HCO_3$, 10% acetonitrile was added, and the gel pieces were left to incubate at room temperature overnight.

#### 2.7.1.4 Peptide Extraction

The samples were sonicated in an FS200b heated ultrasonic bath (Decon) for 15 minutes with 15 µL acetonitrile, and the supernatant was collected after centrifugation for 1 minute at 5,000 rpm. The samples were sonicated in the ultrasound bath for 15 minutes in 30 µL 50% acetonitrile, 5% formic acid. The supernatant was collected after centrifugation for 1 minute at 5,000 rpm, combined with the previous supernatant, and stored at -20°C.

### 2.7.2 Nanoscale Liquid Chromatography-Mass Spectrometry/Mass Spectrometry Analysis

Samples were analysed by Liquid Chromatography-Mass Spectrometry/Mass Spectrometry (LC-MS/MS) both in-house and by our collaborator, Guillaume Jacquemet (Turku Bioscience, Finland). In liquid chromatography, the peptides in a sample will interact and have varying affinities with the mobile and stationary phases; therefore, they will elute from the column at different times. An interface ionises and evaporates the peptides, enabling their entry into the mass spectrometer, which operates under a vacuum (Ho et al., 2003). Mass spectrometry identifies the mass-to-charge ratios (m/z) of the peptides, allowing a mass spectrum to be produced where m/z is plotted against relative abundance. The data collected from the LC-MS/MS, such as retention time, m/z, and abundance, was used in computational analysis to identify the proteins in the samples through peptide evaluation.

#### 2.7.2.1 LC-MS/MS at Turku Bioscience, BioCity, Finland

An EASY-nLC™ 1200 System (Thermo Fisher Scientific) coupled to a Q-Exactive HF mass spectrometer with a nano-electrospray ionisation interface (Thermo Fisher Scientific) was used to analyse the samples. Samples were initially loaded onto a trap column for further concentration and purification, then directed through a 75 µm x 15 cm ReproSil-Pur basic C18 column (Dr Maisch). Solvent A (0.1% formic acid) and solvent B (80% acetonitrile with 0.1% formic acid) were used as the mobile phase. Peptides were eluted from the column following a 20-minute linear gradient of 6–39% solvent B.

Thermo Xcalibur 4.1 software (Thermo Fisher Scientific) was used to automatically select MS data from 350-1750 m/z. Only one missed tryptic cleavage was permitted, and only tryptic peptides were included. Many proteins were identified, and the number of peptide-spectrum matches (PSMs) for each protein was listed in the MS analysis. The PSMs for each protein in postsynaptic, presynaptic, and synaptosomal murine neuronal fractions were pooled together and counted as an n-of-3 experiment for 'murine neuronal extract' to generate protein fold change and p-values. The $-\log_2$ (p-value) and $\log_2$ (fold change) of the samples were plotted in a volcano plot, and the proteins with a significant p-value and a fold change above 1 were classified as potential talin binders. The data was further analysed to identify proteins with a significant difference of over 200 PSMs in the postsynaptic and presynaptic samples, and all potential talin binders were analysed bioinformatically.

#### 2.7.2.2 LC-MS/MS at University of Kent, England

Samples were thawed, vacuum dried by an SPD11V SpeedVac™ (Thermo Fisher Scientific), resuspended in 20 µL 5% acetonitrile, 0.1% trifluoroacetic acid, and cleaned using Pierce C18 Spin Tips (Thermo Fisher Scientific), according to the manufacturer's protocol.

An ACQUITY M-Class UPLC (Waters) coupled to a SYNAPT G2-Si mass spectrometer with a nanospray interface (Waters) was used to analyse the samples. Samples were loaded on a 75 µm X 15 cm HSS T3 ACQUITY 100Å, 1.8 µm column (Waters) at 10 µL/min. Solvent A (0.1% formic acid) and solvent B (acetonitrile with 0.1% formic acid) were used as the mobile phase. The peptides were eluted following a 90-minute linear gradient of 5-40% solvent B.

The mass spectrometry data was collected in UDMSe mode and imported into Progenesis QI software (Non-Linear Dynamics) for proteomics analysis. Using an MSE search algorithm, the peptides were identified and searched against a mouse or human proteome database with a 4% false detection rate. The protein abundance quantitation and confidence values were generated by the Apex3D algorithm, and any result with less than three unique peptides was discounted. The fold change values and p-values, if applicable, were calculated and volcano plots were generated by plotting $\log_2$ (fold change) against $-\log_2$ (p-value), or if the p-value could not be calculated, in the case of n-of-1 experiments, $\log_2$ (confidence) was plotted against $\log_2$ (fold change). The proteins with fold change values above 1, confidence scores above 125 and/or significant p-values were identified as potential talin-binding ligands.

## 2.8 X-Ray Crystallography

### 2.8.1 Initial Screening

Initial crystallisation screening for $\mathrm{VD1}^{\mathrm{A50I}}$ and talin 1 R2 helix 6, also known as vinculin binding site helix 6 (VBS6), was carried out using the classic wizard box 1/2 (Rigaku) and JCSG-plus box 1/2 (Molecular Dimensions) screening kits. $\mathrm{VD1}^{\mathrm{A50I}}$ and VBS6 in 20 mM Tris, 335 mM NaCl was mixed in a 1: 1.5 ratio of $\mathrm{VD1}^{\mathrm{A50I}}$: H6 at 420µM: 645µM. Screening solutions were transferred to a 96-well plate, and the screening trials were conducted by a Mosquito LCO liquid handling system (STP Labtech) through hanging drop vapour diffusion. The plates were left to incubate at room temperature, and crystal formation was monitored after 5 days using an MDG41 microscope (Leica). Crystals were identified and marked on a crystal screening chart.

### 2.8.2 Crystal Optimisation

The most promising crystals were observed in well 3H, 6H, and 8H, which corresponded to the JCSG+ box 2 buffers 39 (0.1 M Bis-Tris, pH 5.5, 25% w/v PEG 3350), 42 (0.1 M ammonium acetate, 0.1 M Bis-Tris, pH 5.5, 17% w/v PEG 10,000), and 44 (0.2 M NaCl, 0.1 M Bis-Tris, pH 5.5, 25% w/v PEG 3350). Therefore, a 24-well optimisation plate was created for each buffer. For 3H, an optimisation plate was created varying 0.1 M Bis-Tris pH 5-6.5 and 15-40% PEG 3350. For 6H, an optimisation plate was created varying 0.1 M Bis-Tris pH 5-6.5, 12-22% PEG 10,000, and 0.1-0.2 M ammonium acetate. For 8H, an optimisation plate was created varying 0.1 M Bis-Tris pH 5-6.5, 15-40% PEG 3350, and 0.1-0.2 M NaCl. The plates were left to incubate at room temperature, and crystal formation was monitored after 5 days using an MDG41 microscope (Leica). Crystals were identified and marked on a crystal screening chart.

# Results

## 3 Identifying potential talin binders in synaptic vesicle proteins

### 3.1 Theory Overview

The MeshCODE theory may provide a mechanical insight into many neurological processes, such as the regulation of synaptic vesicle activity (Goult, 2021). Proteomic analyses have identified the proteins present in an average synaptic vesicle, many of which are displayed in Figure 3.1 (Takamori et al., 2006). To determine a link between mechanical signalling and neuronal activity, the synaptic vesicle proteins identified in Takamori et al., 2006 were analysed for the best-characterised talin-binding motif. If any synaptic vesicle proteins were confirmed to interact with talin, a mechanism could be devised demonstrating how talin may regulate vesicular release, thereby providing substantial evidence to support the MeshCODE theory.

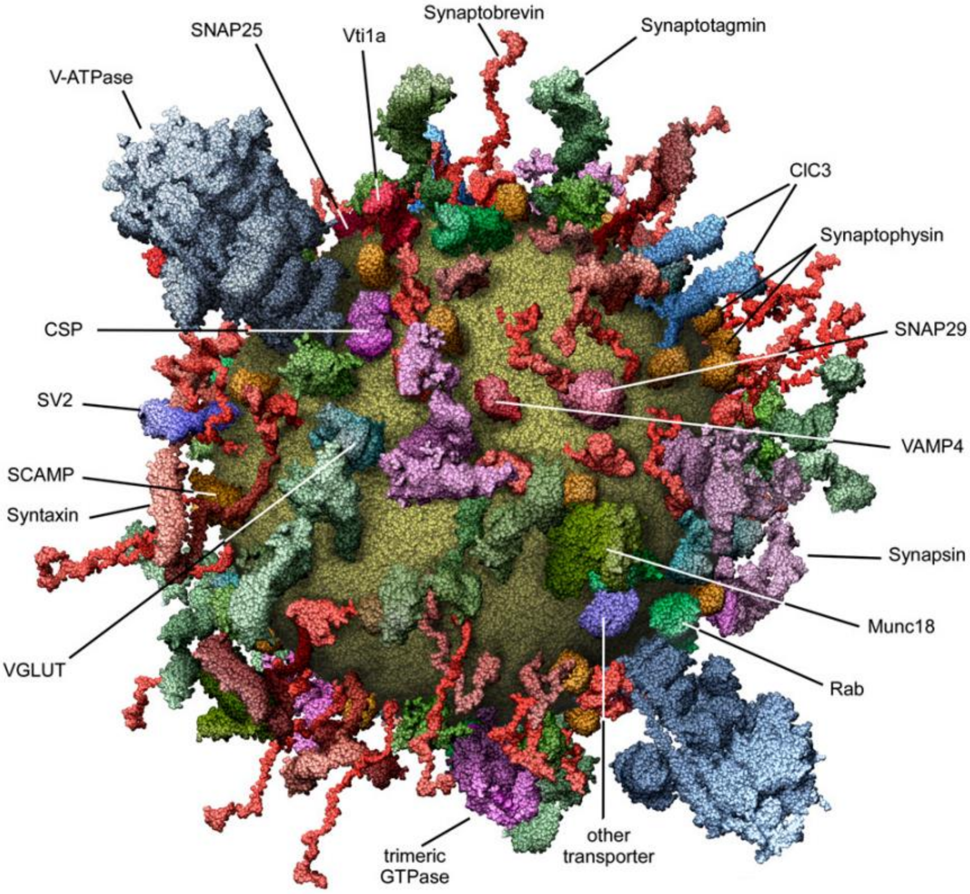

***Figure 3.1: The predominant proteins present on the surface of an average synaptic vesicle (Takamori et al., 2006).***
*There are many proteins on the surface of synaptic vesicles which are fundamental to vesicle function, i.e. synaptobrevin. If talin is found to regulate synaptic vesicular release, these proteins may likely exhibit talin-binding activity.*

## 3.2 A bioinformatics pipeline identified several potential talin-binding motifs in synaptic vesicle proteins

In alpha-helical regions, an I/LD motif, (I/L D X □ □ X X □ X X X X X X □) where '□' represents a hydrophobic residue, has been shown to bind to talin in many proteins when the rod domains are in their folded conformation and is currently the best-characterised talin-binding motif (Gough et al., 2021; Zacharchenko et al., 2016). Secondary structures of the synaptic vesicle protein sequences were predicted using PSIPRED, and any possible I/LD talin-binding motifs in an alpha-helical and intracellular region were identified, to ascertain which motifs would be exposed on the vesicle exterior (McGuffin et al., 2000). Each motif was given a score depending on how similar it was to the I/LD motifs present in known talin binders, i.e. RIAM. One point was given to every I/LD motif present in the proteins, with additional points awarded if the motif had an E/D before the I/LD and if hydrophobic residues were present in the 4th, 5th, 8th, and 15th positions. If the motif had another I/LD motif present within the first 15 residues, it was awarded half a point, allowing the maximum score to be 6.5. Using this approach, the majority of known talin I/LD motifs achieved a score above 5, with the exception of KANK1 and 2, which both scored 3. Out of the synaptic vesicle proteins analysed, the motifs present in syntaxin 6, phosphatidylinositol-binding clathrin assembly protein (PICAL), synaptosomal-associated protein 25 (SNAP 25), and SNARE-associated protein snapin achieved a score of 4 or above, as demonstrated in Table 3.1. Therefore, these proteins were identified with the most promising I/LD binding motifs.

***Table 3.1: Synaptic vesicle proteins identified with the most promising I/LD motifs.***

| Protein | UniProt ID | I/LD motif intracellular region | Position 4 hydrophobic acid | E/D prior residue | Hydrophobic residues at correct positions | Linked motif | Overall Score |
|---|---|---|---|---|---|---|---|
| **Syntaxin 6** | Q9JKK1 | LDNV | V | - | Position 5, 8: M, L | - | 4 |
| **PICAL** | Q7M6Y3 | LDYL | L | - | Position 5, 15: I, I | - | 4 |
| **SNAP 25** | P60879 | IDRI | I | - | Position: 5, 8, 15: M, A, I | - | 5 |
| **SNARE-associated protein (Snapin)** | Q9Z266 | IDNL | L | - | Position 5, 8: A, L | - | 4 |
| | | LDPY | - | D | Position 5, 8, 15: V, L, V | - | 5 |

T-coffee was used to align the promising I/LD motifs in humans against corresponding motifs in other organisms and known talin-binding I/LD motifs (Figures 3.2 and 3.3). Whilst it is difficult to determine the conservation of these potential talin-binding motifs from four eukaryotic homologs, as the identified I/LD binding motifs were conserved in all the organisms chosen, this does provide a positive indication of their importance (Madeira et al., 2019).

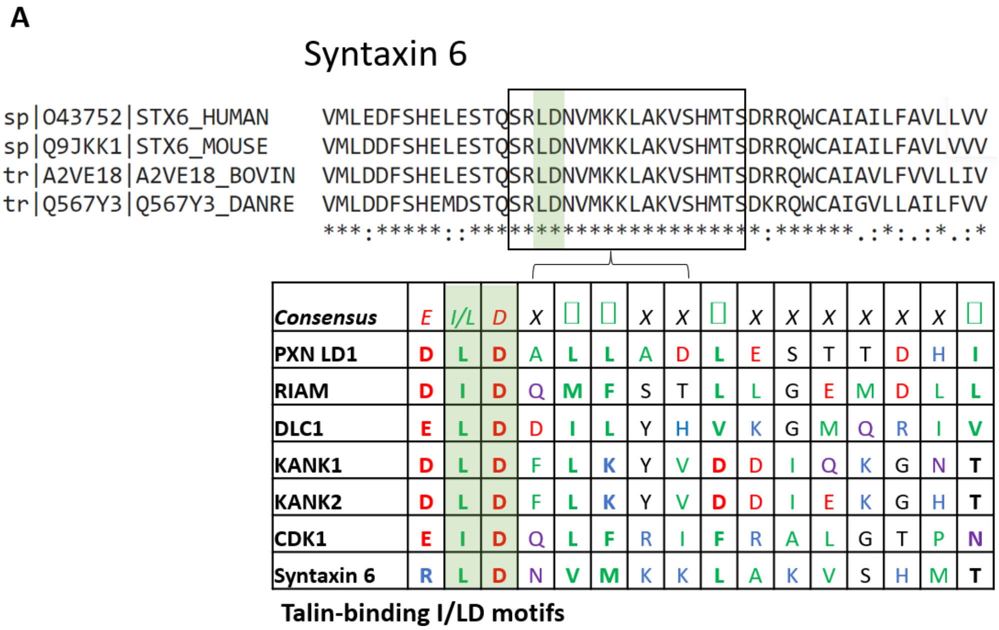

```
sp|O43752|STX6_HUMAN     VMLEDFSHELESTQSRLDNVMKKLAKVSHMTSDRRQWCAIAILFAVLLVV
sp|Q9JKK1|STX6_MOUSE     VMLDDFSHELESTQSRLDNVMKKLAKVSHMTSDRRQWCAIAILFAVLVVV
tr|A2VE18|A2VE18_BOVIN   VMLDDFSHELESTQSRLDNVMKKLAKVSHMTSDRRQWCAIAVLFVVLLIV
tr|Q567Y3|Q567Y3_DANRE   VMLDDFSHEMDSTQSRLDNVMKKLAKVSHMTSDKRQWCAIGVLLAILFVV
                         ***:*****::**********************:******.:*:.:*.:*
```

| **Consensus** | *E* | *I/L* | *D* | *X* | □ | □ | *X* | *X* | □ | *X* | *X* | *X* | *X* | *X* | *X* | □ |
|---|---|---|---|---|---|---|---|---|---|---|---|---|---|---|---|---|
| **PXN LD1** | **D** | **L** | **D** | A | **L** | **L** | A | D | **L** | E | S | T | T | D | H | **I** |
| **RIAM** | **D** | **I** | **D** | Q | **M** | **F** | S | T | **L** | L | G | E | M | D | L | **L** |
| **DLC1** | **E** | **L** | **D** | D | **I** | **L** | Y | H | **V** | K | G | M | Q | R | I | **V** |
| **KANK1** | **D** | **L** | **D** | F | **L** | **K** | Y | V | **D** | D | I | Q | K | G | N | **T** |
| **KANK2** | **D** | **L** | **D** | F | **L** | **K** | Y | V | **D** | D | I | E | K | G | H | **T** |
| **CDK1** | **E** | **I** | **D** | Q | **L** | **F** | R | I | **F** | R | A | L | G | T | P | **N** |
| **Syntaxin 6** | **R** | **L** | **D** | N | **V** | **M** | K | K | **L** | A | K | V | S | H | M | **T** |

**Talin-binding I/LD motifs**

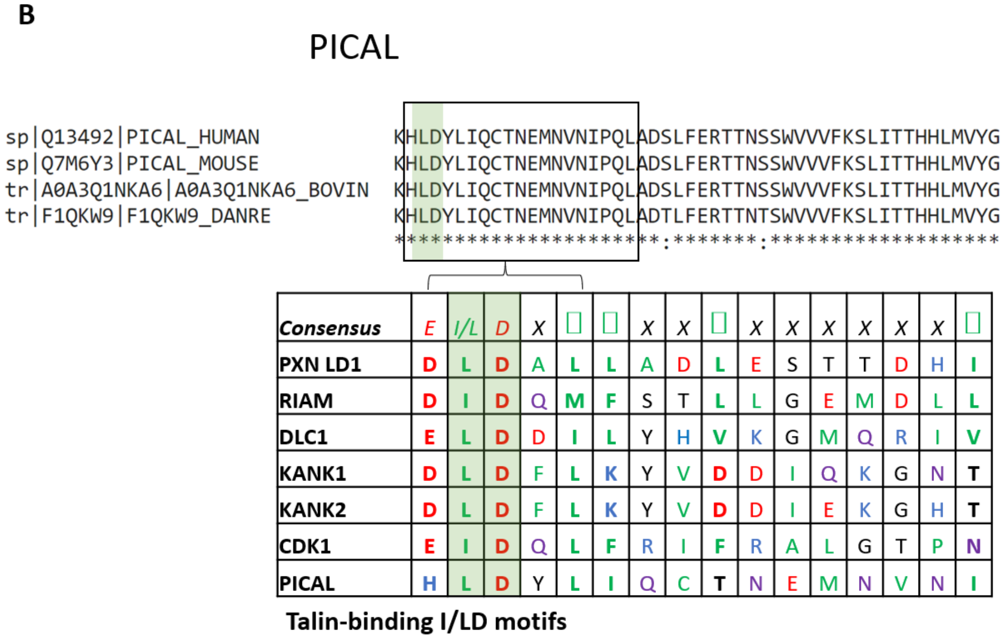

```
sp|Q13492|PICAL_HUMAN            KHLDYLIQCTNEMNVNIPQLADSLFERTTNSSWVVVFKSLITTHHLMVYG
sp|Q7M6Y3|PICAL_MOUSE            KHLDYLIQCTNEMNVNIPQLADSLFERTTNSSWVVVFKSLITTHHLMVYG
tr|A0A3Q1NKA6|A0A3Q1NKA6_BOVIN   KHLDYLIQCTNEMNVNIPQLADSLFERTTNSSWVVVFKSLITTHHLMVYG
tr|F1QKW9|F1QKW9_DANRE           KHLDYLIQCTNEMNVNIPQLADTLFERTTNTSWVVVFKSLITTHHLMVYG
                                 **********************:********:******************
```

| **Consensus** | *E* | *I/L* | *D* | *X* | □ | □ | *X* | *X* | □ | *X* | *X* | *X* | *X* | *X* | *X* | □ |
|---|---|---|---|---|---|---|---|---|---|---|---|---|---|---|---|---|
| **PXN LD1** | **D** | **L** | **D** | A | **L** | **L** | A | D | **L** | E | S | T | T | D | H | **I** |
| **RIAM** | **D** | **I** | **D** | Q | **M** | **F** | S | T | **L** | L | G | E | M | D | L | **L** |
| **DLC1** | **E** | **L** | **D** | D | **I** | **L** | Y | H | **V** | K | G | M | Q | R | I | **V** |
| **KANK1** | **D** | **L** | **D** | F | **L** | **K** | Y | V | **D** | D | I | Q | K | G | N | **T** |
| **KANK2** | **D** | **L** | **D** | F | **L** | **K** | Y | V | **D** | D | I | E | K | G | H | **T** |
| **CDK1** | **E** | **I** | **D** | Q | **L** | **F** | R | I | **F** | R | A | L | G | T | P | **N** |
| **PICAL** | **H** | **L** | **D** | Y | **L** | **I** | Q | C | **T** | N | E | M | N | V | N | **I** |

**Talin-binding I/LD motifs**

***Figure 3.2: I/LD talin-binding motif and sequence alignment for (A) syntaxin 6 and (B) PICAL, against the I/LD motifs of known talin binders.***
*Alignment was carried out by T-Coffee (Madeira et al., 2019). Red residues represent acidic amino acids, blue residues represent basic amino acids, green residues represent hydrophobic amino acids, purple residues represent hydrophilic amino acids, and black residues represent neutral amino acids. An asterisk (*) indicates full residue conservation, a colon (:) indicates conservation between residues with similar properties, and a full stop (.) indicates conservation between residues with weakly similar properties. Figure adapted from (Gough et al., 2021).*

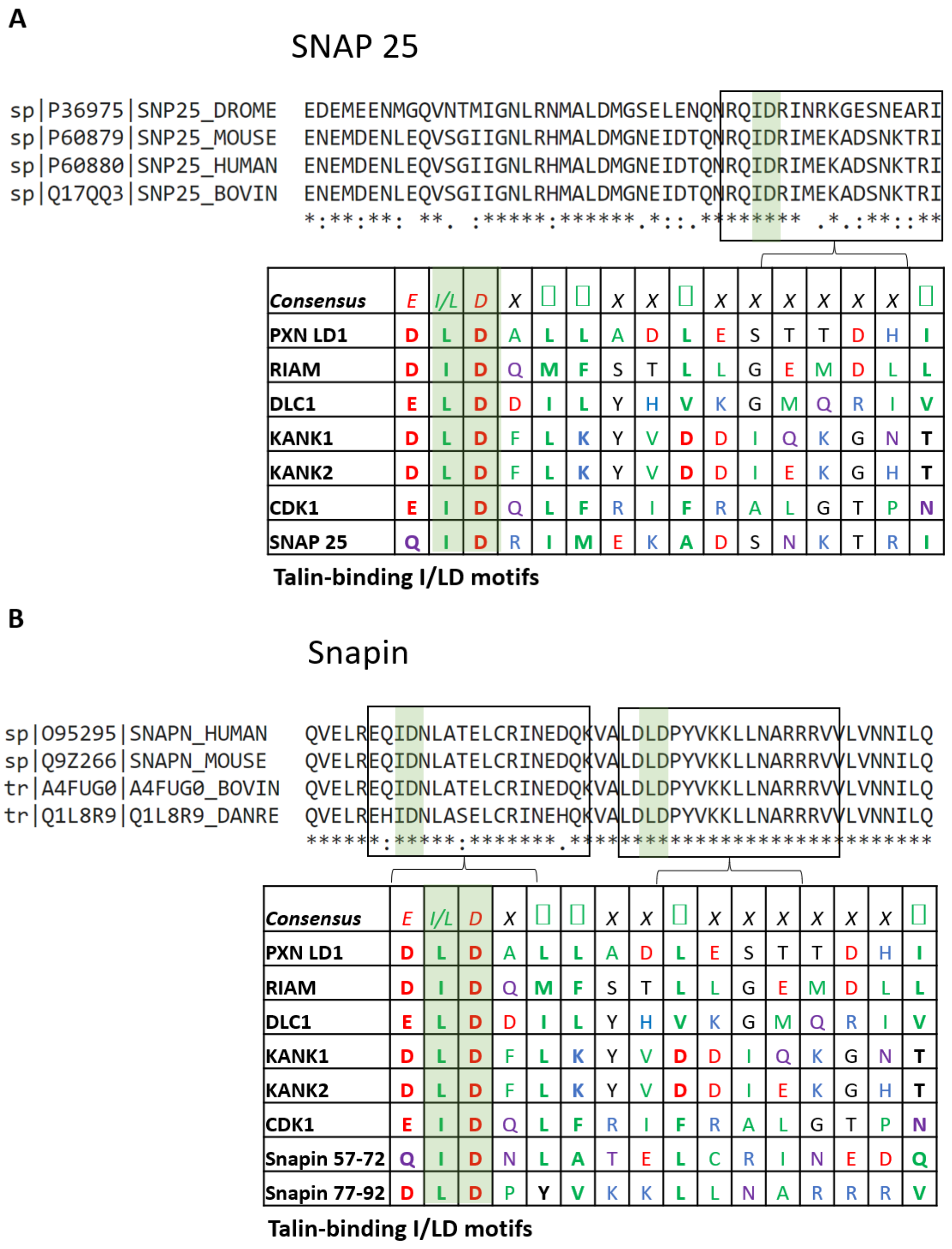

SNAP 25

```
sp|P36975|SNP25_DROME   EDEMEENMGQVNTMIGNLRNMALDMGSELENQNRQIDRINRKGESNEARI
sp|P60879|SNP25_MOUSE   ENEMDENLEQVSGIIGNLRHMALDMGNEIDTQNRQIDRIMEKADSNKTRI
sp|P60880|SNP25_HUMAN   ENEMDENLEQVSGIIGNLRHMALDMGNEIDTQNRQIDRIMEKADSNKTRI
sp|Q17QQ3|SNP25_BOVIN   ENEMDENLEQVSGIIGNLRHMALDMGNEIDTQNRQIDRIMEKADSNKTRI
                        *:**:**:  **.  :*****:******.*::.********  .*.:**::**
```

| Consensus | E | I/L | D | X | □ | □ | X | X | □ | X | X | X | X | X | X | □ |
|---|---|---|---|---|---|---|---|---|---|---|---|---|---|---|---|---|
| **PXN LD1** | D | L | D | A | L | L | A | D | L | E | S | T | T | D | H | I |
| **RIAM** | D | I | D | Q | M | F | S | T | L | L | G | E | M | D | L | L |
| **DLC1** | E | L | D | D | I | L | Y | H | V | K | G | M | Q | R | I | V |
| **KANK1** | D | L | D | F | L | K | Y | V | D | D | I | Q | K | G | N | T |
| **KANK2** | D | L | D | F | L | K | Y | V | D | D | I | E | K | G | H | T |
| **CDK1** | E | I | D | Q | L | F | R | I | F | R | A | L | G | T | P | N |
| **SNAP 25** | Q | I | D | R | I | M | E | K | A | D | S | N | K | T | R | I |

**Talin-binding I/LD motifs**

Snapin

```
sp|O95295|SNAPN_HUMAN   QVELREQIDNLATELCRINEDQKVALDLDPYVKKLLNARRRVVLVNNILQ
sp|Q9Z266|SNAPN_MOUSE   QVELREQIDNLATELCRINEDQKVALDLDPYVKKLLNARRRVVLVNNILQ
tr|A4FUG0|A4FUG0_BOVIN  QVELREQIDNLATELCRINEDQKVALDLDPYVKKLLNARRRVVLVNNILQ
tr|Q1L8R9|Q1L8R9_DANRE  QVELREHIDNLASELCRINEHQKVALDLDPYVKKLLNARRRVVLVNNILQ
                        ******:*****:*******.*****************************
```

| Consensus | E | I/L | D | X | □ | □ | X | X | □ | X | X | X | X | X | X | □ |
|---|---|---|---|---|---|---|---|---|---|---|---|---|---|---|---|---|
| **PXN LD1** | D | L | D | A | L | L | A | D | L | E | S | T | T | D | H | I |
| **RIAM** | D | I | D | Q | M | F | S | T | L | L | G | E | M | D | L | L |
| **DLC1** | E | L | D | D | I | L | Y | H | V | K | G | M | Q | R | I | V |
| **KANK1** | D | L | D | F | L | K | Y | V | D | D | I | Q | K | G | N | T |
| **KANK2** | D | L | D | F | L | K | Y | V | D | D | I | E | K | G | H | T |
| **CDK1** | E | I | D | Q | L | F | R | I | F | R | A | L | G | T | P | N |
| **Snapin 57-72** | Q | I | D | N | L | A | T | E | L | C | R | I | N | E | D | Q |
| **Snapin 77-92** | D | L | D | P | Y | V | K | K | L | L | N | A | R | R | R | V |

**Talin-binding I/LD motifs**

***Figure 3.3: I/LD talin-binding motif and sequence alignment for (A) SNAP 25 and (B) snapin, against the I/LD motifs of known talin binders.***

*Alignment was carried out by T-Coffee (Madeira et al., 2019). Red residues represent acidic amino acids, blue residues represent basic amino acids, green residues represent hydrophobic amino acids, purple residues represent hydrophilic amino acids, and black residues represent neutral amino acids. An asterisk (*) indicates full residue conservation, a colon (:) indicates conservation between residues with similar properties, and a full stop (.) indicates conservation between residues with weakly similar properties. Figure adapted from (Gough et al., 2021).*

To identify whether the promising I/LD motifs were present in a location accessible for talin-binding, the predicted protein structures, obtained using AlphaFold, were aligned to the structure of DLC1 bound to talin R7/8 (PDB: 5FZT) in PyMOL (Figure 3.4).

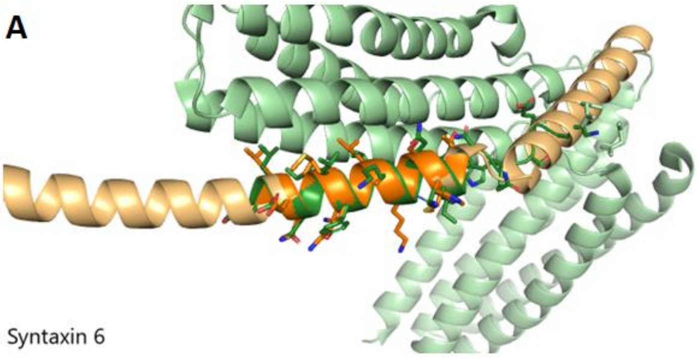

Syntaxin 6

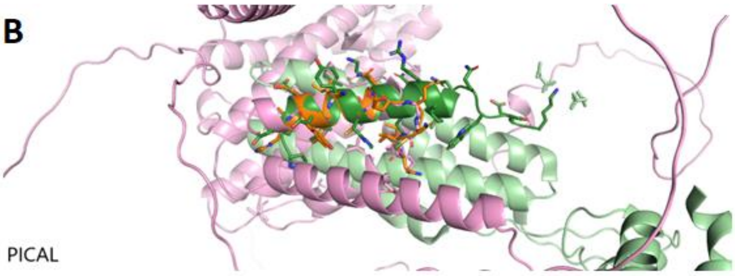

PICAL

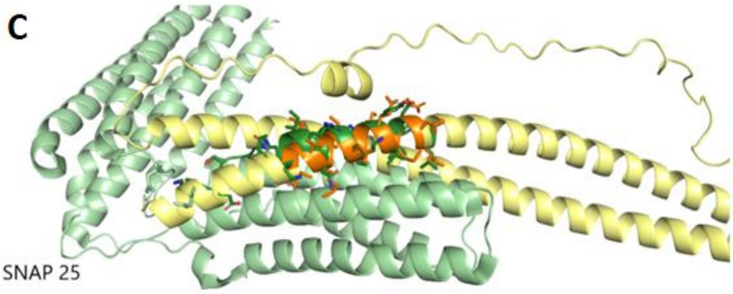

SNAP 25

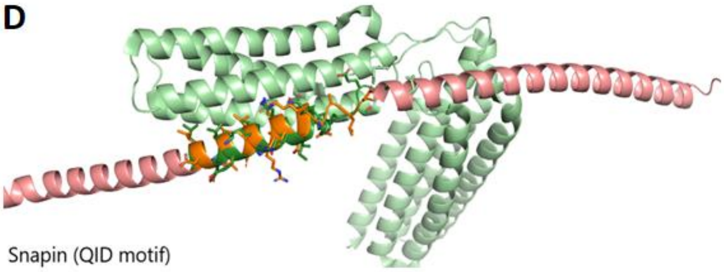

Snapin (QID motif)

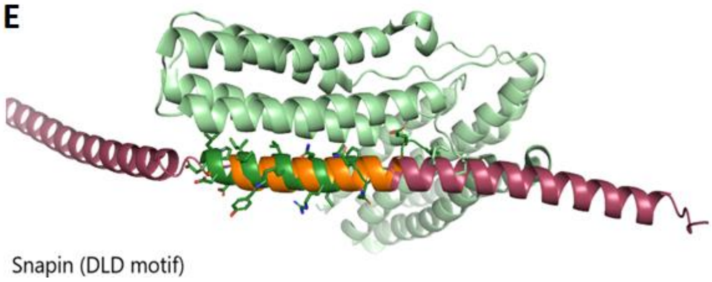

Snapin (DLD motif)

***Figure 3.4: PyMOL alignments of (A) syntaxin 6, (B) PICAL, (C) SNAP 25, (D) snapin QID motif, and (E) snapin DLD motif with DLC1 bound to R7-8.***

*Talin R7-8 is pale green, DLC1 bound to R7-8 is dark green, the possible talin-binding motif in each protein is in orange, syntaxin 6 is light orange, PICAL is pink, SNAP 25 is yellow, whilst snapin is light pink in the QID motif alignment and dark pink in the DLD motif alignment.*

The motifs in syntaxin 6, SNAP 25, and snapin seem to be situated in a very accessible position, therefore implying the structural possibility of talin binding. However, the I/LD motif in PICAL seemed slightly less exposed than the others; nevertheless, as it is present in a helix on the exterior of the protein and not buried in the centre, binding could not be ruled out.

## 3.3 The potential interactors bound to talin with low or no affinity

Synthetic peptides of each potential talin-binding motif were ordered and coupled to fluorescein. The synthetic peptides for syntaxin 6 and PICAL however, could not be synthesised beyond 85% purity and therefore, were not ordered. Direct binding was determined by FP assays for SNAP 25, snapin 55-78 (QID motif), snapin 71-97 (DLD motif), and RIAM TBS1 with talin R4-8, R7-8, R9-10, R11, and R9-12 (Figures 3.5 and 3.6). RIAM TBS1 binds to talin R2, R3, R8, and R11; therefore, TBS1 acts as a positive control for the FP assays involving R4-8, R7-8, R11, and R9-12 (Goult et al., 2013). There is not a RIAM binding site present in R9-10; therefore, for the FP assays involving R9-10, RIAM TBS1 can only bind with low affinity, effectively serving as a negative control (Figure 3.6 A).

As seen in Figures 3.5 and 3.6, compared to the binding exhibited by RIAM TBS1 and R4-8, R7-8, R11, or R9-12, the synthetic peptides of the potential talin binders did not exhibit strong direct binding. In several assays, changes in FP can be observed; however, the data could not be fitted using the Prism one site total binding equation. Therefore, it is not possible to conclusively establish that weak binding has occurred, as the Kd could not be determined. Nevertheless, there is a difference in binding strength between the potential interactors. For all the rod domains tested, a clear absence of binding for snapin 55-78 was observed, allowing the slight differences in binding for the other two peptides (snapin 71-97 and SNAP 25 178-198) to be visualised easily. The clearest example of this can be seen in Figure 3.6 A, where snapin 55-78 evidently does not bind to R9-10, as an increase in R9-10 concentration has no effect on the FP detected. The fluorescence polarisation of the other peptides, however, does increase to a similar level as RIAM TBS1 when the concentration of R9-10 increases. Whilst snapin 55-78 clearly does not bind to any of the talin rod domains trialled, snapin 71-97 seems to demonstrate the best ability to bind to the talin rod domains. The slight increase in FP observed for the assays involving R9-10 can likewise be observed for snapin 71-97 in three additional FP assays with R4-8, R7-8, and R9-12, yet for SNAP 25 it is seen in two additional FP assays with R7-8 and R9-12 (Figures 3.5 and 3.6).

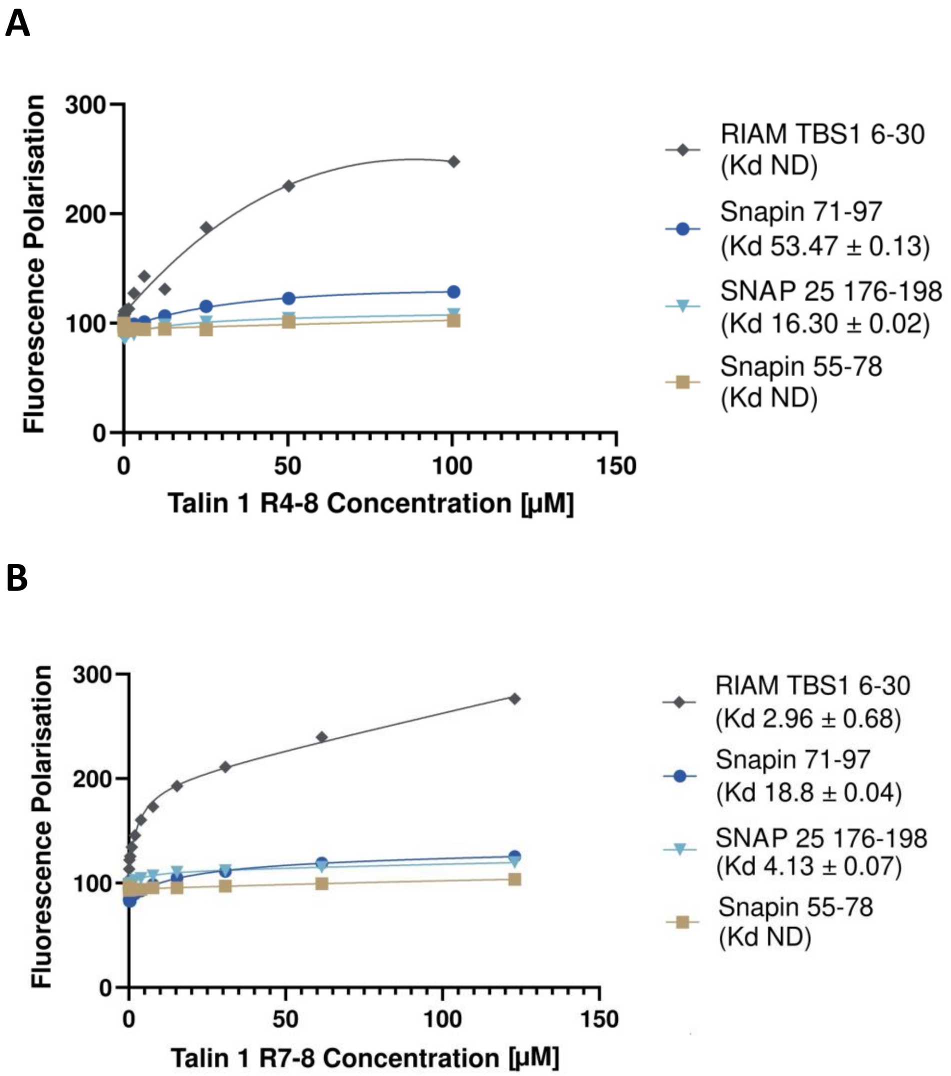

***Figure 3.5: SNAP 25, snapin 55-78, and snapin 71-97 bound to (A) talin R4-8 and (B) R7-8 with low or no affinity.***

*Binding of fluorescein-labelled SNAP 25, snapin 55-78, snapin 71-97, and BODIPY-labelled RIAM TBS1 to talin R4-8 and R7-8 was measured through fluorescence polarisation assays. Experiments were performed in duplicate. The dissociation constants in μM +/- SE are shown in the legend. Error bars are too small for visualisation. ND = not determined. Note: Binding between RIAM TBS1 and R4-8 was clearly observed; however, the Prism one site total binding equation utilised could not determine a Kd.*

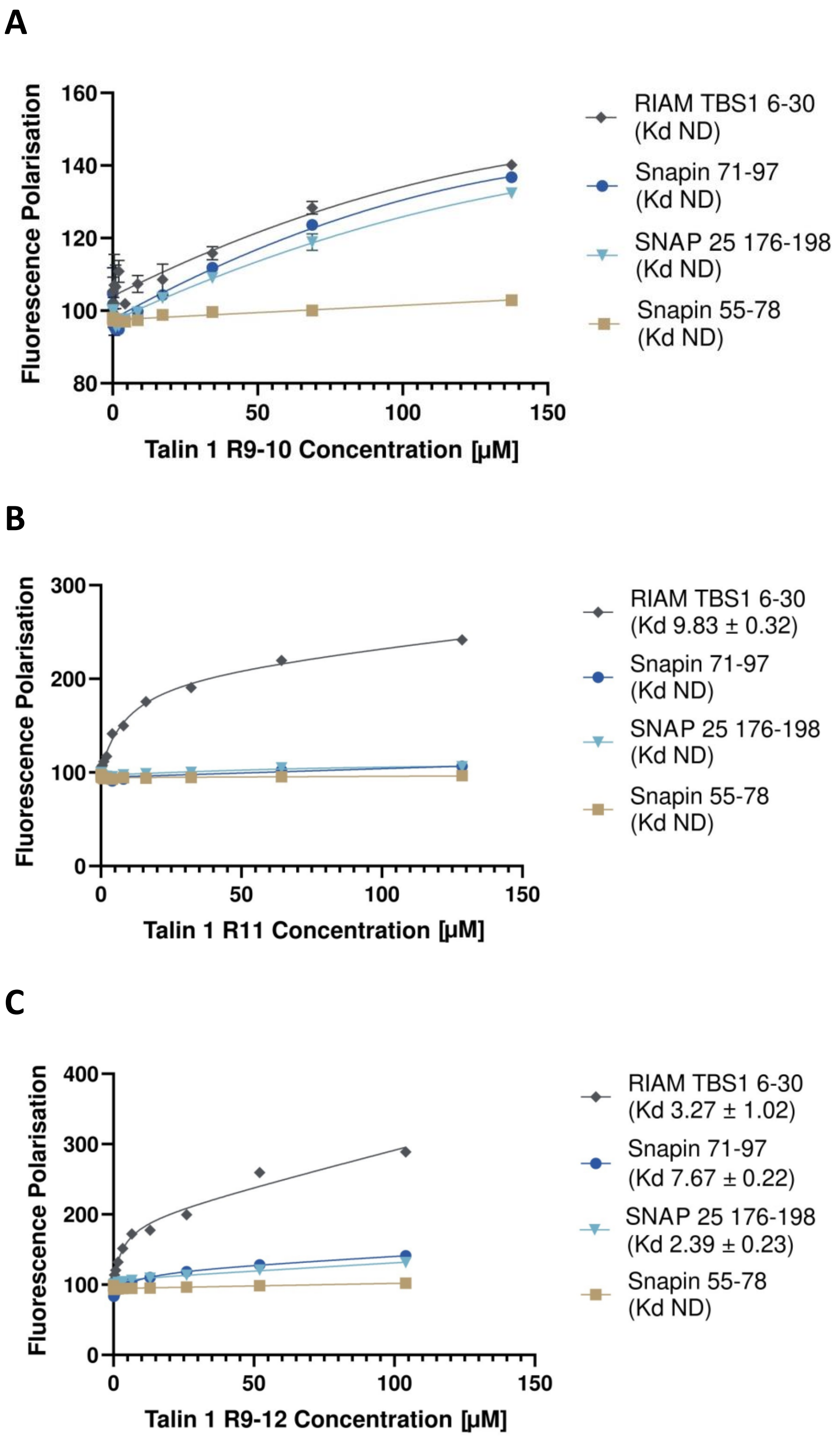

***Figure 3.6: SNAP 25, snapin 55-78, and snapin 71-97 bound to (A) talin R9-10, (B) R11, and (C) R9-12 with low or no affinity.***

*Binding of fluorescein-labelled SNAP 25, snapin 55-78, snapin 71-97, and BODIPY-labelled RIAM TBS1 to talin R9-10, R11, and R9-12 was measured through fluorescence polarisation assays. Experiments were performed in duplicate. The dissociation constants in µM +/- SE are shown in the legend. Error bars are too small for visualisation. ND = not determined.*

# 4 Developing a novel method to identify talin-binding proteins in brain extract

## 4.1 Method Theory: A talin 'fishing' rod

A talin 'fishing' rod experiment was theorised to identify novel talin-binding ligands in various cell extracts, as demonstrated in Figure 4.1. After binding the talin rod to agarose beads through an affinity tag, these talin-bound beads would then be incubated in cell lysate. Talin binders in the cell lysate would bind to the talin, and after the beads were separated from the cell lysate supernatant, any proteins bound could be identified via LC-MS/MS proteomics analysis. The potential talin binders would subsequently be analysed through the bioinformatics pipeline described in section 3 and confirmed biochemically.

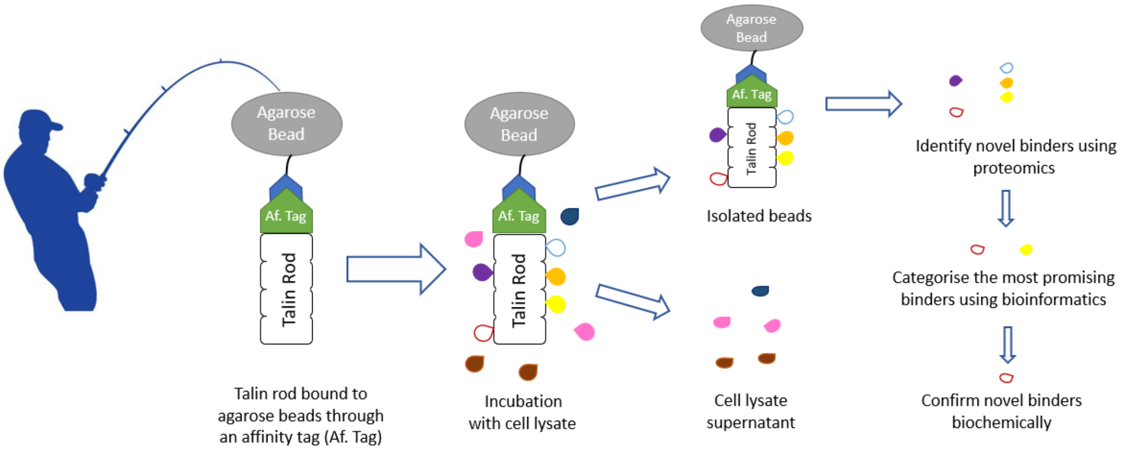

***Figure 4.1: The theorised talin 'fishing' rod experiment to identify novel talin-binding ligands in the brain.*** *To identify novel talin-binding ligands, a method termed the talin 'fishing' rod experiment was hypothesised. The talin rod would be purified and bound to agarose beads through an affinity tag, the talin rod-bound beads would then be incubated with cell lysate to promote talin-ligand interactions. The beads and supernatant would be separated, and the bead fraction would be analysed via MS proteomics to identify novel talin binders. The most promising binders would be determined through utilisation of the bioinformatics pipeline, followed by biochemical confirmation of the novel talin-binding ligands, i.e. via FP.*

## 4.2 Attempting to use GST pulldowns to identify novel talin binders

### 4.2.1 Optimisation of binding talin to GFP-Trap beads

The first method trialled to identify talin-binding ligands were GST pulldowns. The pGEX stretch talin constructs talin 1 and 2 R1-13, with molecular weights of 279 and 274 kDa, respectively, were grown and initially purified via immobilised Ni ion affinity chromatography. The purified constructs were incubated with GSH resin, and the results are presented in Figure 4.2 A. Whilst there are multiple bands at lower molecular weights present in the talin 1 pGEX stretch R1-13 bead sample, talin 1 pGEX stretch R1-13 seems to have expressed and bound to the resin better than talin 2 pGEX stretch R1-13;

therefore, just the talin 1 construct was used for future experiments. Nevertheless, only a small proportion of the expressed protein seemed to have bound to the beads, as the majority remained in the supernatant (Figure 4.2 A). Consequently, the effect of different conditions on the binding of talin 1 pGEX stretch R1-13 was explored, with the final optimisation trial displayed in Figure 4.2 B. Although batch variability occurred within the optimisation process, talin was found to repeatedly bind most favourably when unpurified talin 1 pGEX stretch R1-13 cytosol was incubated with GSH resin for 1 hour at room temperature and washed with PBS, 5 mM DTT at pH 7.4. The additional proteins shown on the gel were presumably degradation products, as they remained consistently visible when large amounts of talin had bound to the GSH resin, despite the different binding/purification conditions trialled.

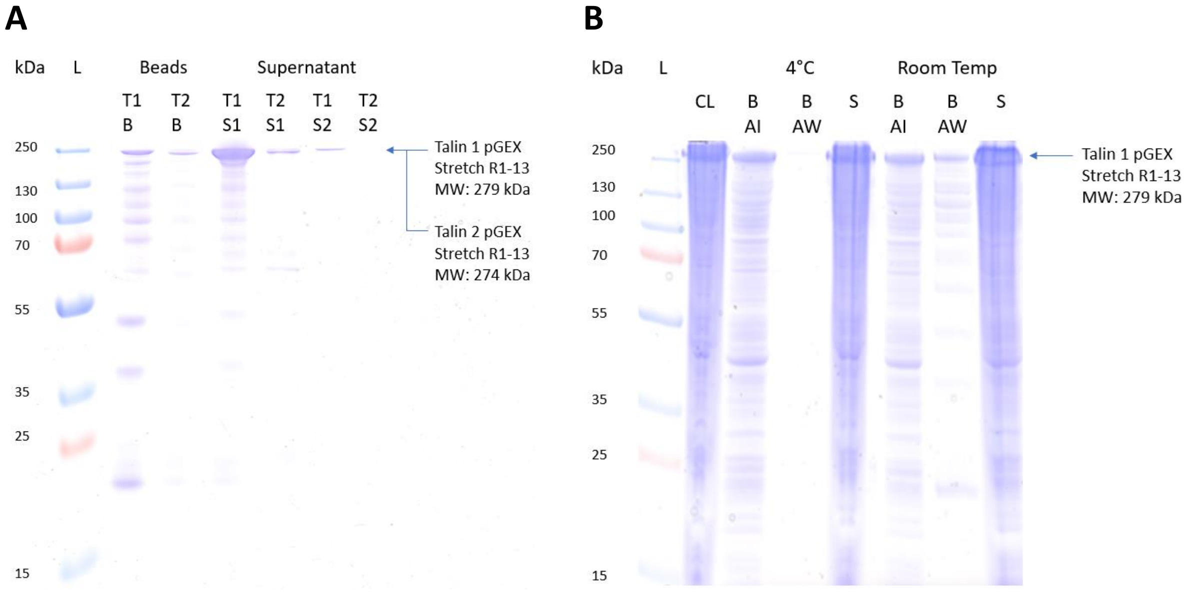

***Figure 4.2: SDS-PAGE gels demonstrating the optimisation process to achieve maximum talin binding to GSH resin.***

***(A)*** *SDS-PAGE gel showing the first attempt at binding Ni-purified talin 1 and 2 pGEX stretch R1-13 to GSH resin. L = protein ladder, T1 = talin 1 pGEX stretch R1-13, T2 = talin 2 pGEX stretch R1-13, B = washed GSH beads after incubation with the Ni-purified construct at room temperature for one hour, S1 = supernatant 1 (the incubation supernatant), and S2 = supernatant 2 (the second supernatant after the first wash).* ***(B)*** *SDS-PAGE gel showing the final optimisation of binding talin 1 pGEX stretch R1-13 cell lysate to GSH resin at 4°C and room temperature for one hour using PBS pH 7.5, 5mM DTT. R1-13 CL = talin 1 pGEX stretch R1-13 cell lysate, B AI = beads after incubation, B AW = beads after washing, 4°C = incubation at 4°C, RT = incubation at room temperature, and S = incubation supernatant. The GSH resin was incubated with talin in a 1:20 mL ratio.*

The binding of additional talin 1 pGEX stretch constructs to GSH resin was also trialled (Figure 4.3). Unlike talin 1 pGEX stretch R1-13, talin pGEX stretch R1-3 expressed extremely well; therefore, although the majority remained in the supernatant, the beads were presumably fully saturated with R1-3, as the amount bound to the beads was significantly larger than the amount of R1-13 bound in previous experiments. As talin pGEX stretch R1-13 is considerably larger than R1-3, it is possible that the GST tag became partially masked by the large size of the protein, hence why less was able to bind. GSH bead binding for talin 2 pGEX stretch R7-9 cell lysate was trialled; however, talin R7-9 did not bind to the GSH resin as well as R1-3. Therefore, the cell lysate was purified through immobilised Ni ion chromatography prior to incubation, which allowed R7-9 to bind more successfully to the GSH resin (Figure 4.3 B).

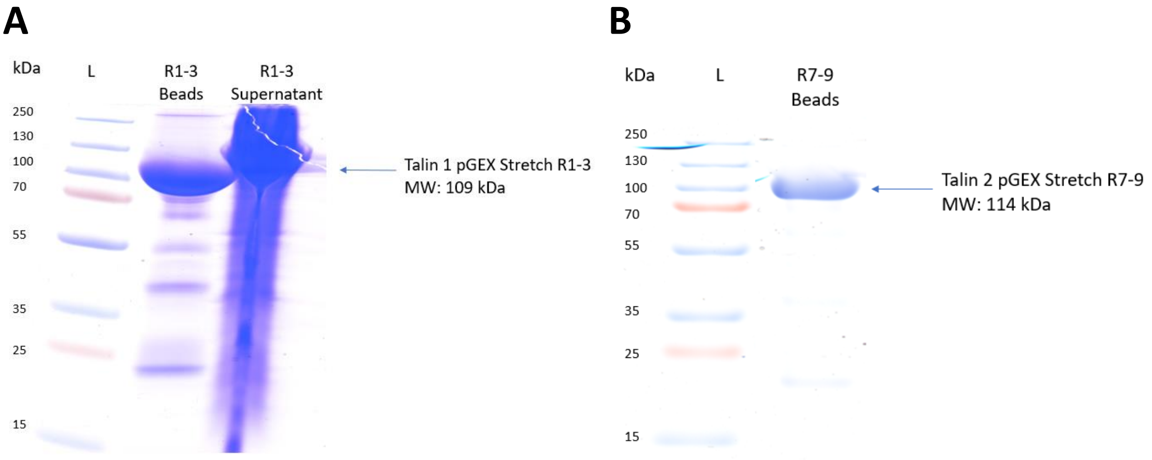

***Figure 4.3: SDS-PAGE gels confirming the binding of talin pGEX stretch R1-3 and R7-9 to GSH resin.*** ***(A)*** *SDS-PAGE gel demonstrating talin 1 pGEX stretch R1-3 bound to GSH resin.* ***(B)*** *SDS-PAGE gel confirming Ni-purified talin 2 pGEX stretch R7-9 bound to GSH resin. Note: R7-9 supernatant is absent due to a lack of space on the gel, and it was not deemed necessary to confirm GSH resin-talin R7-9 binding. The GSH resin was incubated with both talin constructs in a 1:20 mL ratio. L = protein ladder.*

### 4.2.2 GST Pulldowns

#### Theory Overview

GST pulldowns were conducted with the talin pGEX stretch constructs and known talin binders, to determine whether talin-bound GSH resin could be used in the talin ‘fishing’ rod experiment to bind and pull out talin interactors. VD1, which can bind to talin at 11 different binding sites, and a cerulean-tagged KN motif from KANK1, which binds to the talin R7 domain, were used (Bouchet et al., 2016; Gingras et al., 2005). Similar to the GSH bead binding, optimisation was required for the GST pulldowns, with varying volumes and concentrations trialled before 30 µL of GSH talin-bound resin and 170 µL of 150 µM protein was selected to achieve the clear visible bands on the gel, seen in Figure 4.4 A. Although there is not a KANK binding site present in R1-3, there are 5 vinculin binding sites (Goult et al., 2013). Therefore, in the GST pulldowns with talin 1 pGEX stretch R1-3, VD1 acts as a positive control and should bind to the talin-bound beads after incubation and washing, whilst CER-KN acts as a negative control and should remain in the supernatant, unable to bind to the R1-3 talin-bound resin. For the GST pulldowns with talin pGEX stretch R7-9, both CER-KN and VD1 are positive controls, as there are 2 vinculin binding sites in R7-8 and the KN motif binds to R7 (Bouchet et al., 2016; Goult et al., 2013).

### Pulldown Results

In the first VD1 GST pulldown conducted, whilst a small amount of VD1 had bound to the beads after washing, the majority remained in the supernatant (Figure 4.4 A). For the negative control, although CER-KN was found solely in the supernatant, which was expected, the majority of R1-3 seems to have unbound from the GSH resin and was also present in the supernatant (Figure 4.4 A). There was similarly a small amount of R1-3 in the VD1 pulldown supernatant; however, this was not the majority (Figure 4.4 A). In the VD1 R1-13 pulldown, the majority of VD1 was found in the supernatant, whilst R1-13 and VD1 were only very faintly present on the washed beads, despite a decent amount of R1-13 and VD1 being present on the beads before or after incubation (Figure 4.4 A).

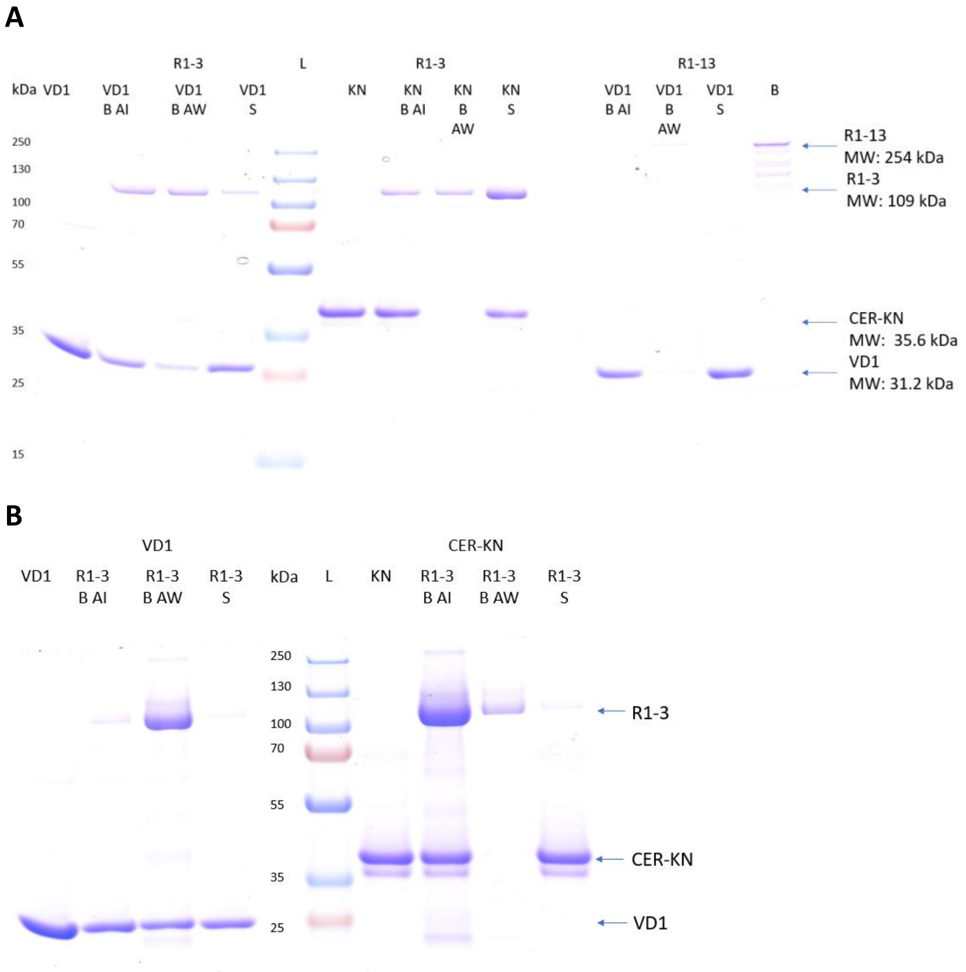

***Figure 4.4: SDS-PAGE gels of GST pulldowns with CER-KN, VD1, talin 1 pGEX stretch R1-13 and R1-3.*** ***(A)*** *SDS-PAGE gel of GST pulldowns with CER-KN, VD1, talin 1 pGEX stretch R1-3 and R1-13.* ***(B)*** *SDS-PAGE gel of GST pulldowns with CER-KN, VD1, and talin 1 pGEX stretch R1-3. L = protein ladder, B = beads before pulldown, B AI = beads after incubation, B AW = beads after washing, S = supernatant, and KN = CER-KN. Molecular weights: talin 1 pGEX stretch R1-13 = 273 kDa, talin 1 pGEX stretch R1-3 = 109 kDa, CER-KN = 35.6 kDa, and VD1 = 31.2 kDa.*

In Figure 4.4 B, the R1-3 CER-KN and VD1 pulldowns were repeated. The R1-3 VD1 pulldown shows the same intensity VD1 band present in both the beads and supernatant samples, which could indicate that the talin was already fully saturated and no more VD1 could bind. Also, there was only a faint band of R1-3 in the supernatant. The R1-3 CER-KN pulldown in Figure 4.4 B worked better than the previous pulldown in Figure 4.4 A, as the majority of R1-3 remained bound to the beads and the CER-KN was found predominantly in the supernatant.

The main problem which persisted with the GST pulldowns was that the results were highly unrepeatable. Figure 4.5 A demonstrates this; two pulldowns were carried out with two different samples of VD1. Although in the previous pulldown, R1-3 remained bound to the beads and little was found in the supernatant, in Figure 4.5 A, one pulldown demonstrated more R1-3 in the supernatant than the beads, whilst the other had an equal amount of R1-3 in the beads and supernatant samples. Though the majority of VD1 was found bound to the beads in both pulldowns, VD1 and R1-3 were found both times in the supernatant, which was not a preferential result.

The pulldown with R7-9 (Figure 4.5 B) demonstrates a successful pulldown with R7-9 and CER-KN, as both the R7-9 and CER-KN were found in the beads after washing and not in the supernatant. Although in the VD1 pulldown, talin was not found in the supernatant like in previous pulldowns, VD1 was predominantly found in the supernatant. Whilst a slight reduction in binding to R7-9 compared to R1-3 is explainable, as there are three fewer vinculin binding sites, clear binding should still be observed, which was not apparent in the results of this pulldown. By comparing the VD1 R7-9 after incubation and after washing bead samples, it is apparent that a reasonable amount of R7-9 was bound to the beads at the beginning of the experiment. Whilst there was a small amount of R7-9 and VD1 in the supernatant, it seems that the majority was lost during washing. This could indicate that VD1 had successfully bound to the R7-9, but as both were lost during the washing process, the success of the pulldown cannot be determined. However, as both the VD1 and CER-KN pulldowns were washed identically, it is perplexing that R7-9 and CER-KN remained bound to the GSH resin, whilst R7-9 and VD1 did not.

### GST Pulldown Conclusions

Throughout the GST pulldown optimisation, the CER-KN R1-3 pulldown, displayed in Figure 4.4 B, was the only repeatable experiment. Whilst the CER-KN R7-9 pulldown worked correctly in Figure 4.5 B, it continued to work incorrectly when repeated. Although VD1 was found in the beads for pulldowns in Figures 4.4 A/B and 4.5 A, it was also found significantly in the supernatant, often with the pGEX talin construct, which is problematic. If talin is present in both the beads and supernatant samples, it is difficult to determine whether the presence of VD1 in the supernatant is because the talin-bound GSH beads are fully saturated with VD1, or because the VD1 is bound to the talin present in the supernatant. After pulldown optimisation, the next step would have been to conduct GST pulldowns in cell extract and identify which proteins bind to the talin-bound GSH beads. If this problem persisted and talin was found in both bead and supernatant samples, it would cause confusion as it will be harder to ascertain whether the proteins present in the supernatant did not bind to talin or bound to the talin found in the supernatant. As the GST pulldowns were unable to clearly and repeatedly pull out known talin binders, it would similarly be ineffective to pull out novel talin binders in cell extract; therefore, no further work was conducted on GST pulldowns.

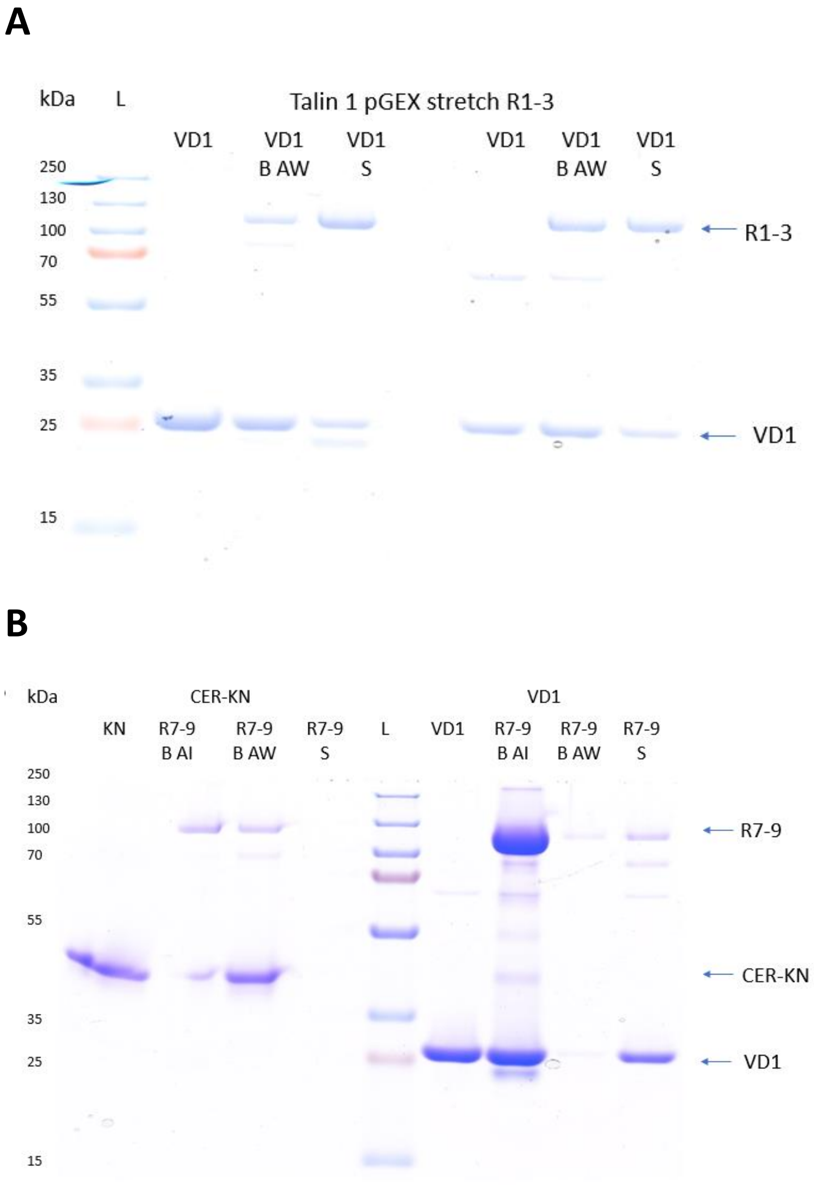

***Figure 4.5: SDS-PAGE gels of GST pulldowns with CER-KN, VD1, talin pGEX stretch R1-3 and R7-9.***
***(A)*** *SDS-PAGE gel of two GST pulldowns for talin 1 pGEX stretch R1-3 and VD1.* ***(B)*** *SDS-PAGE gel of GST pulldowns with talin 2 pGEX stretch R7-9, CER-KN, and VD1. L = protein ladder, B AI = beads after incubation, B AW = beads after washing, and S = supernatant. Molecular weights: talin 1 pGEX stretch R1-3 = 109 kDa, talin 1 pGEX stretch R7-9 = 114 kDa, CER-KN = 35.6 kDa, and VD1 = 31.2 kDa.*

## 4.3 GFP-Trap immunoprecipitation to identify novel talin binders

### 4.3.1 Optimisation of binding GFP Talin R1-13 to GFP-Trap beads

As GST pulldowns did not work as expected, GFP-Trap immunoprecipitation was utilised as an alternative method to identify novel talin-binding ligands. A GFP-talin 1 rod (R1-13) construct was purified using Ni batch purification, and various incubation conditions were optimised to maximise Ni resin binding, before settling on 30 minutes at 4°C and 30 minutes at room temperature. The Ni-purified GFP-talin rod and unpurified cell lysate were incubated with GFP-Trap beads (ChromoTek), to determine the effect of purification on GFP-Trap bead binding (Figure 4.6). Although the opposite was likely expected, when analysed by SDS-PAGE, the GFP-Trap beads incubated with unpurified GFP-talin rod cell lysate looked cleaner on the gel and had less contamination compared to the GFP-Trap beads incubated with Ni-purified GFP-talin rod (Figure 4.6 A). Therefore, GFP-talin rod cell lysate was used for GFP-Trap bead binding.

To minimize the number of contaminants, which also appeared to bind to the GFP-Trap agarose beads, the number of washes and washing buffer components were varied (Figure 4.6 B). It seemed that 6 washes and using a buffer with a higher NaCl/Triton X-100 concentration removed the extra contaminants visualised in the bead samples; however, it also reduced the amount of GFP-talin rod.

To increase the amount of GFP-talin rod bound to the beads, different volumes of beads and cell lysate were trialled and washed with the most stringent washing buffer (150 mM NaCl, 10 mM Tris, 0.5 mM EDTA and 0.05% Triton X-100) six times. 5 mL of GFP-rod cytosol with 50 µL of GFP-Trap beads was found to be the optimum ratio. However, although a larger proportion of GFP-talin was found bound to the beads, the additional bands thought to be contaminants, also seemed more prominent and increasing washing intensity did not remove them (Figure 4.7 A). Therefore, anti-His and anti-GFP immunoblotting was carried out to identify whether these contaminants were possibly talin fragments (Figure 4.7 B/C). The bands on the gel were illuminated in both immunoblots, indicating that they were indeed GFP-talin fragments, thereby explaining why increasing the stringency of washing did not affect their presence. It is reasonable to predict that these additional bands could be the result of degradation or incomplete translation, as the weight of the bands corresponds to the weight of various domains in the GFP-talin rod (Figure 4.7 C). As both immunoblots confirmed that the additional bands visualised on the SDS-PAGE gels, were simply GFP-talin rod fragments, nothing could be done to remove them from the GFP-Trap beads without the corresponding removal of the GFP-talin rod. Therefore, as the binding of the GFP-talin rod to GFP-Trap beads had been accomplished effectively, further optimisation was no longer necessary.

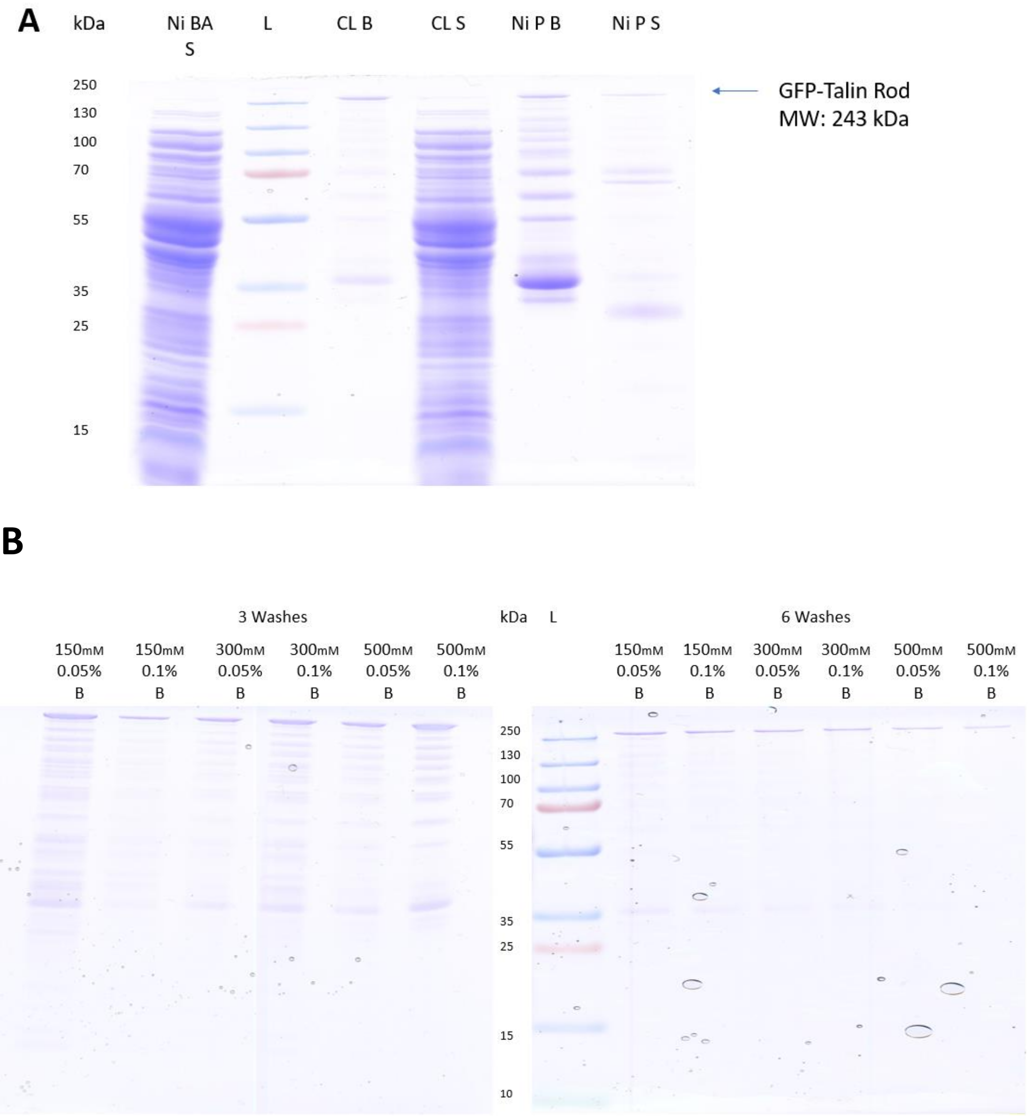

***Figure 4.6: SDS-PAGE gels demonstrating the optimisation of binding GFP-talin rod to GFP-Trap beads.*** ***(A)*** *SDS-PAGE gel evaluating the binding of Ni-purified GFP-talin rod and unpurified GFP-talin rod cell lysate to GFP-Trap beads. L = protein ladder, Ni BA S = the supernatant obtained after Ni batch purification on the GFP-talin rod, CL B = GFP-talin rod cell lysate beads, CL S = GFP-talin rod cell lysate supernatant, Ni P B = GFP-talin rod Ni purified beads, and Ni P S = GFP-talin rod Ni purified supernatant. (B) SDS-PAGE gel evaluating the binding of GFP-talin rod to GFP-Trap beads, using different buffers and 3-6 washing steps. The amount of EDTA and Tris in each buffer remained the same (10 mM Tris, 0.5 mM EDTA); however, the concentration of NaCl was varied from 150-500 mM, and the percentage of Triton X-100 was varied from 0.05-0.1%. L = protein ladder and B = beads.*

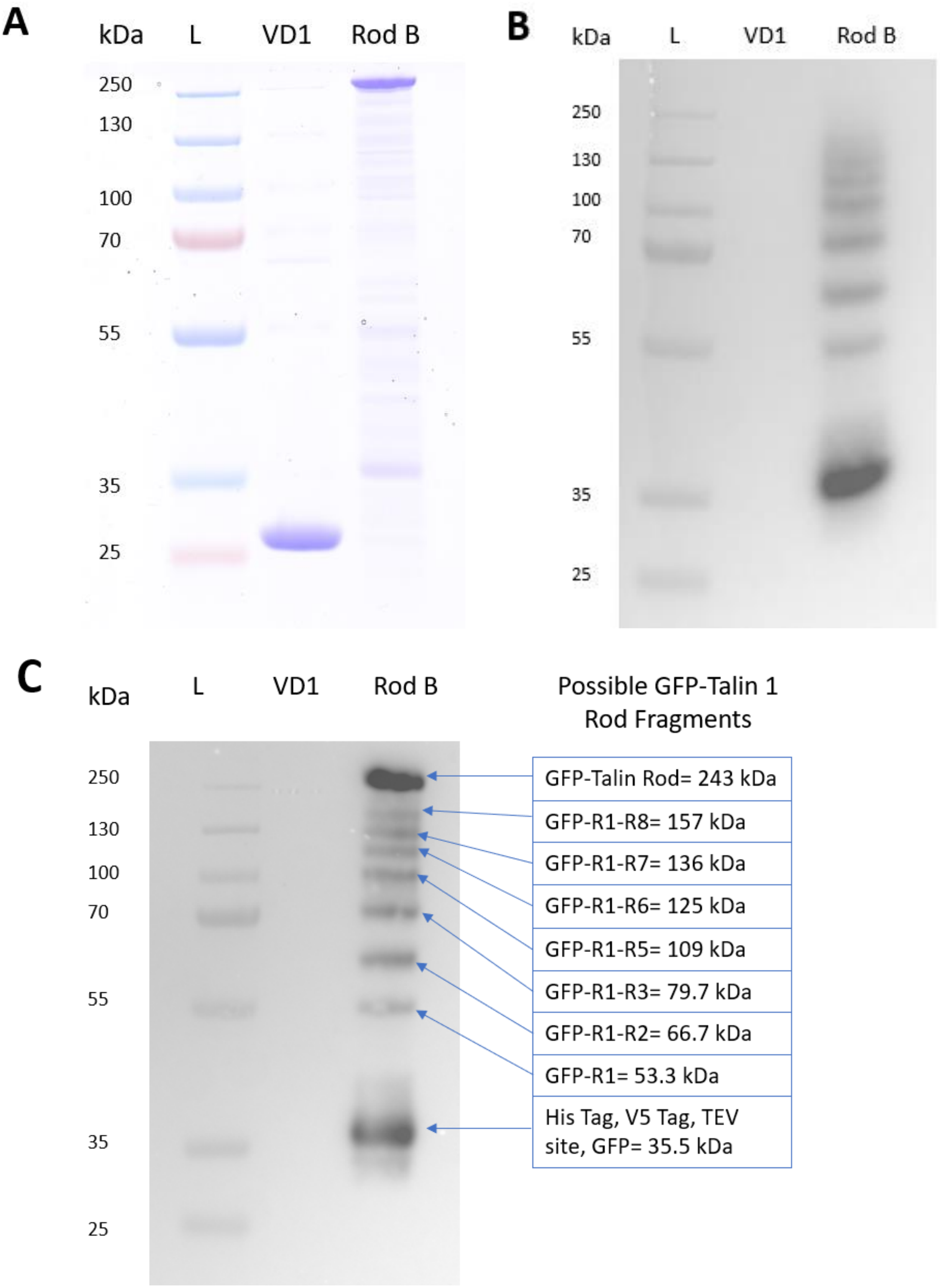

***Figure 4.7: Anti-His and GFP immunoblots demonstrated that the additional bands visualised on prior SDS-PAGE gels are GFP-talin rod fragments.***

*__(A)__ Reference SDS-PAGE gel for immunoblotting demonstrated that using the most stringent washing conditions did not remove the additional bands visualised on the SDS-PAGE gel when GFP-talin rod binds to GFP-Trap beads. L = protein ladder and Rod B = GFP-talin rod beads __(B)__ Anti-His immunoblot of GFP-Trap immunoprecipitation with GFP-talin rod and VD1. __(C)__ Anti-GFP immunoblot of GFP-Trap immunoprecipitation with GFP-talin rod and VD1. Possible GFP-talin rod fragments corresponding to the bands visualised on the gel are labelled on the anti-GFP immunoblot, and VD1 was used as a negative control in both immunoblots.*

### 4.3.2 GFP-Trap pulldown in CaSki cell lysate

#### Theory Overview

As the GFP-talin rod had bound successfully to GFP-Trap beads, to determine whether GFP-Trap immunoprecipitation could be used to identify novel talin binders in cell extract, it was imperative to prove that a GFP-Trap pulldown could identify known talin binders. To validate the method, a GFP-Trap pulldown was conducted using cell lysate of the endocervical cancer CaSki cell line as it was easy to obtain and grow. Immunoblots of known talin binders were carried out on the GFP-Trap pulldown samples, to identify whether known talin binders could be pulled out of cell lysate through GFP-Trap immunoprecipitation.

#### Determination of CaSki cell lysate concentration

CaSki cell pellets were obtained from Fenton lab, University of Kent and lysed with CSK buffer. The absorbance values obtained from a BCA assay of BCA standards were used to plot a BCA standard curve, and the CaSki cell lysate concentration was calculated to be 3.06 µg/µL (Figure 4.8).

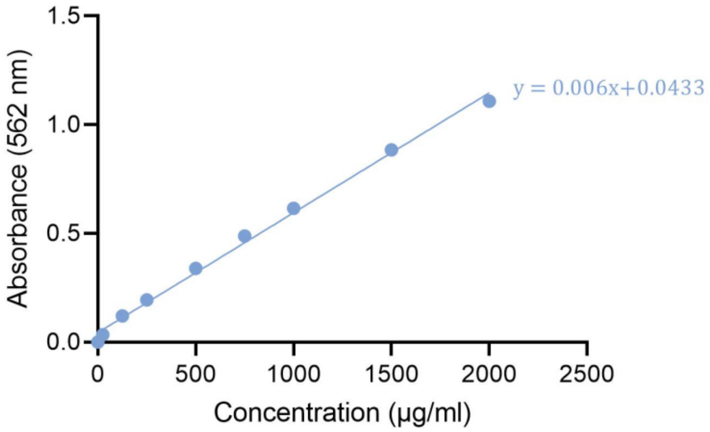

***Figure 4.8: BCA assay standard curve.***
*The $y = mx + c$ equation was used to determine the concentration of the lysed CaSki pellet.*

#### Method Validation

After the GFP-talin rod and GFP were bound to GFP-Trap beads (Figure 4.9 A), they were incubated with 306 µg CaSki cell lysate and anti-CDK1/KANK2 immunoblots were performed (Figure 4.9 B). As CDK1 and KANK2 are known talin binders, if either protein was identified in the GFP-talin rod beads sample, this would validate that GFP immunoprecipitation can be used in the talin 'fishing' rod experiment to identify talin binders in cell extract. As only a small sample of CaSki cell lysate obtained through CSK lysis buffer remained, this required dilution before it was used for the immunoblot. Therefore, additional CaSki cell lysate from the Fenton lab (lysed by RIPA buffer) was used in the immunoblots to represent a higher concentration of CaSki cell lysate, hence why both KANK2 and CDK1 are more abundantly found in the RIPA sample than the CSK sample.

CDK1 was only found in both CaSki inputs and the GFP/GFP-talin rod supernatant samples, indicating that it was present in the pulldown, but had not bound to either group of beads. However, whilst KANK2 was present in the cell lysate inputs, the GFP supernatant, and faintly in the GFP-talin rod supernatant, it was also abundantly found in the GFP-talin rod beads sample. This indicated that the majority of KANK2 in the CaSki cell lysate had successfully bound to the GFP-talin rod beads. As KANK2 was abundantly present in the GFP-talin rod beads sample yet absent in the negative control GFP beads sample, this clearly validated the method and indicated that GFP-Trap pulldowns can successfully be used in the talin ‘fishing’ rod experiment to identify talin binders in cell extract.

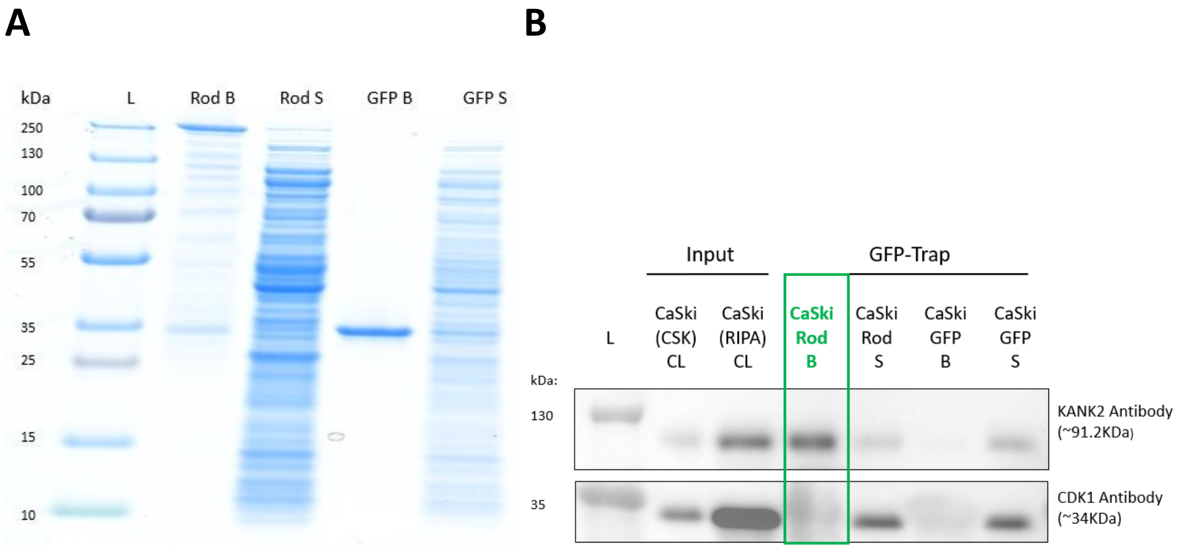

***Figure 4.9: KANK2 was identified by ‘fishing’ with the GFP-talin rod in CaSki cell lysate.***
***(A)*** *SDS-PAGE gel of GFP-talin rod and GFP bound to GFP-Trap beads. L = protein ladder, Rod B = GFP-talin rod-bound GFP-Trap beads, Rod S = GFP-talin rod GFP-Trap supernatant, GFP B = GFP-bound GFP-Trap beads and GFP S = GFP GFP-Trap supernatant.* ***(B)*** *Anti-CDK1 and KANK2 immunoblots of the talin ‘fishing’ rod experiment in CaSki cell lysate. L = protein ladder, CaSki (CSK) CL = diluted CaSki cell lysate (lysed through CSK buffer), which was used for the talin ‘fishing’ rod experiment, CaSki (RIPA) CL = CaSki Cell lysate (lysed through RIPA buffer) to represent undiluted CaSki cell lysate, CaSki Rod B (highlighted in green) = GFP-talin rod-bound GFP-Trap beads incubated in the CaSki cell lysate, CaSki Rod S = GFP-talin rod CaSki supernatant, CaSki GFP B = GFP-bound GFP-Trap beads incubated in the CaSki cell lysate, and CaSki GFP S = GFP CaSki supernatant.*

### 4.3.3 Trialling the talin 'fishing' rod experiment in murine neuronal extract

#### Theory Overview: Murine neuronal fractions

As GFP-Trap immunoprecipitation had effectively identified known talin binders in CaSki cell lysate, to discover a link between mechanical signalling and neuronal activity, the newly developed talin 'fishing' rod experiment was trialled in murine neuronal fractions. Cytosolic, PSD, non-PSD, and synaptosomal neuronal fractions, obtained from Devrim Kilinc, PhD, Institut Pasteur de Lille, were used to represent all components of the synapse. PSD refers to postsynaptic density, a protein complex attached to the postsynaptic membrane; therefore, the PSD fraction represents the postsynaptic neuron, whilst the non-PSD fraction represents the presynaptic neuron (Figure 4.10) (Kaizuka & Takumi, 2018; Pereda, 2014). The identification of novel talin binders in these murine neuronal fractions, through the talin 'fishing' rod experiment, will aid to confirm the theorised role of talin in neuronal signalling, as described in the MeshCODE theory.

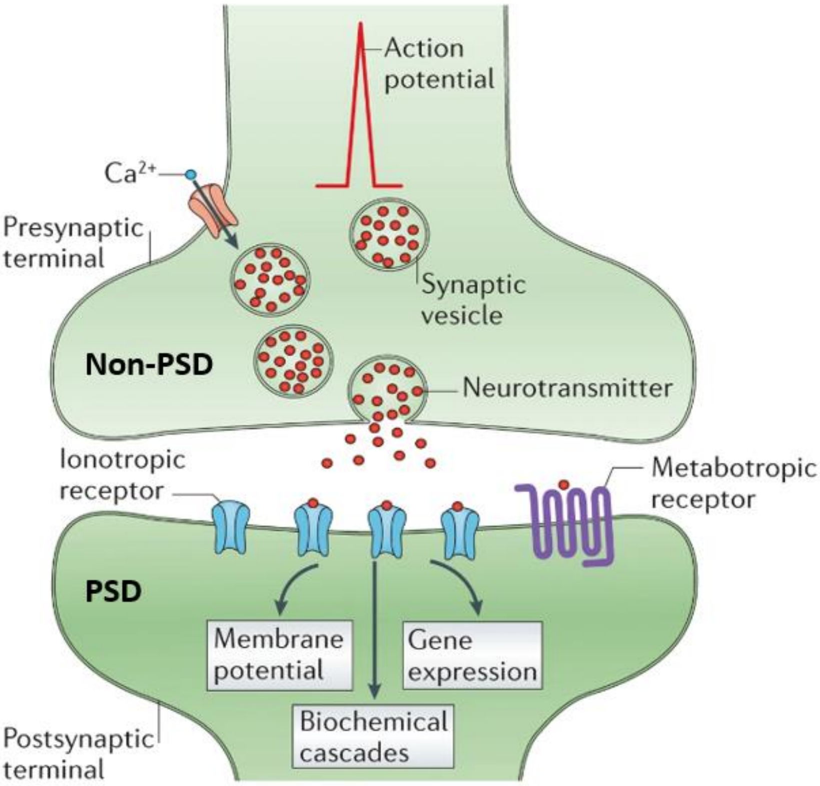

***Figure 4.10: A simplified representation of a chemical synapse illustrating the PSD and non-PSD fractions.*** *The non-PSD and PSD murine neuronal fractions obtained from Devrim Kilinc, PhD, Institut Pasteur de Lille, represent the presynaptic neuron and postsynaptic neuron of a chemical synapse. Adapted from (Pereda, 2014).*

### ‘Fishing’ in murine neuronal extract

GFP and GFP-talin rod were bound to four batches of GFP-Trap beads, then incubated with 250 µg of murine neuronal cytosolic, PSD, non-PSD, and synaptosomal fractions (Figure 4.11).

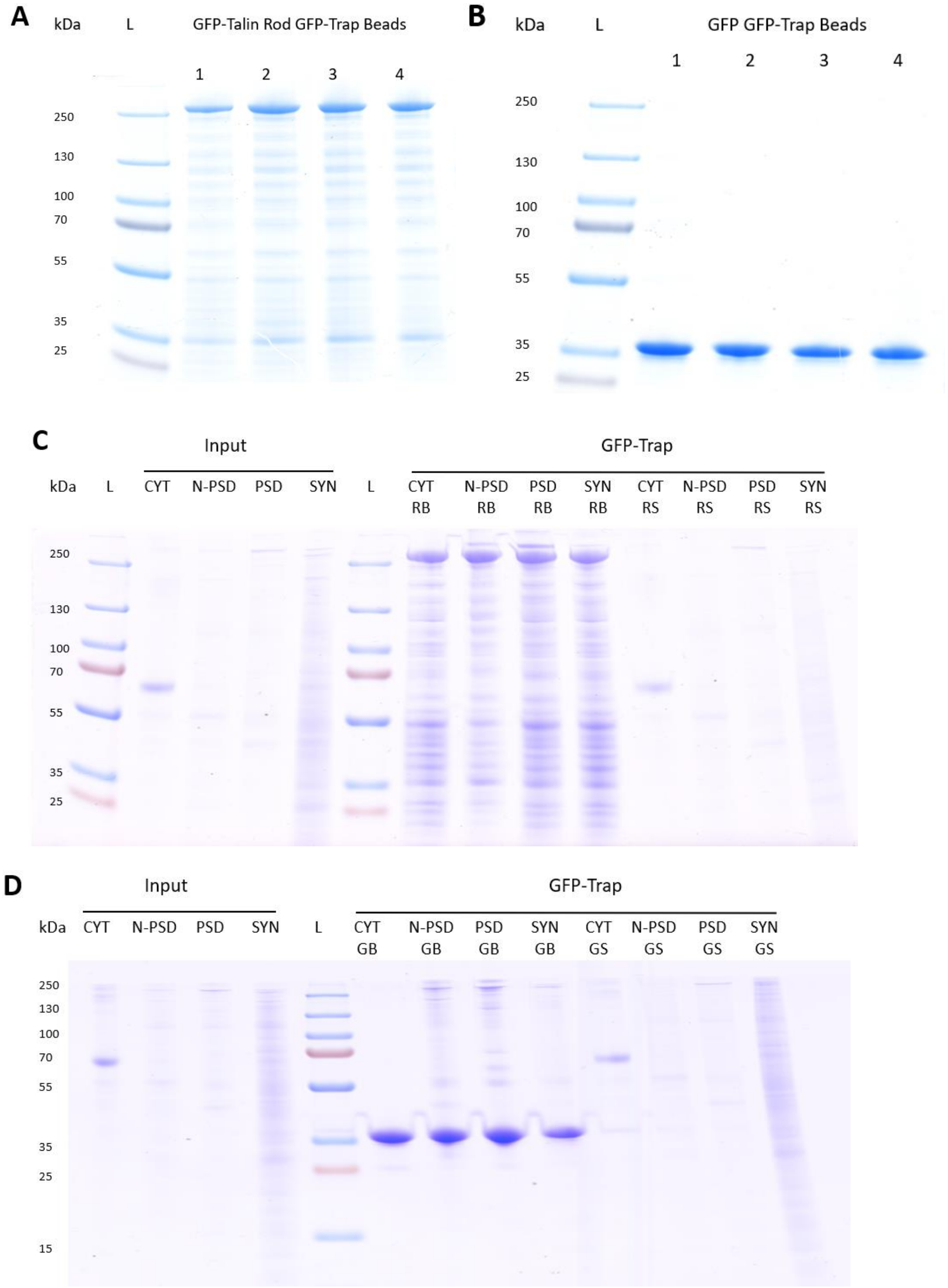

***Figure 4.11: SDS-PAGE gels demonstrating the first talin ‘fishing’ rod experiment in murine neuronal extract.***
***(A)*** *SDS-PAGE gel showing GFP-talin rod bound to four sets of GFP-Trap beads.* ***(B)*** *SDS-PAGE gel showing GFP bound to four sets of GFP-Trap beads* ***(C)*** *SDS-PAGE gel after the incubation of GFP-talin rod-bound beads in the murine neuronal fractions.* ***(D)*** *SDS-PAGE gel after the incubation of GFP-bound beads in the murine neuronal fractions. L = protein ladder, CYT = cytosolic fraction, N-PSD = non-PSD fraction, PSD = PSD fraction, SYN = synaptosomal fraction, RB = GFP-talin rod beads, RS = GFP-talin rod supernatant, GB = GFP beads, and GS = GFP supernatant.*

### Method Validation

To validate whether the talin 'fishing' rod experiment in murine neuronal fractions could successfully identify talin binders, as it had in CaSki cell lysate, anti-KANK2 immunoblotting was performed. As demonstrated in Figure 4.12 A and highlighted in green, KANK2 was visualised in all four GFP-talin rod bead samples. As KANK2 was not present in the input or supernatant samples, this may indicate that it was present at very low concentrations, therefore could not be visualised on the immunoblot. However, after the pulldown, a significant amount of KANK2 had bound to the talin, allowing KANK2 to be visualised in the talin bead samples. The presence of KANK2 solely in the GFP-talin rod beads samples indicated that the method had succeeded in pulling out a known talin binder in all four murine neuronal fractions; therefore, LC-MS/MS analysis of the samples could presumably identify any additional talin binders in the murine neuronal extract.

### LC-MS/MS proteomics analysis

The bead samples were sent to Turku Bioscience BioCity, Finland to undergo LC-MS/MS proteomics analysis and identify any novel talin binders present in the murine neuronal fractions. Identification of murine proteins in the proteomics analysis proved to be more difficult than expected, due to interference from *E. coli* protein contamination in the samples. The cytosolic samples contained more *E. coli* contamination than the other fractions, and identification of any murine proteins was found to be too unreliable; therefore, the cytosolic samples were removed from the proteomics results. Furthermore, GFP-talin was extremely abundant in the samples and overshadowed the MS results, causing difficulty during the identification of other proteins. Nevertheless, the proteomics results displayed the PSMs of each protein identified in the three GFP and GFP-talin rod PSD, non-PSD, and synaptosomal samples. Although KANK2 was visualised in the anti-KANK2 immunoblot, the LC-MS/MS analysis did not identify KANK2 in any of the samples. However, this is understandable as immunoblotting is typically more sensitive than mass spectrometry.

Whilst using four different murine neuronal fractions was ambitious, no repeats were conducted. Therefore, by treating the three PSD, non-PSD, and synaptosomal samples as repeats, the p-values of the PSMs and the fold change between the control GFP and talin samples could be calculated. The $-\log_2$ (p-value) and $\log_2$ (fold change) of the samples were plotted in a volcano plot and displayed in Figure 4.12 B. The proteins predominantly found in the talin samples, as opposed to the GFP samples, have a fold change above 1, a positive $\log_2$ (fold change) and are visible in the unshaded area of the volcano plot. However, most of the proteins identified in the proteomics analysis were predominantly present in the control GFP samples. This is demonstrated in the volcano plot (Figure 4.12 B), as most proteins are present in the shaded area, indicating a fold change below 1 and a negative $\log_2$ (fold change). This is presumably caused by the overwhelming presence of talin, which made identifying other proteins more difficult, resulting in the identification of fewer PSMs in the talin samples than the GFP samples. The proteins with a significant p-value less than 0.05 are highlighted in red (Figure 4.12), and proteins with both a fold change above 1 and a significant p-value are identified in Table 4.1. As demonstrated in Table 4.1, only talin 1 and 2 were identified with PSMs larger than 50 in the samples; therefore, the additional proteins listed may need to be viewed with scepticism and are unlikely to confidently be identified as potential talin binders.

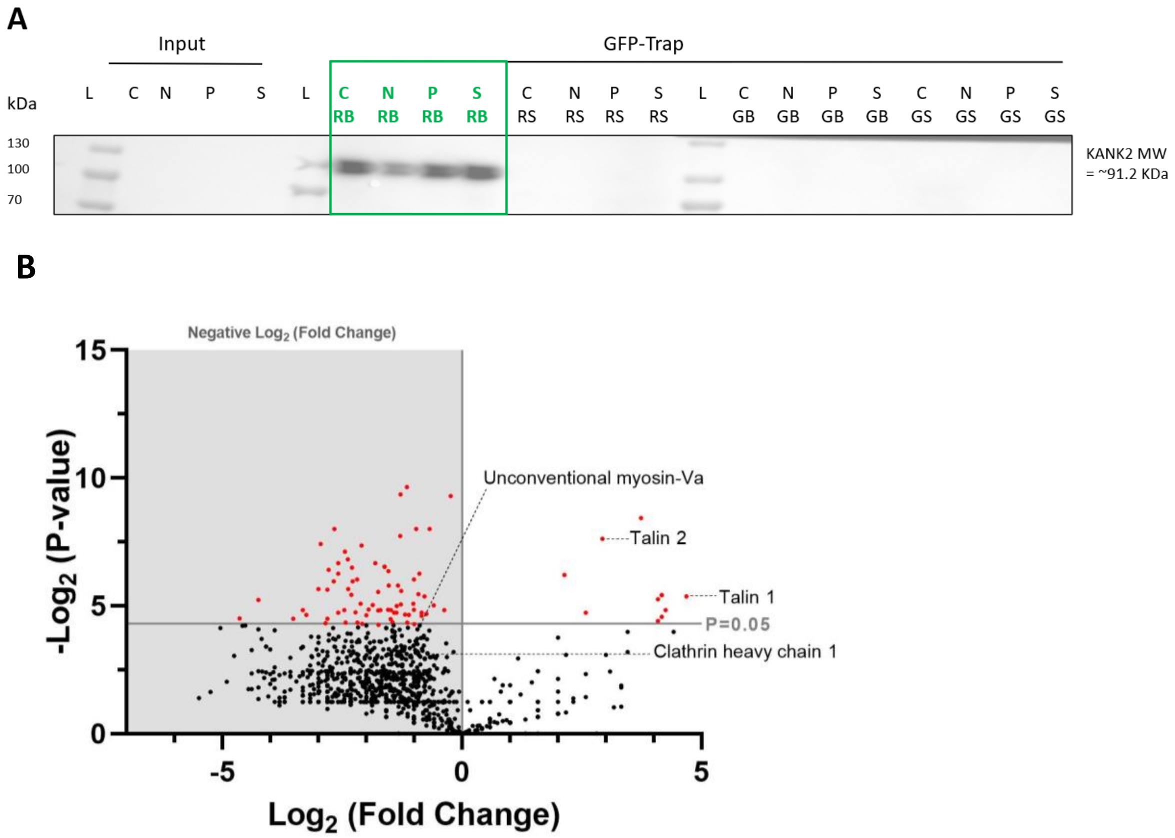

***Figure 4.12: KANK2 and additional potential talin-binding ligands were identified after 'fishing' in the murine neuronal fractions.***

***(A)*** *Anti-KANK2 immunoblot of the talin 'fishing' rod experiment in four murine neuronal fractions. L = protein ladder, C = cytosolic fraction, N = non-PSD fraction, P = PSD fraction, S = synaptosomal fraction, RB = GFP-talin rod beads, GB = GFP beads, RS = GFP-talin rod supernatant, and GS = GFP supernatant. The GFP-talin rod bead samples are highlighted in green.* ***(B)*** *Volcano plot displaying the LC-MS/MS proteomics analysis results of the talin 'fishing' rod experiment in three murine neuronal fractions. The shaded grey area of the plot represents a negative* $\log_2$ *(fold change), which occurs when the fold change is below 1, as the proteins were predominantly present in the control GFP samples. The unshaded, white area of the plot represents a positive* $\log_2$ *(fold change), which occurs when the fold change is above 1, as the proteins were predominantly present in the GFP-talin rod samples. The proteins identified with a significant p-value of less than 0.05 are identified in red and those with both a significant p-value and a positive* $\log_2$ *(fold change) are visualised in Table 4.1. Key proteins identified are labelled; however, KANK2 was not identified.*

***Table 4.1: Proteins identified in the MS analysis volcano plot (Figure 4.12) with a fold change above 1 and a significant p-value.***

| Protein | UniProt ID | P-value | Fold change | Average GFP PSMs | Average Talin PSMs |
|---|---|---|---|---|---|
| **Talin 1** | P26039 | 0.02 | 25.65 | 325 | 8336.5 |
| **Talin 2** | Q71LX4 | 0.005 | 7.607 | 56 | 426 |
| **Pecanex-like protein 3** | Q8VI59 | 0.003 | 13.33 | 1.5 | 20 |
| **GTP-binding protein Di-Ras 2** | Q5PR73 | 0.01 | 4.4 | 5 | 22 |
| **Microtubule organisation protein AKNA** | Q80VW7 | 0.026 | 17 | 0.5 | 8.5 |
| **Coiled-coil domain-containing protein 13** | D3YV10 | 0.0233 | 18 | 0.5 | 9 |
| **Rab GTPase-binding effector protein 2** | Q91WG2 | 0.042 | 18 | 0.5 | 9 |
| **Regulator of G-protein signalling 9** | O54828 | 0.0422 | 18 | 0.5 | 9 |
| **Phosphatidylinositol 3-kinase catalytic subunit type 3** | Q6PF93 | 0.047 | 19 | 0.5 | 9.5 |
| **ATP-dependent Clp protease ATP-binding subunit clpX-like, mitochondrial** | Q9JHS4 | 0.035 | 17 | 0.5 | 8.5 |
| **Stomatin-like protein 2** | Q99JB2 | 0.0377 | 6 | 0.5 | 3 |

The results of this LC-MS/MS proteomics analysis indicated that the experiment needed further optimisation to identify potential talin binders more confidently. Nevertheless, to ensure that no possible talin binders potentially identified in this analysis were missed, the results were analysed twice more in a more lenient manner. Protein abundance in the control GFP samples was ignored and the proteins identified with a difference of over 200 PSMs between PSD and non-PSD fractions were identified and listed in Table 4.2. Two of the proteins identified in this way, clathrin heavy chain 1 and unconventional myosin-Va, are highlighted on the volcano plot in Figure 4.12 B.

***Table 4.2: Proteins identified in the MS analysis with a difference of at least 200 PSMs between non-PSD and PSD fractions.***

| Protein | UniProt ID | Average Talin PSMs | Difference between Talin PSD and non-PSD samples |
|---|---|---|---|
| **Spectrin alpha chain, non-erythrocytic 1** | P16546 | 1381 | 857 |
| **Spectrin beta chain, non-erythrocytic 1** | Q62261 | 1231.5 | 646 |
| **Ankyrin-2** | Q8C8R3 | 546.5 | 630 |
| **Bassoon** | O88737 | 471 | 384 |
| **Piccolo** | Q9QYX7 | 356 | 455 |
| **Clathrin heavy chain 1** | Q68FD5 | 367 | 564 |
| **Microtubule-associated protein 1A** | Q9QYR6 | 301.5 | 519 |
| **Cytoplasmic dynein 1 heavy chain 1** | Q9JHU4 | 253.5 | 435 |
| **Microtubule-associated protein 1B** | P14873 | 246.5 | 383 |
| **Microtubule-actin cross-linking factor 1** | Q9QXZ0 | 325.5 | 377 |
| **Inositol 1,4,5-triphosphate receptor type 1** | P16546 | 224 | 413 |
| **Nesprin-1** | Q6ZWR6 | 137.5 | 243 |
| **Microtubule-associated protein 2** | P20357 | 127.5 | 232 |
| **Ryanodine receptor 2** | E9Q401 | 118.5 | 235 |
| **Unconventional myosin-Va** | Q99104 | 557.5 | 242 |
| **Ras/Rap GTPase-activating protein SynGAP** | F6SEU4 | 226 | 857 |

The proteomics results were also reanalysed by Turku Bioscience, and the proteins with the highest fold change values are also presented in Table 4.3.

***Table 4.3: Proteins identified in the MS analysis with the highest fold change values.***
*If the GFP PSM value was 0, to calculate the fold change, a value of 0.5 was used. Proteins highlighted in green are also identified in the MS volcano plot and in Table 4.1.*

| Protein | Uniprot ID | Average GFP PSMs | Average Talin PSMs | Fold change |
|---|---|---|---|---|
| **Glyceraldehyde-3-phosphate dehydrogenase, testis-specific** | Q64467 | 0 | 17 | 34 |
| **Leucine-rich repeat and immunoglobulin-like domain containing-NOGO receptor-interacting protein 4** | Q149C3 | 0.5 | 13 | 26 |
| **Flavin-containing monooxygenase 5** | P97872 | 1.5 | 32 | 21.3 |
| **Crossover junction endonuclease EME1** | Q8BJW7 | 0 | 9.5 | 19 |
| **Phosphatidylinositol 3-kinase catalytic subunit type 3** | Q6PF93 | 0.5 | 9.5 | 19 |
| **Coiled-coil domain-containing protein 13** | D3YV10 | 0.5 | 9 | 18 |
| **Rab GTPase-binding effector protein 2** | Q91WG2 | 0.5 | 9 | 18 |
| **Regulator of G-protein signalling 9** | O54828 | 0.5 | 9 | 18 |
| **DNA-directed RNA polymerases I and III subunit RPAC2** | P97304 | 0.5 | 8.5 | 17 |
| **Microtubule organisation protein AKNA** | Q80VW7 | 0.5 | 8.5 | 17 |
| **ATP-dependent Clp protease ATP-binding subunit clpX-like mitochondria** | Q9JHS4 | 0.5 | 8.5 | 17 |
| **Prolactin-6A1** | O35257 | 0.5 | 7.5 | 15 |
| **Keratin, type I cytoskeletal 9** | Q6RHW0 | 0.5 | 7 | 14 |
| **Pecanex-like protein 3** | Q8VI59 | 1.5 | 20 | 13.3 |
| **Ninein** | Q61043 | 0 | 6.5 | 13 |
| **Islet cell autoantigen 1** | P97411 | 0.5 | 6.5 | 13 |
| **Centrosomal protein 43** | Q66JX5 | 0.5 | 5.5 | 11 |
| **Bifunctional peptidase and arginyl-hydroxylase** | JMJD5 | 0.5 | 5.5 | 11 |
| **Proliferation marker protein Ki-67** | E9PVX6 | 1 | 7 | 7 |
| **GTP-binding protein Di-Ras 2** | Q5PR73 | 5 | 22 | 4.4 |

### Utilising the bioinformatics pipeline

The proteins identified in all three analyses were then evaluated by the bioinformatics pipeline, described in section 3, to identify whether they contained a potential talin-binding site similar to those present in known talin binders. The majority of proteins were over 1000 residues (the maximum input sequence length for PSIPRED), and when overlapping sections were inputted into PSIPRED, the secondary structure prediction differed; therefore, PSIPRED was not used to accurately predict the secondary structure or intracellular regions for these proteins. Nevertheless, the proteins containing the most promising motifs with a score above 4.5 are listed in Table 4.4.

*Table 4.4: Proteins identified by the proteomics analyses with the most promising I/LD motifs scored at 4.5 or above.*

| Protein | Uniprot ID | I/LD motif | Position 4 Hydrophobic acid | Prior E/D residues | Hydrophobic residues at the correct positions | Linked motif | Overall Score |
|---|---|---|---|---|---|---|---|
| **Spectrin alpha chain, non-erythrocytic 1** | P16546 | LDEF | F | - | Position 5, 8, 15: A, L, A | | 5 |
| **Spectrin beta chain, non-erythrocytic 1** | Q62261 | IDAW | W | D | Position 5, 8: M, I | LDIL | 5.5 |
| | | LDDF | F | D | Position 8, 15: L, I | - | 5 |
| | | LDKW | W | D | Position 5, 8: L, L | - | 5 |
| | | LDKW | W | D | Position 5, 8: L, L | - | 5 |
| **Ankyrin-2** | Q8C8R3 | LDKV | V | - | Position 5, 8: V, L | IDIN | 4.5 |
| | | LDQV | V | - | Position 5, 8, 15: I, P, L | LDYM | 5.5 |
| | | LDYM | M | - | Position 8: F | LDQV | 4.5 |
| **Bassoon** | O88737 | LDRD | - | E | Position 5, 8, 15: L, V, L | - | 5 |
| | | LDEE | - | E | Position 8, 15: I, L | EIDAK | 4.5 |
| | | IDAK | - | E | Position 5, 8: L, L | ELDEE | 4.5 |
| **Piccolo** | Q9QYX7 | IDRE | - | D | Position 8, 15: V, L | LDLV | 4.5 |
| | | LDEE | - | E | Position 8, 15: I, L | IDAK | 4.5 |
| **Plectin** | Q9QXS1 | LDKA | A | D | Position 8, 15: I, V | - | 5 |
| | | IDDA | A | D | Position 15: L | IDRS, LDQY | 5 |
| **Microtubule-associated protein 1A** | Q9QYR6 | IDSV | V | - | Position 5, 15: L, P | LDRI | 4.5 |
| | | LDFP | P | - | Position 5, 8, 15: A, F, P | - | 5 |
| **Clathrin heavy chain 1** | Q68FD5 | IDQV | V | - | Position 5, 8, 15: V, A, P | | 5 |
| **Microtubule-associated protein 1B** | P14873 | LDFP | P | - | Position 5, 8, 15: A, F, P | - | 5 |

| | | | | | | | |
|---|---|---|---|---|---|---|---|
| **Microtubule-actin cross-linking factor 1** | Q9QXZ0 | IDVI | I | - | Position 5, 8, 15: V, M, V | - | 5 |
| | | LDAL | L | - | Position 5, 8: A, I | LDIQ | 4.5 |
| | | IDAL | L | - | Position 5, 8, 15: L, V, L | LDWV | 5.5 |
| | | IDEC | C | - | Position 8, 15: M, L | LDPV | 4.5 |
| | | LDKL | L | - | Position 5, 8, 15: V, A, I | - | 5 |
| | | IDAA | A | E | Position 5, 15: I, A | - | 5 |
| | | LDNL | L | - | Position 5, 8, 15: L, V, V | - | 5 |
| | | LDLV | V | D | Position 5, 8: M, M | - | 5 |
| **Inositol 1,4,5-triphosphate receptor type 1** | P11881 | LDQL | L | D | Position 8, 15: V, V | - | 5 |
| | | IDTF | F | E | Position 5, 8: V, V | - | 5 |
| | | LDDI | I | - | Position 5, 8, 15: V, V, P | - | 5 |
| | | LDSQ | - | D | Position 5, 8, 15: V, L, I | - | 5 |
| **Nesprin-1** | Q6ZWR6 | LDLL | L | - | Position 5, 8, 15: C, C, V | - | 5 |
| | | LDGC | C | E | Position 8, 15: L, I | ELDAA | 5.5 |
| | | LDDA | A | E | Position 5, 8, 15: I, F, L | - | 6 |
| | | LDDA | A | - | Position 8, 15: L, L | LDVE | 4.5 |
| | | LDHW | W | E | Position 5, 15: L, A | | |
| | | IDTQ | - | E | Position 5, 8, 15: L, L, A | - | 5 |
| | | IDSD | - | E | Position: 5, 8, 15: L, M, L | - | 5 |
| | | LDHW | W | E | Position 5, 15: L, A | LDVA | 5.5 |
| | | LDLM | M | - | Position 5, 8, 15: A, V, L | | 5 |
| | | LDEL | L | E | Position 8, 15: C, V | - | 5 |

| | | | | | | | |
|---|---|---|---|---|---|---|---|
| **Unconventional myosin-Va** | Q99104 | LDSI | I | - | Position 5, 8, 15: L, L, M | - | 5 |
| **Talin 2** | Q71LX4 | LDSL | L | E | Position 5, 15: P, V | - | 5 |
| | | IDSA | A | E | Position 5, 8, 15: L, V, L | - | 6 |
| | | IDPI | I | - | Position 5, 8, 15: A, A, L | - | 5 |
| | | LDTT | D | D | Position 5, 8, 15: I, A, A | - | 5 |
| **Microtubule-associated protein 2** | P20357 | LDFA | A | - | Position 5, 8, 15: A, A, I | LDIK | 5.5 |
| | | LDNA | A | - | Position 8, 15: P, I | IDSQ | 4.5 |
| **Ryanodine receptor 2** | E9Q401 | LDAL | L | - | Position 8, 15: V, L | IDLP | 4.5 |
| | | IDLP | P | - | Position 5, 8, 15: I, V, L | LDAL | 5.5 |
| | | LDVL | L | - | Position 5, 8, 15: C, L, V | - | 5 |
| | | IDGL | L | - | Position 5, 8, 15: F, V, I | - | 5 |
| | | LDVA | A | - | Position 5, 8, 15: A, V, A | - | 5 |
| | | LDTA | A | - | Position 5, 8, 15: A, A, L | - | 5 |
| | | LDSV | V | - | Position 8, 15: L, A | LDNA | 4.5 |
| | | LDNA | A | - | Position 5, 8, 15: A, L, L | LDSV | 5.5 |
| **Myosin-10** | Q61879 | LDDL | L | E | Position 8, 15: L, V | DLDHQ | 5.5 |
| **Islet cell autoantigen 1** | P97411 | LDAK | - | D | Position 5, 8, 15: L, F, C | LDLS | 5 |
| **Cytoplasmic dynein 1 heavy chain 1** | Q9JHU4 | LDKI | I | E | Position 8, 15: L, L | - | 5 |
| | | LDGL | L | - | Position 5, 8, 15: L, L, A | | 5 |
| | | LDVP | P | E | Position 5, 8, 15: L, F, V | - | 6 |
| | | IDRI | I | - | Position 5, 8, 15: F, P, I | | 5 |
| | | LDKV | V | D | Position 8, 15: V, V | - | 5 |

### 4.3.4 Further optimisation of the talin 'fishing' rod experiment

#### Theory Overview

The previous MS proteomics analysis identified numerous proteins, many of which contained promising I/LD motifs. However, confident identification of potential talin binders proved to be more difficult than expected, due to *E. coli* protein contamination and the overwhelming presence of talin in the samples. Therefore, the talin 'fishing' rod experiment was adapted, with the aim of reducing both these variables, to improve the MS data and ensure easy, confident identification of talin binders. The overwhelming presence of talin in the previous MS analysis was thought to negatively impact both the identification of proteins in the talin samples and their fold change values. Therefore, an acidic glycine buffer was used to elute the potential talin binders from the talin on the GFP-Trap beads, allowing them to be identified more easily with appropriate fold change values in the MS analysis. Prior purification was also trialled to reduce the *E. coli* protein contaminants found in the bead samples. Furthermore, as the previous proteomics was carried out in collaboration with Turku BioCity in Finland, the LC-MS/MS analysis was adapted to perform it in-house, thereby streamlining the process.

#### Method Adaption

To determine if prior purification would remove any excess *E. coli* contaminants, GFP-Trap beads were incubated in both Ni-purified and unpurified GFP-talin rod cell lysate. Figure 4.13 demonstrates that, once again, although Ni purification of the cell lysate, prior to incubation with GFP-Trap beads, is expected to remove additional contamination from the sample, it simply results in more GFP-talin that has undergone degradation or incomplete translation (Figure 4.13 A), which is confirmed through an anti-His immunoblot (Figure 4.13 B). This indicated that Ni purification could increase the number of *E. coli*-derived proteins in the sample and would not benefit the LC-MS/MS proteomics analysis. Therefore, the GFP-talin cell lysate GFP-Trap beads were utilised for the next incubation step with 475 µg CaSki cell lysate, and Ni purification was no longer considered.

To overcome the difficulty caused by the overwhelming presence of talin when identifying proteins in the MS analysis, protein elution was attempted. After the GFP-talin/GFP-bound beads were washed following incubation in CaSki cell lysate, the potential binders were eluted from the beads with an acidic glycine wash before immediate neutralisation. From Figure 4.13 C, a similar amount of talin appears to be present in both the beads and elution samples. Although elution did not solely remove the potential binders from the beads, as the amount of talin had been split between the samples, this would likely allow the identification of other proteins in the samples to occur more easily.

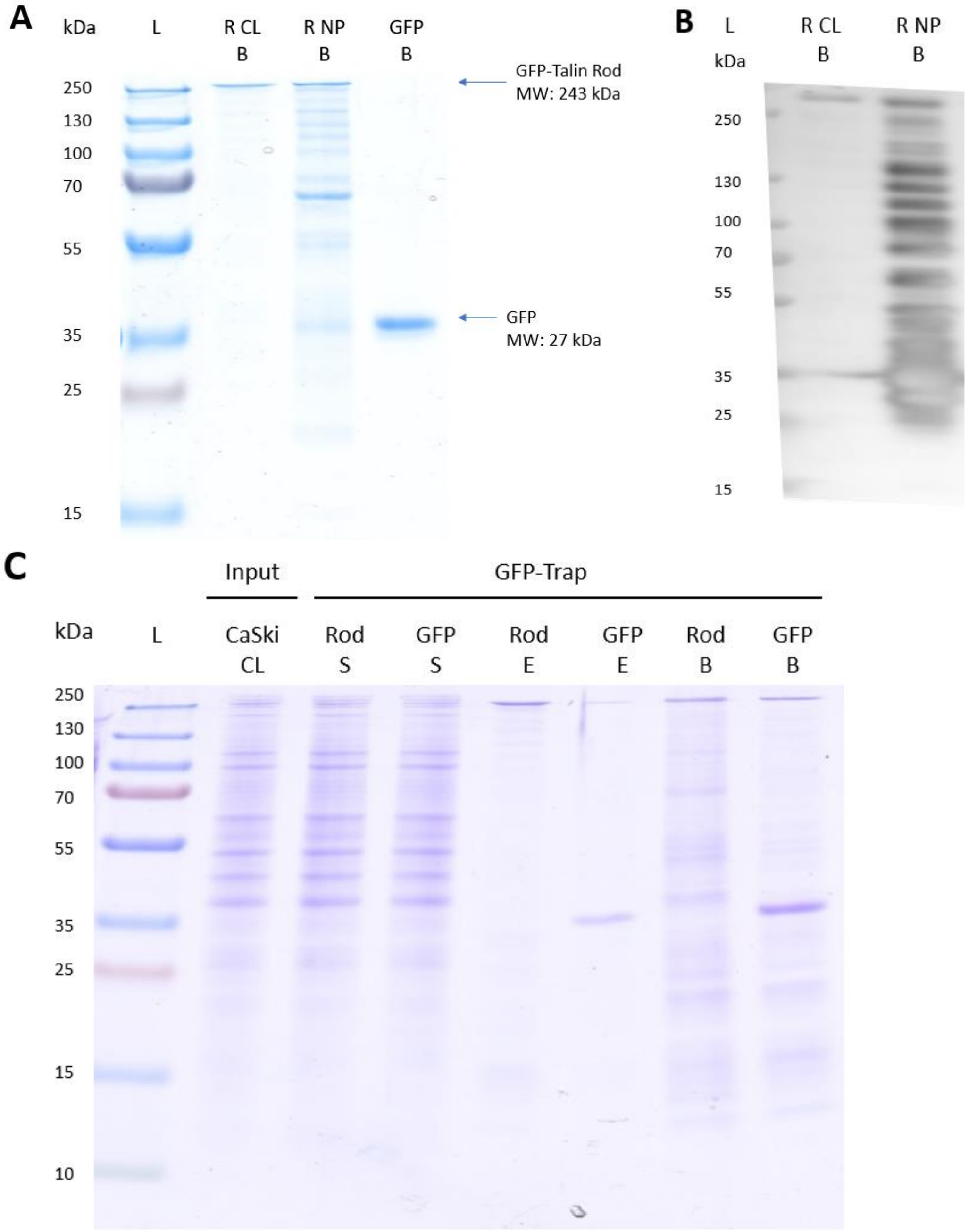

***Figure 4.13: Further optimisation of the talin 'fishing' rod experiment was trialled after feedback from Turku Bioscience.***

***(A)*** *SDS-PAGE gel confirming that Ni Batch purification causes more degradation/incomplete translation of the GFP-talin rod; therefore, it was not used in the adapted method to decrease E. coli protein contamination. L = protein ladder, R CL B = GFP-talin rod cell lysate GFP-Trap beads, R NP B = GFP-talin rod Ni-purified GFP-Trap beads, and GFP B = GFP GFP-Trap beads.* ***(B)*** *Anti-His immunoblot of GFP-Trap beads incubated with unpurified GFP-talin rod cell lysate (R CL B) or Ni-purified GFP-talin rod (R NP B).* ***(C)*** *SDS-PAGE gel of the adapted CaSki talin 'fishing' rod experiment. L = protein ladder, CL = cell lysate, Rod = GFP-talin rod, S = supernatant, E = elution, and B = GFP-Trap beads.*

### Method Validation

Anti-KANK1/2 immunoblots were used to validate whether the adapted talin 'fishing' rod experiment could successfully identify talin binders in CaSki cell lysate. In the anti-KANK1 immunoblot, bands were only visible in the CaSki input sample and the GFP/GFP-talin supernatants, indicating that whilst KANK1 was present in the pulldown, it had not bound to either the GFP or GFP-talin rod- bound beads (Figure 4.14).

In the anti-KANK2 immunoblot, there appears to be two isoforms of KANK2 present in the samples analysed, as bands of two different molecular weights were observed. The most prominent band, visualised at ~100 kDa, is closest to the predicted weight of KANK2 (91.2 kDa) and was present in the talin rod beads sample. Similar to the previous anti-KANK2 immunoblot in Figure 4.12, bands at this height were not seen in the input or supernatant samples, indicating that the concentration of this KANK2 isoform may have been too low for visualisation; however, after the pulldown, a significant amount of KANK2 had bound to the talin, allowing KANK2 to be visualised in the talin beads samples. As KANK2 was only present in the GFP-talin rod beads samples, this indicated that treating the beads with an elution buffer does not remove all talin binders from the talin beads.

The other KANK2 isoform, which was faintly visualised at ~70 kDa, was only present in the input and both supernatant samples; therefore, it had not bound to the talin in this 'fishing' rod experiment. This may have occurred as the KANK2 binding sites on talin were already fully saturated with the larger KANK2 isoform. Nevertheless, as the most prominent band in this immunoblot demonstrated that a known talin binder was effectively 'fished' out of CaSki cell lysate, this validated that the talin 'fishing' rod experiment was successful in identifying talin-binding ligands.

### Method Utilisation: Validating the results of Gough et al., 2021

1433G, septin-2, and Rho GDP Dissociation Inhibitor Alpha (ARHGDIA) were identified as possible talin binders in a GFP-talin pulldown MS proteomics analysis, conducted in a previous paper (Gough et al., 2021). All three proteins were analysed by the bioinformatics pipeline, created in section 3, and ARHGDIA/1433G were identified with the most promising I/LD motifs (Table 4.5). Through immunoblotting, the talin 'fishing' rod experiment successfully identified the talin binder KANK2 when GFP-Trap pulldowns were conducted in both CaSki cell lysate and murine neuronal extract. Therefore, the talin 'fishing' rod experiment was utilised to validate the results of Gough et al., 2021, which recognised these proteins as potential talin binders, and immunoblots of all three proteins were conducted on the talin 'fishing' rod experiment samples. Whilst 1433G, ARHGDIA, and septin-2 were all present in the pulldown, bands were only visible in the CaSki input sample and both the GFP/GFP-talin supernatants, indicating that the proteins had not bound to either the GFP or GFP-talin rod beads (Figure 4.14).

*Table 4.5: The most promising I/LD motifs present in 1433G, ARHGDIA, and septin-2.*

| Protein | Uniprot ID | I/LD motif | Position 4 Hydrophobic acid | Prior E/D residues | Hydrophobic residues at correct positions | Linked motif | Overall Score |
|---|---|---|---|---|---|---|---|
| **1433G** | P61981 | LDTL | L | E | Position 15: I | - | 4 |
| **ARHGDIA** | P52565 | LDKD | - | E | Position 8, 15: L, L | - | 4 |
| **Septin-2** | Q15019 | IDEQ | - | - | Position 5, 15: F, L | - | 3 |

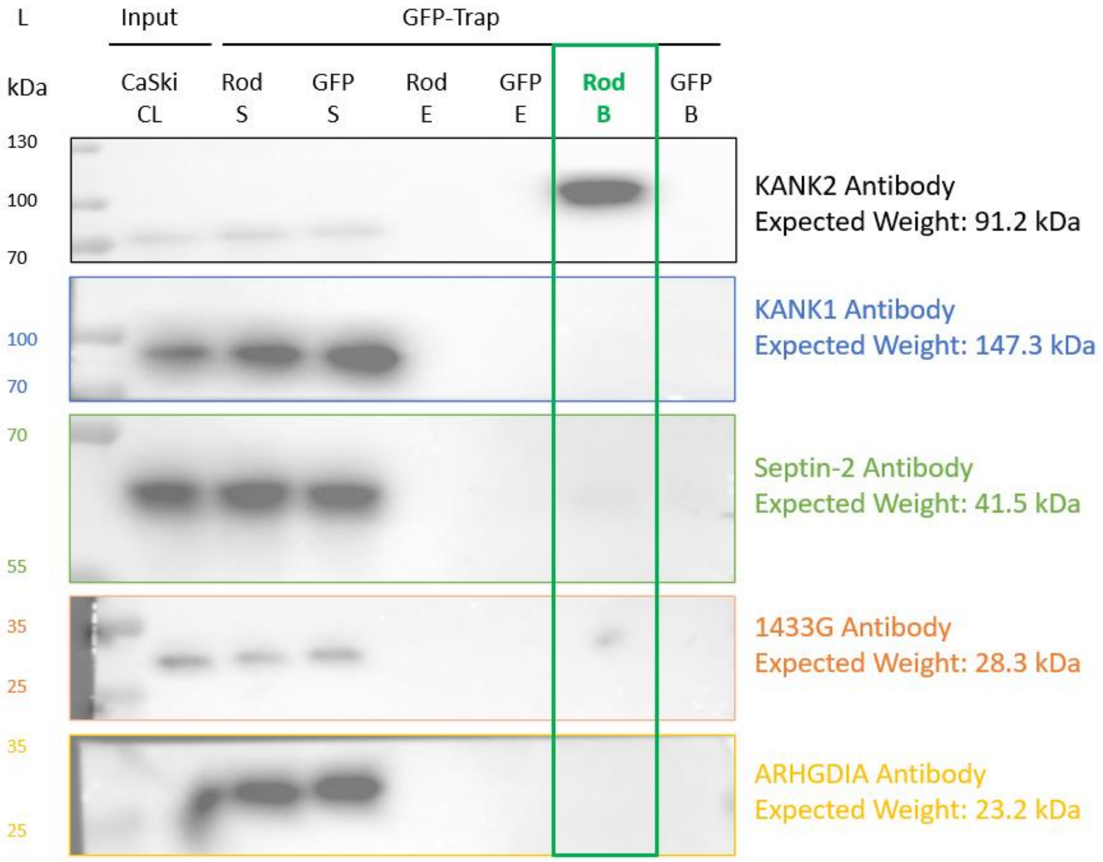

***Figure 4.14: Anti-KANK1/2, septin-2, 1433G, and ARHGDIA immunoblots of the adapted CaSki talin 'fishing' rod experiment.***

*L = protein ladder, CL = cell lysate, Rod = GFP-talin rod, S = supernatant, E = elution and B = GFP-Trap beads. The GFP-talin rod beads sample is highlighted in green.*

### Development of LC-MS/MS proteomics pipeline in-house

The bead and elution samples were analysed by LC-MS/MS proteomics using Progenesis QI software and the Apex3D algorithm at the University of Kent, with invaluable aid from Kevin Howland. The GFP elution sample was contaminated during the cleaning process with Pierce C18 Spin Tips (Thermo Fisher Scientific), and therefore, was not analysed. Nevertheless, the abundance fold change was calculated between the GFP bead sample and the GFP-talin rod bead or elution samples, and any protein identified with less than three unique peptides was deleted. As no repeats of the experiment were conducted, the p-values of protein abundance could not be calculated. However, as the Apex3D algorithm generated a confidence score for each protein identified, $\log_2$ (confidence) and $\log_2$ (fold change) were used to create the volcano plots displayed in Figure 4.15. The proteins predominantly found in the talin bead or elution samples compared to the GFP bead sample have a fold change above 1 or a positive $\log_2$ (fold change) and are visible in the unshaded, white area of the volcano plot. The proteins with a confidence score higher than 125 are highlighted in red and those with a confidence score higher than 125 and a fold change above 1 for both plots are identified in Tables 4.6 and 4.7.

As demonstrated in Figure 4.15, there are more proteins which have a positive $\log_2$ (fold change) identified in (A) the GFP-talin rod bead (RB) sample plot than (B) the GFP-talin rod elution (RE) sample plot. This is shown as more proteins are present in the white section of the RB plot than in the RE plot, indicating a positive $\log_2$ (fold change). This could be attributed to the usage of the GFP bead sample as a control for both the GFP-talin rod bead and elution samples when calculating fold change, as the GFP elution sample was no longer able to be utilised. Therefore, had it been utilised, the number of proteins with a positive $\log_2$ (fold change) between the bead and elution samples may have been more equal.

The overwhelming presence of talin in the previous MS analysis was thought to negatively impact both the identification of proteins in the talin samples and their fold change values. However, in the rod bead samples, more proteins had a positive $\log_2$ (fold change) than a negative $\log_2$ (fold change); therefore, they were predominantly present in the talin sample rather than the GFP sample, which was not achieved in the previous volcano plot (Figure 4. 12 B). This indicated that, unlike the previous MS analysis, the fold change of proteins identified in the talin samples, was not negatively affected by the presence of talin.

The intention of treating the bead samples with an acidic glycine buffer was to remove the proteins bound to the talin, so that the presence of talin did not hinder the ability to identify other proteins in the MS analysis. As the contamination of the GFP elution sample may have affected the fold change calculations in the second plot, further repeats were necessary to confirm that eluting the proteins from the beads with an acidic glycine buffer had the intended effect. However, whilst the most abundant protein in both the elution and bead samples was talin, it did not seem to negatively affect the other proteins identified by the proteomics analysis, as many were identified with a fold change above 1 and a high confidence score at appropriate abundances, which did not occur in the previous MS analysis. Therefore, this indicated that the overwhelming presence of talin, which was thought to negatively affect the identification of proteins in the previous proteomics analysis, was no longer an issue, and it was highly likely that elution of the proteins had a positive effect on the MS proteomics analysis. In fact, vinculin, a known talin binder, was identified in this MS analysis with a positive $\log_2$ (fold change) and a confidence score higher than 125 in both samples.

Furthermore, unlike the previous LC-MS/MS analysis conducted on the murine neuronal extract, there did not seem to be any problems with *E. coli* protein contamination, as the Progenesis QI software only identified proteins of human origin. This indicated that the adaptions made to the talin ‘fishing’ rod experiment were extremely beneficial and successfully allowed potential talin binders to be identified more confidently in the proteomics analysis. As MS proteomics was conducted successfully in-house, this ensured that results can be achieved easily and efficiently at a lower cost, thereby streamlining the proteomics process. Consequently, the identification of talin binders, through usage of the talin ‘fishing’ rod experiment, can now be conducted more conveniently and proficiently in the future.

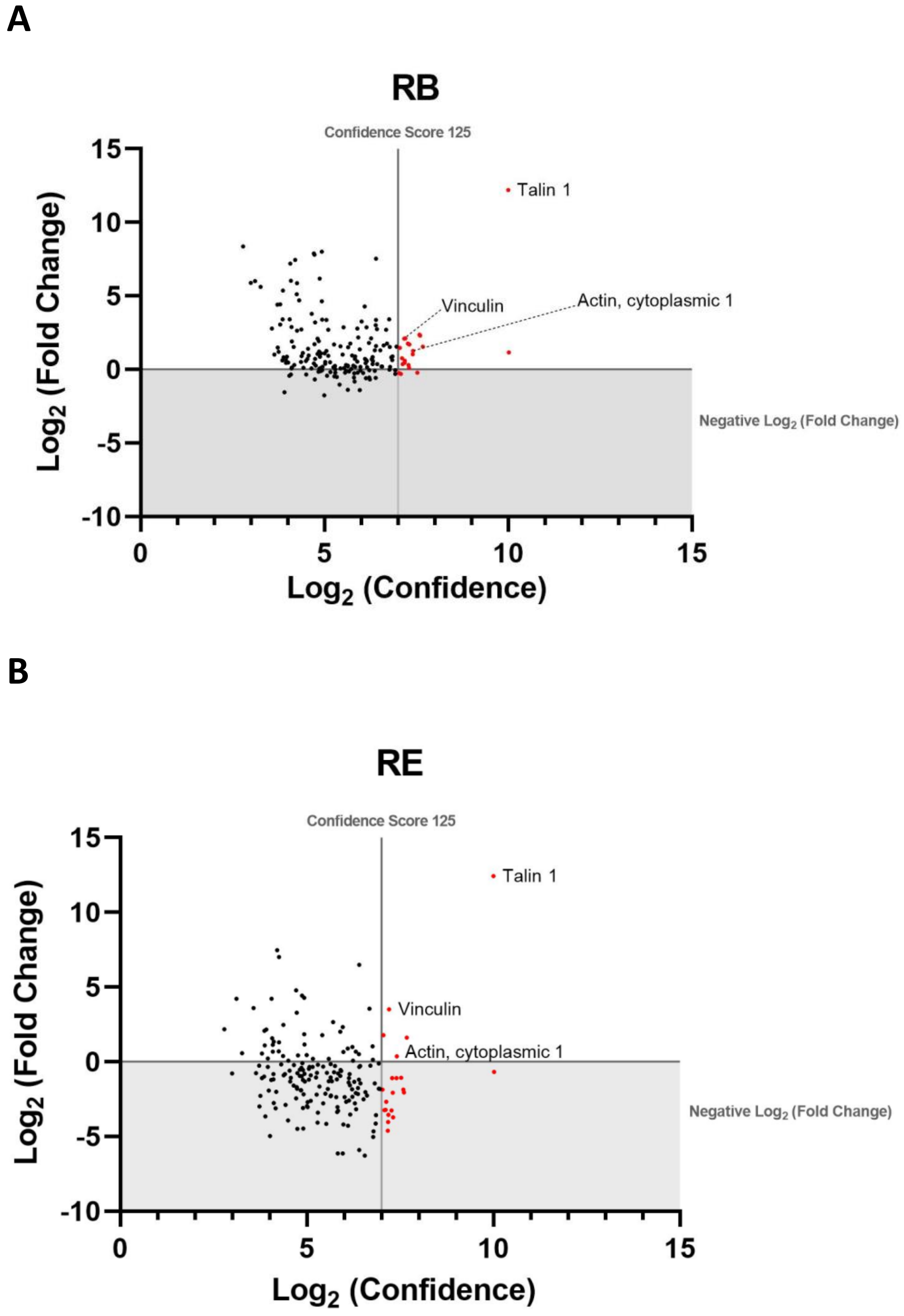

***Figure 4.15: MS proteomics analysis of the adapted CaSki talin 'fishing' rod experiment successfully identified potential talin binders.***

***(A)*** *Volcano plot displaying the Progenesis QI LC-MS/MS proteomics results for the GFP-talin rod bead (RB) sample in the adapted CaSki talin 'fishing' rod experiment.* ***(B)*** *Volcano plot displaying the Progenesis QI LC-MS/MS proteomics results for the GFP-talin rod elution (RE) sample in the adapted CaSki talin 'fishing' rod experiment. The shaded grey area of the plot represents a negative* $\log_2$ *(fold change), which occurs when the fold change is below 1, as the proteins were predominantly present in the control GFP samples. The unshaded, white area of the plot represents a positive* $\log_2$ *(fold change), which occurs when the fold change is above 1, as the proteins were predominantly present in the GFP-talin rod samples. The proteins identified with a confidence score above 125 are highlighted in red and those with both a confidence score above 125 and a positive* $\log_2$ *(fold change) are visualised in Tables 4.6 and 4.7. Key proteins identified are labelled.*

***Table 4.6: Proteins identified in the RB volcano plot (Figure 4.15 A) with a confidence score higher than 125 and a fold change above 1.***
*The proteins in bold and underlined are present in both the GFP-talin rod beads (RB) and elution (RE) tables (Tables 4.6 and 4.7).*

**RB**

| **Protein** | **Uniprot ID** | **Confidence** | **Fold change** |
|---|---|---|---|
| **Myosin-9** | P35579 | 1041 | 2.24 |
| **Talin 1** | **Q9Y490** | **1024** | **4701** |
| **40S ribosomal protein S16** | P62249 | 205 | 2.94 |
| **Tubulin beta-4B chain** | P68371 | 194 | 4.95 |
| **Tubulin beta chain** | P07437 | 192 | 5.12 |
| **Actin cytoplasmic 1** | **P60709** | **170** | **2.40** |
| **Heterogenous nuclear ribonucleoprotein** | Q00839 | 170 | 2.04 |
| **60S ribosomal protein L3** | P39023 | 159 | 3.26 |
| **60S ribosomal protein L7a** | P62424 | 158 | 1.08 |
| **Histone H4** | P62805 | 156 | 1.23 |
| **60S ribosomal protein L4** | P36578 | 154 | 3.38 |
| **Vinculin** | **P18206** | **148** | **4.35** |
| **40S ribosomal protein S9** | P46781 | 146 | 1.52 |
| **60S ribosomal protein L7** | P18124 | 145 | 1.36 |
| **Tubulin alpha-3C chain** | P0DPH7 | 144 | 4.27 |
| **Coatomer subunit alpha** | P53621 | 140 | 1.28 |
| **60S ribosomal protein L27** | P61353 | 138 | 1.69 |
| **Myosin-14** | **Q7Z406** | **135** | **2.76** |

***Table 4.7: Proteins identified in the RE volcano plot (Figure 4.15 B) with a confidence score higher than 125 and a fold change above 1.***
*The proteins in bold and underlined are present in both the GFP-talin rod beads (RB) and elution (RE) tables (Tables 4.6 and 4.7).*

**RE**

| **Protein** | **Uniprot ID** | **P-value** | **Fold change** |
|---|---|---|---|
| **Talin 1** | **Q9Y490** | **1024** | **5468.37** |
| **40S ribosomal protein S16** | P62249 | 205 | 3.07 |
| **Actin cytoplasmic 1** | **P60709** | **170** | **1.29** |
| **Vinculin** | **P18206** | **148** | **11.40** |
| **Myosin-14** | **Q7Z406** | **135** | **3.45** |

## 4.4 Using the finalised talin ‘fishing’ rod experiment to identify talin-binding ligands in CaSki cell lysate

### 4.4.1 Theory Overview

The previous talin ‘fishing’ rod experiment effectively managed to identify known talin binders in CaSki cell lysate: KANK2 through immunoblotting and vinculin through the adapted MS proteomics analysis. As no repeats were conducted, the experiment was carried out twice more in CaSki cell lysate to achieve a broader list of potential talin binders and confirm the assumption of the previous MS analysis, that eluting potential binders from the beads had the intended effect and was beneficial to the process.

### 4.4.2 ‘Fishing’ in CaSki cell lysate

Five batches of GFP-Trap beads were bound to both the GFP-talin rod and GFP, as displayed in Figure 4.16. Two batches of the GFP and GFP-talin rod-bound GFP-Trap beads in Figure 4.16 were incubated with 545 µg CaSki cell lysate, and the results of the pulldown are demonstrated in Figure 4.17. In the first repeat, more talin was present in the elution sample than the beads sample; however, in the second repeat, the opposite had occurred, indicating that elution separated the potential binders from talin more successfully (Figure 4.17). Nevertheless, as the amount of talin had been successfully split between the samples, this would allow other proteins to be identified easily as they were in the previous MS proteomics analysis.

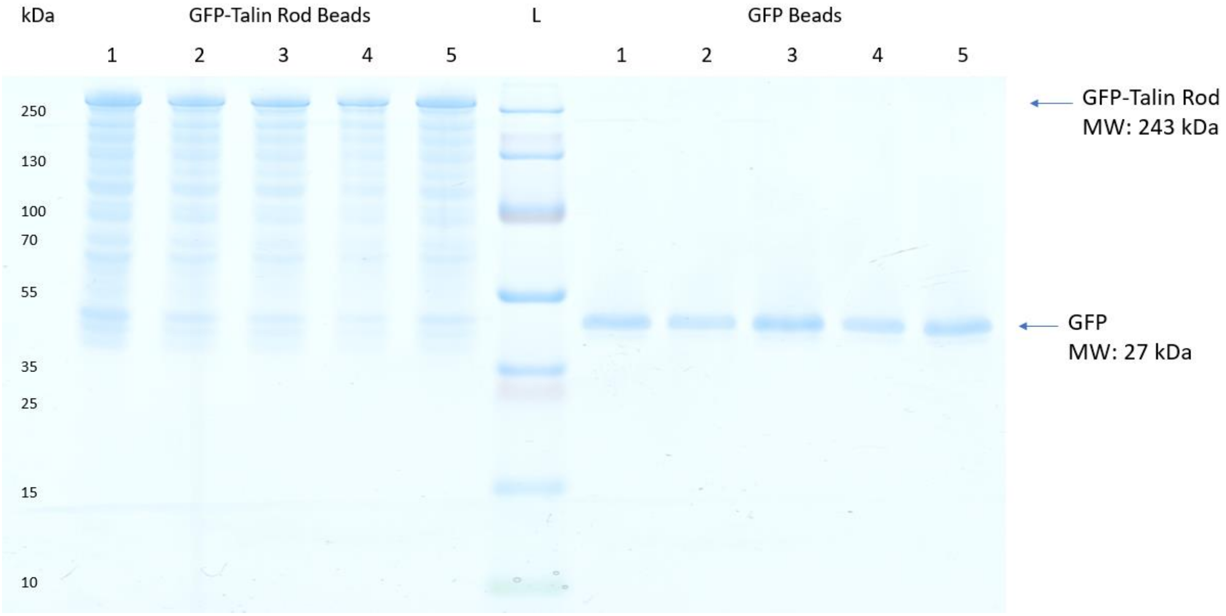

***Figure 4.16: SDS-PAGE gel demonstrating five batches of GFP-talin rod and GFP bound to GFP-Trap beads, prior to incubation with CaSki cell lysate or murine neuronal extract.***
*L = protein ladder.*

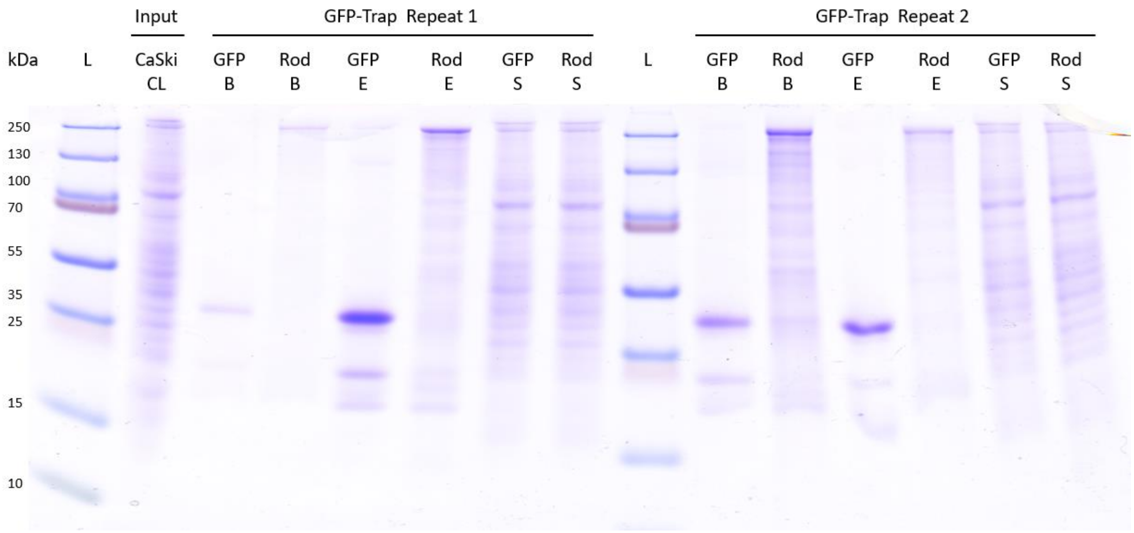

***Figure 4.17: SDS-PAGE gel of the finalised talin 'fishing' rod experiment in CaSki cell lysate.***
*L = protein ladder, CL = cell lysate, B = beads, Rod = GFP-talin rod, E = elution, and S = supernatant.*

### 4.4.3 Method Validation

Anti-KANK1/2 and CDK1 immunoblots were used to validate whether the talin 'fishing' rod experiment could successfully identify talin binders in CaSki cell lysate (Figure 4.18). In the KANK1 and CDK1 immunoblots, the proteins were only visualised in the CaSki cell lysate and the GFP/GFP-talin rod supernatants, indicating that whilst the proteins were present in the pulldown, they did not bind to either set of beads.

In the KANK2 immunoblot, the most prominent bands were visualised between 100 and 130 kDa, which is slightly higher than the expected molecular weight of KANK2 (91.2 kDa); nevertheless, the bands are at a similar position to those present in Figure 4.9 B. The most prominent bands were visualised in the rod bead and elution samples, with fainter bands present in the talin supernatant samples. This indicated that the majority of KANK2 bound to the talin in the pulldown, which either remained bound to the beads or was eluted. For the GFP samples, the most prominent bands were present in the supernatants, indicating that the majority of KANK2 did not bind to GFP. However, there was a faint band visible in the GFP bead samples. This is much fainter than those present in the supernatant, or the rod bead samples. Therefore, it is unlikely that this indicates binding, although it could indicate that perhaps the beads required further washing as some KANK2 remained.

There were also faint KANK2 bands present at a lower molecular weight of ~70 kDa, indicating the presence of another KANK2 isoform. These bands were at a similar molecular weight to those present in the CaSki cell lysate and supernatant samples in Figure 4.14; however, they only seemed to appear in the rod bead and elution samples. Therefore, unlike the previous KANK2 immunoblot where the bands at this molecular weight were visualised in only the cell lysate or supernatant samples and thus did not bind to talin (Figure 4.14), the KANK2 isoform at ~70 kDa in this experiment had bound to the talin rod. As both the KANK2 isoforms visualised on this KANK2 immunoblot were 'fished' out of the CaSki cell lysate by binding to talin, this validated that the talin 'fishing' rod experiment successfully identified talin binders in CaSki cell lysate.

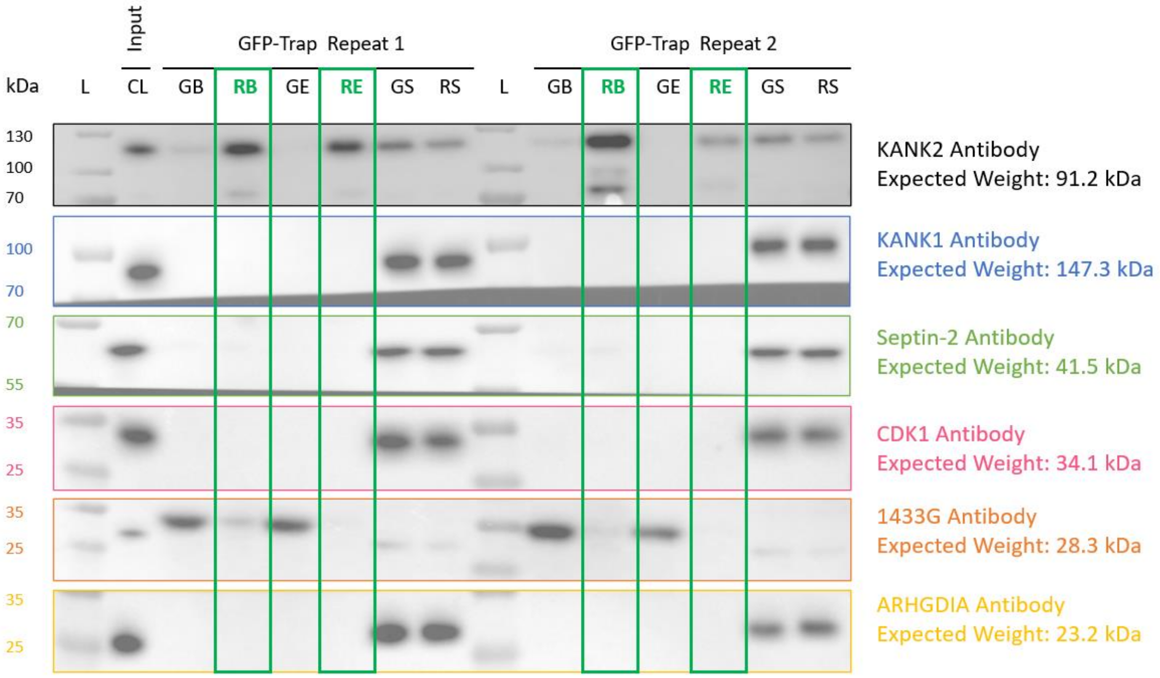

***Figure 4.18: Anti-KANK1/2, septin-2, CDK1, 1433G, and ARHGDIA immunoblots of the finalised talin 'fishing' rod experiment in CaSki cell lysate.***
*L = protein ladder, CCL = CaSki cell lysate, G = GFP, R = GFP-talin rod, B = beads, E = elution, and S = supernatant. The GFP-talin rod bead and elution samples are highlighted in green.*

### 4.4.4 Method Utilisation: Validating the results of Gough et al., 2021

As the talin 'fishing' rod experiment was validated by the identification of KANK2 in the talin samples, the pulldown samples were then utilised and anti-1433G, ARHGDIA, and septin-2 immunoblots were carried out to verify the results of Gough et al., 2021 (Figure 4.18). In the ARHGDIA and septin-2 immunoblots, the proteins were only visualised in the CaSki cell lysate and the GFP/GFP-talin rod supernatants indicating that, whilst the proteins were present in the pulldown, they did not bind to either set of beads in the talin 'fishing' rod experiment.

The 1433G immunoblot suggested that two 1433G isoforms were present in the CaSki cell lysate. The isoform with the higher intensity bands and a higher molecular weight (slightly below 35 kDa) was predominantly present in the GFP beads and elution samples, but only slightly present in the talin rod beads sample. This would imply that the 1433G isoform had bound to the GFP, which is unexpected. It was not present in the CaSki cell lysate or supernatant samples, which could suggest that the concentration may have been too low for visualisation; however, after the pulldown, a significant amount of 1433G had bound to the GFP, allowing 1433G to be visualised in the GFP samples. Although this is something seen previously in KANK2 immunoblots with talin (Figure 4.14), it can be explained as KANK2 is a known strong talin binder. However, as 1433G is not known to bind to GFP, this result is unexpected. The second isoform of 1433G, visualised on the immunoblot at a lower molecular weight (between 25-35 kDa), seems to be the same isoform visualised in the previous 1433G immunoblot in Figure 4.14. This 1433G isoform was visualised in the CaSki cell lysate and both the GFP/GFP-talin rod supernatants, suggesting that it had not bound to either the talin or the GFP in the pulldown, which is also a reflection of the results in the previous 1433G immunoblot (Figure 4.14).

### 4.4.5 MS proteomics analysis

The bead and elution samples were once again analysed by LC-MS/MS proteomics using Progenesis QI software and the Apex3D algorithm at the University of Kent, with invaluable aid from Kevin Howland. Any protein identified with less than three unique peptides was deleted and the abundance fold change between the beads and elution samples for both GFP and GFP-talin rod was calculated. As two repeats were conducted, the p-value of these results could be calculated. The $-\log_2$ (p-value) was plotted against the $\log_2$ (fold change) to create the volcano plots displayed in Figure 4.19. The proteins predominantly found in the talin bead/elution samples compared to the GFP bead/elution samples have a fold change above 1, a positive $\log_2$ (fold change), and are visible in the unshaded area of the volcano plot. The proteins with a significant p-value below 0.05 are highlighted in red and those with a significant p-value and a fold change above 1 for both plots are identified in Tables 4.8 and 4.9, highlighted in blue.

As the Apex3D algorithm generated a confidence score for each protein identified, the MS data was also analysed through confidence, and proteins with both a fold change above 1 and a confidence score higher than 125 are identified in Tables 4.8 and 4.9, highlighted in yellow. The proteins with a significant p-value, fold change above 1, and a confidence score higher than 125 are highlighted in green (Tables 4.8 and 4.9).

The intention of treating the bead samples with an acidic glycine buffer was to prevent the overwhelming presence of talin from negatively impacting both the identification of proteins in the talin samples and their fold change values. In the previous MS analysis, as the GFP elution sample could not be used to calculate fold change for the talin elution sample, and the GFP beads sample was used instead, this may have affected the fold change values present in the previous RE volcano plot (Figure 4.15 B). Therefore, it was not possible to confirm whether treating the beads with an elution buffer had the intended effect on the fold change of potential binders. The results of this talin 'fishing' rod experiment identified 35 promising potential talin binders with fold change values above 1, appropriate abundances and confidence scores. In both plots, there is a decent ratio of proteins with a positive and negative $\log_2$ (fold change), in contrast to both Figures 4.12 B and 4.15 B. This confirms that the aim of treating the beads with an acidic buffer was successful, as it split the talin between both samples, allowing potential talin binders to be identified more easily with fold change values above 1 at appropriate abundances.

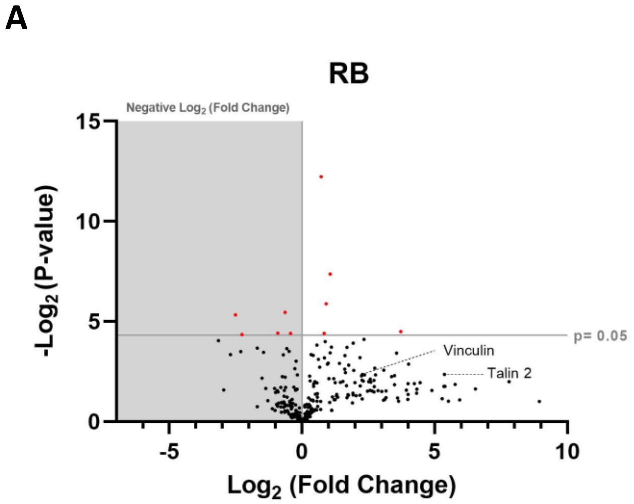

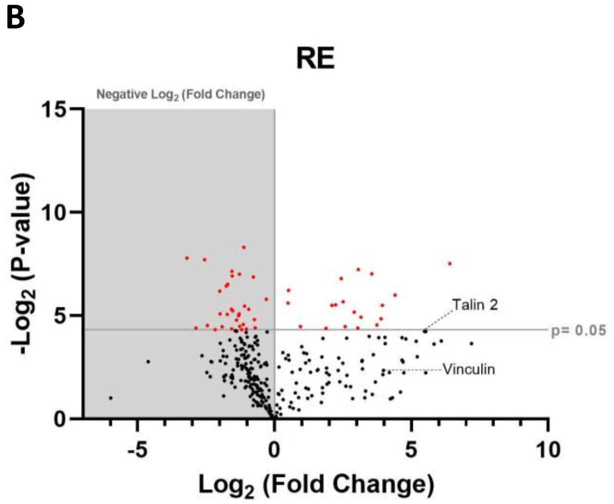

***Figure 4.19: Volcano plots of the MS proteomics analysis for the finalised talin 'fishing' rod experiment in CaSki cell lysate identified many potential talin binders.***

***(A)*** *Volcano plot displaying the Progenesis QI LC-MS/MS proteomics results for the GFP-talin rod bead (RB) sample in the finalised CaSki talin 'fishing' rod experiment.* ***(B)*** *Volcano plot displaying the Progenesis QI LC-MS/MS proteomics results for the GFP-talin rod elution (RE) sample in the finalised CaSki talin 'fishing' rod experiment. The shaded grey area of the plot represents a negative $\log_2$ (fold change), which occurs when the fold change is below 1, as the proteins were predominantly present in the control GFP samples. The unshaded, white area of the plot represents a positive $\log_2$ (fold change), which occurs when the fold change is above 1, as the proteins were predominantly present in the GFP-talin rod samples. The proteins identified with a significant p-value of less than 0.05 are highlighted in red and those with both a significant p-value and a positive $\log_2$ (fold change) are identified in Tables 4.8 and 4.9, highlighted in blue. Key proteins identified are labelled.*

***Table 4.8: Proteins identified in the finalised CaSki RB volcano plot (Figure 4.19 A), with a fold change above 1 and a confidence score higher than 125 or a significant p-value.***

*The proteins with a significant p-value and fold change above 1 are highlighted in blue. The proteins with a confidence score higher than 125 and a fold change above 1 are highlighted in yellow. The proteins with a significant p-value, fold change above 1, and a confidence score higher than 125 are highlighted in green. The proteins in bold and underlined are present in both the GFP-talin rod beads (RB) and elution (RE) tables (Tables 4.8 and 4.9). *Proteins are also identified in the previous MS proteomics analysis in CaSki cell lysate and are displayed in Tables 4.6 and 4.7.*

| Protein | Uniprot ID | Confidence | Fold-change | P-value |
|---|---|---|---|---|
| **Tubulin beta-2B chain** | Q9BVA1 | 192 | 1.64 | 0.0002 |
| **Nuclear mitotic apparatus protein 1** | Q14980 | 95 | 13.23 | 0.045 |
| **<u>Heat shock-related 70 kDa protein 2</u>** | **<u>P54652</u>** | **<u>88</u>** | **<u>1.88</u>** | **<u>0.017</u>** |
| **Tubulin beta chain*** | P07437 | 196 | 1.78 | 0.047 |
| **Eukaryotic translation initiation factor 4 gamma 2 (Fragment)** | D3DQV9 | 36 | 2.08 | 0.006 |
| **<u>Myosin-9*</u>** | **<u>P35579</u>** | **<u>840</u>** | **<u>5.53</u>** | **<u>0.34</u>** |
| **<u>Unconventional myosin-Ib</u>** | **<u>O43795</u>** | **<u>351</u>** | **<u>20.09</u>** | **<u>0.33</u>** |
| **60S ribosomal protein L3*** | P39023 | 221 | 1.36 | 0.67 |
| **60S ribosomal protein L7*** | P18124 | 213 | 1.12 | 0.75 |
| **<u>Myosin-14*</u>** | **<u>Q7Z406</u>** | **<u>166</u>** | **<u>6.03</u>** | **<u>0.25</u>** |
| **Poly [ADP-ribose] polymerase 1** | P09874 | 164 | 1.11 | 0.92 |
| **40S ribosomal protein S3a** | P61247 | 158 | 1.08 | 0.59 |
| **60S acidic ribosomal protein P0** | P05388 | 156 | 1.15 | 0.80 |
| **FACT complex subunit SSRP1** | Q08945 | 148 | 1.27 | 0.64 |
| **<u>Myosin-11</u>** | **<u>P35749</u>** | **<u>142</u>** | **<u>16.21</u>** | **<u>0.14</u>** |
| **40S ribosomal protein s4_ X isoform** | P62701 | 137 | 1.15 | 0.75 |
| **40S ribosomal protein S13** | P62277 | 136 | 1.09 | 0.86 |
| **40S ribosomal protein S7** | P62081 | 131 | 1.13 | 0.87 |
| **Plectin (Fragment)** | E9PMV1 | 126.5 | 2.17 | 0.68 |

***Table 4.9: Proteins identified in the finalised CaSki RE volcano plot (Figure 4.19 B), with a fold change above 1 and a confidence score higher than 125 or a significant p-value.***

*The proteins with a significant p-value and fold change above 1 are highlighted in blue. The proteins with a confidence score higher than 125 and a fold change above 1 are highlighted in yellow. The proteins with a significant p-value, fold change above 1, and a confidence score higher than 125 are highlighted in green. The proteins in bold and underlined are present in both the GFP-talin rod beads (RB) and elution (RE) tables (Tables 4.8 and 4.9). *Proteins are also identified in the previous MS proteomics analysis in CaSki cell lysate and are displayed in Tables 4.6 and 4.7.*

| Protein | Uniprot ID | Confidence | Fold-change | P-value |
|---|---|---|---|---|
| **Kinesin-like protein KIF1C** | O43896 | 16.3 | 84.56 | 0.005 |
| **Unconventional myosin-Ib** | **O43795** | **351** | **21.23** | **0.016** |
| **Alpha-actinin-1** | P12814 | 115 | 11.72 | 0.008 |
| **Protein fantom** | A0A087WX | 43 | 15.40 | 0.022 |
| **Uncharacterised protein** | A0A2R8Y4 | 16 | 14.83 | 0.035 |
| **LIM domain and actin binding protein** | Q9UHB6 | 121 | 13.39 | 0.043 |
| **Zinc finger protein 518B** | Q9C0D4 | 30 | 8.36 | 0.007 |
| **ATP-dependent RNA helicase A** | Q08211 | 33 | 8.90 | 0.033 |
| **Disks large homolog 2** | A0A3B3ISW2 | 44 | 8.25 | 0.047 |
| **Rho GTPase-activating protein 28** | Q9P2N2 | 30 | 7.53 | 0.028 |
| **ATP-dependent RNA helicase DDX3X** | O00571 | 83 | 5.42 | 0.009 |
| **Disks large homolog 4** | P78352 | 19 | 4.69 | 0.022 |
| **60S ribosomal protein L27a** | P46776 | 59 | 5.98 | 0.045 |
| **Glyceraldehyde-3-phosphate dehydrogenase** | P04406 | 92 | 4.28 | 0.022 |
| **Carboxypeptidase D** | O75976 | 17 | 3.68 | 0.048 |
| **60 ribosomal protein L27*** | P61353 | 71 | 1.93 | 0.045 |
| **60 ribosomal protein L32** | P62910 | 41 | 1.43 | 0.013 |
| **Heat shock-related 70 kDa protein 2** | **P54652** | **88** | **1.41** | **0.020** |
| **Myosin 9*** | **P35579** | **840** | **6.24** | **0.067** |
| **Myosin 14*** | **Q7Z406** | **166** | **5.68** | **0.020** |
| **Myosin 11** | **P35749** | **142** | **16.40** | **0.065** |

# 5 Using a novel method, the finalised talin 'fishing' rod experiment, to identify talin-binding ligands in the brain

## 5.1 'Fishing' in murine neuronal extract

The murine cytosolic, PSD, and non-PSD fractions, used in section 4.3.3, were combined so that repeats of the talin 'fishing' rod experiment in murine neuronal extract could be conducted. Three batches of GFP and GFP-talin rod-bound GFP-Trap beads, from Figure 4.16, were incubated with 1.58 µg/µL of the combined neuronal extract, and the results are displayed in Figure 5.1. The amount of talin was successfully split between the GFP-talin rod beads and elution samples, indicating that MS analysis of potential talin binders would occur easily.

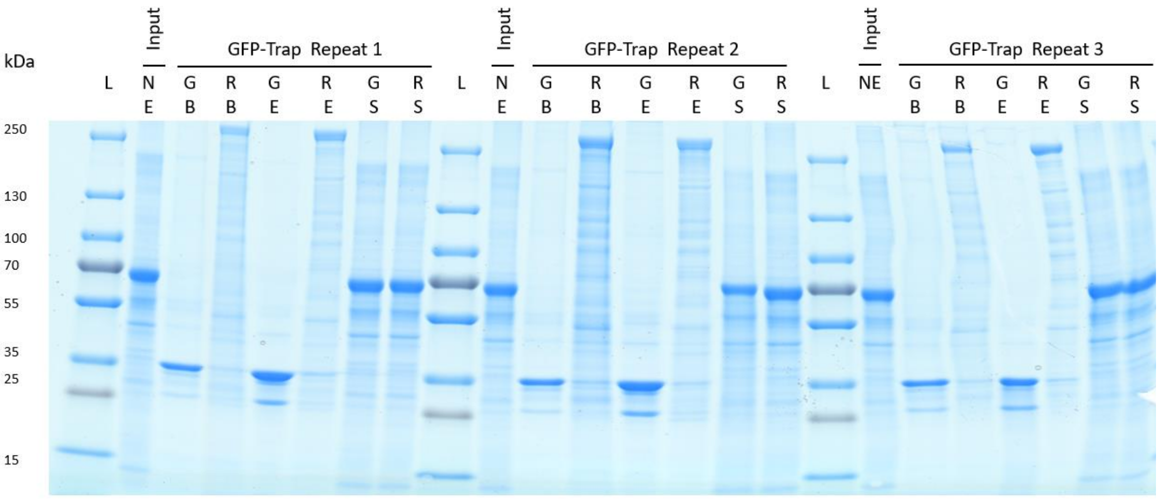

***Figure 5.1: SDS-PAGE gel of the finalised talin 'fishing' rod experiment in murine neuronal extract.*** *L= protein ladder, B = beads, Rod = GFP-talin rod, E = elution, and S = supernatant.*

## 5.2 Method Validation

To validate whether the talin 'fishing' rod experiment could successfully identify talin-binding ligands in murine neuronal extract, anti-KANK1/2 and CDK1 immunoblots were conducted (Figure 5.2). Unlike the previous immunoblots which were all imaged using a G:BOX Chemi XRQ gel doc system (Syngene), the immunoblots in Figure 5.2 were imaged using film, which is more sensitive. When imaging using film, different proteins require different exposure times, and as this had to be done manually, the intensity of the blots differ as the optimum exposure time for each protein was unknown.

There were several bands of varying molecular weights present in the anti-KANK2 immunoblot. The most prominent bands in each repeat were either in the GFP-talin rod beads or elution samples, at approximately 70 kDa, which is not surprising as a murine KANK2 isoform of ~65 kDa has previously been identified (Bateman et al., 2021). Bands of this molecular weight have also been visible in previous immunoblots, such as in Figure 4.14 where this isoform did not bind to talin, or in Figure 4.18 where it did. Similar to previous KANK2 immunoblots, these bands were not accompanied by bands at equal heights in the input or supernatant samples, which once again could indicate that the concentration of KANK2 was too low for visualisation in these samples; however, after the pulldown, a significant amount of KANK2 had bound to talin, enabling visualisation. As the most prominent KANK2 bands were all present in the talin beads/elution samples, this validated that the talin 'fishing' rod experiment had successfully identified a known talin binder in murine neuronal extract.

There were additional bands present in the anti-KANK2 immunoblot at a lower molecular weight, slightly above 55 kDa, which was not observed in any previous anti-KANK2 immunoblot. This could represent another isoform of KANK2 or a cleaved/digested form of KANK2. The protein did not seem to bind to talin and was only present in the neuronal extract input and both the GFP/GFP-talin rod supernatants.

In the anti-KANK1 immunoblot, the bands were most easily visible in the second repeat, and there were multiple bands present at varying molecular weights. The majority of bands seem to be at ~130 kDa, which is the expected molecular weight of murine KANK1. At 130 kDa, there were very faint bands for the input neuronal extract and the supernatants, stronger bands for the GFP bead samples in two repeats, and a very prominent band in the talin rod bead sample for the second repeat. This indicated that the majority of KANK1 present in the neuronal extract had bound to the talin rod in the second repeat; however, in two repeats KANK1 had also bound to the GFP. This was not the desired outcome as GFP was intended to be a negative control. There were also two additional bands in the rod beads sample at lower molecular weights from 100-130 kDa. Likewise, for the band at the lowest molecular weight (100 kDa), there were two faint bands at the same molecular weight in both supernatants. The additional bands could possibly be different isoforms of KANK1 present in the murine neuronal extract or the same KANK1 protein that has undergone degradation or modification of some sort, hence its difference in molecular weight. Nevertheless, although the rod beads sample had the most intense bands at each molecular weight, the fact that a band was visualised in the GFP beads samples in two repeats indicated that this immunoblot could not be used to validate whether the talin 'fishing' rod experiment had effectively identified KANK1 through talin binding in murine neuronal extract.

Although further exposure time was required for the anti-CDK1 immunoblot, bands of two molecular weights can faintly be visualised. Bands were present between 25-35 kDa in the GFP bead and elution samples, which is peculiar as GFP was intended to be the negative control. Bands were also present between 55-70 kDa in the input extract sample and both supernatants, implying that this protein did not bind to talin or GFP. As the expected molecular weight of CDK1 is 34.1 kDa, the bands between 55-70 kDa may represent a CDK1 dimer.

## 5.3 Method Utilisation: Validating the results of Gough et al., 2021

As the talin 'fishing' rod experiment was validated by the identification of KANK2 in the talin samples, anti-1433G, ARHGDIA, and septin-2 immunoblots were once again conducted on the pulldown samples to verify the results of Gough et al., 2021 (Figure 5.2).

The previous anti-1433G immunoblot (Figure 4.18) demonstrated bands between 25-35 kDa in the GFP bead and elution samples, which were also seen in this immunoblot (Figure 5.2). Similar to the CDK1 immunoblot, there were no bands visible in the neuronal extract input or supernatant samples. However, whilst another isoform of 1433G was visualised in the previous anti-1433G immunoblot (Figure 4.18), no further bands were visualised in the latest 1433G immunoblot (Figure 5.2).

A similar pattern is demonstrated in the anti-ARHGDIA immunoblot, there were bands at a similar weight (between 25-35 kDa) in the GFP bead and elution samples. However, for the ARHGDIA immunoblot, the bands present in the GFP bead and elution samples were not the most prominent bands in the immunoblot. There were additional bands at a lower molecular weight (25 kDa), which are more intense. These bands were visualised in the input extract and both supernatant samples, demonstrating that whilst ARHGDIA was present, it did not bind to either talin or GFP. As these bands were more prominent, with a molecular weight closest to the expected weight of ARHGDIA (23 kDa), and demonstrate the same pattern shown in previous immunoblots (Figures 4.14 and 4.18), they likely represent the main isoform of ARHGDIA.

The bands between 25-35 kDa present in the GFP bead and elution samples, for the anti-1433G, ARHGDIA and CDK1 immunoblots were very unexpected as GFP was intended to be the negative control that would not bind to any protein. Also, the fact that these bands were only present in the GFP elution and beads samples indicates that the concentration of these proteins was too low for visualisation in the input and supernatant samples; however, after the pulldown, significant amounts of these proteins had bound tightly to GFP, enabling visualisation. The bands were all between 25-35 kDa and the expected molecular weights for 1433G, ARHGDIA, and CDK1 are 23.2, 28.3, and 34.1 kDa, respectively. However, the weight of GFP is approximately 27 kDa; therefore, the bands observed may not be a result of binding to 1433G, ARGHDIA, and CDK1, but of cross-reactivity to the GFP present in the samples.

Curiously, the anti-septin-2 immunoblot demonstrated that septin-2 was present in all the samples, but most predominantly in the GFP and talin bead samples. Whilst this was confusing at first, the MS results confirmed that septin-2 was present in both the GFP/GFP-talin rod beads and elution samples. From yeast to mammals, septins are a family of GTPases and a crucial component of the cytoskeleton conserved in eukaryotes (Cho et al., 2011; Mostowy & Cossart, 2012). They are also highly expressed in neurons as they are required for dendritic branching, which is reflected in the MS analysis results, as 10 septins were identified in the samples (Kaplan et al., 2017). As westerns are more sensitive than LC-MS/MS, the reason why septin-2 was found in all samples could be a result of the large abundance of septin-2 in the murine neuronal extract. In the previous septin-2 immunoblots, although septin-2 was found in the pulldown input, it was only ever found in the supernatants, indicating that it had not bound to GFP or talin. It was also not found in the previous proteomics results conducted on the samples obtained from 'fishing' in CaSki cell lysate. Septin-2 was likely so extremely abundant in the neuronal extract, as opposed to the other proteins which were not found in the proteomics analysis, that even an amount large enough for immunoblot visualisation remained after washing the beads. Therefore, although the results of this immunoblot indicate that septin-2 was pulled out in both the talin and negative control GFP-bound beads, it cannot be used to confidently imply that binding to either occurred.

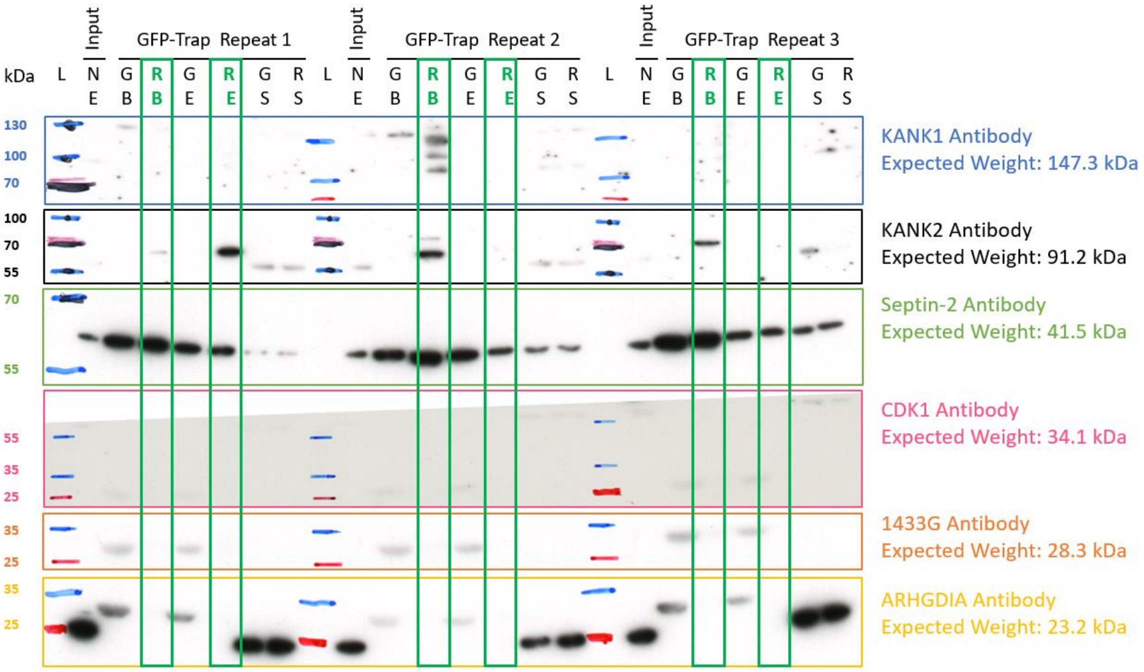

***Figure 5.2: Anti-KANK1/2, septin-2, CDK1, 1433G, and ARHGDIA immunoblots of the finalised talin 'fishing' rod experiment in the combined murine neuronal extract.***

*L = protein ladder, NE = murine neuronal extract, G = GFP, R = GFP-talin rod, B = beads, E = elution, and S = supernatant. The GFP-talin rod bead and elution samples are highlighted in green. Immunoblots were imaged using film at different exposure times: KANK1 (5 mins), KANK2 (5 mins), septin-2 (1 min), CDK1 (20 mins), 1433G (5 mins), and ARHGDIA (1 min).*

## 5.4 Identification of potential talin binders in murine neuronal extract.

The MS proteomics results were analysed, as explained in section 4.4.5, to generate the volcano plots displayed in Figure 5.3. The plots generated for the GFP-talin rod beads and elution samples do not seem to differ particularly in appearance and a similar number of proteins were identified with a significant p-value and a fold change above 1. Tables 5.1 and 5.2 display the proteins identified with a fold change above 1 and a significant p-value or confidence score higher than 125 in the GFP-talin rod bead and elution samples.

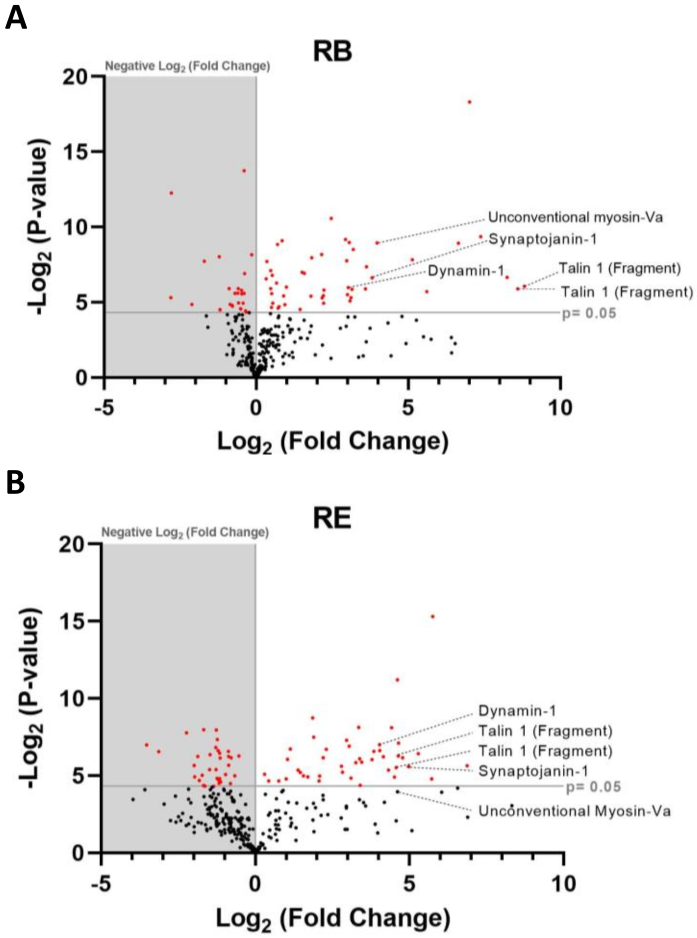

***Figure 5.3: Volcano plots of the MS proteomics analysis for the finalised talin 'fishing' rod experiment in the combined murine neuronal extract identified potential talin binders.***

***(A)*** *Volcano plot displaying the Progenesis QI LC-MS/MS proteomics results for the GFP-talin rod bead (RB) sample in the finalised neuronal talin 'fishing' rod experiment.* ***(B)*** *Volcano plot displaying the Progenesis QI LC-MS/MS proteomics results for the GFP-talin rod elution (RE) sample in the finalised neuronal talin 'fishing' rod experiment. The shaded grey area of the plot represents a negative $log_2$ (fold change), which occurs when the fold change is below 1, as the proteins were predominantly present in the control GFP samples. The unshaded, white area of the plot represents a positive $log_2$ (fold change), which occurs when the fold change is above 1, as the proteins were predominantly present in the GFP-talin rod samples. The proteins identified with a significant p-value of less than 0.05 are highlighted in red and those with both a significant p-value and a positive $log_2$ (fold change) are identified in Tables 5.1 and 5.2, highlighted in blue. Key proteins identified are labelled.*

***Table 5.1: Proteins identified in the finalised murine neuronal RB volcano plot (Figure 5.3 A) with a fold change above 1 and a confidence score higher than 125 or a significant p-value.***

*The proteins with a significant p-value and fold change above 1 are highlighted in blue. The proteins with a confidence score higher than 125 and a fold change above 1 are highlighted in yellow. The proteins with a significant p-value, fold change above 1, and a confidence score higher than 125 are highlighted in green. The proteins in bold and underlined are present in both the GFP-talin rod beads (RB) and elution (RE) tables (Tables 5.1 and 5.2). *Proteins are also identified in the previous murine neuronal extract MS proteomics analysis and are displayed in Table 4.2.*

| Protein | Uniprot ID | Confidence | Fold change | P-value |
|---|---|---|---|---|
| **Talin 1 Fragment** | **F6S1V7** | **185** | **451.5** | **0.0150** |
| **Talin 1 (Fragment)** | **F6SX70** | **176** | **389.7** | **0.0169** |
| **HECT domain and RLD 3** | **A6H6S0** | **27** | **306.2** | **0.0099** |
| **Zinc finger protein 644** | E9QA22 | 65 | 167.2 | 0.0015 |
| **E3 ubiquitin-protein ligase BRE1A** | **Q5DTM8** | **17** | **100.5** | **0.0021** |
| **Microtubule-associated protein** | **A0A668KLC6** | **107** | **49.0** | **0.0190** |
| **Ogdhl protein** | B2RXT3 | 90 | 35.2 | 0.0044 |
| **Synaptojanin-1** | **Q8CHC4** | **95** | **14.0** | **0.0101** |
| **Ankyrin-3** | **G5E8K5** | **108** | **12.4** | **0.0061** |
| **ATP-dependent 6-phosphofrucrokinase_ muscle type** | **P47857** | **54** | **9.1** | **0.0028** |
| **Hexokinase** | **G3UVV4** | **34** | **8.9** | **0.0173** |
| **E3 ubiquitin-protein ligase RNF123** | Q5XPI3 | 21 | 8.7 | 0.0253 |
| **NCK-associated protein 5** | **E9QAE1** | **40** | **8.5** | **10.9** |
| **Dynamin- 1** | **P39053** | **236** | **8.2** | **0.0160** |
| **cAMP-dependent protein kinase catalytic subunit beta** | **P68181** | **17** | **8.0** | **0.0221** |
| **Phospholipid-transporting ATPase** | A0A286YC | 18 | 7.9 | 0.0046 |
| **Heat shock protein 75 kDa, mitochondrial** | **Q9CQN1** | **29** | **5.5** | **0.0007** |
| **Katanin p60 ATPase-containing subunit A like 1** | **Q8K0T4** | **29** | **4.4** | **0.0035** |
| **Uncharacterised protein C9orf131 homolog** | **Q3V0E1** | **21** | **128.6** | **3.07 x$10^{-6}$** |
| **ELKS/Rab6-interacting/CAST family member 1** | F8VPM7 | 52 | 4.7 | 0.0179 |
| **E3 ubiquitin-protein ligase HECW1** | **Q8K4P8** | **20** | **4.6** | **0.0253** |
| **Brain-specific angiogenesis inhibitor 1-associated protein 2** | **Q8BKX1** | **59** | **4.5** | **0.0255** |
| **Plasma membrane calcium-transporting ATPase 1** | G5E829 | 69 | 3.5 | 0.0040 |
| **Inactive tyrosine-protein kinase PEAK1** | **Q69Z38** | **20** | **3.5** | **0.0235** |
| **Disks large homolog 2** | A0A338P6J0 | 69 | 3.0 | 0.0082 |
| **Guanine nucleotide-binding protein G (o) subunit alpha** | **P18872** | **144** | **2.8** | **0.0079** |
| **Conserved oligomeric Golgi complex subunit 6** | A0A0R4J0L5 | 15 | 2.7 | 0.0432 |
| **Alpha-actinin-4** | A0A1L1SV25 | 67 | 2.0 | 0.0156 |

| | | | | |
|---|---|---|---|---|
| **PH and SEC7 domain-containing protein 3** | **A0A1DR5MH7** | **32** | **1.9** | **0.0232** |
| **Alpha-adducin** | Q9QYC0 | 95 | 1.8 | 0.0018 |
| **Glutamine synthetase** | **P15105** | **83** | **1.7** | **0.0384** |
| **Myosin 10** | Q61879 | 319 | 1.6 | 0.0411 |
| **ATP-dependent 6-phosphofructokinase** | Q8C605 | 48 | 1.6 | 0.0022 |
| **Sodium/potassium-transporting ATPase subunit alpha-3** | **Q6PIC6** | **340** | **1.6** | **0.0130** |
| **Microtubule-associated protein 6** | Q7TSJ2 | 133 | 1.4 | 0.0073 |
| **Multiple PDZ domain protein** | D3YUX2 | 38 | 1.4 | 0.0090 |
| **Tubulin beta-4A chain** | **Q9D6F9** | **310** | **1.3** | **0.0107** |
| **Thioredoxin-dependent peroxiredoxin** | G3UZJ445 | 45 | 1.4 | 0.0167 |
| **Phosphatidylinositol 4-kinase alpha** | A0A140T8I9 | 31 | 1.4 | 0.0209 |
| **Centrosomal protein of 170 kDa** | Q6A065 | 67 | 1.5 | 0.0326 |
| **ATP synthase subunit d mitochondrial** | Q9DCX2 | 24 | 1.4 | 0.0395 |
| **Clathrin heavy chain 1*** | **Q68FD5** | **1007** | **1.5** | **0.1966** |
| **Tubulin beta-5 chain** | P99024 | 417 | 1.0 | 0.8178 |
| **Dihydropyrimidinase-related protein 2** | **O08553** | **395** | **1.3** | **0.1305** |
| **AP-2 complex subunit alpha 1** | **P17426** | **310** | **1.2** | **0.3273** |
| **AP-2 complex subunit alpha-2** | P17427 | 301 | 10.3 | 0.3886 |
| **Unconventional myosin-Va*** | **D3YZ62** | **291** | **15.8** | **0.0020** |
| **Tubulin alpha chain fragment** | A0A0A0MQM5 | 247 | 1.1 | 0.7019 |
| **Sodium/potassium-transporting ATPase subunit alpha 1** | **Q8VDN2** | **231** | **1.2** | **0.1066** |
| **ADP/ATP translocase 1** | P48962 | 231 | 1.4 | 0.2374 |
| **Tubulin beta-6 chain** | Q922F4 | 203 | 1.1 | 0.1130 |
| **2’_3’-cyclic-nucleotide 3’ phosphodiesterase** | P16330 | 198 | 1.1 | 0.4657 |
| **Src kinase signalling inhibitor 1** | Q9QWI6 | 189 | 1.1 | 0.7883 |
| **MICOS complex subunit Mic 60** | Q8CAQ8 | 179 | 1.2 | 0.1853 |
| **Alpha-internexin** | **P46660** | **197** | **1.9** | **0.0349** |
| **AP-2 complex subunit mu** | **P84091** | **181** | **2.2** | **0.06647** |
| **Vesicle-fusing ATPase** | P46460 | 170 | 4.5 | 0.2252 |
| **Creatine kinase U-type _ mitochondrial** | **P30275** | **173** | **1.4** | **0.1086** |
| **2-oxoglutarate dehydrogenase mitochondrial** | Q60597 | 161 | 1.3 | 0.3165 |
| **ATP synthase subunit O mitochondrial** | Q9DB20 | 131 | 1.3 | 0.1913 |
| **Synaptogamin-1** | P46096 | 128 | 1.4 | 0.1424 |
| **Contactin-2** | P12960 | 149 | 1.3 | 0.1134 |
| **Disks large homolog 4** | A0A338P6E5 | 149 | 1.8 | 0.1262 |
| **Calcium-binding mitochondrial carrier protein Aralar 1** | Q8BH59 | 266 | 1.0 | 0.9143 |

***Table 5.2: Proteins identified in the finalised murine neuronal RE volcano plot (Figure 5.3 B) with a fold change above 1 and a confidence score higher than 125 or a significant p-value.***

*The proteins with a significant p-value and fold change above 1 are highlighted in blue. The proteins with a confidence score higher than 125 and a fold change above 1 are highlighted in yellow. The proteins with a significant p-value, fold change above 1, and a confidence score higher than 125 are highlighted in green. The proteins in bold and underlined are present in both the GFP-talin rod beads (RB) and elution (RE) tables (Tables 5.1 and 5.2). *Proteins are also identified in the previous murine neuronal extract MS proteomics analysis and are displayed in Table 4.2.*

| Protein | Uniprot ID | Confidence | Fold-change | P-value |
|---|---|---|---|---|
| **Microtubule-associated protein** | **A0A668KLC6** | **107** | **116.8** | **0.0200** |
| **Serine/threonine- protein kinase MRCK alpha** | Q3UU96 | 28 | 52.8 | 0.0362 |
| **E3 ubiquitin-protein ligase BRE1A** | **Q5DTM8** | **17** | **54.0** | **2.45 X10$^{-5}$** |
| **cAMP-dependent protein kinase catalytic subunit beta** | **P68181** | **17.3** | **39.0** | **0.0117** |
| **Synaptojanin-1** | **Q8CHC4** | **95** | **31.6** | **0.0208** |
| **Guanine nucleotide-binding protein G (i) subunit alpha-2** | P08752 | 57 | 24.4 | 0.0004 |
| **Uncharacterised protein C9orf131 homolog** | **Q3V0E1** | **21** | **21.4** | **0.0036** |
| **Ankyrin-3** | **G5E8K5** | **108** | **27.5** | **0.0140** |
| **Liprin-beta-1** | Q8C8U0 | 27 | 22.9 | 0.0335 |
| **HECT domain and RLD 3** | **A6H6S0** | **27** | **20.0** | **0.0243** |
| **ATP synthase F (0) complex subunit B1_ mitochondrial** | Q9CQQ7 | 66 | 17.8 | 0.0134 |
| **ATP-dependent 6-phosphofructase_muscle type** | **P47857** | **54** | **16.4** | **0.0101** |
| **Dynamin 1** | **P39053** | **236** | **16.3** | **0.0078** |
| **Heat shock protein 75 kDa, mitochondrial** | **Q9CQN1** | **29** | **14.4** | **0.0102** |
| **AMP deaminase** | A0A1L1SRX2 | 37 | 10.2 | 0.0036 |
| **E3 ubiquitin-protein ligase HECW1** | **Q8K4P8** | **20** | **9.6** | **0.0174** |
| **Brain-specific angiogenesis inhibitor 1-associated protein 2** | **Q8BKX1** | **59** | **10.6** | **0.0480** |
| **NCK-associated protein 5** | **E9QAE1** | **40** | **10.9** | **0.0170** |
| **SH3 and multiple ankyrin repeat domains protein 3** | Q4ACU6 | 57 | 13.8 | 0.0151 |
| **Tubulin beta-1 chain** | A2AQ07 | 58 | 8.6 | 0.0347 |
| **Hexokinase** | **G3UVV4** | **34** | **8.3** | **0.0083** |
| **Non-specific serine/threonine protein kinase** | E9QMP6 | 20 | 7.8 | 0.0064 |
| **Protein ELYS** | Q8CJF7 | 86 | 7.0 | 0.0204 |
| **Transcriptional activator protein Pur-alpha** | P42669 | 79 | 7.1 | 0.0266 |
| **PH and SEC7 domain-containing protein 3** | **A0A1D5RMH7** | **32** | **4.9** | **0.0096** |

| | | | | |
|---|---|---|---|---|
| **Exostosin-2** | E9Q1M5 | 15 | 4.6 | 0.0139 |
| **Girdin** | Q5SNZ0 | 40 | 3.6 | 0.0023 |
| **Inactive tyrosine-protein kinase PEAK1** | **Q69Z38** | **20** | **3.7** | **0.0056** |
| **Katanin p60 ATPase-containing subunit A-like 1** | **Q8K0T4** | **29** | **3.3** | **0.0329** |
| **Tensin 1 (Fragment)** | A0A087WQ94 | 34 | 2.9 | 0.0313 |
| **Alpha-internexin** | **P46660** | **197** | **2.8** | **0.0270** |
| **Glutamine synthetase** | **P15105** | **83** | **2.2** | **0.0094** |
| **Kinesin-like protein KIF21B** | Q9QXL1 | 20 | 2.1 | 0.0150 |
| **Myelin basic protein** | P04370 | 48 | 2.0 | 0.0360 |
| **WD repeat-containing protein 19** | Q3UGF1 | 24 | 1.7 | 0.0395 |
| **Neural cell adhesion molecule 1** | P13595 | 24 | 1.4 | 0.0395 |
| **Sodium/potassium-transporting ATPase subunit alpha-3** | **Q6PIC6** | **340** | **1.2** | **0.0293** |
| **Clathrin heavy chain 1*** | **Q68FD5** | **1007** | **2.5** | **0.1063** |
| **Dihydropyrimidinase-related protein 2** | **O08553** | **395** | **1.4** | **0.1653** |
| **AP-2 complex subunit alpha-1** | **P17426** | **310** | **1.1** | **0.6431** |
| **Tubulin beta-4A chain** | **Q9D6F9** | **310** | **1.4** | **0.4844** |
| **AP-2 complex subunit beta** | Q9DBG3 | 292 | 1.6 | 0.2818 |
| **Unconventional myosin-Va*** | **D3YZ62** | **291** | **24.5** | **0.0644** |
| **Sodium/potassium-transporting ATPase subunit alpha-1** | **Q6PIC6** | **340** | **1.2** | **0.0293** |
| **Talin 1 Fragment** | **F6S1V7** | **185** | **24.8** | **0.0128** |
| **Talin 1 Fragment** | **F6SX70** | **176** | **23.7** | **0.0218** |
| **AP-2 complex subunit mu** | **P84091** | **181** | **2.3** | **0.2645** |
| **Creatine kinase U-type mitochondrial** | **P30275** | **173** | **1.4** | **0.3585** |
| **Guanine nucleotide-binding protein G (o) subunit alpha** | **P18872** | **144** | **4.3** | **0.0319** |
| **Contactin-1** | P12960 | 149 | 1.0 | 0.9215 |

# 6 Side Project: Investigating Vinculin Interactions

## 6.1 Validating the 'talin non-binding' vinculin mutant A50I

### 6.1.1 Theory Overview

The vinculin mutant Vcl$^{A50I}$ is considered a 'talin non-binding' mutant as the alanine residue at position 50, considered to be vital for talin binding, is substituted for isoleucine (Mandal et al., 2021). Vinculin-dependant axon growth seemed to remain unchanged between GFP-Vcl-FL$^{A50I}$ and Vcl-FL when both were expressed in neocortical neurons. Therefore, as axon growth was not affected by a vinculin mutant that supposedly cannot bind to talin, talin was deemed unnecessary in vinculin-dependant axon growth. These results downplay the role of talin in focal adhesions and motility; therefore, further research into the A50I mutant was conducted.

### 6.1.2 Gel filtration results indicate that both VD1 and VD1$^{A50I}$ have a similar molecular weight

After growing, expressing, and purifying both VD1 and VD1$^{A50I}$, samples of each were run in gel filtration chromatography at a concentration of 126 µM for VD1 and 149 µM for VD1$^{A50I}$ (Figure 6.1). The concentration of VD1$^{A50I}$ was slightly higher, which is reflected by the marginally higher refractive index peak of VD1$^{A50I}$. Nevertheless, the gel filtration data for both VD1 and VD1$^{A50I}$ demonstrates the similarity of molecular weights between the two constructs, as both proteins elute predominately at ~15 mL, with the highest concentration of VD1 and VD1$^{A50I}$ eluting at 14.87 mL and 14.98 mL, respectively. There is a slight peak observed at 12.8 mL, for both VD1 and VD1$^{A50I}$; however, it is much larger for VD1 indicating that dimerization of the protein occurs more easily for VD1 than VD1$^{A50I}$.

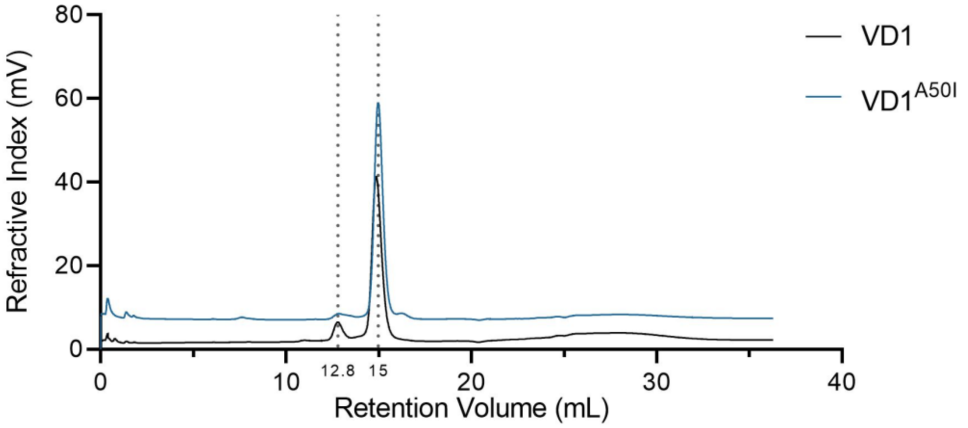

***Figure 6.1: Gel filtration results of VD1 (126 µM) and VD1$^{A50I}$ (149 µM) indicate a similarity in molecular weight between the two constructs.***
*The black line represents VD1, whilst the blue line represents VD1$^{A50I}$.*

### 6.1.3 Circular dichroism results suggest a similarity between VD1 and VD1$^{A50I}$ in thermal stability and secondary structure

To visualise the secondary structures present in both proteins, a far UV CD spectrum was performed on VD1 at 21.2 µM and VD1$^{A50I}$ at 22.4 µM, from 204-260 nm at 20°C. This was repeated at 90°C to visualise the loss of secondary structure, which occurs at elevated temperatures. From the UV spectra conducted at 20°C, a 'double dip', indicative of alpha-helical structures, is present in both proteins (Figure 6.2 A). However, instead of a peak at 220 nm, which is characteristic of alpha-helical structures, there is a trough, suggesting the additional presence of beta-pleated sheets in both VD1 and VD1$^{A50I}$. As expected, the UV spectra conducted at 90°C shows a very linear pattern compared to the UV spectra at 20°C, indicating a loss of structure for both proteins.

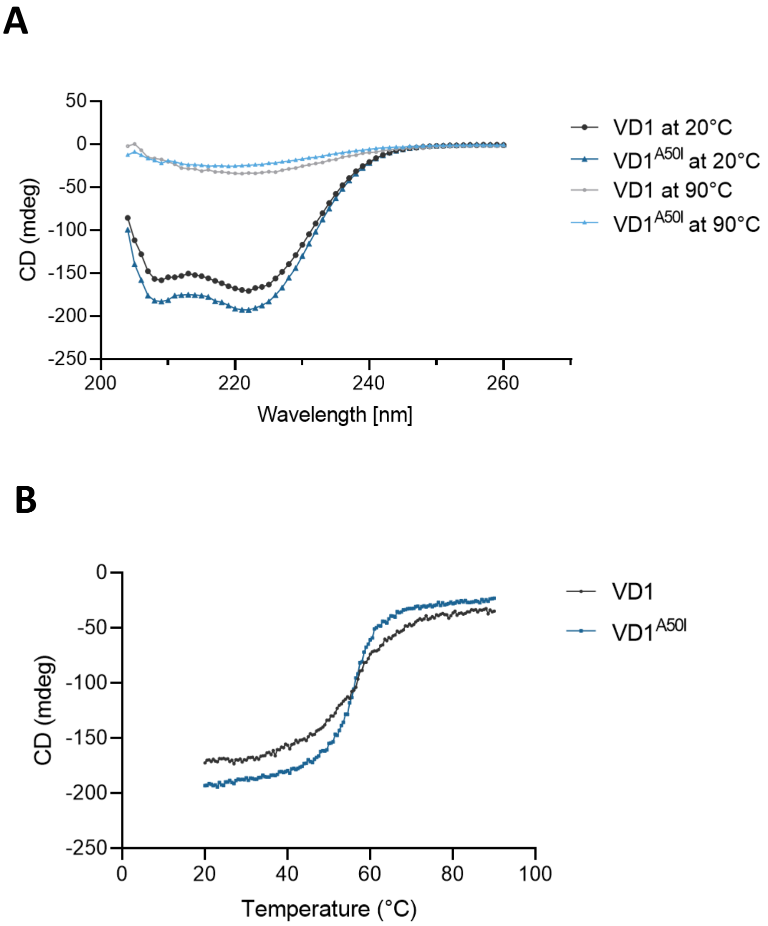

***Figure 6.2: VD1 and VD1$^{A50I}$ CD results imply a similarity in secondary structure and thermal stability between the two constructs.***
***(A)*** *Comparison of VD1 and VD1$^{A50I}$ UV spectra. Black and dark blue points represent VD1 and VD1$^{A50I}$ at 20°C, whilst grey and light blue represent VD1 and VD1$^{A50I}$ at 90°C, respectively.* ***(B)*** *Comparison of VD1 and VD1$^{A50I}$ melting curves. The black points represent VD1, whilst the blue points represent VD1$^{A50I}$.*

The thermal stability of both VD1 and VD1$^{A50I}$ appears to be extremely similar, and from the melting curves, the $T_m$ values for VD1 and VD1$^{A50I}$ were 54°C and 56°C, respectively (Figure 6.2 B). The similarity between the UV spectra and thermal stability for both VD1 and VD1$^{A50I}$ demonstrates that the biophysical properties of the proteins are very similar, despite the mutation.

### 6.1.4 Fluorescent polarisation assays demonstrate that VD1$^{A50I}$ can bind to vinculin binding sites in talin

As VD1$^{A50I}$ is considered a 'talin non-binding' mutant, fluorescence polarisation assays were conducted to confirm this. The binding of VD1 and VD1$^{A50I}$ with three known vinculin binding sites in talin, talin R2 helix 6 (668-687), R8 helix 33 (1525-1544), and R11 helix 50 (2080-2099), was investigated through fluorescence polarisation assays. Contrary to the belief that the A50I mutation completely prevents vinculin-talin binding, it seems that the mutation only reduces the ability of vinculin to bind to certain vinculin binding sites in talin.

Out of the three vinculin binding sites tested, VD1$^{A50I}$ binds to talin helix 6 and helix 50 with a similar affinity to the VD1 wildtype (Figure 6.3 A and C). For talin helix 6 and helix 50, both the wildtype VD1 and VD1$^{A50I}$ reach a fluorescence polarisation value of ~250 at exceptionally low concentrations, and both proteins have Kd values under 0.5 µM for helix 6 and 0.2 µM for helix 50, suggesting that the A50I mutation did not perturb talin-vinculin binding at these vinculin binding sites.

However, there is a clear difference in binding between the wildtype VD1 and VD1$^{A50I}$ for the fluorescence polarisation assay with talin helix 33, as demonstrated in Figure 6.3 B. This is seen most evidently by the Kd values for the binding of helix 50 and VD1/VD1$^{A50I}$; whilst the wildtype VD1 has a KD of 0.04 µM, VD1$^{A50I}$ has a Kd of 82.41 µM. This clearly indicates that although the A50I mutation does not affect vinculin binding to talin helix 6 and 50, it does inhibit binding to helix 33.

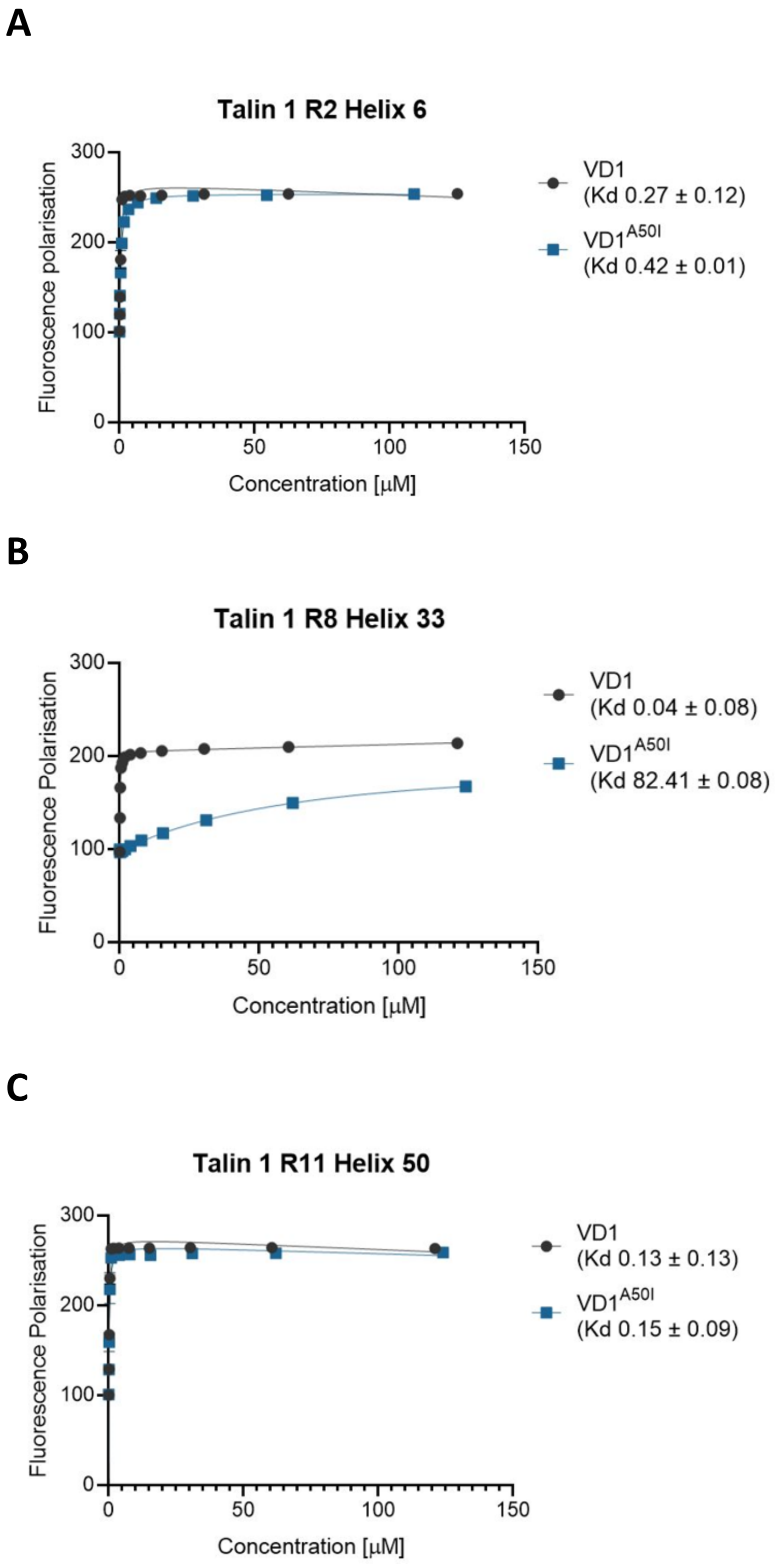

***Figure 6.3: Fluorescence polarisation assays indicate that the vinculin A50I mutation only inhibits vinculin-talin binding at certain vinculin binding sites.***

*Binding of wildtype VD1 and VD1$^{A50I}$ to fluorescein labelled talin 1* ***(A)*** *R2 helix 6,* ***(B)*** *R8 helix 33, and* ***(C)*** *R11 helix 50. Experiments were performed in triplicate. The dissociation constants in µM +/- SE are shown in the legend. Error bars are too small for visualisation.*

### 6.1.5 Crystallography trials for VD1$^{A50I}$ and talin R2 helix 6

Crystallography screening for a complex of VD1$^{A50I}$ and talin R2 helix 6 was conducted. The initial screening for VD1$^{A50I}$ and talin R2 helix 6 proved highly successful, and multiple buffer conditions seemed to produce clear crystals (Figure 6.4).

Out of the four conditions where crystals were best visualised (JCSG+ box 1 buffer 2, box 2 buffer 39, 42, and 44) (Figure 6.4 A-H), three were optimised (box 2 buffer 39, 42, and 44) (Figure 6.4 C-H). Visible crystals were observed in multiple wells of the optimisation plates, with the most abundant crystals present in 0.1 M BIS-Tris, pH 5.0, 20 % w/v PEG 3350 (Figure 6.5 A and B), 0.1 M BIS-Tris, pH 6.5, 25 % w/v PEG 3350 (Figure 6.5 C and D), and 0. 1 M sodium chloride, 0.1 M BIS-Tris, pH 6.0, 20 % w/v PEG 3350 (Figure 6.5 E and F). Whilst there were crystals visible in the optimisation plates for buffers 39 and 44, optimisation of buffer 42 proved unsuccessful. Nevertheless, although many visible crystals were produced by the optimisation plates for buffers 39 and 44, the crystals created by the initial crystallisation screening plates seemed better defined and were easier to visualise; therefore, further optimisation is required to achieve crystals large enough for x-ray crystallography.

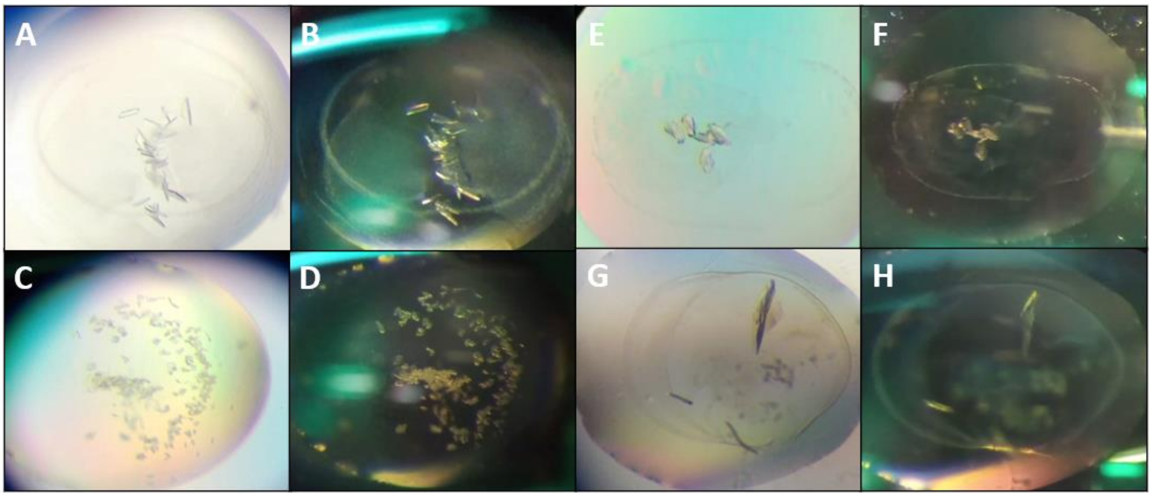

***Figure 6.4: Crystals present in the initial crystallography screening for VD1$^{A50I}$ and talin R2 helix 6.***
*VD1$^{A50I}$ and talin R2 helix 6 crystals formed in JCSG+ Box 1 condition 2 (0.1 M sodium citrate pH 5.5, 20% w/v PEG 3000)* ***(A)*** *under brightfield illumination and* ***(B)*** *under darkfield illumination. VD1$^{A50I}$ and talin R2 helix 6 crystals formed in JCSG+ Box 2 condition 39 (0.1 M BIS-Tris, pH 5.5, 25% w/v PEG 3350) under* ***(C)*** *brightfield illumination and* ***(D)*** *under darkfield illumination. VD1$^{A50I}$ and talin R2 helix 6 crystals formed in JCSG+ Box 2 condition 42 (0.1 M ammonium acetate, 0.1 M BIS-Tris, pH 5.5, 17% w/v PEG 10,000)* ***(E)*** *under brightfield illumination and* ***(F)*** *under darkfield illumination. VD1$^{A50I}$ and talin R2 helix 6 crystals formed in JCSG+ Box 2 condition 44 (0.2 M sodium chloride, 0.1 M BIS-Tris, pH 5.5, 25% w/v PEG 3350) under* ***(G)*** *brightfield illumination and* ***(H)*** *under darkfield illumination.*

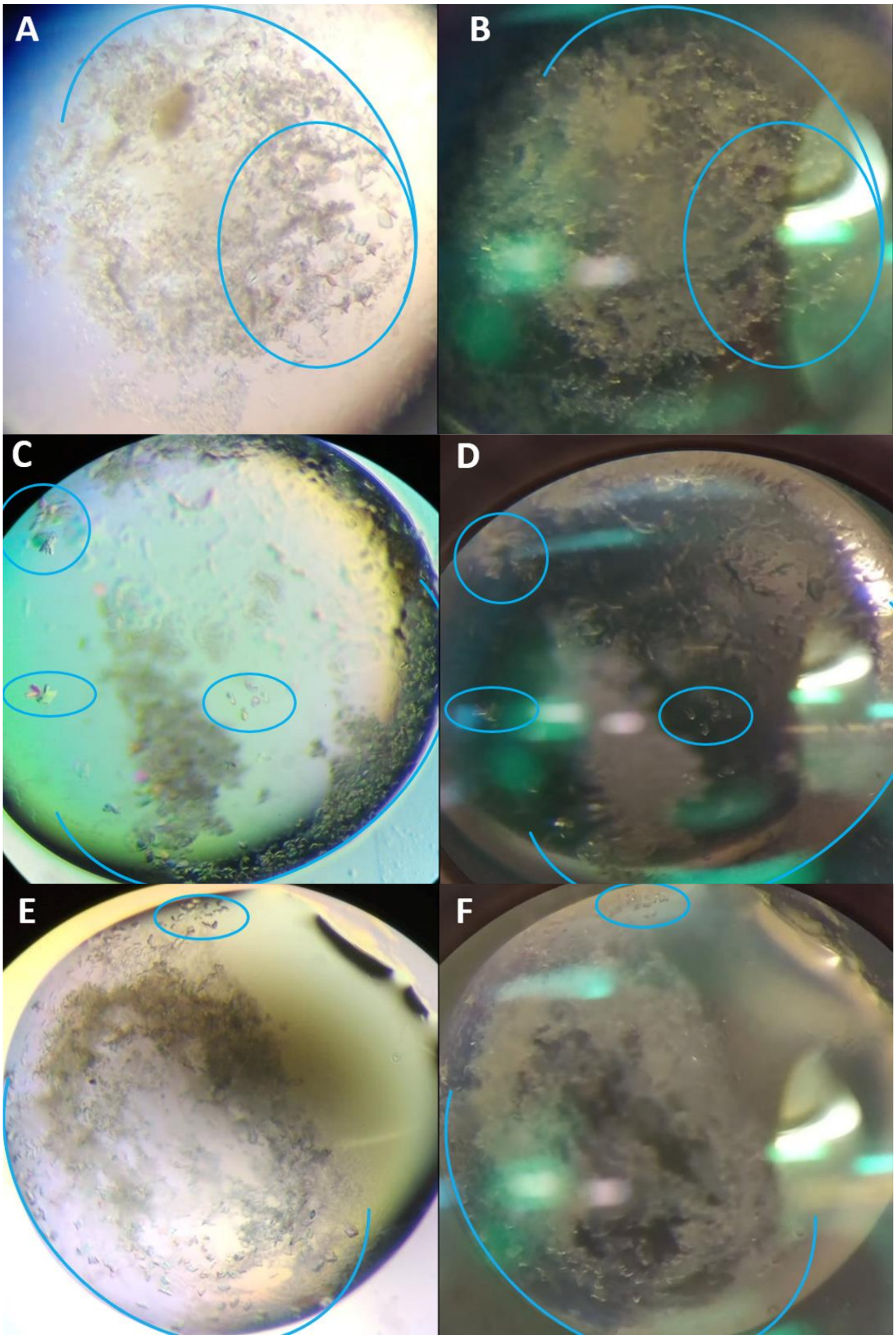

***Figure 6.5: Crystals visualised in the optimisation crystallography screening for VD1$^{A50I}$ and talin R2 helix 6**. VD1$^{A50I}$ and talin R2 helix 6 crystals formed in 0.1 M BIS-Tris, pH 5.0, 20% w/v PEG 3350 **(A)** under brightfield illumination and **(B)** under darkfield illumination. VD1$^{A50I}$ and talin R2 helix 6 crystals formed in 0.1 M BIS-Tris, pH 6.5, 25% w/v PEG 3350 **(C)** under brightfield illumination and **(D)** under darkfield illumination. VD1$^{A50I}$ and talin R2 helix 6 crystals formed in 0.1 M sodium chloride, 0.1 M BIS-Tris, pH 6.0, 20% w/v PEG 3350 under **(E)** brightfield illumination and **(F)** under darkfield illumination. Blue annotations are used to indicate the presence of crystals.*

## 6.2 Testing the theorised binding of VD1 and vinexin (276-299)

### 6.2.1 Theory Overview

Talin, and other identified vinculin binding proteins, have been known to interact with vinculin through their amphipathic helical regions, which then stimulates the conformational change in vinculin to its active open state. Identification of two amphipathic helical regions in α vinexin, through the programme PORTER, prompted the identification of how α vinexin induces the conformational change in vinculin (Hino et al., 2019; Pollastri & McLysaght, 2005). From the work of Xuyao Priscilla Liu, National University of Singapore, another potential vinculin binding domain in vinexin was identified through the visualisation of another amphipathic alpha-helix in vinexin by AlphaFold. This amphipathic alpha-helix was present in vinexin (276-299), and alignment of vinexin (276-299) in PyMOL with VD1b seemed to strongly infer the likelihood of binding. This could indicate that an amphipathic helix was missed when PORTER was used to predict vinexin secondary structure and therefore, was not investigated during the determination of how α vinexin induces a substrate stiffness-dependent conformational change in vinculin (Hino et al., 2019).

### 6.2.2 Fluorescence polarisation assays demonstrate that vinexin (276-299) does not bind to VD1

To confirm the predicted binding of vinexin 276-299 and VD1, a synthetic peptide of the potential binding domain 276-299 was created and coupled to fluorescein. Direct binding of vinexin (276-299) to VD1 was investigated through fluorescence polarisation assays, and talin R11 helix 50 was used as a positive control. Unfortunately, contrary to the prediction, no binding was observed between vinexin and VD1 (Figure 6.6). Whilst talin helix 50 bound to VD1 with high affinity, reaching a maximum fluorescence polarisation of 254 with a Kd of 0.47 µM, vinexin did not bind to VD1, and the fluorescence polarisation value remained at ~100, even when the concentration of VD1 increased above 100 µM.

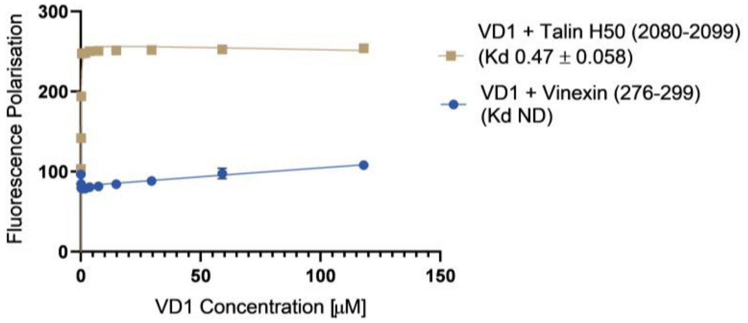

***Figure 6.6: Binding of vinexin to VD1 was not observed through fluorescence polarisation assays.***
*Binding of fluorescein-labelled vinexin (276-299) to VD1 was measured through fluorescence polarisation assays, whilst binding of VD1 and fluorescein-labelled talin R11 helix 50 (H50) (2080-2099) was used as a positive control. As expected, talin helix 50 bound to VD1 with high affinity, however vinexin did not. Experiments were performed in triplicate. The dissociation constants in µM +/- SE are shown in the legend. Error bars are too small for visualisation. ND = not determined.*

# Discussion

The fundamental aim of this project was to validate the concepts presented in the MeshCODE theory by uncovering a link between talin-mediated mechanical signalling and neuronal activity, through the identification of neuronal protein-talin interactions (Goult, 2021). A bioinformatics approach was explored alongside the development of an innovative method to identify novel talin binders in a variety of cell extracts, which resulted in the detection of many potential neuronal talin binders.

# 7 Bioinformatics Pipeline

## 7.1 Identification of talin-binding I/LD motifs

Following the assumption that talin plays a greater role than previously anticipated in synaptic vesicle activity, a bioinformatics pipeline and scoring system was developed to identify potential talin-binding ligands, through the analysis of I/LD motifs in synaptic vesicle-associated proteins identified by Takamori et al., 2006. FP assays were conducted to characterise the binding between talin rod domains and three promising I/LD motifs from SNAP 25 and snapin (Figures 3.5 and 3.6). Whilst direct binding was not observed between the motifs and R4-8, R7-8, R9-10, R11, and R9-12, a clear distinction of binding was seen, particularly for R9-10, between snapin 55-78, which exhibited no binding, and SNAP 25 or snapin 71-97, which both demonstrated an increase in FP similar to that of RIAM TBS1 (Figures 3.5 and 3.6). Although RIAM TBS1 is a talin-binding site with the ability to bind to R2, R3, R8, and R11, it does not bind to R9-10; however, a slight increase in FP was observed as the concentration of R9/10 increased (Figure 3.6 A). A similar increase in FP was seen in the FP assays involving SNAP 25 and snapin 71-97 for multiple domains trialled, which may indicate that whilst these motifs do not bind to the rod domains tested, they may bind to others, as RIAM TBS1 does.

The difference in bioinformatics scoring for each I/LD motif, demonstrated in Table 3.1, was reflected in the talin binding observed (Figures 3.5 and 3.6). The I/LD motif in snapin 55-78 achieved a score of 4 and clearly demonstrated an inability to bind to all the talin rod domains tested. However, a slight increase in FP was observed between the talin rod domains and the I/LD motifs present in SNAP 25 and snapin 71-97, which both achieved a score of 5 (Figures 3.5 and 3.6). Therefore, this indicates that the scoring system developed is effective at identifying the most promising potential talin-binding I/LD motifs in proteins.

## 7.2 SNAP 25 and Snapin

If talin binding to either snapin or SNAP 25 is confirmed, it may imply that the synaptic functions of both proteins are facilitated by talin binding, subsequently providing substantial evidence to support the MeshCODE theory. Synaptic vesicle exocytosis can only occur if sufficient energy is provided to overcome the membrane tension and perturb the electrostatic attraction/hydration repulsion preventing membrane fusion (Han et al., 2017; Sauvola & Littleton, 2021). Following an action potential, $Ca^{2+}$ influx promotes interaction of the vesicle-associated (v-) SNARE, synaptobrevin, with nerve terminal-associated (t-) SNAREs, SNAP 25 and syntaxin, in the opposing presynaptic and vesicle membranes (Han et al., 2017; Sauvola & Littleton, 2021). This results in the formation of an energetically favourable, structured, coiled-coil SNARE complex, via a zippering mechanism to permit vesicle exocytosis and neurotransmitter release (Figure 7.1) (Han et al., 2017; Sauvola & Littleton, 2021). The SNARE complex has also been implicated in synaptic vesicle endocytosis (SVE), as each core component has been found to interact with SVE-associated proteins (Antonucci et al., 2016). Furthermore, the t-SNARE has demonstrated the ability to modify synaptic plasticity through receptor trafficking and dendritic spine morphogenesis in postsynaptic neurons (Antonucci et al., 2016). Justifiably, the absence of SNAP 25 fully inhibits neuronal transmission, whilst SNAP 25 defects have been associated with multiple synaptopathies, such as schizophrenia and bipolar disorder (Antonucci et al., 2016).

Vesicle docking describes the process whereby vesicles line up at fusion sites, prior to vesicle exocytosis, whilst the formation of the SNARE complex primes the vesicle for imminent fusion, by promoting apposition of the vesicle and presynaptic membrane (S. C. Yu et al., 2013). Snapin has been found to facilitate vesicle priming by stabilising the SNARE complex through SNAP 25 interactions, with snapin-homolog mutations in *C. elegans* populations shown to reduce the optimal state of vesicular release and the number of docked, primed vesicles (Figure 7.1) (S. C. Yu et al., 2013). Cortical neurons from snapin mutant mice demonstrate a further reduction in total vesicle number and desynchronisation of vesicle fusion, through miniature excitatory postsynaptic current (EPSC) frequency and peak alteration, promoting a severe effect on spike-dependent plasticity and subsequent neuronal function (Pan et al., 2009). The calcium sensor, synaptotagmin, has significant roles in vesicle exocytosis, particularly during priming, by interacting with both membrane lipids and the SNARE complex to maintain vesicle hemifusion, prior to the promotion of neurotransmitter release via $Ca^{2+}$ influx (Dickman et al., 2012; Pan et al., 2009). Association between the synaptotagmin-SNARE complex and snapin dimers stabilises the complex throughout vesicle priming, enabling effective, precise, synchronous vesicle exocytosis, with the introduction of snapin mutants in mice populations shown to markedly perturb this interaction (Pan et al., 2009). Following the discovery of an interaction with dysbindin, a protein severely implicated in schizophrenia-susceptibility, snapin has also been considered to act in conjunction with dysbindin, and possibly SNAP 25, to mediate synaptic homeostatic plasticity (Dickman et al., 2012).

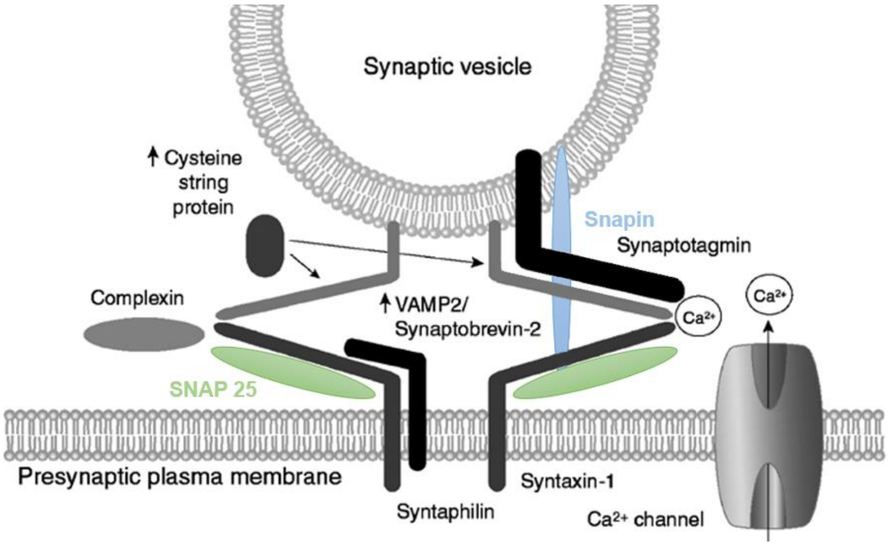

***Figure 7.1: Assembly of the SNARE complex and associated proteins during vesicle fusion.***
*To promote synaptic vesicle exocytosis, the SNARE complex is formed through the interaction of many synaptic proteins. SNAP 25 and snapin are represented in green and blue, respectively. Figure adapted from (Lesch & Schmitt, 2002).*

## 7.3 Future work

The talin R8 domain is considered a binding nexus for proteins with I/LD motifs, i.e. RIAM or DLC1, and is a component of the R4-R8 actin-binding site, ABS2 (Goult et al., 2018; G. Li et al., 2011; Yao et al., 2016). This is likely due to the unique position it holds in the talin rod, as the insertion of R8 into R7 shields R8 slightly from the direct linear force pathway, enabling R8 to remain folded upon greater force exertion (Goult et al., 2018; Yao et al., 2016). Although direct binding of R8 with the I/LD motifs of snapin or SNAP 25 was not observed, it is not the only domain that has been shown to bind to I/LD motifs. The I/LD motif in RIAM is able to bind to R2, R3, R8, and R11; therefore, as binding to R2R3 was not explored, it would be worth determining, as well as the remaining rod domains, to conclusively establish whether the I/LD motifs in SNAP 25 and snapin 71-97 bind to the talin rod (Goult et al., 2013). Additionally, a future direction could include investigating the binding of full/intact domains or full-length SNAP 25 and snapin to the talin rod using nuclear magnetic resonance titration.

Although ~150 synaptic vesicle (SV) proteins were analysed for I/LD binding motifs, many additional proteins are listed in Takamori et al., 2006; therefore, there are others that have not yet been analysed and may potentially bind to talin. Furthermore, although the talin I/LD binding motif is the most characterised, it is by far not the only talin-binding motif identified in talin-binding proteins, i.e. the NPxY/F talin-binding motif in integrin. Therefore, even though binding to talin through I/LD motifs can be determined using this bioinformatics pipeline, it is simply one possible mechanism of talin binding, thus, binding to talin through alternative mechanisms is a likely possibility and cannot be overlooked.

# 8 Identification of novel talin binders in murine neuronal extract

## 8.1 The talin 'fishing' rod experiment

Through extensive optimisation, a novel method to identify new talin binders in a range of cell extracts was successfully developed. As the role of talin has predominantly been investigated in cell lines and fibroblasts, this novel method allows the investigation of talin function outside of these limited cell types.

The initial theorised method involved incubating talin-bound beads in cell extract and utilising LC-MS/MS proteomics to identify the presence of additional proteins bound to talin (Figure 4.1). GSH agarose was used primarily and after optimisation, three pGEX stretch talin constructs (R1-3, R7-9, and R1-13) successfully bound to the GSH beads (Figures 4.2 and 4.3). GST pulldowns were conducted with known talin binders, VD1 and a cerulean-tagged KN motif from KANK1, to determine whether this method was effective in identifying talin-binding ligands. However, the pulldown results varied significantly and were not repeatable; therefore, GFP immunoprecipitation was used as an alternative method.

Upon binding a GFP-talin rod construct to GFP-Trap resin, additional bands were visualised on the SDS-gel. These were confirmed as talin fragments, through anti-His and GFP immunoblotting, indicating that incomplete translation or degradation of talin occurred (Figure 4.7). Nevertheless, the successful binding of GFP and GFP-talin rod to GFP-Trap beads prompted the first trial of a GFP-Trap pulldown in CaSki cell lysate (Figure 4.9 A). To validate whether GFP immunoprecipitation could be used to identify talin binders in cell extract, immunoblots of two known talin binders, KANK2 and CDK1, were performed (Figure 4.9 B). The anti-KANK2 immunoblot demonstrated that KANK2 had bound solely to the GFP-talin rod beads, implying that GFP-Trap immunoprecipitation is an effective method to identify talin-binding ligands in cell extract.

The talin 'fishing' rod experiment was subsequently conducted in murine neuronal extract and once again validated by a successful anti-KANK2 immunoblot, demonstrating the exclusive identification of KANK2 in the GFP-talin beads samples (Figures 4.11/ 4.12 A). An LC-MS/MS proteomics analysis was conducted in collaboration with Turku Bioscience, Finland. Whilst various proteins were recognized as potential talin binders (Tables 4.1-3), confident identification of potential talin binders proved to be more difficult than expected, due to *E. coli* protein contamination and the overwhelming presence of talin in the samples. Therefore, the talin 'fishing' rod experiment was successfully adapted in CaSki cell lysate (Figure 4.13). Treatment of the bead samples with an acidic glycine buffer, following incubation and washing, aided to reduce both these variables, improving the MS data substantially and enabling easy, confident identification of the known talin binder vinculin, among many additional potential talin binders (Figure 4.15, Tables 4.6-7). The LC-MS/MS proteomics analysis was effectively completed in-house with invaluable aid from Kevin Howland, enabling the proteomics component of the talin 'fishing' rod experiment to be streamlined, thereby allowing the identification of talin-binding ligands to occur more conveniently and proficiently in the future.

The finalised talin 'fishing' rod experiment was conducted twice more in CaSki cell lysate to obtain a broader list of potential talin-binding ligands (Figure 4.17, Tables 4.8-9). It was then carried out in triplicate for murine neuronal extract and validated through anti-KANK2 immunoblotting, resulting in the identification of many potential talin-binding ligands in the brain (Figures 5.1-2 and Tables 5.1-2).

### 8.1.1 Immunoblotting Limitations

Immunoblotting was successfully used to validate whether the talin 'fishing' rod experiment could identify known talin binders in cell extract, prior to proteomics analysis. It was also conducted in an attempt to validate the putative novel interactors identified by previous MS proteomics results, which listed 1433G, ARHGDIA, and septin-2 as potential talin binders (Gough et al., 2021). Although the immunoblots were unable to confirm that 1433G, ARHGDIA, or septin-2 interact with talin (Figures 4.14, 4.18, and 5.2), this does not imply that they cannot bind to talin. The immunoblots of known talin binders, CDK1 and KANK1, initially performed to act as positive controls, also did not demonstrate an interaction with talin in the talin 'fishing' rod experiments conducted, even though both proteins were present in the cell extracts (Gough et al., 2021). This presumably occurred due to the occupation or obstruction of the CDK1/KANK1 binding sites by other proteins, i.e. the preferential binding of KANK2, which occurred consistently in every talin 'fishing' rod experiment and likely prevented KANK1 binding. It is also a possibility that the conformation of the talin rod is slightly altered as a result of binding to the GFP-Trap beads, which may prevent interactions with talin binders. However, as the GFP affinity tag is at the N-terminus of the talin construct, it should not interfere with the conformation of the downstream talin rod, and no evidence was obtained to suggest that non-specific binding between the talin rod and GFP affinity tag had occurred which would alter talin binding capabilities. Nevertheless, it is possible that the 1433G, ARHGDIA, and septin-2 binding sites in talin were occupied or obstructed, either in the current talin configuration or by other talin-binding proteins.

## 8.2 Successful identification of possible talin binders

Through utilisation of the novel talin 'fishing' rod experiment, many neuronal proteins were identified as possible talin binders. Two proteins identified in the final MS proteomics analysis, synaptojanin-1, and dynamin-1, were also present in the list of synaptic vesicle proteins analysed by the bioinformatics pipeline, described in section 3. Dynamin-1 was identified with fold change values of 8.2 and 16.3, p-values of 0.0160 and 0.0078, and a confidence score of 236 in the GFP-talin rod beads/elution samples, respectively (Tables 5.1 and 5.2). Furthermore, synaptojanin-1 was identified with fold change values of 14.0 and 31.6, p-values of 0.0101 and 0.0208, and a confidence score of 95 in the GFP-talin rod beads/elution samples, respectively (Tables 5.1 and 5.2). As both proteins obtained a fold change considerably higher than 1, a significant p-value, and in the case of dynamin-1 also obtained a confidence score above 125 in both the GFP-talin rod beads/elution samples, they are both very promising talin binders.

Clathrin heavy chain 1 (CHC1) and unconventional myosin-Va are two proteins listed in both MS proteomics analyses obtained from ‘fishing’ in murine neuronal extract (Tables 4.2, 5.1 and 5.2). In the final MS analysis, CHC1 was identified with fold change values of 1.5 and 2.5, p-values of 0.1966 and 0.1063, and a confidence score of 1007 in the GFP-talin rod beads/elution samples, respectively (Tables 5.1 and 5.2). Myosin-Va, in the final MS analysis, was identified with fold change values of 15.8 and 24.5, p-values of 0.0020 and 0.0644, and a confidence score of 291 in the GFP-talin rod beads/elution samples, respectively (Tables 5.1 and 5.2). Myosin-Va was also recognized as a synaptic vesicle protein in Takamori et al., 2006; however, was not previously analysed by the bioinformatics pipeline due to time constraints. Whilst the first attempt at identifying talin-binding proteins in murine neuronal extract did not identify potential talin binders as confidently as the final MS analysis, since these proteins were identified in both experiments, it is compelling evidence that the proteins may be promising potential talin binders, especially myosin-Va as the confidence and fold change values are considerably higher.

### 8.2.1 Bioinformatics Analysis

Utilisation of the bioinformatics pipeline revealed that the I/LD motifs present in dynamin-1 were not fully enclosed in an alpha-helical and intracellular region, whilst the sequences of CHC1, synaptojanin-1, and myosin-Va were too long to run in PSIPRED; therefore, prediction of the alpha-helical and intracellular regions could not be made. This demonstrates why the I/LD motifs in dynamin-1 and synaptojanin-1 were not analysed further after the initial bioinformatic analysis, in favour of syntaxin 6, PICAL, SNAP 25, and SNAPIN, whose I/LD motifs were confirmed to be fully enclosed in alpha-helical, intracellular regions.

Through utilisation of Porter 5.0 and AlphaFold, the secondary structure of promising I/LD motifs with scores of 4 or above were identified in CHC1, synaptojanin-1, and myosin-Va (Table 8.1). Whilst only two motifs were fully enclosed in an alpha-helical region according to Porter 5.0, as demonstrated by the double-asterisk (**), a single asterisk (*) indicates the motifs partially enclosed in alpha-helical regions (Table 8.1). The motifs are also highlighted according to the AlphaFold per-residue confidence score, where blue represents confidence above 70 and orange indicates confidence above 50. Nevertheless, as PSIPRED analysis was unavailable for these proteins due to length, it is uncertain whether these motifs reside in an intracellular, transmembrane, or extracellular region.

***Table 8.1: The I/LD motifs present in clathrin heavy chain 1, synaptojanin-1, and unconventional myosin-Va with a score of 4 or higher.***

*The predicted secondary structures of CHC1, synaptojanin-1, and unconventional myosin-Va were re-analysed by Porter 5.0 and AlphaFold, as they were too long for the initial secondary structure prediction by PSIPRED. *Motifs which are partially enclosed in alpha-helical regions, according to the predicted structure obtained using Porter 5.0. ** Motifs which are fully enclosed in alpha-helical regions, according to the Porter 5.0 predicted secondary structure. The motifs highlighted in blue and orange are partially enclosed in alpha-helical regions with an AlphaFold per-residue confidence score between 70-100 and 50-100, respectively. The motifs highlighted in grey are not present in an alpha-helical region according to AlphaFold.*

| Protein | Uniprot ID | I/LD motif | Position 4 Hydrophobic acid | Prior E/D residues | Hydrophobic residues at correct positions | Linked motif | Overall Score |
|---|---|---|---|---|---|---|---|
| **Clathrin heavy chain 1** | Q68FD5 | IDQV* | V | - | Position 5, 8, 15: V, A, P | - | 5 |
| **Synaptojanin-1** | Q8CHC4 | IDVL* | L | - | Position 5, 15: L, A | - | 4 |
| **Unconventional myosin-Va** | Q99104 | LDLL* | L | D | Position 8, 15: F, L | - | 5 |
| | | IDIF* | F | D | Position 8: A | IDID | 4.5 |
| | | IDEL* | L | - | Position 5, 8 and 15: L, F, I | - | 5 |
| | | LDSI** | I | - | Position 5, 8, 15: L, L, M | - | 5 |
| | | LDEE* | - | - | Position 5, 8, 15: C, P, W | LDLL | 4.5 |
| | | LDVR** | - | E | Position 8, 15: V, L | - | 4 |

Although a re-analysis of secondary structure revealed potential talin-binding I/LD motifs in CHC1, synaptojanin-1, and myosin-Va, the I/LD motifs in dynamin-1 are not enclosed in an alpha-helical, intracellular region according to PSIPRED predictions; therefore, binding to talin through these motifs is unlikely. However, whilst the talin-binding I/LD motif is seen amongst multiple talin-binding proteins and is the most characterised, it is not the only talin-binding motif. Therefore, whilst the I/LD motifs in dynamin-1, or even the motifs listed in Table 8.1, may not demonstrate binding to talin rod domains, as the results of this project demonstrate that all four proteins are promising potential talin binders, they may likely bind to talin through alternative mechanisms.

## 8.3 The functions of identified potential talin binders

CHC1, dynamin-1, synaptojanin-1, and myosin-Va, as well as other proteins listed in the final MS proteomics analysis, play significant roles in mediating neuronal function. Whilst interactions with talin have yet to be confirmed, as the proteins were identified confidently in the MS proteomics analysis, it is compelling evidence that they may exhibit talin-binding activity and subsequently assist talin in mediating synaptic transmission, as described in the MeshCODE theory.

### 8.3.1 Synaptic Vesicle Endocytosis: CHC1, dynamin-1, and synaptojanin-1

To meet the demands of synaptic vesicle exocytosis, sustain synaptic transmission, and avoid excessive membrane expansion, SV endocytosis is tightly coupled to SV exocytosis, enabling the recycling of SVs, membrane retrieval, and maintenance of the synaptic vesicle pool (Soykan et al., 2017). The precise mechanisms for synaptic vesicle recycling (SVR) have remained a subject of debate for many years; however, several distinct endocytosis pathways have been suggested with varying kinetics, to meet the specific demands of signalling through each synapse (Delvendahl et al., 2016). Nevertheless, the GTPase dynamin, implicated in membrane fission, the polyphosphoinositide phosphatase synaptojanin, primarily required for vesicle uncoating, and CHC1, a significant component of the clathrin coat, are all integral in multiple pathways of synaptic vesicle endocytosis.

#### 8.3.1.1 Clathrin-mediated Endocytosis

Various approaches in multiple studies have indicated that clathrin-mediated endocytosis (CME) is the predominant synaptic vesicle recycling pathway in the nerve terminal, following mild or moderate synaptic stimulation (Clayton et al., 2008; Cremona & de Camilli, 1997; Granseth et al., 2006; Saheki & de Camilli, 2012; Smith et al., 2008). Whilst CME was previously considered to primarily occur at the presynaptic membrane, recent evidence contradicts this, demonstrating the prevalence of CME at synaptic endosomal structures, generated via ultrafast endocytosis (Milosevic, 2018; Soykan et al., 2017; S. Watanabe et al., 2014).

##### Clathrin Coats

Synaptic vesicle recycling from the presynaptic membrane can be separated into four phases: clathrin coating, vesicle budding, fission/scission, and clathrin coat removal (Cremona & de Camilli, 1997; Harris et al., 2000). Clathrin coats function as molecular sorters, enabling the generation of homogenously sized vesicles with specific protein composition, hence the predominance of CME in synaptic vesicle recycling (Saheki & de Camilli, 2012). The clathrin coat consists of an outer layer, termed the clathrin lattice, a complex meshwork of clathrin triskelia subunits formed from three clathrin heavy and light chains, attached to the membrane via an inner layer of adaptor proteins (Feliciano et al., 2011; Saheki & de Camilli, 2012).

### Membrane Curvature

Amphipathic helices, which are highly abundant in the talin rod, and indirect force induction through the actin cytoskeleton have previously been shown to promote membrane curvature, via perturbation of the symmetry between plasma membrane leaflets (Drin et al., 2007; Saheki & de Camilli, 2012). The association of curved transmembrane domains, such as Bin-Amphiphysin-Rys (BAR) domains, with the plasma membrane, is also thought to induce membrane curvature and tubulation (Saheki & de Camilli, 2012; S. Watanabe et al., 2018). Therefore, endophilin, which contains amphipathic helices and a BAR domain, is considered a primary determinant of membrane curvature, enabling the coupling of vesicle fission and uncoating, through interaction with synaptojanin and dynamin (Ringstad et al., 1999; Saheki & de Camilli, 2012).

### Dynamin

Vesicle fission, through the action of dynamin, enables the development from a clathrin-coated pit to a vesicle. Dynamin, a 100 kDa GTPase, consists of an unstructured C-terminal proline-rich domain (PRD), associated with SH3 domain protein binding, a GTPase effector domain (GED), a PH domain, required for PIP2 binding, and a middle region connected to the N-terminal GTPase domain (Figure 8.1 A) (Antonny et al., 2016; Ford et al., 2011). A three-helix bundle, termed the bundle signalling element (BSE), is formed through the interaction of the GED with both the amino and carboxyl GTPase domain termini, allowing the PRD to extend past the N-terminus of the protein and enabling the transmission of dynamin conformational changes to and from the GTPase domain (Figure 8.1 B, C) (Antonny et al., 2016; Chappie et al., 2009, 2011). Through the oligomerisation of dynamin in a spiral ring formation at the necks of clathrin-coated pits, dimerisation of adjacent spiral notches encourages an increase in the proximity of two dynamin GTPase domains, prompting a >100-fold enhancement of GTPase activity (Figure 8.1 D, E) (Chappie et al., 2011; Ferguson & de Camilli, 2012; Saheki & de Camilli, 2012). Subsequent GTP hydrolysis induces conformational changes in dynamin, promoting plasma membrane cleavage through dynamin constriction (Figure 8.1 F) (Ferguson & de Camilli, 2012).

Regarding the three dynamin isoforms present in mammals, dynamin-2 is ubiquitously expressed at low levels in all cells, dynamin-1 is the predominant isoform enriched in the brain, whilst dynamin-3 is expressed in the brain and testis (Cao et al., 1998; Ferguson et al., 2007; Saheki & de Camilli, 2012). Knockout studies in various animals have revealed the significance of dynamin in synapses, with dynamin-1 knock-out studies in mice demonstrating an inability to survive past 2 weeks (Ferguson et al., 2007; Milosevic, 2018). Whilst low levels of SVR can occur in the absence of dynamin through bulk endocytosis, upon dynamin photoinactivation in flies, maintenance of neurotransmitter release proved unsuccessful due to the severe impairment of SVR (Kasprowicz et al., 2014).

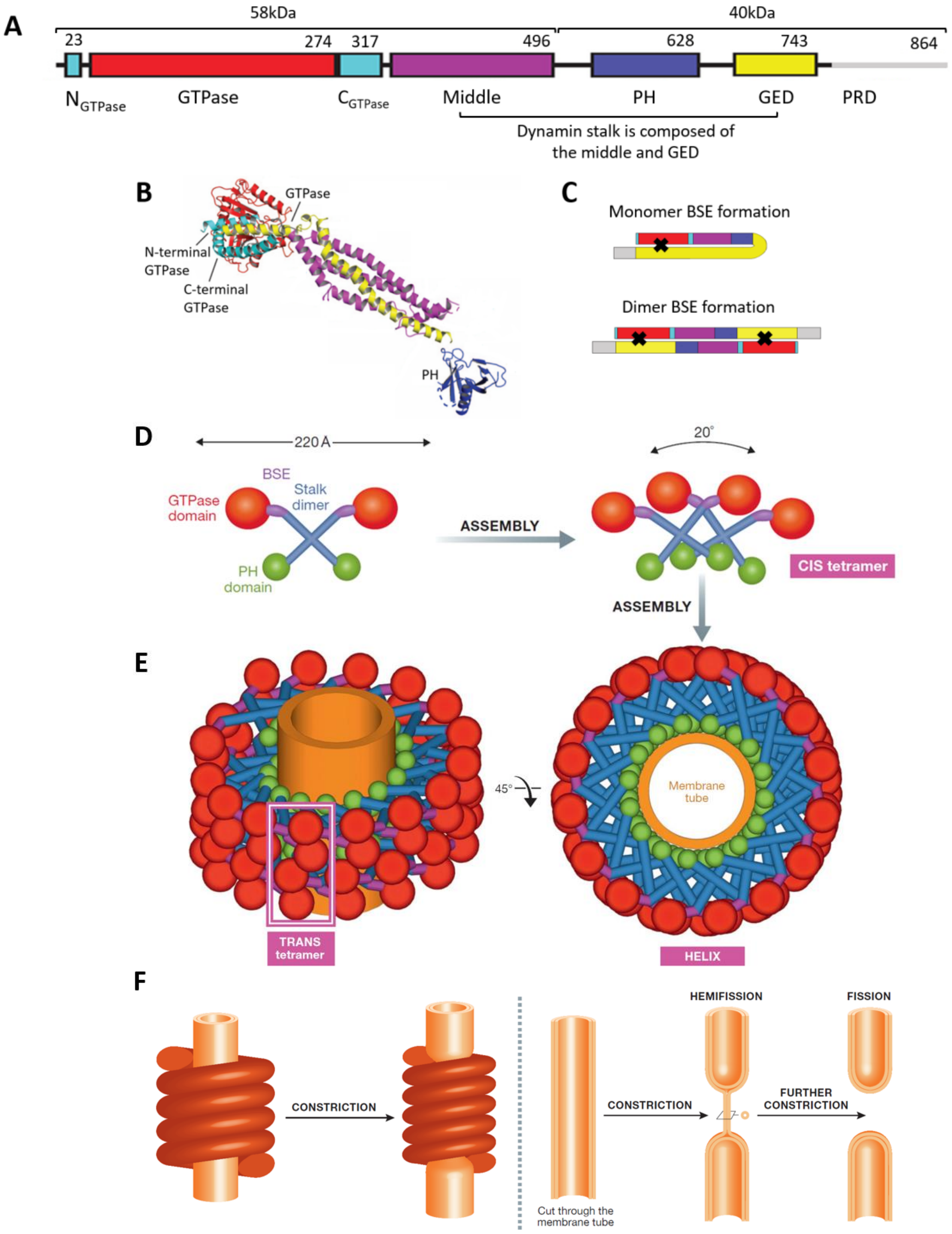

***Figure 8.1: Dynamin structure and assembly in dynamin-mediated membrane fission.***
*(A) Dynamin structural domains (Ford et al., 2011) (B) Crystallisation structure of a dynamin monomer (Ford et al., 2011) (C) BSE formation in a dynamin monomer and dimer (Chappie et al., 2011). The interaction of a dynamin GED with the GTPase domain results in BSE formation. A swapped-domain dynamin dimer is produced via the interaction of a GED from one monomer with the GTPase domain of another (Chappie et al., 2011). (D) Dynamin dimer and tetramer structure (Antonny et al., 2016). The proline rich and GTPase effector domains are not visualised for simplicity. (E) Visualisation of dynamin oligomerisation in a cylindrical helix formation on the vesicle neck (Antonny et al., 2016). (F) Constriction of dynamin promotes hemi-fission, followed by complete fission (Antonny et al., 2016).*

Dynamin recruitment occurs in two consecutive stages: initially at lower levels during the primary phase of clathrin coat maturation, followed by a stronger burst of dynamin recruitment prior to membrane fission (Cocucci et al., 2014). The dynamin proline-rich and PH domains are considered to facilitate dynamin recruitment to vesicle collars of developing vesicles, through binding to the SH3 domains on BAR domain-containing proteins, i.e. endophilin/amphiphysin, and membrane lipids, i.e. PIP2, respectively (Saheki & de Camilli, 2012). Similarly, dynamin photoinactivation in flies not only demonstrated the vital significance of the protein in vesicle fission, but also in earlier stages of SV regeneration through the recruitment of clathrin and adaptor protein (AP) 2, a predominant protein present in clathrin coats (Cremona & de Camilli, 1997; Kasprowicz et al., 2014)

### Synaptojanin

Whilst the PIPKIγ-talin interaction potentiates the generation of PIP2 pools for clathrin coat formation and actin nucleation, synaptojanin antagonises PIPKIγ function and is responsible for the dephosphorylation of PIP2, among other phosphatidylinositol (PI) family members (di Paolo et al., 2002; Morgan et al., 2004; Wenk et al., 2001). Although synaptojanin-1 is highly abundant in nerve terminals, the second isoform, synaptojanin-2 is present in a broader range of tissue types (Nemoto et al., 1997). This also coincidentally mirrors the tissue-specific distribution of the two synaptojanin-1 isoforms, as the shorter synaptojanin-1 isoform of 145 kDa is primarily localised in the brain, whereas the longer isoform of 170 kDa has a wider tissue distribution (Choudhry et al., 2021). Synaptojanin is named after the two-faced Roman god Janus for its dual PI phosphatase domains, one of which is termed the SAC1 domain as it is analogous to a domain present in SAC1 and is capable of

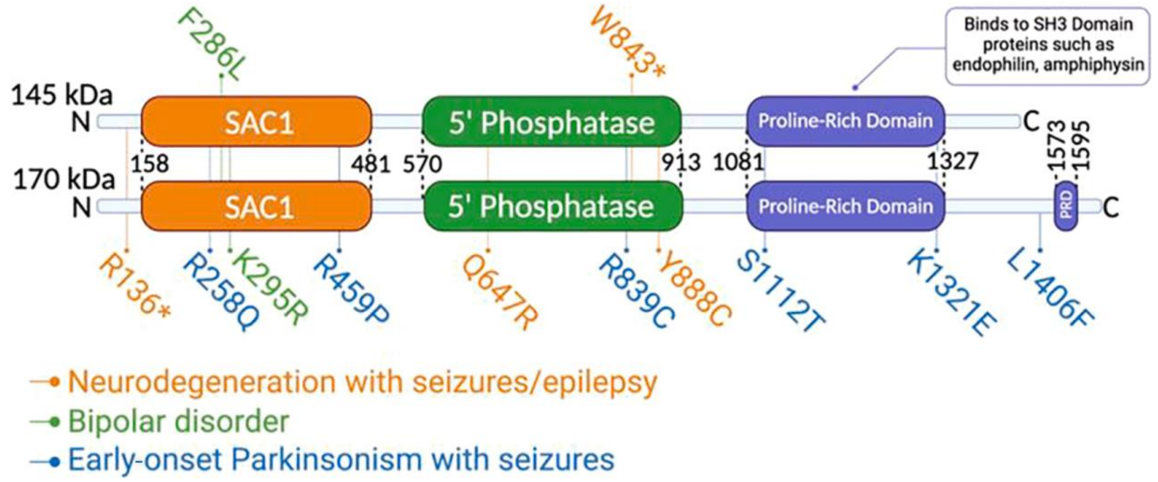

***Figure 8.2: Synaptojanin-1 isoform structures and the location of mutations associated with neurodegeneration, bipolar disorder, and Parkinson's disease (Choudhry et al., 2021).***

*There are two synaptojanin-1 isoforms, with varying molecular weights of 145 and 178 kDa. Both synaptojanin-1 isoforms contain a SAC1, 5' phosphatase, and proline-rich domain; however, the longer isoform contains an additional, smaller proline-rich domain. Different mutations have been identified in both isoforms, which can result in neurodegeneration, bipolar disorder, or early-onset Parkinson's disease.*

dephosphorylating 3-, 4-, 5-phosphates in PIs, whilst the 5' phosphatase domain solely specialises in PI-5 phosphorylation (Figure 8.2) (Harris et al., 2000). Synaptojanin also contains a C-terminal proline-rich domain, similar to dynamin (Figure 8.2) (Harris et al., 2000).

Following CME, vesicle uncoating is facilitated through the combined action of synaptojanin, the ATPase heat shock cognate (HSC) 70, and its DNAJ cofactor, auxilin, to enable SV exocytosis and recycle the clathrin coat components for subsequent, rapid CME upon stimulation (Lemmon, 2001; Milosevic, 2018; Saheki & de Camilli, 2012). Both synaptojanin phosphatase domains mediate dephosphorylation of PIP2 to PIP via PI4P generation, modifying the cytoskeleton-vesicle interactions previously regulated by PIP2, encouraging vesicle travel, and decreasing the affinity of clathrin adaptors to the vesicle membrane, whilst auxilin, recruited by PI4P formation, and HSC 70 facilitate clathrin triskelion removal (Saheki & de Camilli, 2012; Verstreken et al., 2003; S. Watanabe et al., 2018). Coincidentally, the final MS proteomics analyses revealed the presence of heat shock-related 70 kDa protein 2 in CaSki cell lysate and the mitochondrial heat shock protein of 75 kDa in murine neuronal extract, with significant p-values and high fold change values of 5.5 and 14.4, suggesting the feasibility of an additional talin-HSC 70 interaction in the vesicle uncoating process.

Whilst early findings indicated a primary role for synaptojanin in SV uncoating, studies in *C. elegans* with a mutated synaptojanin-1 ortholog, *unc-26,* demonstrated a broader role for synaptojanin in several aspects of SV recycling (Harris et al., 2000). Comparable to dynamin-1 knock-out studies, the deletion of synaptojanin in mice triggered an inability to survive past 15 days, with 85% lethality occurring before 24 hours (Cremona et al., 1999; Harris et al., 2000). Deficiencies in *C. elegans unc-26* mutants were observed for endocytic protein recruitment, vesicle fission, vesicle uncoating, and vesicle attachment to the actin cytoskeleton in reserve pools (Harris et al., 2000). Synaptojanin may also contribute to membrane curvature through the dephosphorylation of membrane PIs, aiding to diminish the negative charges present in the inner membrane leaflet, which prevent lipid-packing, thereby eliminating charged lipid repulsion (Harris et al., 2000). Multiple SVE steps facilitated by PI binding endocytic proteins, i.e. dynamin, AP-2, and synaptotagmin, which are all coincidentally present in the final MS proteomics analysis (Tables 5.1 and 5.2), were stalled in *unc-26* mutants (Harris et al., 2000). Therefore, it has been proposed that synaptojanin-mediated dephosphorylation of membrane PIs may also promote the release and activation of these proteins, enabling SVE progression (Harris et al., 2000). Whilst SVR, to some extent, can still occur in *unc-26* mutants, the phenotype observed indicates a kinetic deceleration in SVR, implying the likelihood that synaptojanin acts to accelerate SVE, enabling the effective neurotransmission required for survival (Harris et al., 2000).

Recruitment of the two synaptojanin-1 isoforms at different endocytic stages has been suggested to account for the varying functions of synaptojanin throughout CME, with the larger isoform thought to act in the early stages of endocytosis, presumably facilitating the activation of endocytic proteins (i.e. clathrin and AP-2), whilst the shorter isoform acts in the later phases of CME to promote vesicle uncoating (Perera et al., 2006). *Drosophila* endophilin-1 null mutants demonstrated synaptojanin mislocalisation and destabilisation, whilst mutations in both proteins displayed near-identical phenotypes, implying a close association of the proteins in the same endocytic steps, particularly the essential role of endophilin in synaptojanin recruitment and stabilisation (Verstreken et al., 2003).

Whilst synaptojanin mutants have demonstrated phenotypes reflective of early-onset neurodegenerative disorders, additional defects in synaptojanin have been implicated in many neurological or neuropsychiatric diseases, such as schizophrenia, Alzheimer’s, and Parkinson’s disease (Figure 8.2) (Choudhry et al., 2021). With recent studies also demonstrating the importance of both synaptojanin phosphatase domains in autophagosome maturation, often linked to the development of neurodegenerative diseases, synaptojanin-1 is emphasised as a vital component in maintaining effective brain function (Choudhry et al., 2021; George et al., 2016; Vanhauwaert et al., 2017).

#### 8.3.1.2 Additional Endocytic Pathways

Bulk Endocytosis

Following intense synaptic stimulation, to avoid excessive membrane expansion, the escalation of exocytosis events promotes the parallel activation of bulk endocytosis (BE) alongside CME, whereby sizeable membrane growth potentiates the formation of large membrane infoldings, which act as endosome-like vacuole structures (ELVSs), to generate a new population of synaptic vesicles (Figure 8.3) (Cousin, 2009; Saheki & de Camilli, 2012). The specific mechanisms rudimentary to BE are under debate; nevertheless, this fast endocytic pathway enables the demands of synaptic vesicle exocytosis to be met under elevated stimulation and rapidly terminates once stimulation has ceased (Clayton et al., 2008). $Ca^{2+}$ influx is thought to act as a primary promotor for BE via the action of calcineurin, as this protein is considered to have an affinity for $Ca^{2+}$ exclusively in high concentrations, permitting calcineurin activation solely upon intense stimulation (Cousin, 2009; Morton et al., 2015). Calcineurin is thought to promote synaptic vesicle endocytosis through the dephosphorylation of 8 dephosphins, a group of phosphoproteins (i.e. dynamin, PIPKIγ, and synaptojanin), each individually fundamental to synaptic vesicle endocytosis (Clayton et al., 2009; Cousin & Robinson, 2001; Evans & Cousin, 2007). Dephosphorylation of PIPKIγ through calcineurin enables the talin-PIPKIγ interaction required for protein activation and rapid generation of the PIP2 pool (Sang et al., 2005). Following the absence of synaptic stimulation, $Ca^{2+}$ concentration decreases and inhibition of calcineurin activation presumably occurs, justifying the immediate termination of bulk endocytosis once stimulation has ceased (Clayton et al., 2008; Cousin, 2009). However, recent evidence has demonstrated that whilst calcineurin is still implicated in BE, it is also associated with CME, as a calcineurin gene knockout in mice was shown to impede the speed of both slow and fast endocytosis pathways (X. S. Wu et al., 2014).

Whilst bulk endocytosis is considered a clathrin-independent process, the role of dynamin is disputed, with some studies suggesting that inhibition of dynamin-1 and -3 may enhance bulk endosome formation, whilst others demonstrate that the maturation of bulk endosomes is a dynamin-dependant process (Clayton & Cousin, 2009; Nguyen et al., 2012; Y. Wu et al., 2014). A dynamin phosphorylation cycle has been suggested as a BE-exclusive requirement (Clayton et al., 2010). Dynamin dephosphorylation through calcineurin enables an interaction with syndapin, whose F-BAR domain is implicated in the shallow curvature of membranes, typically associated with large invaginations, and disruption of this syndapin-dynamin interaction results in BE perturbation (Clayton et al., 2009; Clayton & Cousin, 2009). Dynamin can also indirectly recruit neuronal Wiskott-Aldrich syndrome protein (N-WASP) through syndapin, which can bind to both syndapin and dynamin simultaneously via oligomerisation, enabling N-WASP-Arp2/3 interactions to alter actin dynamics and promote BE through facilitation of membrane curvature (Clayton & Cousin, 2009; Takenawa & Miki, 2001).

Synaptojanin-endophilin interactions and dual phosphatase domain activity are required for effective SV recycling in conditions depicting both short and prolonged stimulation, indicating the necessity of synaptojanin in both BE and CME (Mani et al., 2007). Whilst the 5’ phosphatase domain of synaptojanin is considered to promote CME upon minibrain kinase phosphorylation, it has also been implicated in BE suppression (Peng et al., 2021). This is presumably through increased PIP2 dephosphorylation, as a high PIP2 abundance, following prolonged stimulation, is necessary to induce the actin polymerisation required for ELVS formation (T. N. Li et al., 2020; Peng et al., 2021). Similarly, synaptojanin dephosphorylation by calcineurin, following intense prolonged stimulation, is thought to promote BE through enhanced SAC1 activity and suppress 5’ phosphatase activity, preventing the removal of PIP2 (Peng et al., 2021). The presence of PI4P in membranes is considered to promote the tight membrane curvature required for single vesicle formation. Therefore, through enhanced SAC1 activity, increased phosphorylation of PI4P to PI occurs, enabling the formation of more shallow membrane curvature and subsequent ELVSs (Furse et al., 2012; Peng et al., 2021).

Following BE-mediated membrane retrieval, the mechanisms for vesicle formation have not been fully determined. Large membrane infoldings have recently been implicated as preferential sites for clathrin-coated pit formation at physiological temperatures, subsequently implying cooperation between both CME and BE pathways (Arpino et al., 2022; Milosevic, 2018; Soykan et al., 2017; S. Watanabe & Boucrot, 2017). Nevertheless, unperturbed vesicle budding from bulk endosomes has previously occurred at synapses lacking dynamin-1 and -3, indicating the possibility of additional clathrin-independent pathways for vesicle reformation, perhaps working in parallel with CME (Figure 8.3) (Y. Wu et al., 2014).

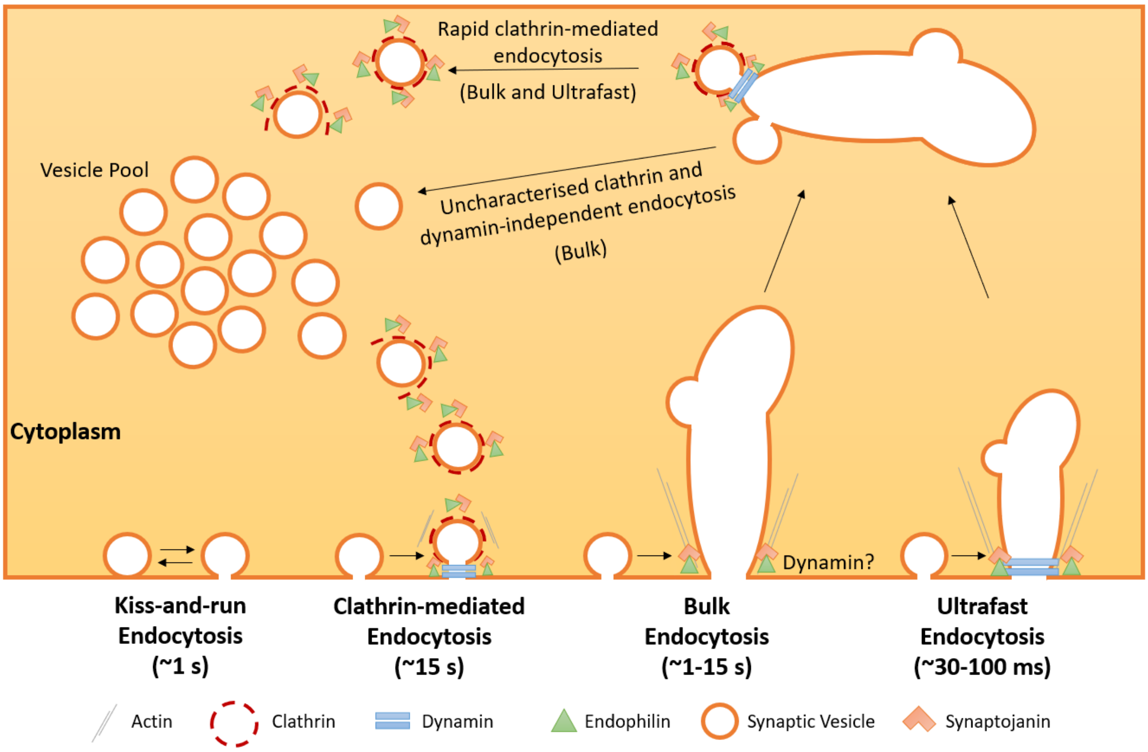

***Figure 8.3: Synaptic vesicle endocytosis pathways.***
*Kiss-and-run endocytosis describes the incomplete collapse of vesicles within the membrane due to the formation of a flickering fusion pore, permitting neurotransmitter release and enabling rapid vesicle reformation. Clathrin-mediated endocytosis (CME) at the membrane is a relatively slow process, occurring in ~15 seconds, whereby membrane curvature is promoted by actin, endophilin, and synaptojanin. Vesicle fission is dynamin-dependant, whilst clathrin uncoating is facilitated by auxilin, HSC 70, and synaptojanin. Bulk endocytosis occurs following sustained intense stimulation, at speeds between 1-15 seconds. Membrane curvature is mediated by actin, endophilin, and synaptojanin, in conjunction with calcineurin, prompting the formation of endosomal-like vacuole structures (ELVSs). However, the role of dynamin in bulk endocytosis fission is still under debate. Ultrafast endocytosis refers to the rapid formation of ELVSs, in response to brief stimulation. Membrane curvature is thought to occur through the generation of formin (mDia1)-mediated actin structures, whilst synaptojanin and endophilin act cooperatively in narrowing the vesicle neck, promoting dynamin-facilitated fission with the aid of myosin II. Following membrane retrieval by bulk and ultrafast endocytosis, vesicle formation is considered to occur through CME, although the presence of additional clathrin-independent pathways have also been implicated in bulk endocytosis. Auxilin, HSC 70, formin (mDia1), and myosin II are not pictured for simplicity. Figure inspired by (Rodal & Littleton, 2008).*

### Ultrafast Endocytosis

Upon mild stimulation, the predominant mechanism of synaptic vesicle recycling is considered to occur through the cooperation of ultrafast endocytosis (UFE) and CME, as ELVSs are initially formed through UFE, in a mechanism similar to BE, followed by the generation of vesicles via endosome-localised CME (Figure 8.3) (Kononenko et al., 2014; Milosevic, 2018; S. Watanabe & Boucrot, 2017).

Brief stimulation, as opposed to the longer, more intense stimulation that induces BE, promotes the formation of ELVSs in a span of milliseconds, through a clathrin-independent mechanism (Milosevic, 2018; Soykan et al., 2017). In UFE, the curvature required for membrane invagination is induced by formin (mDia1)-mediated actin complexes whilst synaptojanin, specifically the 5’ phosphatase domain, and endophilin act cooperatively in narrowing the endosome neck to less than 20 nm, promoting dynamin-facilitated fission with the aid of myosin II (Soykan et al., 2017; S. Watanabe et al., 2018). Following membrane retrieval by UFE at speeds between 30-100 milliseconds, vesicle formation is considered to occur through CME at rapid speeds between 5-6 seconds, as opposed to the speed of ~15 seconds for membrane-localised CME Figure 8.3) (S. Watanabe et al., 2013, 2014).

#### Kiss-and-run

Kiss-and-run endocytosis describes a mechanism where vesicles are not fully incorporated into the presynaptic membrane, therefore enabling the preservation of vesicle integrity and rapid vesicle reformation in ~1 second (Figure 8.3) (Granseth et al., 2006; Saheki & de Camilli, 2012). Whilst persuasive evidence has been obtained to demonstrate the occurrence of kiss-and-run endocytosis since the initial proposal of the pathway, further evidential information regarding this mechanism has been difficult to obtain, prompting the perception that kiss-and-run endocytosis only plays a minor role in synaptic vesicle recycling (Cousin, 2009; Fesce et al., 1994; Smith et al., 2008; Stevens & Williams, 2000).

### 8.3.2 The potential role of talin in synaptic vesicle endocytosis

The presence of dynamin-1 and synaptojanin-1 in the final MS proteomics experiment (Tables 5.1 and 5.2) may implicate a potential role for talin in vesicle neck constriction, vesicle fission, and clathrin uncoating, three processes seemingly linked through other proteins, such as endophilin, alongside a broader function in enabling SVE progression. The role of actin has been mentioned previously in the promotion of vesicle endocytosis, especially in membrane curvature, yet the extent of its function and the exact mechanism have not been fully established. Like talin, both dynamin and synaptojanin have been associated with the, albeit indirect, modification of actin structure through interactions with actin regulators such as N-WASP, profilin, or PIP2 (Ringstad et al., 1999). Whilst the true role of talin in synaptic vesicle endocytosis has yet to be fully understood, it is interesting to speculate that further clarification of talin activity may facilitate the parallel elucidation of actin function also. Many proteins that bind dynamin have also similarly been found to associate with synaptojanin; therefore, as both proteins were found together in the final MS analysis, it further supports the likelihood of a talin interaction (Saheki & de Camilli, 2012).

The final MS proteomics talin 'fishing' rod experiment analysis identified CHC1 and four subunits (α1, α2, β, and μ) of the heterotetrameric clathrin adaptor protein 2 (AP2) complex, as potential talin binders, albeit at lower fold change values than synaptojanin-1 and dynamin-1 (Tables 5.1 and 5.2). Similar to the role of talin upon PIPKI binding, it is possible that talin may act to enhance the activity of these proteins or facilitate their recruitment. Following the generation of PIP2 through talin-PIPKIγ interactions, an alteration of the talin rod domain switch pattern upon synaptic signalling may aid in the initial stages of vesicle formation, either directly by binding to both AP2 subunits and CHC 1, or indirectly via clathrin and AP2 recruitment through talin-dynamin/synaptojanin interactions. Further signalling and modification of the switch pattern, may promote talin-mediated actin structure formation, possibly in association with dynamin and/or synaptojanin, which may cooperate with the amphipathic helices abundant in talin to induce membrane curvature. This may subsequently be succeeded by the promotion of vesicle neck constriction and fission via talin-dynamin/synaptojanin-1 interactions, prior to the facilitation of clathrin uncoating through talin binding to synaptojanin-1, CHC1, or the AP2 subunits. As two members of the 70 kDa heat shock protein family were also identified in the final CaSki and neuronal MS analyses, the possibility that talin may also bind to HSC 70 arises, suggesting the feasibility of an additional talin-mediated interaction to facilitate vesicle uncoating. The potential interactions between talin and AP2 subunits, CHC 1, dynamin-1, HSC 70, or synaptojanin-1 may subsequently enable talin to regulate the number of available vesicles in a synapse, whilst the altered spatial positioning of talin and bound ligands, promoted by domain unfolding, suggests how talin may interact with these proteins during both membrane-adjacent and synaptic endosomal CME (Barnett & Goult, 2022). Therefore, a possible mechanism can now be proposed detailing how talin may mediate homeostatic synaptic scaling in the brain, by modifying synaptic strength through the regulation of available vesicle number, previously described in the MeshCODE theory (Goult, 2021; Turrigiano, 2008).

As dynamin-1 and synaptojanin-1 have both been heavily implicated in BE and UFE involvement, talin may facilitate not only CME, but also all other SVR endocytic pathways, with the exception of kiss-and-run endocytosis, whose mechanism is not yet fully understood. Depending on the talin binding loci for each protein, in addition to interactions in a singular context, complex formation may similarly be considered as interestingly, a complex of synaptojanin, dynamin, endophilin/amphiphysin and AP2 has previously been identified (Harris et al., 2000). Whilst this is all currently hypothetical, the identification of several potential talin binders with varying yet significant roles in multiple aspects of SVE facilitates the acquisition of evidence to support the MeshCODE theory and validates the hypothesis of this project, which theorised that talin may play a more fundamental role in synaptic vesicle activity than previously anticipated.

### 8.3.3 Unconventional Myosin-Va

Myosins are a group of actin-associated, molecular motor proteins implicated in vesicle, organelle, and macromolecule tethering/transportation, which utilise ATP hydrolysis for the generation of energy, enabling movement across the cytoskeleton (Assis et al., 2017; Fili & Toseland, 2020; Rudolf et al., 2011). Variation in myosin structure permits the classification of myosins into 12 groups, which can then be further categorised as conventional or unconventional (Fili & Toseland, 2020). Myosin-Va is a class V unconventional myosin that exists as a homodimer of heavy chains, comprising of a motor head domain primarily involved in ATP hydrolysis and actin association, a lever neck region containing six IQ-motifs implicated in calmodulin and other light chain binding, followed by a tail of coiled-coils which form upon dimerisation and a C-terminal globular tail domain (GTD) (Figure 8.4) (Fili & Toseland, 2020; Kneussel & Wagner, 2013; Rudolf et al., 2011).

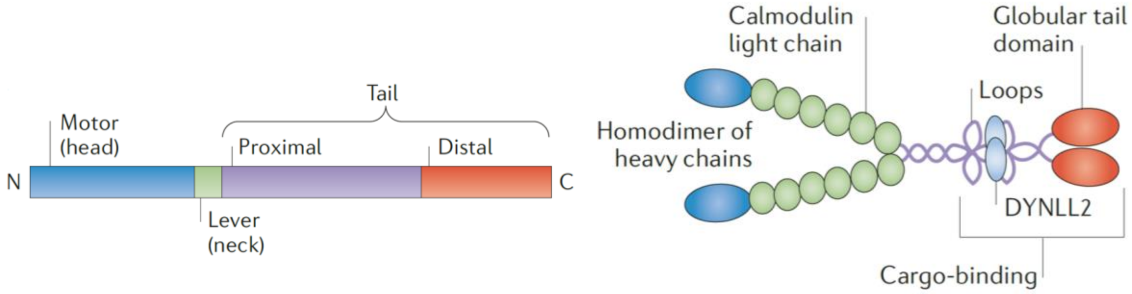

***Figure 8.4: Myosin-Va structure.***
*Myosin-Va exists as a homodimer of heavy chains, consisting of a motor head domain, a lever neck region of six IQ motifs that bind calmodulin light chains, followed by a tail, implicated in cargo binding, of dimerised heavy chains, which form coiled coils disrupted by loops, and a globular tail domain. Figure adapted from (Kneussel & Wagner, 2013).*

Mutations in the MYO5A gene, encoding myosin-Va, have been associated with the development of Griscelli syndrome type 1, also known as Elejalde syndrome, which causes severe neurological defects resulting in an impeded lifespan (Assis et al., 2017; Rudolf et al., 2011). Whilst myosin-Va null mutations cause lethality within 21 days, a myosin-Va mutant in mice (termed Flailer), which perturbs encoding of the actin-binding domain, is viable (Pandian et al., 2020; Yoshii et al., 2013). The study of this mutation has demonstrated that myosin-Va, a protein highly enriched in the PSD of neurons, facilitates synaptic component organisation upon neuronal stimulation, for effective glutamate-mediated postsynaptic depolarisation and activity (Pandian et al., 2020; Yoshii et al., 2013). This predominantly occurs through the direct transport of major PSD scaffolding proteins (i.e. PSD-95/ Homer), among other vital cargo, and the following indirect recruitment of additional proteins, such as dynamin-3 (Pandian et al., 2020; Yoshii et al., 2013). Myosin-Va also facilitates AMPAR endocytosis, enabling synaptic plasticity through glutamate receptor-dependent LTD, with the absence of myosin-

Va activity resulting in the defective depression of synaptic pathways to perturb hippocampal memory, producing phenotypes similar to those displayed in anxiety or autism spectrum disorders (Pandian et al., 2020; Yoshii et al., 2013). Myosin-Va has been implicated in the regulation of neuronal activity, particularly synaptic plasticity, following several observations: myosin-Va contains a calpain cleavage site, implying it may partake in the theorised formation of calpain-mediated hippocampal LTP, is associated with large dense-core vesicle (LDCV) exocytosis, whereby LDCVs transport cargo influencing synaptic plasticity, and is highly enriched in the hippocampus and cerebellum, significant regions of the brain implicated in spatial, episodic, and implicit memory formation (Kneussel & Wagner, 2013; Rudolf et al., 2011).

However, the role of myosin-Va in synaptic transmission is disputed, as early findings implicate its irrelevance, whilst more recent studies seem to contradict this (Maschi et al., 2018, 2021; Schnell & Nicoll, 2001; M. Watanabe et al., 2005). $Ca^{2+}$-dependent interactions between myosin-Va and SNARE proteins, such as syntaxin 1A and synaptobrevin, have been observed (Prekeris & Terrian, 1997; M. Watanabe et al., 2005). $Ca^{2+}$-mediated disruption of myosin-Va-calmodulin binding at the IQ motifs, enables syntaxin 1A association, with perturbation of the myosin-Va-syntaxin 1A interaction resulting in decreased exocytic activity (M. Watanabe et al., 2005). Recently myosin-Va activity has been implicated in regulating SV exocytosis and neurotransmitter release, by acting as a vesicle tether to retain SVs at the presynaptic membrane (Maschi et al., 2018, 2021). SV exocytosis can occur at multiple release loci in the synaptic active zone, with the number, re-use, and distances between these loci considered to modify neuronal signalling (Maschi et al., 2021). The timing and vigour of neuronal signalling is also highly dictated by the docking of vesicles at these exocytosis loci, a process controlled by myosin-Va through the regulation of vesicle retention (Maschi et al., 2021). A gradient of exocytosis loci usage occurs in the active zone, with the furthest peripheral loci experiencing a fourfold decrease in usage compared to the central loci (Maschi et al., 2021; Maschi & Klyachko, 2020). This is also referred to as the gradient of vesicular release probability, which regulates the temporal usage of these loci during synaptic vesicle exocytosis (Maschi et al., 2021). Vesicles are typically exocytosed at central loci during basal stimulation, yet upon sustained transmission, vesicle release is less refined and tends to occur at more peripheral sites (Maschi et al., 2018). Nevertheless, myosin-Va dictates the location of vesicular release, and following sustained stimulation, regulates peripheral loci usage by promoting exocytosis at more central sites (Maschi et al., 2018). This is achieved via the regulation of vesicle retention at the presynaptic membrane, by reducing the vesicle detachment rate, which has been speculated to occur through enhancing the $Ca^{2+}$-dependent myosin-Va-SNARE protein interactions (Maschi et al., 2018). Myosin-Va inhibition resulted in the overall promotion of peripheral loci usage and a temporal delay of events throughout multi-vesicular release, by expanding the area of exocytosis loci in the active zone, consequently reducing the gradient of release probability (Maschi et al., 2021). Therefore, following a $Ca^{2+}$ increase in response to an action potential, myosin-Va is considered to dictate the strength and extent of vesicle retention, enabling regulation of neuronal signalling by determining the vesicle exocytosis loci, subsequently modifying transmission duration and the gradient of vesicular release probability (Maschi et al., 2021).

#### Talin binding implications

The identification of myosin-Va as a potential talin-binding ligand is extremely beneficial to support the theorised role of talin in the MeshCODE theory, as myosin-Va is highly implicated in multiple aspects of synaptic vesicle exocytosis and synaptic plasticity. Although definitive confirmation of binding between talin and myosin-Va is required, it is interesting to speculate how this association may affect myosin-Va function. Upon synaptic stimulation, the alteration of talin rod domain switch pattern, and subsequent modification of talin spatial organisation, may promote myosin-Va autoinhibition perturbation, which is predominantly achieved through myosin-Va-adaptor protein interactions, or enhance myosin-Va activity and recruitment in the synapses, to indirectly alter synaptic plasticity and enable effective synaptic vesicle exocytosis.

In sections 8.3.1-2, the potential role of talin in SVE and a possible mechanism proposing how talin may regulate the number of available vesicles in synaptic signalling were discussed. Recent evidence suggests that myosin-Va may dictate synaptic transmission duration and the gradient of vesicular release probability via regulation of vesicle exocytosis loci. This similarly implies that talin may indirectly determine the probability of vesicular release through myosin-Va activity, thereby providing an additional model demonstrating how talin may control homeostatic synaptic scaling in the brain via the modification of synaptic strength, as previously described in the MeshCODE theory (Goult, 2021; Maschi & Klyachko, 2020; Turrigiano, 2008).

### 8.3.4 Future Work

Due to time constraints, the bioinformatics pipeline developed in this project was not applied to all identified potential talin-binding ligands in Tables 4.6-9 and 5.1-2. Therefore, the future recognition of any promising I/LD motifs in these proteins will be highly beneficial in the determination of novel talin binders. If this is not achieved through the current bioinformatics pipeline, upon future characterisation of additional talin-binding motifs, the potential talin binders identified in this project may be analysed further to nonetheless assist in the identification of novel talin-binding ligands.

The development of an innovative method and the identification of many promising talin-binding ligands in the brain, i.e. dynamin-1, synaptojanin-1, and unconventional myosin-Va, is highly promising and may have a significant impact on future studies. Nevertheless, confirmation of binding is required to gain substantial evidence in support of the MeshCODE theory. This can be achieved through various methods, although GFP-Trap pulldowns may be the easiest option. However, the talin fragments also visualised on the SDS-PAGE gels following GFP-Trap bead binding, presumably created through degradation or incomplete translation, could be deemed a limitation, as they may increase the difficulty of determining whether binding has occurred. Although this may be overcome through optimisation of the method to ensure easier visualization for pulldowns and western blotting, modification of the GFP-talin rod construct could be considered. Currently, the GFP-talin rod used in this project had both a His and GFP tag at the N-terminus. If an N-terminal His-tagged talin rod construct was created with a C-terminal GFP tag, this may aid in reducing the additional bands visualised on the gel. The C-terminal GFP would ensure that only fully translated talin may bind to the GFP-Trap beads and would limit degradation to occur solely at the N-terminus. Moreover, if this persists, it may be reduced by adapting the method. Through the creation of this construct, the band representing GFP-talin R1-13 will appear more pronounced, enabling pulldowns to be conducted with ease. However, this may also prove detrimental as the additional fragments obtained through utilisation of the current construct could represent talin molecules with varying switch patterns. Therefore, pulldowns may demonstrate ligand binding which would not be identified solely by using the full construct of GFP-talin R1-13, whose rod domains are likely in their folded configuration. Nevertheless, if this is indeed the case, it may cause future difficulty when attempting to identify the binding loci, as recreating talin in that exact state may not be straightforward. Furthermore, the production of a GFP-talin 2 rod construct for future experiments may be highly beneficial, as whilst there is ~74-76% homology between the two talin isoforms, talin 2 is more predominantly expressed in the brain (Debrand et al., 2009; Goult et al., 2018).

Following a successful pulldown result, further characterisation of the interaction will be highly advantageous to determine both the binding kinetics and loci, i.e. from nuclear magnetic resonance spectroscopy and assays such as FP or microscale thermophoresis. This will enable the acquisition of sufficient evidence to conclusively determine that talin is indeed the predominant data storage molecule in the brain, thereby validating the mechanical basis of memory.

# 9 Side Project: Investigating Vinculin Interactions

The vinculin mutant Vcl$^{A50I}$ is considered a 'talin non-binding' mutant, and its expression in neocortical neurons led to the assumption that talin is not required for vinculin-mediated axon growth (Mandal et al., 2021). Following the utilisation of FP assays, it has been conclusively determined that whilst the A50I mutation in vinculin inhibits talin-vinculin binding at certain VBSs, such as talin R8 helix 33, it does not affect the binding at other VBSs, such as talin R2 helix 6 or R11 helix 50. Therefore, the A50I mutation can no longer be utilised to imitate a scenario independent of talin-vinculin binding, since that is not the case. As the A50I mutation in vinculin still permits talin-vinculin binding at multiple VBSs, with an affinity similar to wildtype vinculin, the role of talin in both the GFP-Vcl-FL$^{A50I}$ mutant and Vcl-FL wildtype groups from Mandal et al., 2021 is likely unchanged, and thus no conclusion can be made regarding the role of talin in vinculin-mediated axon growth from the results of this paper (Mandal et al., 2021). Successful crystallography trials for VD1$^{A50I}$ and helix 6 further support this conclusion; however, additional optimisation is required to determine the crystal structure depicting a VD1$^{A50I}$-talin H6 complex.

# 10 Final Conclusions

The development of a novel method to identify new talin-binding ligands has been successfully achieved in this project, which can be applied to a variety of cell types, enabling the expansion of adhesion protein identification previously limited to cell lines and fibroblasts. Optimisation of the method to perform MS proteomics in-house streamlined the process considerably, enabling the identification of talin binders to occur effectively, at greater convenience and proficiency. Through the application of the bioinformatics pipeline and subsequent scoring system established in this project, many proteins can be analysed to recognise probable talin binders via the identification and evaluation of the most promising talin-binding I/LD motifs. Whilst clear binding was not demonstrated between the I/LD motifs and rod domains selected for FP, the increase in FP observed between proteins of different scores, implies that both the bioinformatics pipeline and scoring system is effective in identifying the most promising talin binders, inferring its advantageous potential for future utilisation. The combined development of innovative experimental and bioinformatics methodology to identify novel talin binders, may not only provide an auspicious approach to greatly expand the current knowledge of adhesome proteins, but through optimisation may be adapted for a variety of different applications.

The recently published MeshCODE theory describes a model whereby data storage in the brain arises from the mechanicalistic action of talin, therefore creating the possibility that talin may play a greater, yet currently unexplored, role in synaptic transmission (Goult, 2021). Among the detection of many novel prospective talin-binding ligands in both CaSki cell lysate and murine neuronal extract, three extremely promising proteins with considerably high fold change values, dynamin-1, synaptojanin-1, and unconventional myosin-Va, were identified in this project. All three proteins exhibit particular significance to many aspects of synaptic transmission, with specific emphasis on their contributions to regulate the number of available vesicles or the probability of vesicular release. If binding to these proteins is confirmed in the future, it would represent a major step towards proving the MeshCODE theory, thereby enabling the scientific community to gain understanding regarding the enigma of memory storage at long last.

# 11 Bibliography

Akamatsu, M., Vasan, R., Serwas, D., Ferrin, M., Rangamani, P., & Drubin, D. G. (2020). Principles of self-organization and load adaptation by the actin cytoskeleton during clathrin-mediated endocytosis. *ELife*, *9*. https://doi.org/10.7554/ELIFE.49840

Antonny, B., Burd, C., Camilli, P. de, Chen, E., Daumke, O., Faelber, K., Ford, M., Frolov, V. A., Frost, A., Hinshaw, J. E., Kirchhausen, T., Kozlov, M. M., Lenz, M., Low, H. H., McMahon, H., Merrifield, C., Pollard, T. D., Robinson, P. J., Roux, A., & Schmid, S. (2016). Membrane fission by dynamin: what we know and what we need to know. *The EMBO Journal*, *35*(21), 2270–2284. https://doi.org/10.15252/EMBJ.201694613

Antonucci, F., Corradini, I., Fossati, G., Tomasoni, R., Menna, E., & Matteoli, M. (2016). SNAP-25, a Known presynaptic protein with emerging postsynaptic functions. *Frontiers in Synaptic Neuroscience*, *8*(MAR), 7. https://doi.org/10.3389/FNSYN.2016.00007/BIBTEX

Arias-Salgado, E. G., Lizano, S., Sarkar, S., Brugge, J. S., Ginsberg, M. H., & Shattil, S. J. (2003). Src kinase activation by direct interaction with the integrin β cytoplasmic domain. *Proceedings of the National Academy of Sciences of the United States of America*, *100*(23), 13298. https://doi.org/10.1073/PNAS.2336149100

Arpino, G., Somasundaram, A., Shin, W., Ge, L., Villareal, S., Chan, C. Y., Ashery, U., Shupliakov, O., Taraska, J. W., & Wu, L. G. (2022). Clathrin-mediated endocytosis cooperates with bulk endocytosis to generate vesicles. *IScience*, *25*(2), 103809. https://doi.org/10.1016/J.ISCI.2022.103809

Assis, L. H. P., Silva-Junior, R. M. P., Dolce, L. G., Alborghetti, M. R., Honorato, R. v., Nascimento, A. F. Z., Melo-Hanchuk, T. D., Trindade, D. M., Tonoli, C. C. C., Santos, C. T., Oliveira, P. S. L., Larson, R. E., Kobarg, J., Espreafico, E. M., Giuseppe, P. O., & Murakami, M. T. (2017). The molecular motor Myosin Va interacts with the cilia-centrosomal protein RPGRIP1L. *Scientific Reports 2017 7:1*, *7*(1), 1–10. https://doi.org/10.1038/srep43692

Atherton, P., Stutchbury, B., Wang, D. Y., Jethwa, D., Tsang, R., Meiler-Rodriguez, E., Wang, P., Bate, N., Zent, R., Barsukov, I. L., Goult, B. T., Critchley, D. R., & Ballestrem, C. (2015). Vinculin controls talin engagement with the actomyosin machinery. *Nature Communications 2015 6:1*, *6*(1), 1–12. https://doi.org/10.1038/ncomms10038

Baade, T., Paone, C., Baldrich, A., & Hauck, C. R. (2019). Clustering of integrin β cytoplasmic domains triggers nascent adhesion formation and reveals a protozoan origin of the integrin-talin interaction. *Scientific Reports 2019 9:1*, *9*(1), 1–13. https://doi.org/10.1038/s41598-019-42002-6

Barnett, S. F. H., & Goult, B. T. (2022). The MeshCODE to scale – Visualising synaptic binary information. *BioRxiv*, 2022.06.16.496395. https://doi.org/10.1101/2022.06.16.496395

Bateman, A., Martin, M. J., Orchard, S., Magrane, M., Agivetova, R., Ahmad, S., Alpi, E., Bowler-Barnett, E. H., Britto, R., Bursteinas, B., Bye-A-Jee, H., Coetzee, R., Cukura, A., da Silva, A., Denny, P., Dogan, T., Ebenezer, T. G., Fan, J., Castro, L. G., … Zhang, J. (2021). UniProt: the universal protein knowledgebase in 2021. *Nucleic Acids Research*, *49*(D1), D480–D489. https://doi.org/10.1093/NAR/GKAA1100

Bays, J. L., & DeMali, K. A. (2017). Vinculin in cell–cell and cell–matrix adhesions. *Cellular and Molecular Life Sciences*, *74*(16), 2999. https://doi.org/10.1007/S00018-017-2511-3

Beaty, B. T., Wang, Y., Bravo-Cordero, J. J., Sharma, V. P., Miskolci, V., Hodgson, L., & Condeelis, J. (2014). Talin regulates moesin-NHE-1 recruitment to invadopodia and promotes mammary tumor metastasis. *The Journal of Cell Biology*, *205*(5), 737–751. https://doi.org/10.1083/JCB.201312046

Berndt, K. D., & Birkbeck College. (1996, May 31). *4.2.1 Circular dichroism spectroscopy*. http://www.cryst.bbk.ac.uk/PPS2/course/section8/ss-960531_21.html

Bliss, T. V. P., & Cooke, S. F. (2011). Long-term potentiation and long-term depression: a clinical perspective. *Clinics*, *66*(Suppl 1), 3. https://doi.org/10.1590/S1807-59322011001300002

Bouaouina, M., Goult, B. T., Huet-Calderwood, C., Bate, N., Brahme, N. N., Barsukov, I. L., Critchley, D. R., & Calderwood, D. A. (2012). A conserved lipid-binding loop in the kindlin FERM F1 domain is required for kindlin-mediated αIIbβ3 integrin coactivation. *The Journal of Biological Chemistry*, *287*(10), 6979–6990. https://doi.org/10.1074/JBC.M111.330845

Bouaouina, M., Lad, Y., & Calderwood, D. A. (2008). The N-terminal Domains of Talin Cooperate with the Phosphotyrosine Binding-like Domain to Activate β1 and β3 Integrins *. *Journal of Biological Chemistry*, *283*(10), 6118–6125. https://doi.org/10.1074/JBC.M709527200

Bouchet, B. P., Gough, R. E., Ammon, Y. C., van de Willige, D., Post, H., Jacquemet, G., Maarten Altelaar, A. F., Heck, A. J. R., Goult, B. T., & Akhmanova, A. (2016). Talin-KANK1 interaction controls the recruitment of cortical microtubule stabilizing complexes to focal adhesions. *ELife*, *5*(JULY). https://doi.org/10.7554/ELIFE.18124

Cachope, R., Mackie, K., Triller, A., O'Brien, J., & Pereda, A. E. (2007). Potentiation of electrical and chemical synaptic transmission mediated by endocannabinoids. *Neuron*, *56*(6), 1034–1047. https://doi.org/10.1016/J.NEURON.2007.11.014

Calderwood, D. A., Campbell, I. D., & Critchley, D. R. (2013). Talins and kindlins; partners in integrin-mediated adhesion. *Nature Reviews. Molecular Cell Biology*, *14*(8), 503. https://doi.org/10.1038/NRM3624

Campbell, I. D., & Humphries, M. J. (2011). Integrin Structure, Activation, and Interactions. *Cold Spring Harbor Perspectives in Biology*, *3*(3), 1–14. https://doi.org/10.1101/CSHPERSPECT.A004994

Cao, H., Garcia, F., & McNiven, M. A. (1998). Differential distribution of dynamin isoforms in mammalian cells. *Molecular Biology of the Cell*, *9*(9), 2595–2609. https://doi.org/10.1091/MBC.9.9.2595

Carisey, A., & Ballestrem, C. (2011). Vinculin, an adapter protein in control of cell adhesion signalling. *European Journal of Cell Biology*, *90*(2–3), 157. https://doi.org/10.1016/J.EJCB.2010.06.007

Cassini, L., & Lee, J. (2018). On the synaptic tagging and capture hypothesis and the process of memory reconsolidation. *European Neuropsychopharmacology*, *28*, S56. https://doi.org/10.1016/J.EURONEURO.2017.12.087

Chappie, J. S., Acharya, S., Liu, Y. W., Leonard, M., Pucadyil, T. J., & Schmid, S. L. (2009). An Intramolecular Signaling Element that Modulates Dynamin Function In Vitro and In Vivo. *Molecular Biology of the Cell*, *20*(15), 3561. https://doi.org/10.1091/MBC.E09-04-0318

Chappie, J. S., Mears, J. A., Fang, S., Leonard, M., Schmid, S. L., Milligan, R. A., Hinshaw, J. E., & Dyda, F. (2011). A pseudo-atomic model of the dynamin polymer identifies a hydrolysis-dependent powerstroke. *Cell*, *147*(1), 209. https://doi.org/10.1016/J.CELL.2011.09.003

Cho, S. J., Lee, H., Dutta, S., Song, J., Walikonis, R., & Moon, I. S. (2011). Septin 6 Regulates the Cytoarchitecture of Neurons through Localization at Dendritic Branch Points and Bases of Protrusions. *Molecules and Cells*, *32*(1), 89. https://doi.org/10.1007/S10059-011-1048-9

Choo, C. K., Rorke, E. A., & Eckert, R. L. (1994). Differentiation-independent constitutive expression of the human papillomavirus type 16 E6 and E7 oncogenes in the CaSki cervical tumour cell line. *The Journal of General Virology*, *75 ( Pt 5)*(5), 1139–1147. https://doi.org/10.1099/0022-1317-75-5-1139

Choudhry, H., Aggarwal, M., & Pan, P. Y. (2021). Mini-review: Synaptojanin 1 and its implications in membrane trafficking. *Neuroscience Letters*, *765*, 136288. https://doi.org/10.1016/J.NEULET.2021.136288

Cigognini, D., Lomas, A., Kumar, P., Satyam, A., English, A., Azeem, A., Pandit, A., & Zeugolis, D. (2013). Engineering in vitro microenvironments for cell based therapies and drug discovery. *Drug Discovery Today*, *18*(21–22), 1099–1108. https://doi.org/10.1016/J.DRUDIS.2013.06.007

Cingolani, L. A., Thalhammer, A., Yu, L. M. Y., Catalano, M., Ramos, T., Colicos, M. A., & Goda, Y. (2008). Activity-Dependent Regulation of Synaptic AMPA Receptor Composition and Abundance by β3 Integrins. *Neuron*, *58*(5), 749–762. https://doi.org/10.1016/J.NEURON.2008.04.011/ATTACHMENT/55FF6E94-45F9-4AAC-9E87-4C184FACC465/MMC1.PDF

Clayton, E. L., Anggono, V., Smillie, K. J., Chau, N., Robinson, P. J., & Cousin, M. A. (2009). The phospho-dependent dynamin-syndapin interaction triggers activity-dependent bulk endocytosis of synaptic vesicles. *The Journal of Neuroscience : The Official Journal of the Society for Neuroscience*, *29*(24), 7706–7717. https://doi.org/10.1523/JNEUROSCI.1976-09.2009

Clayton, E. L., & Cousin, M. A. (2009). The Molecular Physiology of Activity-Dependent Bulk Endocytosis of Synaptic Vesicles. *Journal of Neurochemistry*, *111*(4), 901. https://doi.org/10.1111/J.1471-4159.2009.06384.X

Clayton, E. L., Evans, G. J. O., & Cousin, M. A. (2008). Bulk Synaptic Vesicle Endocytosis Is Rapidly Triggered during Strong Stimulation. *Journal of Neuroscience*, *28*(26), 6627–6632. https://doi.org/10.1523/JNEUROSCI.1445-08.2008

Clayton, E. L., Sue, N., Smillie, K. J., O'Leary, T., Bache, N., Cheung, G., Cole, A. R., Wyllie, D. J., Sutherland, C., Robinson, P. J., & Cousin, M. A. (2010). Dynamin I phosphorylation by GSK3 controls activity-dependent bulk endocytosis of synaptic vesicles. *Nature Neuroscience*, *13*(7), 845. https://doi.org/10.1038/NN.2571

Cocucci, E., Gaudin, R., & Kirchhausen, T. (2014). Dynamin recruitment and membrane scission at the neck of a clathrin-coated pit. *Molecular Biology of the Cell*, *25*(22), 3595–3609. https://doi.org/10.1091/MBC.E14-07-1240/ASSET/IMAGES/LARGE/3595FIG10.JPEG

Cohen, D. M., Chen, H., Johnson, R. P., Choudhury, B., & Craig, S. W. (2005). Two distinct head-tail interfaces cooperate to suppress activation of vinculin by talin. *Journal of Biological Chemistry*, *280*(17), 17109–17117. https://doi.org/10.1074/JBC.M414704200/ATTACHMENT/FBD13242-5A1B-4F79-B47D-2015DEADF4AE/MMC1.PDF

Collins, K. L., Gates, E. M., Gilchrist, C. L., & Hoffman, B. D. (2017). Bio-Instructive Cues in Scaffolds for Musculoskeletal Tissue Engineering and Regenerative Medicine. *Bio-Instructive Scaffolds for Musculoskeletal Tissue Engineering and Regenerative Medicine*, 3–35. https://doi.org/10.1016/B978-0-12-803394-4.00001-X

ConductScience. (2019, June 26). *Gel Filtration Chromatography Protocol – Conduct Science*. https://conductscience.com/gel-filtration-chromatography-protocol/

Connors, B. W., & Long, M. A. (2004). ELECTRICAL SYNAPSES IN THE MAMMALIAN BRAIN. *Http://Dx.Doi.Org/10.1146/Annurev.Neuro.26.041002.131128*, *27*, 393–418. https://doi.org/10.1146/ANNUREV.NEURO.26.041002.131128

Cousin, M. A. (2009). Activity-Dependent Bulk Synaptic Vesicle Endocytosis - a Fast, High Capacity Membrane Retrieval Mechanism. *Molecular Neurobiology*, *39*(3), 185. https://doi.org/10.1007/S12035-009-8062-3

Cousin, M. A., & Robinson, P. J. (2001). The dephosphins: dephosphorylation by calcineurin triggers synaptic vesicle endocytosis. *Trends in Neurosciences*, *24*(11), 659–665. https://doi.org/10.1016/S0166-2236(00)01930-5

Cremona, O., & de Camilli, P. (1997). Synaptic vesicle endocytosis. *Current Opinion in Neurobiology*, *7*(3), 323–330. https://doi.org/10.1016/S0959-4388(97)80059-1

Cremona, O., di Paolo, G., Wenk, M. R., Lüthi, A., Kim, W. T., Takei, K., Daniell, L., Nemoto, Y., Shears, S. B., Flavell, R. A., McCormick, D. A., & de Camilli, P. (1999). Essential Role of Phosphoinositide Metabolism in Synaptic Vesicle Recycling. *Cell*, *99*(2), 179–188. https://doi.org/10.1016/S0092-8674(00)81649-9

Debrand, E., Conti, F. J., Bate, N., Spence, L., Mazzeo, D., Pritchard, C. A., Monkley, S. J., & Critchley, D. R. (2012). Mice carrying a complete deletion of the talin2 coding sequence are viable and fertile. *Biochemical and Biophysical Research Communications*, *426*(2), 190–195. https://doi.org/10.1016/J.BBRC.2012.08.061

Debrand, E., el Jai, Y., Spence, L., Bate, N., Praekelt, U., Pritchard, C. A., Monkley, S. J., & Critchley, D. R. (2009). Talin 2 is a large and complex gene encoding multiple transcripts and protein isoforms. *The FEBS Journal*, *276*(6), 1610–1628. https://doi.org/10.1111/J.1742-4658.2009.06893.X

Delvendahl, I., Vyleta, N. P., von Gersdorff, H., & Hallermann, S. (2016). Fast, Temperature-Sensitive and Clathrin-Independent Endocytosis at Central Synapses. *Neuron*, *90*(3), 492–498. https://doi.org/10.1016/J.NEURON.2016.03.013/ATTACHMENT/71D47F99-C99A-433C-B1A9-7B80C9D249C2/MMC1.PDF

di Paolo, G., Pellegrini, L., Letinic, K., Cestra, G., Zoncu, R., Voronov, S., Chang, S., Guo, J., Wenk, M. R., & de Camilli, P. (2002). Recruitment and regulation of phosphatidylinositol phosphate kinase type 1γ by the FERM domain of talin. *Nature 2002 420:6911*, *420*(6911), 85–89. https://doi.org/10.1038/nature01147

Dickman, D. K., Tong, A., & Davis, G. W. (2012). Snapin is Critical for Presynaptic Homeostatic Plasticity. *The Journal of Neuroscience*, *32*(25), 8716. https://doi.org/10.1523/JNEUROSCI.5465-11.2012

Drin, G., Casella, J. F., Gautier, R., Boehmer, T., Schwartz, T. U., & Antonny, B. (2007). A general amphipathic α-helical motif for sensing membrane curvature. *Nature Structural & Molecular Biology 2007 14:2*, *14*(2), 138–146. https://doi.org/10.1038/nsmb1194

Dürst, C. D., Wiegert, J. S., Schulze, C., Helassa, N., Török, K., & Oertner, T. G. (2020). The vesicular release probability sets the strength of individual Schaffer collateral synapses. *BioRxiv*, 2020.08.02.232850. https://doi.org/10.1101/2020.08.02.232850

Evans, G. J. O., & Cousin, M. A. (2007). Activity-Dependent Control of Slow Synaptic Vesicle Endocytosis by Cyclin-Dependent Kinase 5. *Journal of Neuroscience*, *27*(2), 401–411. https://doi.org/10.1523/JNEUROSCI.3809-06.2007

Faber, D. S., & Pereda, A. E. (2018). Two forms of electrical transmission between neurons. *Frontiers in Molecular Neuroscience*, *11*, 427. https://doi.org/10.3389/FNMOL.2018.00427/BIBTEX

Feliciano, D., Bultema, J. J., Ambrosio, A. L., & di Pietro, S. M. (2011). In vivo and in vitro Studies of Adaptor-clathrin Interaction. *Journal of Visualized Experiments : JoVE*, *47*. https://doi.org/10.3791/2352

Ferguson, S. M., Brasnjo, G., Hayashi, M., Wölfel, M., Collesi, C., Giovedi, S., Raimondi, A., Gong, L. W., Ariel, P., Paradise, S., O'Toole, E., Flavell, R., Cremona, O., Miesenböck, G., Ryan, T. A., & de Camilli, P. (2007). A selective activity-dependent requirement for dynamin 1 in synaptic vesicle endocytosis. *Science (New York, N.Y.)*, *316*(5824), 570–574. https://doi.org/10.1126/SCIENCE.1140621

Ferguson, S. M., & de Camilli, P. (2012). Dynamin, a membrane-remodelling GTPase. *Nature Reviews Molecular Cell Biology 2012 13:2*, *13*(2), 75–88. https://doi.org/10.1038/nrm3266

Fesce, R., Grohovaz, F., Valtorta, F., & Meldolesi, J. (1994). Neurotransmitter release: fusion or "kiss-and-run"? *Trends in Cell Biology*, *4*(1), 1–4. https://doi.org/10.1016/0962-8924(94)90025-6

Fili, N., & Toseland, C. P. (2020). Unconventional Myosins: How Regulation Meets Function. *International Journal of Molecular Sciences*, *21*(1). https://doi.org/10.3390/IJMS21010067

Ford, M. G. J., Jenni, S., & Nunnari, J. (2011). The crystal structure of dynamin. *Nature*, *477*(7366), 561. https://doi.org/10.1038/NATURE10441

Frey, U., & Morris, R. G. M. (1997). Synaptic tagging and long-term potentiation. *Nature 1997 385:6616*, *385*(6616), 533–536. https://doi.org/10.1038/385533a0

Furse, S., Brooks, N. J., Seddon, A. M., Woscholski, R., Templer, R. H., Tate, E. W., Gaffney, P. R. J., & Ces, O. (2012). Lipid membrane curvature induced by distearoyl phosphatidylinositol 4-phosphate. *Soft Matter*, *8*(11), 3090–3093. https://doi.org/10.1039/C2SM07358G

Gasteiger, E., Hoogland, C., Gattiker, A., Duvaud, S., Wilkins, M. R., Appel, R. D., & Bairoch, A. (2005). Protein Identification and Analysis Tools on the ExPASy Server. *The Proteomics Protocols Handbook*, 571–607. https://doi.org/10.1385/1-59259-890-0:571

George, A. A., Hayden, S., Stanton, G. R., & Brockerhoff, S. E. (2016). Arf6 and the 5'phosphatase of Synaptojanin 1 regulate autophagy in cone photoreceptors. *Inside the Cell*, *1*(2), 117–133. https://doi.org/10.1002/ICL3.1044

Gingras, A. R., Bate, N., Goult, B. T., Hazelwood, L., Canestrelli, I., Grossmann, J. G., Liu, H. J., Putz, N. S. M., Roberts, G. C. K., Volkmann, N., Hanein, D., Barsukov, I. L., & Critchley, D. R. (2008). The structure of the C-terminal actin-binding domain of talin. *The EMBO Journal*, *27*(2), 458–469. https://doi.org/10.1038/SJ.EMBOJ.7601965

Gingras, A. R., Bate, N., Goult, B. T., Patel, B., Kopp, P. M., Emsley, J., Barsukov, I. L., Roberts, G. C. K., & Critchley, D. R. (2010). Central Region of Talin Has a Unique Fold That Binds Vinculin and Actin. *The Journal of Biological Chemistry*, *285*(38), 29577. https://doi.org/10.1074/JBC.M109.095455

Gingras, A. R., Ziegler, W. H., Frank, R., Barsukov, I. L., Roberts, G. C. K., Critchley, D. R., & Emsley, J. (2005). Mapping and consensus sequence identification for multiple vinculin binding sites within the talin rod. *Journal of Biological Chemistry*, *280*(44), 37217–37224. https://doi.org/10.1074/JBC.M508060200/ATTACHMENT/62E52CFB-6A38-4CA5-B9AE-A9C877181E21/MMC1.PDF

Ginsberg, M. H., Partridge, A., & Shattil, S. J. (2005). Integrin regulation. *Current Opinion in Cell Biology*, *17*(5), 509–516. https://doi.org/10.1016/J.CEB.2005.08.010

Goley, E. D., & Welch, M. D. (2006). The ARP2/3 complex: an actin nucleator comes of age. *Nature Reviews Molecular Cell Biology 2006 7:10*, *7*(10), 713–726. https://doi.org/10.1038/nrm2026

Golji, J., & Mofrad, M. R. K. (2010). A Molecular Dynamics Investigation of Vinculin Activation. *Biophysical Journal*, *99*(4), 1073. https://doi.org/10.1016/J.BPJ.2010.05.024

Golji, J., Wendorff, T., & Mofrad, M. R. K. (2012). Phosphorylation Primes Vinculin for Activation. *Biophysical Journal*, *102*(9), 2022. https://doi.org/10.1016/J.BPJ.2012.01.062

Gough, R. E., & Goult, B. T. (2018). The tale of two talins – two isoforms to fine-tune integrin signalling. *FEBS Letters*, *592*(12), 2108–2125. https://doi.org/10.1002/1873-3468.13081

Gough, R. E., Jones, M. C., Zacharchenko, T., Le, S., Yu, M., Jacquemet, G., Muench, S. P., Yan, J., Humphries, J. D., Jørgensen, C., Humphries, M. J., & Goult, B. T. (2021). Talin mechanosensitivity is modulated by a direct interaction with cyclin-dependent kinase-1. *Journal of Biological Chemistry*, *297*(1). https://doi.org/10.1016/J.JBC.2021.100837/ATTACHMENT/1BDDCDE4-4620-4A3E-A646-2ED6CE8BF295/MMC3.PDF

Goult, B. T. (2021). The Mechanical Basis of Memory – the MeshCODE Theory. *Frontiers in Molecular Neuroscience*, *14*, 21. https://doi.org/10.3389/FNMOL.2021.592951/BIBTEX

Goult, B. T., Bate, N., Anthis, N. J., Wegener, K. L., Gingras, A. R., Patel, B., Barsukov, I. L., Campbell, I. D., Roberts, G. C. K., & Critchley, D. R. (2009). The Structure of an Interdomain Complex That Regulates Talin Activity. *The Journal of Biological Chemistry*, *284*(22), 15097. https://doi.org/10.1074/JBC.M900078200

Goult, B. T., Bouaouina, M., Harburger, D. S., Bate, N., Patel, B., Anthis, N. J., Campbell, I. D., Calderwood, D. A., Barsukov, I. L., Roberts, G. C., & Critchley, D. R. (2009). The structure of the N-terminus of kindlin-1: a domain important for alphaiibbeta3 integrin activation. *Journal of Molecular Biology*, *394*(5), 944–956. https://doi.org/10.1016/J.JMB.2009.09.061

Goult, B. T., Yan, J., & Schwartz, M. A. (2018). Talin as a mechanosensitive signaling hub. *Journal of Cell Biology*, *217*(11), 3776–3784. https://doi.org/10.1083/JCB.201808061

Goult, B. T., Zacharchenko, T., Bate, N., Tsang, R., Hey, F., Gingras, A. R., Elliott, P. R., Roberts, G. C. K., Ballestrem, C., Critchley, D. R., & Barsukov, I. L. (2013). RIAM and vinculin binding to talin are mutually exclusive and regulate adhesion assembly and turnover. *Journal of Biological Chemistry*, *288*(12), 8238–8249. https://doi.org/10.1074/JBC.M112.438119/ATTACHMENT/4F92C301-4898-4990-A4C8-1E69A19C5A34/MMC1.PDF

Granseth, B., Odermatt, B., Royle, S. J. J., & Lagnado, L. (2006). Clathrin-Mediated Endocytosis Is the Dominant Mechanism of Vesicle Retrieval at Hippocampal Synapses. *Neuron*, *51*(6), 773–786. https://doi.org/10.1016/J.NEURON.2006.08.029

GraphPad. (2020). *GraphPad Prism 9 Curve Fitting Guide - Equation: One site -- Total binding*. https://www.graphpad.com/guides/prism/latest/curve-fitting/reg_one_site_total.htm

Grashoff, C., Hoffman, B. D., Brenner, M. D., Zhou, R., Parsons, M., Yang, M. T., McLean, M. A., Sligar, S. G., Chen, C. S., Ha, T., & Schwartz, M. A. (2010). Measuring mechanical tension across vinculin reveals regulation of focal adhesion dynamics. *Nature*, *466*(7303), 263. https://doi.org/10.1038/NATURE09198

Han, J., Pluhackova, K., & Böckmann, R. A. (2017). The multifaceted role of SNARE proteins in membrane fusion. *Frontiers in Physiology*, *8*(JAN), 5. https://doi.org/10.3389/FPHYS.2017.00005/BIBTEX

Harjunpää, H., Asens, M. L., Guenther, C., & Fagerholm, S. C. (2019). Cell adhesion molecules and their roles and regulation in the immune and tumor microenvironment. *Frontiers in Immunology*, *10*(MAY), 1078. https://doi.org/10.3389/FIMMU.2019.01078/BIBTEX

Harris, T. W., Hartwieg, E., Horvitz, H. R., & Jorgensen, E. M. (2000). Mutations in Synaptojanin Disrupt Synaptic Vesicle Recycling. *The Journal of Cell Biology*, *150*(3), 589. https://doi.org/10.1083/JCB.150.3.589

Hino, N., Ichikawa, T., Kimura, Y., Matsuda, M., Ueda, K., & Kioka, N. (2019). An amphipathic helix of vinexin α is necessary for a substrate stiffness-dependent conformational change in vinculin. *Journal of Cell Science*, *132*(2). https://doi.org/10.1242/JCS.217349/265613/AM/AN-AMPHIPATHIC-HELIX-OF-VINEXIN-IS-NECESSARY-FOR

Ho, C. S., Lam, C. W. K., Chan, M. H. M., Cheung, R. C. K., Law, L. K., Lit, L. C. W., Ng, K. F., Suen, M. W. M., & Tai, H. L. (2003). Electrospray Ionisation Mass Spectrometry: Principles and Clinical Applications. *The Clinical Biochemist Reviews*, *24*(1), 3. /pmc/articles/PMC1853331/

Humphries, J. D., Wang, P., Streuli, C., Geiger, B., Humphries, M. J., & Ballestrem, C. (2007). Vinculin controls focal adhesion formation by direct interactions with talin and actin. *Journal of Cell Biology*, *179*(5), 1043–1057. https://doi.org/10.1083/JCB.200703036/VIDEO-4

Izard, T., Evans, G., Borgon, R. A., Rush, C. L., Bricogne, G., & Bois, P. R. J. (2003). Vinculin activation by talin through helical bundle conversion. *Nature 2004 427:6970*, *427*(6970), 171–175. https://doi.org/10.1038/nature02281

Janiszewska, M., Primi, M. C., & Izard, T. (2020). Cell adhesion in cancer: Beyond the migration of single cells. *Journal of Biological Chemistry*, *295*(8), 2495–2505. https://doi.org/10.1074/JBC.REV119.007759

Kahner, B. N., Kato, H., Banno, A., Ginsberg, M. H., Shattil, S. J., & Ye, F. (2012). Kindlins, Integrin Activation and the Regulation of Talin Recruitment to αIIbβ3. *PLOS ONE*, *7*(3), e34056. https://doi.org/10.1371/JOURNAL.PONE.0034056

Kaizuka, T., & Takumi, T. (2018). Postsynaptic density proteins and their involvement in neurodevelopmental disorders. *The Journal of Biochemistry*, *163*(6), 447–455. https://doi.org/10.1093/JB/MVY022

Kaplan, C., Steinmann, M., Zapiorkowska, N. A., & Ewers, H. (2017). Functional redundancy of septin homologs in dendritic branching. *Frontiers in Cell and Developmental Biology*, *5*(FEB), 11. https://doi.org/10.3389/FCELL.2017.00011/BIBTEX

Karimi, F., O'Connor, A. J., Qiao, G. G., & Heath, D. E. (2018). Integrin Clustering Matters: A Review of Biomaterials Functionalized with Multivalent Integrin-Binding Ligands to Improve Cell Adhesion, Migration, Differentiation, Angiogenesis, and Biomedical Device Integration. *Advanced Healthcare Materials*, *7*(12), 1701324. https://doi.org/10.1002/ADHM.201701324

Kasprowicz, J., Kuenen, S., Swerts, J., Miskiewicz, K., & Verstreken, P. (2014). Dynamin photoinactivation blocks Clathrin and α-adaptin recruitment and induces bulk membrane retrieval. *The Journal of Cell Biology*, *204*(7), 1141. https://doi.org/10.1083/JCB.201310090

Khan, R. B., & Goult, B. T. (2019). Adhesions Assemble!—Autoinhibition as a Major Regulatory Mechanism of Integrin-Mediated Adhesion. *Frontiers in Molecular Biosciences*, *6*, 144. https://doi.org/10.3389/FMOLB.2019.00144/BIBTEX

Kilinc, D. (2018). The emerging role of mechanics in synapse formation and plasticity. *Frontiers in Cellular Neuroscience*, *12*, 483. https://doi.org/10.3389/FNCEL.2018.00483/BIBTEX

Kioka, N., Sakata, S., Kawauchi, T., Amachi, T., Akiyama, S. K., Okazaki, K., Yaen, C., Yamada, K. M., & Aota, S. (1999). Vinexin: A Novel Vinculin-binding Protein with Multiple SH3 Domains Enhances Actin Cytoskeletal Organization. *Journal of Cell Biology*, *144*(1), 59–69. https://doi.org/10.1083/JCB.144.1.59

Kneussel, M., & Wagner, W. (2013). Myosin motors at neuronal synapses: drivers of membrane transport and actin dynamics. *Nature Reviews Neuroscience 2013 14:4*, *14*(4), 233–247. https://doi.org/10.1038/nrn3445

Kononenko, N. L., Puchkov, D., Classen, G. A., Walter, A. M., Pechstein, A., Sawade, L., Kaempf, N., Trimbuch, T., Lorenz, D., Rosenmund, C., Maritzen, T., & Haucke, V. (2014). Clathrin/AP-2 mediate synaptic vesicle reformation from endosome-like vacuoles but are not essential for membrane retrieval at central synapses. *Neuron*, *82*(5), 981–988. https://doi.org/10.1016/J.NEURON.2014.05.007

Kumar, A. (2011). Long-term potentiation at CA3-CA1 hippocampal synapses with special emphasis on aging, disease, and stress. *Frontiers in Aging Neuroscience*, *3*(MAY), 1–20. https://doi.org/10.3389/FNAGI.2011.00007/BIBTEX

Kwiatkowski, A. v., Gertler, F. B., & Loureiro, J. J. (2003). Function and regulation of Ena/VASP proteins. *Trends in Cell Biology*, *13*(7), 386–392. https://doi.org/10.1016/S0962-8924(03)00130-2

Landismari, C. E., & Connors, B. W. (2005). Long-term modulation of electrical synapses in the mammalian thalamus. *Science (New York, N.Y.)*, *310*(5755), 1809–1813. https://doi.org/10.1126/SCIENCE.1114655

Leal, G., Bramham, C. R., & Duarte, C. B. (2017). BDNF and Hippocampal Synaptic Plasticity. *Vitamins and Hormones*, *104*, 153–195. https://doi.org/10.1016/BS.VH.2016.10.004

Lemmon, S. K. (2001). Clathrin uncoating: Auxilin comes to life. *Current Biology*, *11*(2), R49–R52. https://doi.org/10.1016/S0960-9822(01)00010-0

Lesch, K. P., & Schmitt, A. (2002). Antidepressants and gene expression profiling: How to SNARE novel drug targets. *Pharmacogenomics Journal*, *2*(6), 346–348. https://doi.org/10.1038/SJ.TPJ.6500150

Levy, A. D., Omar, M. H., & Koleske, A. J. (2014). Extracellular matrix control of dendritic spine and synapse structure and plasticity in adulthood. *Frontiers in Neuroanatomy*, *8*(OCT). https://doi.org/10.3389/FNANA.2014.00116

Li, G., Du, X., Vass, W. C., Papageorge, A. G., Lowy, D. R., & Qian, X. (2011). Full activity of the deleted in liver cancer 1 (DLC1) tumor suppressor depends on an LD-like motif that binds talin and focal adhesion kinase (FAK). *Proceedings of the National Academy of Sciences of the United States of America*, *108*(41), 17129–17134. https://doi.org/10.1073/PNAS.1112122108/-/DCSUPPLEMENTAL

Li, T. N., Chen, Y. J., Lu, T. Y., Wang, Y. T., Lin, H. C., & Yao, C. K. (2020). A positive feedback loop between flower and pi(4,5)p2 at periactive zones controls bulk endocytosis in drosophila. *ELife*, *9*, 1–33. https://doi.org/10.7554/ELIFE.60125

Liu, J., Wang, Y., Goh, W. I., Goh, H., Baird, M. A., Ruehland, S., Teo, S., Bate, N., Critchley, D. R., Davidson, M. W., & Kanchanawong, P. (2015). Talin determines the nanoscale architecture of focal adhesions. *Proceedings of the National Academy of Sciences of the United States of America*, *112*(35), E4864–E4873. https://doi.org/10.1073/PNAS.1512025112/SUPPL_FILE/PNAS.201512025SI.PDF

Lodish, H. (2007). *Molecular Cell Biology* (6th Edition). W.H. Freeman.

López-Colomé, A. M., Lee-Rivera, I., Benavides-Hidalgo, R., & López, E. (2017). Paxillin: a crossroad in pathological cell migration. *Journal of Hematology & Oncology 2017 10:1*, *10*(1), 1–15. https://doi.org/10.1186/S13045-017-0418-Y

Lovinger, D. M. (2008). Communication Networks in the Brain: Neurons, Receptors, Neurotransmitters, and Alcohol. *Alcohol Research & Health*, *31*(3), 196. /pmc/articles/PMC3860493/

Luo, B. H., Carman, C. v., & Springer, T. A. (2007). Structural Basis of Integrin Regulation and Signaling. *Annual Review of Immunology*, *25*, 619. https://doi.org/10.1146/ANNUREV.IMMUNOL.25.022106.141618

Ma, Y., Juntti, S. A., Hu, C. K., Huguenard, J. R., & Fernald, R. D. (2015). Electrical synapses connect a network of gonadotropin releasing hormone neurons in a cichlid fish. *Proceedings of the National Academy of Sciences of the United States of America*, *112*(12), 3805–3810. https://doi.org/10.1073/PNAS.1421851112/SUPPL_FILE/PNAS.1421851112.SM01.AVI

Madeira, F., Park, Y. M., Lee, J., Buso, N., Gur, T., Madhusoodanan, N., Basutkar, P., Tivey, A. R. N., Potter, S. C., Finn, R. D., & Lopez, R. (2019). The EMBL-EBI search and sequence analysis tools APIs in 2019. *Nucleic Acids Research*, *47*(W1), W636–W641. https://doi.org/10.1093/NAR/GKZ268

Mandal, P., Belapurkar, V., Nair, D., & Ramanan, N. (2021). Vinculin-mediated axon growth requires interaction with actin but not talin in mouse neocortical neurons. *Cellular and Molecular Life Sciences*, *78*(15), 5807–5826. https://doi.org/10.1007/S00018-021-03879-7/FIGURES/7

Mani, M., Lee, S. Y., Lucast, L., Cremona, O., di Paolo, G., de Camilli, P., & Ryan, T. A. (2007). The dual phosphatase activity of Synaptojanin1 is required for both efficient synaptic vesicle internalization and re-availability at nerve terminals. *Neuron*, *56*(6), 1004–1018. https://doi.org/10.1016/J.NEURON.2007.10.032

Maschi, D., Gramlich, M. W., & Klyachko, V. A. (2018). Myosin V functions as a vesicle tether at the plasma membrane to control neurotransmitter release in central synapses. *ELife*, *7*. https://doi.org/10.7554/ELIFE.39440

Maschi, D., Gramlich, M. W., & Klyachko, V. A. (2021). Myosin V Regulates Spatial Localization of Different Forms of Neurotransmitter Release in Central Synapses. *Frontiers in Synaptic Neuroscience*, *13*, 15. https://doi.org/10.3389/FNSYN.2021.650334/BIBTEX

Maschi, D., & Klyachko, V. A. (2020). Spatiotemporal dynamics of multi-vesicular release is determined by heterogeneity of release sites within central synapses. *ELife*, *9*. https://doi.org/10.7554/ELIFE.55210

McGuffin, L. J., Bryson, K., & Jones, D. T. (2000). The PSIPRED protein structure prediction server. *Bioinformatics*, *16*(4), 404–405. https://doi.org/10.1093/BIOINFORMATICS/16.4.404

Milosevic, I. (2018). Revisiting the role of clathrin-mediated endoytosis in synaptic vesicle recycling. *Frontiers in Cellular Neuroscience*, *12*, 27. https://doi.org/10.3389/FNCEL.2018.00027/BIBTEX

Mishra, Y. G., & Manavathi, B. (2021). Focal adhesion dynamics in cellular function and disease. *Cellular Signalling*, *85*, 110046. https://doi.org/10.1016/J.CELLSIG.2021.110046

Moerke, N. J. (2009). Fluorescence Polarization (FP) Assays for Monitoring Peptide-Protein or Nucleic Acid-Protein Binding. *Current Protocols in Chemical Biology*, *1*(1), 1–15. https://doi.org/10.1002/9780470559277.CH090102

Morgan, J. R., di Paolo, G., Werner, H., Shchedrina, V. A., Pypaert, M., Pieribone, V. A., & de Camilli, P. (2004). A role for talin in presynaptic function. *The Journal of Cell Biology*, *167*(1), 43. https://doi.org/10.1083/JCB.200406020

Morgan, J. R., Skye Comstra, H., Cohen, M., & Faundez, V. (2013). Presynaptic Membrane Retrieval and Endosome Biology: Defining Molecularly Heterogeneous Synaptic Vesicles. *Cold Spring Harbor Perspectives in Biology*, *5*(10). https://doi.org/10.1101/CSHPERSPECT.A016915

Morton, A., Marland, J. R. K., & Cousin, M. A. (2015). Synaptic vesicle exocytosis and increased cytosolic calcium are both necessary but not sufficient for activity-dependent bulk endocytosis. *Journal of Neurochemistry*, *134*(3), 405–415. https://doi.org/10.1111/JNC.13132

Mostowy, S., & Cossart, P. (2012). Septins: the fourth component of the cytoskeleton. *Nature Reviews Molecular Cell Biology 2012 13:3*, *13*(3), 183–194. https://doi.org/10.1038/nrm3284

Nemoto, Y., Arribas, M., Haffner, C., & DeCamilli, P. (1997). Synaptojanin 2, a novel synaptojanin isoform with a distinct targeting domain and expression pattern. *The Journal of Biological Chemistry*, *272*(49), 30817–30821. https://doi.org/10.1074/JBC.272.49.30817

Nguyen, T. H., Maucort, G., Sullivan, R. K. P., Schenning, M., Lavidis, N. A., McCluskey, A., Robinson, P. J., & Meunier, F. A. (2012). Actin- and Dynamin-Dependent Maturation of Bulk Endocytosis Restores Neurotransmission following Synaptic Depletion. *PLoS ONE*, *7*(5). https://doi.org/10.1371/JOURNAL.PONE.0036913

Okuno, H., Minatohara, K., & Bito, H. (2018). Inverse synaptic tagging: An inactive synapse-specific mechanism to capture activity-induced Arc/arg3.1 and to locally regulate spatial distribution of synaptic weights. *Seminars in Cell & Developmental Biology*, *77*, 43–50. https://doi.org/10.1016/J.SEMCDB.2017.09.025

Pan, P. Y., Tian, J. H., & Sheng, Z. H. (2009). Snapin facilitates the synchronization of synaptic vesicle fusion. *Neuron*, *61*(3), 412. https://doi.org/10.1016/J.NEURON.2008.12.029

Pandian, S., Zhao, J. P., Murata, Y., Bustos, F. J., Tunca, C., Almeida, R. D., & Constantine-Paton, M. (2020). Myosin Va Brain-Specific Mutation Alters Mouse Behavior and Disrupts Hippocampal Synapses. *ENeuro*, *7*(6). https://doi.org/10.1523/ENEURO.0284-20.2020

Peng, Y. J., Geng, J., Wu, Y., Pinales, C., Langen, J., Chang, Y. C., Buser, C., & Chang, K. T. (2021). Minibrain kinase and calcineurin coordinate activity-dependent bulk endocytosis through synaptojanin. *Journal of Cell Biology*, *220*(12). https://doi.org/10.1083/JCB.202011028/212674

Pereda, A. E. (2014). Electrical synapses and their functional interactions with chemical synapses. *Nature Reviews Neuroscience 2014 15:4*, *15*(4), 250–263. https://doi.org/10.1038/nrn3708

Pereda, A. E., Bell, T. D., Chang, B. H., Czernik, A. J., Nairn, A. C., Soderling, T. R., & Faber, D. S. (1998). Ca2+/calmodulin-dependent kinase II mediates simultaneous enhancement of gap-junctional conductance and glutamatergic transmission. *Proceedings of the National Academy of Sciences of the United States of America*, *95*(22), 13272–13277. https://doi.org/10.1073/PNAS.95.22.13272

Perera, R. M., Zoncu, R., Lucast, L., de Camilli, P., & Toomre, D. (2006). Two synaptojanin 1 isoforms are recruited to clathrin-coated pits at different stages. *Proceedings of the National Academy of Sciences of the United States of America*, *103*(51), 19332–19337. https://doi.org/10.1073/PNAS.0609795104

Pollastri, G., & McLysaght, A. (2005). Porter: a new, accurate server for protein secondary structure prediction. *Bioinformatics*, *21*(8), 1719–1720. https://doi.org/10.1093/BIOINFORMATICS/BTI203

Prekeris, R., & Terrian, D. M. (1997). Brain Myosin V Is a Synaptic Vesicle-associated Motor Protein: Evidence for a Ca2+-dependent Interaction with the Synaptobrevin–Synaptophysin Complex. *Journal of Cell Biology*, *137*(7), 1589–1601. https://doi.org/10.1083/JCB.137.7.1589

Purves, D., Augustine, G. J., Fitzpatrick, D., Hall, W. C., LaMantia, A.-S., McNamara, J. O., & Williams, S. M. (2004). *Neuroscience* (3rd Edition). Sunderland.

Ramiro-Cortés, Y., Hobbiss, A. F., & Israely, I. (2014). Synaptic competition in structural plasticity and cognitive function. *Philosophical Transactions of the Royal Society B: Biological Sciences*, *369*(1633). https://doi.org/10.1098/RSTB.2013.0157

Ringstad, N., Gad, H., Löw, P., di Paolo, G., Brodin, L., Shupliakov, O., & de Camilli, P. (1999). Endophilin/SH3p4 is required for the transition from early to late stages in clathrin-mediated synaptic vesicle endocytosis. *Neuron*, *24*(1), 143–154. https://doi.org/10.1016/S0896-6273(00)80828-4

Rodal, A. A., & Littleton, J. T. (2008). Synaptic Endocytosis: Illuminating the Role of Clathrin Assembly. *Current Biology*, *18*(6), R259–R261. https://doi.org/10.1016/J.CUB.2008.02.014

Rognoni, E., Ruppert, R., & Fässler, R. (2016). The kindlin family: functions, signaling properties and implications for human disease. *Journal of Cell Science*, *129*(1), 17–27. https://doi.org/10.1242/JCS.161190

Rudolf, R., Bittins, C. M., & Gerdes, H. H. (2011). The role of myosin V in exocytosis and synaptic plasticity. *Journal of Neurochemistry*, *116*(2), 177–191. https://doi.org/10.1111/J.1471-4159.2010.07110.X

Saheki, Y., & de Camilli, P. (2012). Synaptic Vesicle Endocytosis. *Cold Spring Harbor Perspectives in Biology*, *4*(9). https://doi.org/10.1101/CSHPERSPECT.A005645

Sang, Y. L., Voronov, S., Letinic, K., Nairn, A. C., di Paolo, G., & de Camilli, P. (2005). Regulation of the interaction between PIPKIγ and talin by proline-directed protein kinases. *Journal of Cell Biology*, *168*(5), 789–799. https://doi.org/10.1083/JCB.200409028

Sauvola, C. W., & Littleton, J. T. (2021). SNARE Regulatory Proteins in Synaptic Vesicle Fusion and Recycling. *Frontiers in Molecular Neuroscience*, *14*, 165. https://doi.org/10.3389/FNMOL.2021.733138/BIBTEX

Schnell, E., & Nicoll, R. A. (2001). Hippocampal synaptic transmission and plasticity are preserved in myosin Va mutant mice. *Journal of Neurophysiology*, *85*(4), 1498–1501. https://doi.org/10.1152/JN.2001.85.4.1498

Sechi, A. S., & Wehland, J. (2000). The actin cytoskeleton and plasma membrane connection: PtdIns(4,5)P(2) influences cytoskeletal protein activity at the plasma membrane. *Journal of Cell Science*, *113*(21), 3685–3695. https://doi.org/10.1242/JCS.113.21.3685

Shattil, S. J., Kim, C., & Ginsberg, M. H. (2010). The final steps of integrin activation: the end game. *Nature Reviews. Molecular Cell Biology*, *11*(4), 288. https://doi.org/10.1038/NRM2871

Shen, B., Delaney, M. K., & Du, X. (2012). Inside-out, outside-in, and inside-outside-in: G protein signaling in integrin-mediated cell adhesion, spreading, and retraction. *Current Opinion in Cell Biology*, *24*(5), 600. https://doi.org/10.1016/J.CEB.2012.08.011

Shupliakov, O., Bloom, O., Gustafsson, J. S., Kjaerulff, O., Löw, P., Tomilin, N., Pieribone, V. A., Greengard, P., & Brodin, L. (2002). Impaired recycling of synaptic vesicles after acute perturbation of the presynaptic actin cytoskeleton. *Proceedings of the National Academy of*

*Sciences of the United States of America*, *99*(22), 14476. https://doi.org/10.1073/PNAS.212381799

Smith, S. M., Renden, R., & von Gersdorff, H. (2008). Synaptic vesicle endocytosis: fast and slow modes of membrane retrieval. *Trends in Neurosciences*, *31*(11), 559. https://doi.org/10.1016/J.TINS.2008.08.005

Soe, Z. Y., Park, E. J., & Shimaoka, M. (2021). Integrin Regulation in Immunological and Cancerous Cells and Exosomes. *International Journal of Molecular Sciences 2021, Vol. 22, Page 2193*, *22*(4), 2193. https://doi.org/10.3390/IJMS22042193

Song, X., Yang, J., Hirbawi, J., Ye, S., Perera, H. D., Goksoy, E., Dwivedi, P., Plow, E. F., Zhang, R., & Qin, J. (2012). A novel membrane-dependent on/off switch mechanism of talin FERM domain at sites of cell adhesion. *Cell Research 2012 22:11*, *22*(11), 1533–1545. https://doi.org/10.1038/cr.2012.97

Soykan, T., Kaempf, N., Sakaba, T., Vollweiter, D., Goerdeler, F., Puchkov, D., Kononenko, N. L., & Haucke, V. (2017). Synaptic Vesicle Endocytosis Occurs on Multiple Timescales and Is Mediated by Formin-Dependent Actin Assembly. *Neuron*, *93*(4), 854-866.e4. https://doi.org/10.1016/J.NEURON.2017.02.011/ATTACHMENT/7340A4E6-9183-42F9-BC76-CE24AE96FA0B/MMC1.PDF

Stevens, C. F., & Williams, J. H. (2000). “Kiss and run” exocytosis at hippocampal synapses. *Proceedings of the National Academy of Sciences of the United States of America*, *97*(23), 12828–12833. https://doi.org/10.1073/PNAS.230438697/ASSET/C9BC3404-AB41-4385-9D94-5336F63C01DF/ASSETS/GRAPHIC/PQ2304386004.JPEG

Südhof, T. C., & Rizo, J. (2011). Synaptic Vesicle Exocytosis. *Cold Spring Harbor Perspectives in Biology*, *3*(12). https://doi.org/10.1101/CSHPERSPECT.A005637

Sun, Z., Costell, M., & Fässler, R. (2019). Integrin activation by talin, kindlin and mechanical forces. *Nature Cell Biology 2019 21:1*, *21*(1), 25–31. https://doi.org/10.1038/s41556-018-0234-9

Takada, Y., Ye, X., & Simon, S. (2007). The integrins. *Genome Biology*, *8*(5), 1–9. https://doi.org/10.1186/GB-2007-8-5-215/FIGURES/4

Takamori, S., Holt, M., Stenius, K., Lemke, E. A., Grønborg, M., Riedel, D., Urlaub, H., Schenck, S., Brügger, B., Ringler, P., Müller, S. A., Rammner, B., Gräter, F., Hub, J. S., de Groot, B. L., Mieskes, G., Moriyama, Y., Klingauf, J., Grubmüller, H., … Jahn, R. (2006). Molecular anatomy of a trafficking organelle. *Cell*, *127*(4), 831–846. https://doi.org/10.1016/J.CELL.2006.10.030

Takenawa, T., & Miki, H. (2001). WASP and WAVE family proteins: key molecules for rapid rearrangement of cortical actin filaments and cell movement. *Journal of Cell Science*, *114*(Pt 10), 1801–1809. https://doi.org/10.1242/JCS.114.10.1801

Theodosiou, M., Widmaier, M., Böttcher, R. T., Rognoni, E., Veelders, M., Bharadwaj, M., Lambacher, A., Austen, K., Müller, D. J., Zent, R., & Fässler, R. (2016). Kindlin-2 cooperates with talin to activate integrins and induces cell spreading by directly binding paxillin. *ELife*, *5*(JANUARY2016). https://doi.org/10.7554/ELIFE.10130

Tran Van Nhieu, G., & Izard, T. (2007). Vinculin binding in its closed conformation by a helix addition mechanism. *The EMBO Journal*, *26*(21), 4588. https://doi.org/10.1038/SJ.EMBOJ.7601863

Turrigiano, G. G. (2008). The Self-Tuning Neuron: Synaptic Scaling of Excitatory Synapses. *Cell*, *135*(3), 422. https://doi.org/10.1016/J.CELL.2008.10.008

Ussar, S., Wang, H. V., Linder, S., Fässler, R., & Moser, M. (2006). The Kindlins: Subcellular localization and expression during murine development. *Experimental Cell Research*, *312*(16), 3142–3151. https://doi.org/10.1016/J.YEXCR.2006.06.030

Vanhauwaert, R., Kuenen, S., Masius, R., Bademosi, A., Manetsberger, J., Schoovaerts, N., Bounti, L., Gontcharenko, S., Swerts, J., Vilain, S., Picillo, M., Barone, P., Munshi, S. T., Vrij, F. M. de, Kushner, S. A., Gounko, N. v, Mandemakers, W., Bonifati, V., Meunier, F. A., … Verstreken, P. (2017). The SAC1 domain in synaptojanin is required for autophagosome maturation at presynaptic terminals. *The EMBO Journal*, *36*(10), 1392. https://doi.org/10.15252/EMBJ.201695773

Verstreken, P., Koh, T. W., Schulze, K. L., Zhai, R. G., Hiesinger, P. R., Zhou, Y., Mehta, S. Q., Cao, Y., Roos, J., & Bellen, H. J. (2003). Synaptojanin Is Recruited by Endophilin to Promote Synaptic Vesicle Uncoating. *Neuron*, *40*(4), 733–748. https://doi.org/10.1016/S0896-6273(03)00644-5

Vinogradova, O., Velyvis, A., Velyviene, A., Hu, B., Haas, T. A., Plow, E. F., & Qin, J. (2002). A Structural Mechanism of Integrin αIIbβ3 "Inside-Out" Activation as Regulated by Its Cytoplasmic Face. *Cell*, *110*(5), 587–597. https://doi.org/10.1016/S0092-8674(02)00906-6

Wang, J. H. (2012). Pull and push: Talin activation for integrin signaling. *Cell Research 2012 22:11*, *22*(11), 1512–1514. https://doi.org/10.1038/cr.2012.103

Wang, Y., Yao, M., Baker, K. B., Gough, R. E., Le, S., Goult, B. T., & Yan, J. (2021). Force-Dependent Interactions between Talin and Full-Length Vinculin. *Journal of the American Chemical Society*, *143*(36), 14726–14737. https://doi.org/10.1021/JACS.1C06223

Watanabe, M., Nomura, K., Ohyama, A., Ishikawa, R., Komiya, Y., Hosaka, K., Yamauchi, E., Taniguchi, H., Sasakawa, N., Kumakura, K., Ushiki, T., Sato, O., Ikebe, M., & Igarashi, M. (2005). Myosin-Va regulates exocytosis through the submicromolar Ca2+-dependent binding of syntaxin-1A. *Molecular Biology of the Cell*, *16*(10), 4519–4530. https://doi.org/10.1091/MBC.E05-03-0252

Watanabe, S., & Boucrot, E. (2017). Fast and ultrafast endocytosis. *Current Opinion in Cell Biology*, *47*, 64–71. https://doi.org/10.1016/J.CEB.2017.02.013

Watanabe, S., Mamer, L. E., Raychaudhuri, S., Luvsanjav, D., Eisen, J., Trimbuch, T., Söhl-Kielczynski, B., Fenske, P., Milosevic, I., Rosenmund, C., & Jorgensen, E. M. (2018). Synaptojanin and endophilin mediate neck formation during ultrafast endocytosis. *Neuron*, *98*(6), 1184. https://doi.org/10.1016/J.NEURON.2018.06.005

Watanabe, S., Rost, B. R., Camacho-Pérez, M., Davis, M. W., Söhl-Kielczynski, B., Rosenmund, C., & Jorgensen, E. M. (2013). Ultrafast endocytosis at mouse hippocampal synapses. *Nature 2013 504:7479*, *504*(7479), 242–247. https://doi.org/10.1038/nature12809

Watanabe, S., Trimbuch, T., Camacho-Pérez, M., Rost, B. R., Brokowski, B., Söhl-Kielczynski, B., Felies, A., Davis, M. W., Rosenmund, C., & Jorgensen, E. M. (2014). Clathrin regenerates synaptic vesicles from endosomes. *Nature 2014 515:7526*, *515*(7526), 228–233. https://doi.org/10.1038/nature13846

Wen, K. K., Rubenstein, P. A., & DeMali, K. A. (2009). Vinculin Nucleates Actin Polymerization and Modifies Actin Filament Structure. *The Journal of Biological Chemistry*, *284*(44), 30463. https://doi.org/10.1074/JBC.M109.021295

Wenk, M. R., Pellegrini, L., Klenchin, V. A., di Paolo, G., Chang, S., Daniell, L., Arioka, M., Martin, T. F., & de Camilli, P. (2001). PIP Kinase Iγ Is the Major PI(4,5)P2 Synthesizing Enzyme at the Synapse. *Neuron*, *32*(1), 79–88. https://doi.org/10.1016/S0896-6273(01)00456-1

Wright, C. F., Teichmann, S. A., Clarke, J., & Dobson, C. M. (2005). The importance of sequence diversity in the aggregation and evolution of proteins. *Nature 2005 438:7069*, *438*(7069), 878–881. https://doi.org/10.1038/nature04195

Wu, X. S., Zhang, Z., Zhao, W. D., Wang, D., Luo, F., & Wu, L. G. (2014). Calcineurin is universally involved in vesicle endocytosis at neuronal and non-neuronal secretory cells. *Cell Reports*, *7*(4), 982. https://doi.org/10.1016/J.CELREP.2014.04.020

Wu, Y., O'Toole, E. T., Girard, M., Ritter, B., Messa, M., Liu, X., McPherson, P. S., Ferguson, S. M., & de Camilli, P. (2014). A dynamin 1-, dynamin 3- and clathrin-independent pathway of synaptic vesicle recycling mediated by bulk endocytosis. *ELife*, *3*. https://doi.org/10.7554/ELIFE.01621

Yamashita, H., Ichikawa, T., Matsuyama, D., Kimura, Y., Ueda, K., Craig, S. W., Harada, I., & Kioka, N. (2014). The role of the interaction of the vinculin proline-rich linker region with vinexin α in sensing the stiffness of the extracellular matrix. *Journal of Cell Science*, *127*(9), 1875–1886. https://doi.org/10.1242/JCS.133645/VIDEO-12

Yan, J., Yao, M., Goult, B. T., & Sheetz, M. P. (2015). Talin Dependent Mechanosensitivity of Cell Focal Adhesions. *Cellular and Molecular Bioengineering*, *8*(1), 151–159. https://doi.org/10.1007/S12195-014-0364-5/FIGURES/4

Yancey, K. B. (2017). The Biology of the Basement Membrane. In *Dermatology* (Fourth Edition, pp. 483–493). Elsevier.

Yang, X. da, Korn, H., & Faber, D. S. (1990). Long-term potentiation of electrotonic coupling at mixed synapses. *Nature*, *348*(6301), 542–545. https://doi.org/10.1038/348542A0

Yang, J., Zhu, L., Zhang, H., Hirbawi, J., Fukuda, K., Dwivedi, P., Liu, J., Byzova, T., Plow, E. F., Wu, J., & Qin, J. (2014). Conformational activation of talin by RIAM triggers integrin-mediated cell adhesion. *Nature Communications 2014 5:1*, *5*(1), 1–9. https://doi.org/10.1038/ncomms6880

Yao, M., Goult, B. T., Chen, H., Cong, P., Sheetz, M. P., & Yan, J. (2014). Mechanical activation of vinculin binding to talin locks talin in an unfolded conformation. *Scientific Reports*, *4*. https://doi.org/10.1038/SREP04610

Yao, M., Goult, B. T., Klapholz, B., Hu, X., Toseland, C. P., Guo, Y., Cong, P., Sheetz, M. P., & Yan, J. (2016). The mechanical response of talin. *Nature Communications*, *7*. https://doi.org/10.1038/NCOMMS11966

Yoshii, A., Zhao, J. P., Pandian, S., van Zundert, B., & Constantine-Paton, M. (2013). A Myosin Va Mutant Mouse with Disruptions in Glutamate Synaptic Development and Mature Plasticity in Visual Cortex. *The Journal of Neuroscience*, *33*(19), 8472. https://doi.org/10.1523/JNEUROSCI.4585-12.2013

Yu, M., Le, S., Ammon, Y. C., Goult, B. T., Akhmanova, A., & Yan, J. (2019). Force-Dependent Regulation of Talin-KANK1 Complex at Focal Adhesions. *Nano Letters*, *19*(9), 5982–5990. https://doi.org/10.1021/ACS.NANOLETT.9B01732/SUPPL_FILE/NL9B01732_LIVESLIDES.MP4

Yu, S. C., Klosterman, S. M., Martin, A. A., Gracheva, E. O., & Richmond, J. E. (2013). Differential Roles for Snapin and Synaptotagmin in the Synaptic Vesicle Cycle. *PLoS ONE*, *8*(2). https://doi.org/10.1371/JOURNAL.PONE.0057842

Zacharchenko, T., Qian, X., Goult, B. T. T., Jethwa, D., Almeida, T. B. B., Ballestrem, C., Critchley, D. R. R., Lowy, D. R. R., & Barsukov, I. L. L. (2016). LD Motif Recognition by Talin: Structure of the Talin-DLC1 Complex. *Structure(London, England:1993)*, *24*(7), 1130. https://doi.org/10.1016/J.STR.2016.04.016

Zhang, K., & Chen, J. F. (2012). The regulation of integrin function by divalent cations. *Cell Adhesion & Migration*, *6*(1), 20. https://doi.org/10.4161/CAM.18702

Zhu, L., Liu, H., Lu, F., Yang, J., Byzova, T. v., & Qin, J. (2019). Structural Basis of Paxillin Recruitment by Kindlin-2 in Regulating Cell Adhesion. *Structure*, *27*(11), 1686-1697.e5. https://doi.org/10.1016/J.STR.2019.09.006

Ziegler, W. H., Liddington, R. C., & Critchley, D. R. (2006). The structure and regulation of vinculin. *Trends in Cell Biology*, *16*(9), 453–460. https://doi.org/10.1016/J.TCB.2006.07.004